TECHNISCHE UNIVERSITÄT MÜNCHEN

Lehrstuhl für Raumfahrttechnik

Dynamic thermal modeling for moving objects on the Moon

Dipl.-Ing. Univ. Philipp Benjamin Hager

Vollständiger Abdruck der von der Fakultät für Maschinenwesen der Technischen Universität München zur Erlangung des akademischen Grades eines

Doktor-Ingenieurs (Dr.-Ing.)

genehmigten Dissertation.

Vorsitzender: Univ.- Prof. Dr.-Ing. Manfred Hajek

Prüfer der Dissertation: 1.) Univ.-Prof. Dr.rer.nat. Dr. h.c. Ulrich Walter

                          2.) Associate Professor, David M. Klaus, Ph.D. (University of Colorado at Boulder, USA)

Preface

A quote that inspires me since my 18th birthday:

> *"Our deepest fear is not that we are inadequate. Our deepest fear is that we are powerful beyond measure. It is our light, not our darkness that frightens us most. We ask ourselves, 'Who am I to be brilliant, gorgeous, talented, and famous?' Actually, who are you not to be? You are a child of God. Your playing small does not serve the world. There is nothing enlightened about shrinking so that people won't feel insecure around you. We were born to make manifest the glory of God that is within us. It's not just in some of us; it's in all of us. And when we let our own light shine, we unconsciously give other people permission to do the same. As we are liberated from our own fear, our presence automatically liberates others."*

> \- Used by Nelson Mandela in his *1994* inaugural speech

Acknowledgments

Abstract

In this work a new method was developed, implemented, and verified to calculate the transient thermal environment for man-made objects on the surface of the Moon. A differentiated design based on transient heat fluxes for a moving object is now possible, in contrast to the worst case design approach prevailing in spacecraft thermal engineering of today.

The thermal surface environment of the Moon is harsh and diverse, and thus poses demanding requirements to the design of surface-crafts. A lack of atmosphere and the insulating surface material lead to temperatures ranging from 25 K in permanently shadowed craters at the lunar poles to 390 K at the subsolar point on the lunar equator. Furthermore, local surface temperatures can bridge 200 K from sunlit to shadowed spots, over a couple of centimeters. The lunar topography is characterized by craters and boulders of a large variety of sizes. Each crater and boulder alters local surface temperatures. The developed method provides a means to take into account these local and global points of influence, determine the transient thermal environment, and subsequently calculate component temperatures for a mobile object on the lunar surface. The software implementation of the method, was named - the *Thermal Moon Simulator* (*TherMoS*). *TherMoS* consists of models to reproduce surface and surface feature temperatures on the Moon, define the position of the Sun, to perform ray tracing for infrared and solar heat fluxes, and to predict heat fluxes, heat flux rates and temperatures on mobile surface-crafts.

The thermal lunar surface models used in the *TherMoS* tool were verified against remote sensing data from the US Lunar Reconnaissance Orbiter (LRO) and literature. The verification showed a deviation of less than 10 % for undisturbed regolith in isolated surface patches as well as entire landscapes. Only in regions with different material properties, such as steep slopes or depressions the deviations were higher. In general, the deviations were lower at higher surface temperatures and vice versa.

The case studies were performed with exploration rovers of varying detail and a spacesuit in different postures. Rover and spacesuit sample bodies were set in a variety of lunar landscapes, moved along predefined paths, and performed operations imitating geological tasks. A multitude of simulation runs were performed and compared to evaluate the impact of lunar surface temperatures and features. Transits in front of sunlit boulders can increase received infrared heat by up to 330 % and the transit through a small bowl shaped crater can decrease solar heat flux by 86 % compared to the same transit over an unobstructed plane. The results indicate that the impact of surface features, in relative as well as absolute numbers, is more pronounced at lower solar elevation angles. Heat flux rates of < 5 W$\cdot$m$^{-2}\cdot$s^{-1} occurred for 72.6 % of the time, and heat flux rates > 40 W$\cdot$m$^{-2}\cdot$s^{-1} occurred at less than 1 % of the time at a solar elevation angle of 10°. The decline has the shape of a power function with negative exponent. Smaller heat flux rates have a higher occurrence at lower surface temperatures and vice versa.

From the results, one can conclude that paths and operations on the Moon must be investigated thoroughly in the view of local surface features and temperatures. Transient analysis can help in the profiling of mission scenarios and the derivation of requirements. In subsequent phases of a project, transient analysis can help in the design of technologies, equipment, and the entire surface-craft. Especially emerging technologies profit from transient thermal calculations, such as electrochromic or digital radiators, or buffering technologies such as phase change material. Finally, transient analysis enables more detailed mission operations for example thermal path planning and scheduling of tasks.

This work points out the necessity for transient calculations and provides a new method for the thermal analysis of surface-craft, to support future exploration on and of the surface of the Moon.

Zusammenfassung

In dieser Arbeit wurde eine neue Methode entwickelt, implementiert und verifiziert welche die Berechnung der transienten thermischen Umwelt für bewegliche Objekte auf dem Mond erlaubt. Dies stellt eine Ergänzung zu der, gegenwärtig vorherrschenden Vorgehensweise zur thermischen Auslegung von Raumfahrzeugen dar, welche auf Extremwertbetrachtungen basiert.

Die thermischen Umweltbedingungen auf dem Mond sind unwirtlich, variieren stark von Ort zu Ort und sind daher anspruchsvoll für die Auslegung von Raumfahrzeugen. Der Mond besitzt keine Atmosphäre und die Oberfläche ist von einem isolierenden Material, dem regolith, bedeckt. Diese Kombination führt zu Temperaturen, die von 25 K in permanent abgeschatteten Kratern an den Mondpolen, bis hin zu 400 K am sub-solaren Punkt am Mondäquator, reichen. Lokale Temperaturgradienten können bis zu 200 K erreichen, bereits über Distanzen von wenigen Zentimetern zwischen sonnenbeschienen und abgeschatteten Orten. Die für den Mond charakteristischen Krater und Gesteinsbrocken unterschiedlichster Größen verändern die lokalen thermischen Umweltbedingungen. In dieser Arbeit wurde eine Simulationsmethode entwickelt um diesen thermischen Einfluss, auf sich bewegende Objekte auf der Mondoberfläche, zu bestimmen. Die *Thermal Moon Simulator (TherMoS)* genannte Simulationsmethode besteht aus einzelnen Sub-Modellen zur Bestimmung der Mondoberflächentemperaturen, der Sonnenposition, zur Berechnung des Wärmeaustausches durch Strahlung und damit des zeitaufgelösten thermischen Zustandes des Raumfahrzeuges.

Die in *TherMoS* verwendeten thermischen Modelle der Mondoberfläche wurden gegen Fernerkundungsdaten des amerikanischen Lunar Reconnaissance Orbiters (LRO) und gegen Literaturdaten verifiziert. Dabei zeigten sich Temperaturabweichungen des regolith kleiner 10 %. In Regionen mit veränderten Materialeigenschaften des Bodens, etwa an Kraterwänden oder in Senken und bei niedrigen regolith-temperaturen, zeigten sich größere Abweichungen.

Als bewegliche Objekte wurden robotische Erkundungsfahrzeuge (Rover) und Raumanzüge untersucht. In den durchgeführten Fallstudien bewegen sich Rover- und Raumanzugmodelle durch Mondlandschaften entlang definierter Pfadsegmente und werden mit einem Transit über eine Ebene ohne Hindernisse verglichen. Der Transit eines Rovers vor einem sonnenbeschienen Gesteinsbrocken kann die empfangene infrarote Wärmeflussdichte um bis zu 330 % erhöhen, und ein Transit durch einen kleinen Primärkrater kann die solare Wärmeflussdichte um 86 % reduzieren. Es zeigte sich zudem, dass der Einfluss von Kratern und Gesteinsbrocken auf Raumfahrzeuge bei niedrigen Sonnenständen größer ist. Auf der Oberfläche eines Raumanzuges waren die Änderungsraten der Wärmeflussdichte < 5 W·m^{-2}·s^{-1} für 72.6 % der Zeit und nur 1 % der Zeit > 40 W·m^{-2}·s^{-1}, bei Sonneneinfallswinkeln von 10°. Die Abnahme der Wärmeflussdichten entspricht einer Potenzfunktion mit negativem Exponenten. Kleinere Änderungsraten für Wärmeflussdichten treten bei niedrigen Mond-Oberflächentemperaturen häufiger auf und umgekehrt.

Aus den Ergebnissen lässt sich ableiten, dass Operationen von beweglichen Raumfahrzeugen in der Nähe von Kratern oder Gesteinsbrocken auf dem Mond sehr genau untersucht werden müssen. Die Analyse der transienten Wärmebelastung kann dabei helfen Missionsszenarien festzulegen und daraus Anforderungen abzuleiten. In den folgenden Phasen eines Projektes können transiente Analysen dazu eingesetzt werden Technologien, Ausrüstungsgegenstände oder gesamte Raumfahrzeuge auszulegen. Gerade neue Technologien wie zum Beispiel elektrochromatische oder digitale Radiatoren, profitieren von transienten Thermalberechnungen ebenso wie Technologien die Wärmeenergie puffern, wie z.B. Phasenänderungsmaterialien. Im Betrieb der Raumfahrzeuge ermöglichen transiente Analysen z.B. Planung und Optimierung von Operationen auf der Oberfläche.

Diese Arbeit untermauert die Notwendigkeit transienter Thermalberechnungen für Raumfahrzeuge auf dem Mond. Gleichzeitig wird eine neue Methode vorgestellt, mit welcher diese transienten Analysen für Rover oder Raumanzüge ermöglicht werden, um die zukünftige Erforschung der Oberfläche des Mondes zu unterstützen.

Contents

Abbreviations & Acronyms

ACS	Active Control System
AU	Astronomical Unit
ALSEP	Apollo Lunar Surface Experiments Package
ARTG	Advanced Radioisotope Thermoelectric Generator
ASRG	Advanced Sterling Radioisotope Generator
ATC	Active thermal control
ATHLETE	All Terrain Hex Limed Extra Terrestrial Explorer
BOL	Begin of Life
CAD	Computer Aided Design
CCD	Charged Coupled Device
CNSA	China National Space Administration
COTS	Commercial-of-the-Shelf
DLR	Deutsches Zentrum für Luft- und Raumfahrt
DLRE	Diviner Lunar Radiometer Experiment
ECLSS	Environmental Control and Life Support System
ECR	Electrochromic Radiator
EOL	End of Life
ESA	European Space Agency
EVA	Extra vehicular activity
FEM	Finite-Element-Method
FDM	Finite-Difference-Method
FVM	Finite-Volume-Method
GEO	Geostationary Orbit
GLXP	Global Lunar XPrize
GPHS-RTG	General Purpose Heat Source Radioisotope Thermoelectric Generator
GPU	Graphics Processing Unit
GUI	General User Interface
HX	Heat Exchanger
IR	Infrared
ISECG	International Space Exploration Coordination Group
ISRO	Indian Space Research Organization
ISRU	In-situ Resource Utilization
ISS	International Space Station
IXO	International X-Ray Observatory
JAXA	Japan Aerospace Exploration Agency
JPL	Jet Propulsion Laboratory
JSC	Johnston Space Flight Center
KT	Kayser-Threde GmbH
LALT	Laser ALTimeter
LCG	Liquid Cooling Garment
LCROSS	Lunar Crater Observation and Sensing Satellite
LDAB	Lunar dust adhesion bell
LDAP	Lunar Dust Adhesion Bell
LEAG	Lunar Exploration Analysis Group
LEO	Low Earth Orbit
LIDAR	Light Detection and Ranging
LL	Lunar Lander
LOLA	Lunar Orbiter Laser Altimeter
LPM	Lumped Parameter Method
LPRP	Lunar Precursor Robotics Program
LRO	Lunar Reconnaissance Orbiter
LROC	Lunar Reconnaissance Orbiter Camera
LRT	Lehrstuhl für Raumfahrttechnik
LRV	Lunar Roving Vehicle
MCL	Model Confidence Level
MEO	Medium Earth Orbit
MER	Mars Exploration Rover
MET	Mobile Equipment Transporter
MLI	Multi-layer insulation
MMH	Monomethylhydrazine
MMRTG	Multi Mission Radioisotope Thermoelectric Generator
MPE	Mobile Payload Element
MR	Metabolic Rate
MSL	Mars Science Laboratory (Curiosity)
NASA	National Aeronautics and Space Agency

NEO	Near Earth Objects	SPICE	Spacecraft Planet Instrument C-matrix Events
NTO	Nitrogen tetroxide		
PANGU	Planet and Asteroid Natural Scene Generation Utility	SRG	Sterling Radioisotope Generator
		SSWM	Spacesuit Water Membrane Evaporator
PCM	Phase Change Material		
PDS	Planetary Data System	SWIP	Solar Wind Implanted Particles
PI	Principal Investigator	TEG	Thermoelectric Generators
PLSS	Personal Life Support System	TherMoS	Thermal Moon Simulator
PTC	Passive Thermal Control	TRL	Technology Readiness Level
RADAR	Radio Detection and Ranging	TUM	Technische Universität München
RTG	Radioisotope Thermoelectric Generator	UTC	Unified Time Coordination
		USGS	United States Geological Survey
SEV	Space Exploration Vehicle	VCHP	Variable Conductance Heat Pipe
SPCM	Sub-cooled Change Phase Material	VSOP2000A	Variations Séculaires des Orbites Planétaires 2000 release A

Symbols & Indices

Symbols:		SI-units
α	Absorptivity	[-]
α_{az}	Azimuth	[°]
α_{sl}	Slope angle	[°]
β	Heat pulse duty cycle	[-]
ε	Emissivity	[-]
ε_{el}	Elevation	[°]
θ_r	Angle of repose	[°]
θ	Angle of incident	[°]
λ	Wavelength	[m]
λ_l	Longitude	[°]
λ_{lat}	Latitude	[°]
υ	Frequency	[s^{-1}]
ρ	Density	[kg·m^{-3}]
ρ^k	Reflectance	[-]
τ^k	Transmitance	[-]
ω	Solid angle	[°]
Ω	Angular velocity	[s^{-1}]
Υ	Vernal Equinox	[-]
b	Factor in Plancks' law	[-]
C	Capacitor	[J·K^{-1}]
c_p	Specific heat capacity	[J·kg^{-1}·K^{-1}]
D	Diameter	[km]
d	Distance	[m]
E	Total emissive power	[W]
e	Spectral emissive power	[W·m^{-2}·µm^{-1}]
F	View Factor	[-]
G	Conductor	[W·m^{-4}]
I	Intensity	[W·m^{-2}]
k	Thermal conductivity	[W·m^{-1}·K^{-1}]
m	Mass	[kg]
n_r	Refractive index	[-]
n	Number	[-]
$\dot{Q}$	Thermal energy rate = Heat	[W]
q	Heat flux	[W·m^{-2}]
$\dot{q}$	Heat flux rate	[W·m^{-2}·s^{-1}]
R	Radius	[m]
r	Rate	[-]
T	Temperature	[K]
t	Time	[s]
$\dot{w}$	Rate of energy generation per unit volume	[W·m^{-3}]
u	Velocity	[m·s^{-1}]

Constants:

σ Stefan-Boltzmann constant
5.67·e^{-8} W·m^{-2}·K^{-4}
c_0 Speed of light in vacuum
299 292 458 m·s^{-1}
k_B Boltzmann constant
1.380·e^{-23} J·K^{-1}
h Planck constant
6.626·e^{-34} J·s^{-1}

Indices:

Az	Azimuth
B	Boulder
bb	Black body
C	Crater
$cold$	Cold
E	Earth
El	Elevation
env	Environment
F	View Factor
$glob$	Global
hot	Hot
hum	Human
IR	Infrared
in	Incoming
L	Conductive Interface
loc	Local
M	Moon
max	Maximum
$mean$	Mean
min	Minimum
o	Origin
out	Outgoing

R	Radiative Interface		*stat*	Static
rad	Radiator		*suit*	Suit
ray	Ray		*surf*	Surface
r	Rim		*syn*	Synodic
Reg	Regolith		*temp*	Temperature
rov	Rover		*td*	Turndown
s	Surface		*wall*	Crater wall
sl	Slope		*0*	Initial condition
Sol	Solar		*λ*	Wavelength dependent
st	Stored			

1 Thesis Scope

"When I look at the moon I do not see a hostile, empty world. I see the radiant body where man has taken his first steps into a frontier that will never end."

— David R. Scott, Apollo 15 commander

1.1 Motivation

The Moon is awe-inspiring and has been the object of dreams and longings since the dawn of humankind. Scientific questions as well as our immanent desire to explore new lands push forward the frontiers of the human race. The Moon is a symbol of the technological capabilities enabled by this ever searching nature of our species. The Apollo and Luna programs were not the last steps in our wish for knowledge about the Moon, but they marked a cornerstone in our understanding of the Moon. The programs pushed open a window to the riddles still unresolved in our solar system, riddles that cannot be solved even by the most sophisticated remote sensing instruments available nowadays (Jaumann et al. 2012). The Moon bears a chronology of the Earth-Moon system that long has been extinguished on Earth due to plate tectonics, weather and seasons. Future missions will have to return to the surface of the Moon to answer the still open scientific questions. In the long run, the Moon must also be the test bed for any further human exploration of our solar system (ISECG 2011; Claasen et al. 2012). Whereas robotic systems are precursors and pathfinders, as well as valuable helpers, they can never replace the spirit and mind, the knowledge and ability to adapt, to decision making based on the new and unknown, that a human can provide.

Figure 1-1: Astronaut Harrison H. Schmitt investigates a large boulder during a sortie with the lunar roving vehicle (right). One can see the shadowed regions as well as the sunlit side of the boulder and nearby mountains (NASA 1972b).

As robotic systems and humans return to the Moon, they encounter a hazardous environment, characterized by the ultra-high vacuum, radiation from the Sun and the cosmic background, from ultraviolet radiation, and the radiative exchange of heat. One of the driving factors for the design of any spacecraft are the operational temperatures of instruments and equipment (Gilmore, ed. 2002-c2003; Wertz and Larson 1999). The temperature of any piece of equipment in turn is governed by material properties, optical properties, internal heat sources and heat fluxes from the environment. The surface of the Moon is cov-

ered by a porous media with thermally insulating properties, the regolith (Heiken et al. 1991). In the atmosphere-less environment, this material can reach temperatures ranging from 25 K to 400 K, and temperature gradients of tens and hundreds of Kelvin over short distances. Temperature extremes of varying magnitude can be encountered almost everywhere on the Moon. The heat transport from the environment is dominated by radiation, due to the lack of an atmosphere. Figure 1-1 shows astronaut H.H. Scott and the lunar roving vehicle in the vicinity of a boulder close to the Taurus-Lithrow mountain range during Apollo 17. The local latitude, surface features such as boulders, craters, slopes or mountain ranges and the current position of the Sun rule local temperatures. Local temperatures govern the infrared heat fluxes from the environment, and local topography, time of day, and the local latitude govern the solar heat flux. The craters reach from sub-micron size to several hundreds of kilometers. The boulders range from several centimeters to tens of meters in diameter. These surface features are scattered randomly on the lunar surface and lead to a large variety in local temperature and lighting conditions. Rovers and humans in spacesuits will move through this demanding environment and encounter ever changing thermal boundary conditions.

"On the surface of an atmosphereless body, the thermal environment is dictated, as in deep space, by radiative balance. The difference is that there are many radiating and shadowing surfaces around. Whereas in deep space only the Sun and a (spherical) Earth need be considered and calculations can be performed by hand, the evolving thermal environment on the surface of a rotating planet generally requires more elaborate computation using time-marching numerical methods."

– Ball, Andrew J.; "Planetary Landers and entry probes" (2007)

The lunar surface temperature has been modeled and measured from a scientific standpoint for almost 80 years. Numerical methods for the design of spacecraft have evolved throughout the past 30 years but are focused on orbiting spacecraft and interplanetary missions. The general approach for the design of planetary probes is to design for worst case hot and cold conditions. This approach is well suited for first order estimations, relatively benign environments as on the surface of Mars, or if large factors of safety and a higher system mass is acceptable. The thermal environment on the Moon, stringent scientific as well as engineering requirements demand a new and transient approach for the design of surface-craft, of thermal-control components, and mission operations.

1.2 Hypothesis and Problem Statement

As of now, the common approach for the layout of planetary surface-craft is to design for static worst case thermal conditions. For moving surface-craft the environment is neither digital hot/cold nor will the design for maximum and minimum cases yield realistic spacecraft masses. Hence, the hypothesis of this work is:

> **Static thermal simulations are not adequate to predict the thermal behavior of moving spacecraft on atmosphere-less celestial bodies.**

The transient thermal behavior of moving spacecraft has relevance especially for scientific instruments with stringent thermal stability requirements and for emerging technologies for thermal control which facilitate transient effects.

- Emerging technologies are for example electrochromatic radiators (Metts et al. 2011), two phase loop heat pipes (Nabity et al. 2008), digital radiators (Ganapathi et al. 2009), or self-regulated heat exchanger.
- The stringent scientific thermal requirements are the stability of volatile elements on the lunar poles (Greenwood et al. 2011; Colaprete et al. 2010), seismic instruments for the lunar seismic network or optical instruments on Moon based telescopes.

The classic approach towards the thermal design of spacecraft and surface-craft is to start with conservative worst case calculations. The worst case hot is determined by the maximum external or environmental and internally dissipated heat fluxes. The worst case cold in contrast is determined by the minimum external and lowest internally dissipated heat fluxes. During the course of a project, when the subsystems, the operation modes and the overall mission scenario matures, these worst cases become more detailed. For spacecraft in an orbit or on interplanetary trajectories, the environment and with it environment heat fluxes can be predicted based on orbital mechanics. Here the purpose of the spacecraft, its instruments and their attitude towards the central body define the heat fluxes even more precisely. The thermal design further is driven by the used materials and methods in the spacecraft, subsystem and instrument design. The instruments which make up the core purpose or payload of the entire spacecraft dictate the thermal design. Instruments such as telescopes need to operate at extremely low and stable temperatures to avoid erroneous measurements (Pecson et al. 2002-c2003; Choi 2010). Batteries and other electronic equipment on the other hand operate best in a temperature range from 0 to +25°C. If humans are involved their survivability and safety dictates the thermal design.

With the progression of a project, more sophisticated thermal software models are produced, remade and amended and eventually verified against hardware tests in appropriate facilities. Soon the thermal software models cannot be calculated by hand and worst case analyses alone are not sufficient anymore. Common commercially available software packages, such as ESATAN-TMS® or Thermal Desktop/SINDA® were developed for spacecraft in orbit, in Lagrangian points, or on interplanetary trajectories. Beside the commercial tools, space companies developed proprietary thermal-engineering tools for specific problems, such as cryogenic optics or propulsion feed lines. All of the available tools have in common that they were designed to help analyze either static and transient cases for spacecraft orbiting a planet or moon, for spacecraft on interplanetary trajectories, or they were tailored to analyze specific instruments.

If the thermal analysis of surface-craft is possible at all, they are restricted to basic static calculations. In Figure 1-2 a comparison between a static and a transient thermal analysis for a surface-craft is sketched. The static worst case analysis on the left yields a higher temperature range and maximum and minimum temperatures at different times compared to a transient analysis, depicted on the right. By the more detailed transient approach margins can be set more accurate, thermal buffers can be designed and the overall system confidence increases. Rates of change important for the design of control algorithms cannot be addressed by mere static calculations at all.
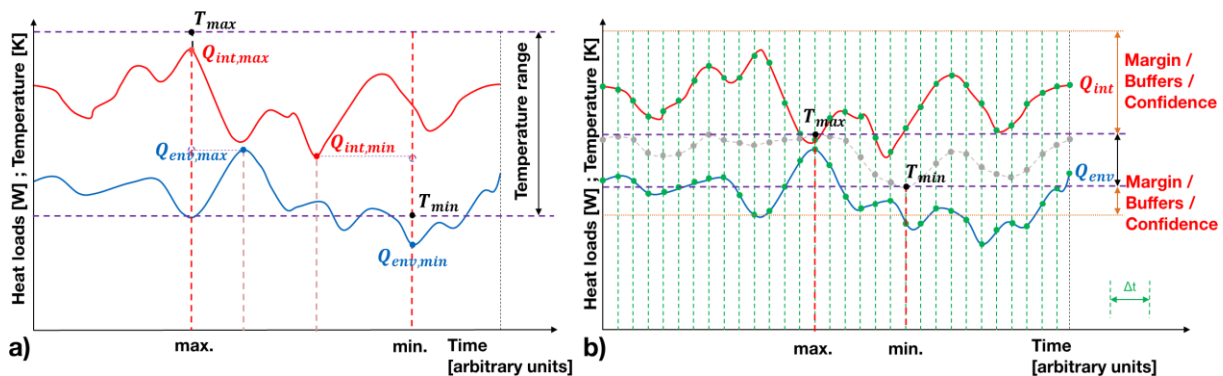
Figure 1-2: Quantitative comparison between the design temperature range obtained by a) a static and by b) a transient approach. The red line denotes the internal heat load and the blue line the environmental heat load. The green lines in b) mark the interval between calculation steps; T_{min} and T_{max} result from either a) worst case or b) time-dependent calculations.

1.3 Approach

"If you want to build a ship, don't rally the men to get wood, distribute responsibilities and divide tasks, but instead teach men the yearning for the wide, endless sea."

- Antoine de Saint-Exupéry

A dissertation cannot be written by mere yearning nor can it be distributed amongst others, hence the tasks must be defined, structured and implemented. The central element of this work is a method to calculate transient heat flux densities on surface-craft. The method was implemented into a MATLAB® based thermal calculation tool, called the *Thermal Moon Simulator - TherMoS*. The objectives for this method are derived from an investigation of past and present spacecraft thermal problems related to the Moon, based on past models on the lunar surface, and placed in a context of political, scientific and engineering demand. The *TherMoS* tool was implemented and verified stepwise based on the objectives and results from other models and remote sensing data.

With the Sun and the surface of the Moon being the sole sources of environmental heat for a surface-craft, the backbone of the used method are models on the lunar landscape and position of the Sun. The availability of existing models and methods was investigated in a first step. The most elementary models were identified for the lunar regolith, global topography, boulders, and craters, orbit propagation and ray tracing. Where possible and applicable existing models were adapted and integrated in the overall tool. In cases in which appropriate models did not exist or were not accessible, new models were created. Not before the functionality of one model was verified was it integrated with other models to form larger modules. This approach is depicted in Figure 1-3.
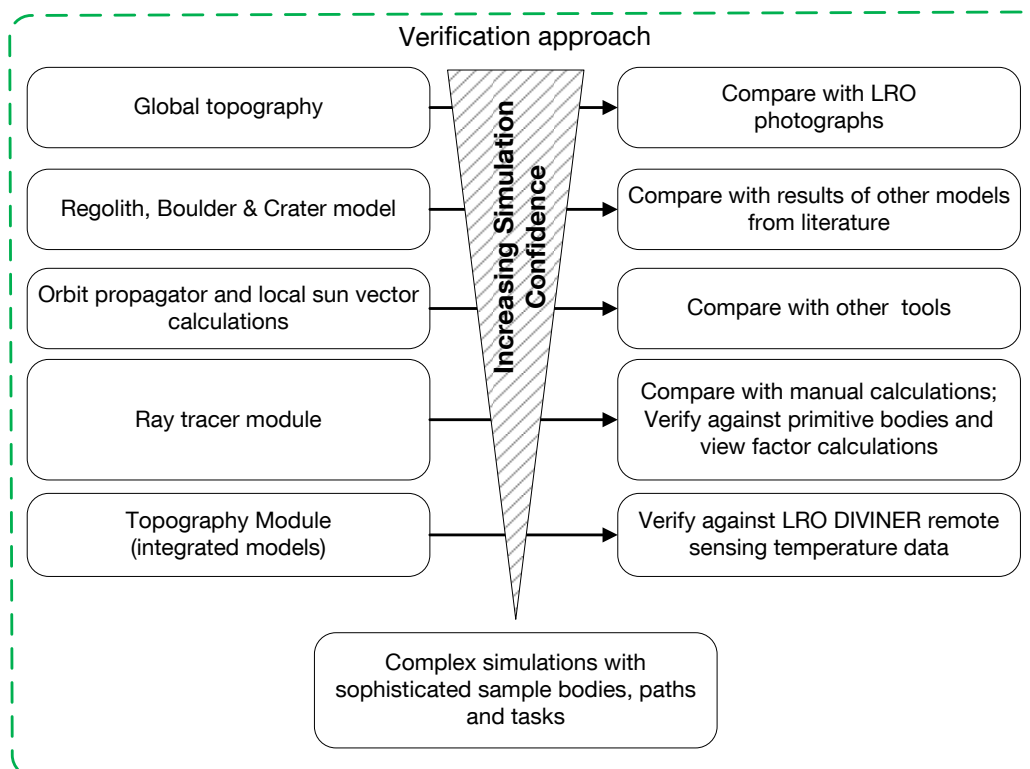
Figure 1-3: Verification approach for the models and modules used during the implementation of the *TherMoS* method.

The structure of the dissertation is presented in Figure 1-4. The thesis is split in three main parts. The first part is the thematic background, the subject of the second part is the used methods, and the third part covers the results and conclusions of the presented work.

Chapters 1 through 3 describe the background of the thesis. The state of the art (chapter 2) addresses past and present surface-craft thermal problems and presents work on scientific and thermal models of the lunar surface. Rovers and spacesuits, mainly from the Apollo era, but also recent concepts are reviewed with regard to thermal design problems created by neglecting transient effects. Thermal subsystem related problems of instruments and equipment such as overheating, and loss of functionality during Apollo and Luna program are pointed out. The intricate active thermal control necessary for spacesuits, caused by varying metabolic loads and the environment, are reviewed from Apollo to the International Space Station (ISS). In chapter 3 political, scientific and engineering demand for transient thermal simulations are evaluated in the view of past and present problems and models that were discussed in chapter 2. In chapter 3 the requirements resulting from programmatic, scientific and engineering perspectives are identified and the objectives for the required method are derived.

Chapter 4 and 5 focus on the building blocks that are necessary to meet the objectives. In chapter 4 the fundamentals for thermal heat transfer, the thermal space environment with a focus on the Moon, thermal spacecraft design and control, and computational methods thereof are introduced. In chapter 5 these fundamentals are merged and a new approach and method to simulate the thermal behavior of moving spacecraft on the Moon is presented (*TherMoS*). The background, introduced in chapter 4, is transformed into separate models. These are first verified individually to gain confidence. Subsequently, the models are integrated in larger modules which are further verified. The verification was obtained by comparison with other established tools, with literature data about other models, and recent remote sensing data from the Lunar Reconnaissance Orbiter (LRO).

In chapter 6 and 7 results and conclusions of the new method are presented and discussed. Chapter 6 contains the results of static, semi-transient and transient thermal calculations for primitive bodies, rovers and a spacesuit. Manual steady state view factor calculations were used as reference to depict the difference between static worst case and transient ray tracing method.

The sample bodies are evaluated in different environmental conditions for a variety of paths. A large number of possible combinations from surface temperatures and different obstacles as well as different task of the rover and spacesuit were evaluated. In chapter 7 the results are discussed, empirical equations derived were appropriate, and the findings are concluded. Simplified equations were generated that were used as initial and boundary conditions for the more sophisticated transient calculation. These equations can also be used independent of the *TherMoS* method. The results of the complex *TherMoS* simulations were also simplified in diagrams and tables to allow for an easier application. The thesis closes with a discussion on open questions and possible future steps.

Part 1
Background

1
Thesis Scope

2
State of the Art

Thermal problems | Thermal models

3
Gap Analysis

Programmatic requirements | Scientific requirements | Engineering requirements | Objectives

Part 2
*The simulation approach &
Building Blocks
(Methods)*

4
Fundamentals

Heat transfer | Space Environment | Thermal Engineering | Thermal Modelling

5
The Thermal Moon Simulator

Module Description | Module Verification

Part 3
Results & Conclusions

6
Case Studies

Static | Semi-transient | Transient long-time | Transient short-time

7
Discussion, Conclusion & Future Work

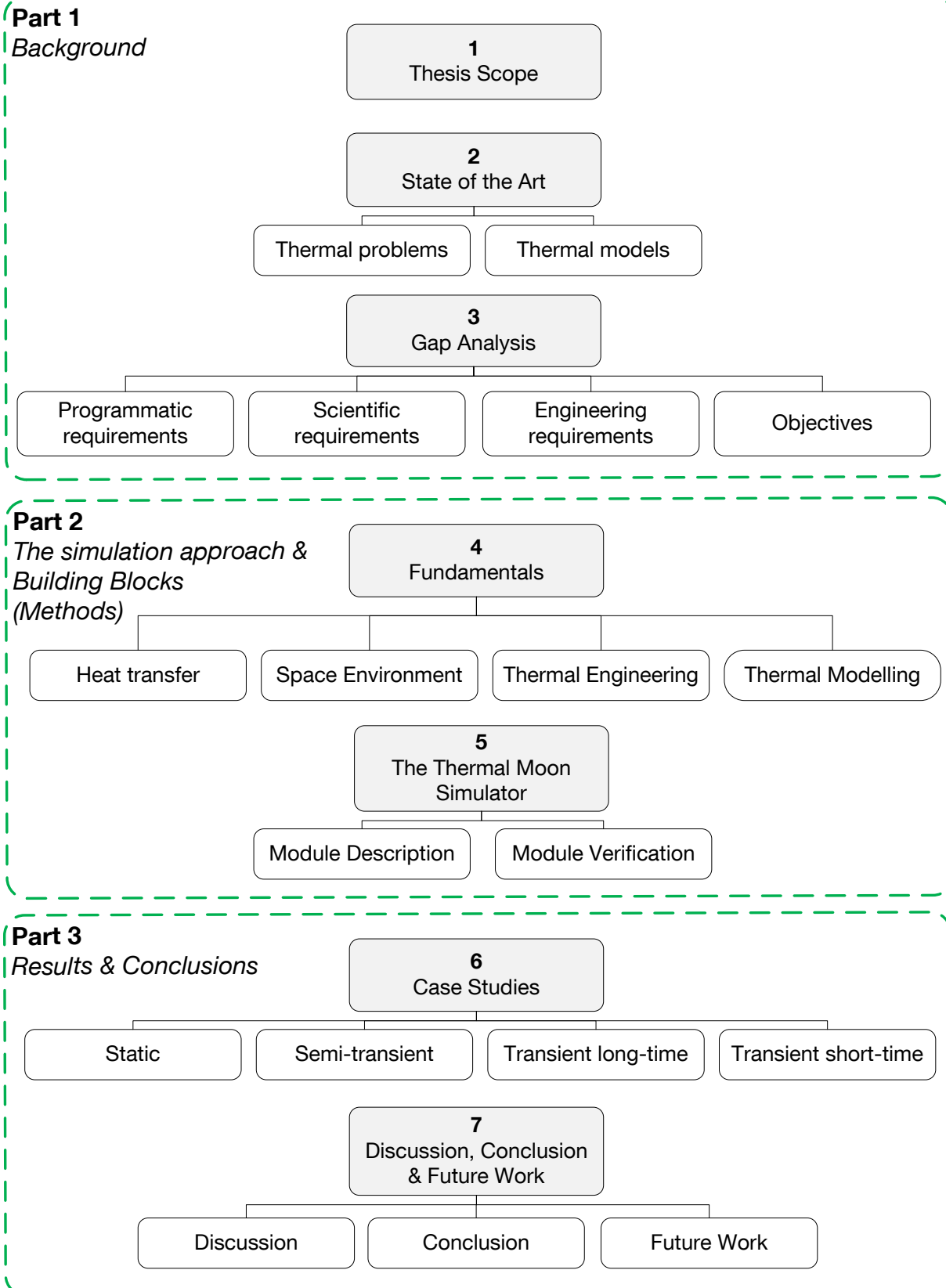Discussion | Conclusion | Future Work

Figure 1-4: Thesis structure.

2   State of the Art

"If knowledge can create problems, it is not through ignorance that we can solve them."

- Isaac Asimov

Since the beginning of spaceflight, almost 60 years ago, a number of missions were send to the Moon. There were dozens of probes in the 1960ths to scout the way for human landings, of which the first took place on 21st of July 1969. The US Apollo program put 12 humans on the surface of the Moon and collected data, lunar soil and rocks. In the Soviet Luna program the large unmanned Lunokhod I & II rovers were placed on the lunar surface in the early 1970s. These extraordinary endeavors still are the most valuable sources of information about how humans and equipment perform on the surface of the Moon, an extreme planetary environment.

In chapter 2.1 the performance of pieces of equipment are reviewed that were used during those missions. A special emphasis is put on instruments used during the Apollo missions and past rovers. Furthermore current concepts for rovers, as well as the performance of spacesuits during Apollo, the Space Shuttle, and MIR programs are discussed.

In the context of the missions and probes send to the Moon, a multitude of models (section 2.2) were developed in order to simulate the temperature behavior of the lunar surface. Most of these models are driven by scientific questions on how our Moon is composed. Other models focused more on the engineering aspects of equipment to be operated on the lunar surface. Yet another group of software tools were written in order to simulate the illumination and lighting conditions on the lunar surface in order to layout habitats or design instruments for landing. A number of models are discussed and compared with regard to their relevance to this work.

2.1   Thermal Problems of Bodies placed on the Lunar Surface

In the following section, thermal problems are named that were reported during past missions with landers and rovers as well as equipment used during the Apollo mission on the Moon. As for rovers, new concepts emerged throughout the past years aiming for a return to the Moon. Since lunar rovers are a popular means in education, an unmanageable number of preliminary designs exist. Only some of the concepts are reviewed and their challenges with regard to thermal design are pointed out. The third section is dedicated to spacesuits and the challenges resulting from the thermal environment during Apollo, Shuttle, MIR, and ISS missions.

2.1.1   Instruments

During Apollo 14 the Modular Equipment Transporter (MET) was used to transport instruments and equipment away from the Lunar Module (LM). The MET was designed to sustain minimal temperatures as low as 216 K. At a certain point during surface operations one wheel fell below that threshold temperature only because it was shadowed by the other parts of the MET (Clawson et al. 2002-c2003). The Apollo Astronauts had to adopt *in-situ* to this unforeseen condition in order not to loose the MET. They overcame the problem by positioning the MET in a way that no shadow was casted on the wheels. Figure 2-1a shows a photograph of the Apollo 14 MET.
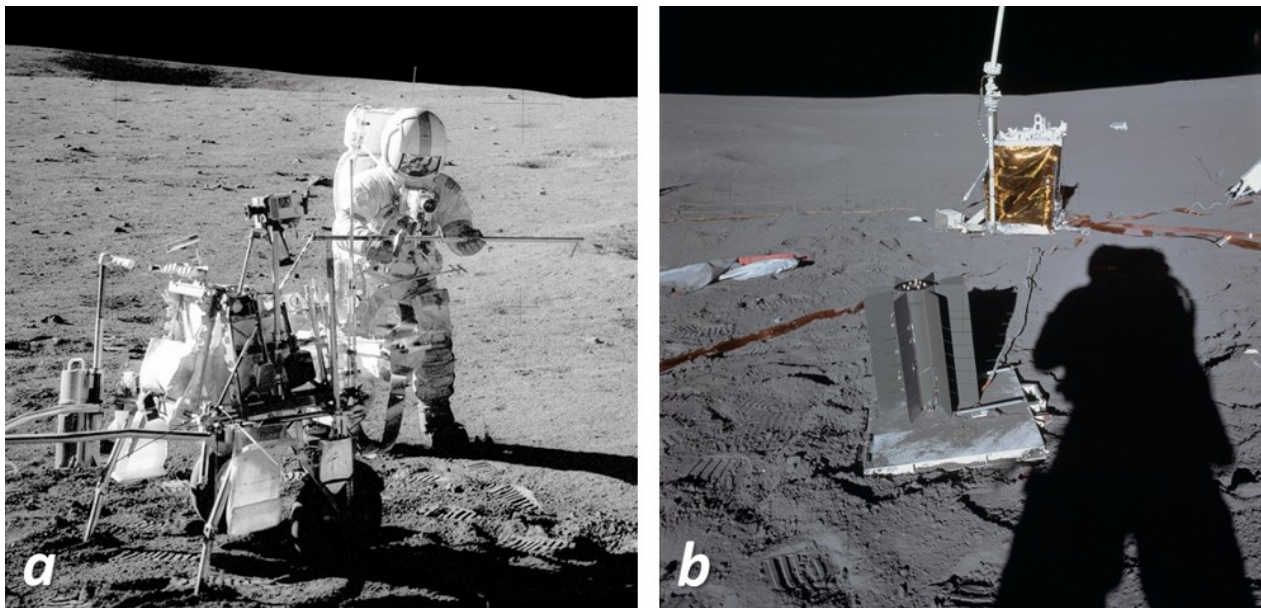
Figure 2-1; a) The Mobile Equipment Transporter (MET) during Apollo 14 (NASA 1971c), and b) Parts of the Apollo Lunar Surface Experiments Package (ALSEP) (NASA 1971a).

During Apollo 12, 14, 15, 16 & 17 the Apollo Lunar Surface Experiments Package (ALSEP) was deployed on the lunar surface. Of a total of eight different instruments a maximum of five were chosen and used per ALSEP. The configuration thus was individual to each mission. The central unit hosted a radioisotope thermoelectric generator (RTG) which distributed electrical energy to the different instruments, shown in Figure 2-1b. The instruments were deployed by the Astronauts in a circle around the central unit. The instruments were the Passive Seismic Experiment, the Lunar Surface Magnetometer, the Solar Wind Spectrometer, the Suprathermal- Ion-Detector Experiment and Cold-Cathode Ion Gage, the Active Seismic Experiment, the Heat Flow Experiment and the Cold-Cathode Gage Experiment (Harris 1972). Each instrument had its own passive thermal design. The instruments were designed to survive several lunar nights and work long after the Astronauts had left the lunar surface. The ALSEP experiments in Apollo 12 and 14 performed well except at three occasions. During Apollo 12 too low temperatures during lunar night were reported. This was probably due to a too large exposed radiator surface area, caused by a louver that did not close as expected. The problem was solved remotely from Earth by activating a mechanism permanently during the lunar night. It produced additional 3 W of heat which was enough to maintain operational temperatures. On Apollo 14 too high temperatures were measured on the passive Seismic Experiment Package. It was designed for temperature as high as 61°C. Due to coverage of the radiators with dust, debris, or combustion products from the ascent stage, the measured maximum temperature reached 89°C (Gaier and Jaworske 2007; Harris 1972). It took three full lunations to reach the temperature cycle. In Apollo 12 the magnetometer temperatures measured at different locations of the instrument were as high as 79°C although it was only designed for temperatures of 65°C. These high temperatures were encountered when the sun angle was between 55 and 140°, equal to a timeframe of 6.6 Earth days (Gaier 2005; Gaier and Jaworske 2007). During Apollo 16, plastic used in the design of the cosmic ray detector exceeded maximum allowable temperatures (54°C). The overheating probably occurred due to surface coating with dust (Gaier 2005). The early ALSEP design was designed to be operated near the lunar equator in a latitude range of +/- 5° (Harris 1972). The north and south facing sides were used as radiators. Apollo 15 through 17 landed at higher latitude, thus modifications of the ALSEP were necessary. Hence the thermal design had to be revisited since the incident solar heat flux would have been readily accumulated by the radiators (Harris 1972).

The Surveyor landers were used as scouts to explore the landing sites, the lunar environment and prove landing capabilities prior to the Apollo landings. They succeeded the Ranger spacecraft. Surveyors' main

target was a soft precision landing on the lunar surface. There were seven missions of which five were successful. Surveyor 1, 3, 4 and 5 landed in the equatorial mare regions on the lunar near side. Figure 2-2a shows a photograph of Surveyor 3 taken during Apollo 12. Surveyor 7 landed in a highland region south of the equator. Surveyor 2 and 4 crashed on the lunar surface. The thermal design of the Surveyor spacecraft was passive. It used white painting, high-infrared emissivity thermal finish and polished aluminum. The electronic equipped was contained in two heat boxes, which were insulated with thermal blankets. Conductive heat paths lead to the structure with which the heat boxes were connected. Heat switches and electronic heaters were used to control the heat flow in and out of the equipment electronic compartments (Ball 2007). The passive thermal design was designed to allow the spacecraft to survive lunar nights. The landings of the Surveyor spacecraft were scheduled to occur shortly after lunar sunrise in order to have the maximum of a lunar day (Ball 2007). Surveyor 1, 5 and 7 were able to survive at least one lunar night based on their passive thermal design (Ball 2007). This means that Surveyor 3 and 6 were functional during lunar day but could not be reactivated after the lunar night.

The Surveyor Science Report states that the temperatures aboard the spacecraft during lunar morning and afternoon were in some places 25 K higher than initially predicted. Amongst other reasons this can be traced back to the lack of understanding in the surface properties of the lunar surface at that time. This lack in knowledge led to insufficient temperature predictions. Better models were established based on the findings of Surveyor and Apollo. Another course for the inaccuracy was traced back to measurement signal processing errors. The value of this error was ± 4 K. On top of this, post mission analysis showed that nearby boulders probably had an effect on the temperature of one of the electronic compartments on Surveyor 7. The report concludes the section with the statement that "*Further discretization efforts should be restricted to the immediate foreground, particularly where craters or rocks exist.*" (JPL,1969).
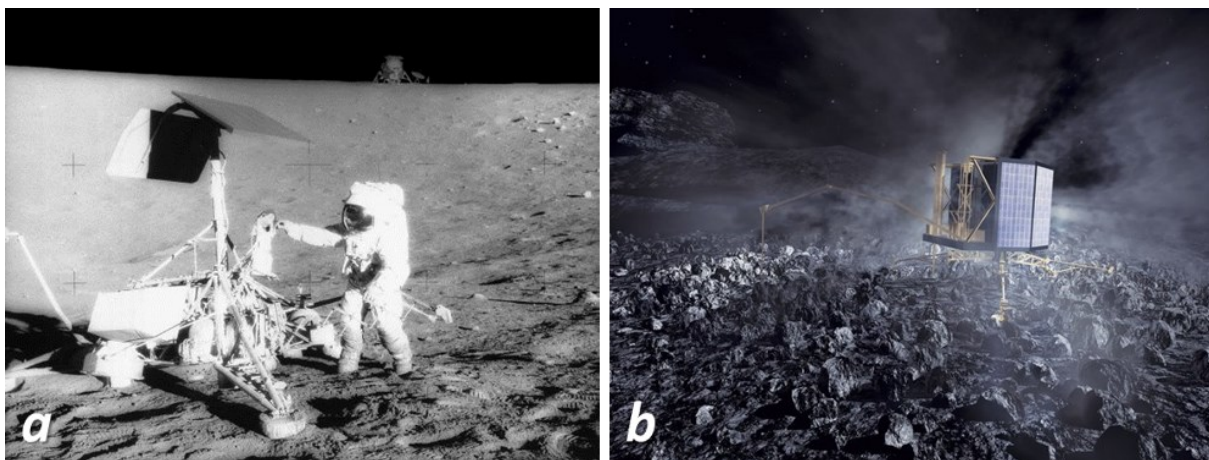
Figure 2-2: a) Apollo 12 astronaut Pete Conrad visits the Surveyor 3 spacecraft in the Sea of Storms (NASA 1969, b) Artists impression of the Philae lander touched down on comet 67P Churyumov–Gerasimenko (ESA 2004).

Beside equipment used during the Apollo era missions to asteroids, such as the ESA Rosetta mission and the JAXA Hayabusa missions also face thermal challenges with respect to surface operations. The Philae lander, depicted in Figure 2-2b, aboard the ESA Rosetta mission is planned to touch down on the surface of the comet 67P Churyumov–Gerasimenko in November 2014 (Biele and Ulamec 2008). One large uncertainty for design and performance of the Philae lander is the variety of thermal conditions due to the elliptical orbit of the target comet. The comet's perihelion is at 1.29 astronomic units (AU)[1] whereas the landing takes place at a distance of 3 AU. This leads to a wide variety of incident solar heat flux and surface temperatures (Ball 2007). The temperature was assumed to be between -80°C and +20°C during

---

[1] The mean distance between Sun and Earth is called one astronomical unit (AU) and has a value of 149.597·10^6 km.

sunlight phases and -200°C during night. This is even more complicated by the comet's rotation rate of 12.3 h (Biele and Ulamec 2008).

Power generating systems such as radioisotope thermoelectric generator (RTGs) or sterling radioisotope generators (SRGs), often used for probes and rovers in regions where the Sun cannot provide sufficient energy, form local heat sources on the surface-craft besides producing electrical energy (Shaltens 2007). Examples are the Apollo instruments ALSEP, the Lunokhod rovers 1 & 2, the Mars Exploration Rovers (MER), the Mars Science Lab (MSL), and the Voyager I and II deep space probes. In case of Lunokhod 1 & 2, MER and MSL complicated fluid circles or heat pipes were used to remove the heat produced by the RTGs to radiators or sublimators. The design of the radiators in turn is driven by the sink temperature and the view factor to it.

2.1.2 Rovers

"Surface mobility systems are the key element in extending exploration activities well beyond the immediate confines of the base and landing area."

- Zakrajsek et al. 2005

Since the beginning of spaceflight an incredible number of rovers have been designed. It has become an appreciated educational task to design a rover in order to learn basic Systems Engineering and the spacecraft design process with all the subsystems, their interfaces, and their individual challenges. Beside educational projects there is a vast number of rover, crawler, climber, or hopper concepts developed in the control and automation domain. These rover concepts concentrate on mechanical aspects such as locomotion principles, number of legs or wheels, structural loads and mechanisms, or on control issues such as system autonomy, path planning and scheduling, on-board processing or sensor integration (see e.g. Kubota et al. 1999; Seeni et al. 2009; Cordes et al. 2010). These concepts mostly neglect the thermal and vacuum environment. New concepts of this type are presented on the International Symposium on Artifical Intelligence, Robotics and Automation in Space (i-SAIRAS) every year. The available literature would fill libraries. Hence, in the following only rovers and rover designs will be discussed that either were used on the lunar surface, are planned by space agencies or are part of the profit driven Google Lunar XPrize competition[2]. Only rovers dedicated to the Moon are accounted for since the rover operated and planned for Mars face other thermal conditions. The rover will be regarded concerning the assumptions and design related to thermal engineering.

Concepts for pressurized rovers such as the NASA Space Exploration Vehicle (SEV) are neglected. Pressurized rovers incorporate environmental control and life support systems (ECLSS) which provides a shirt-sleeve environment for astronauts. This type of rover needs an entirely different thermal approach and faces different challenges. Due to their mass they also have a high thermal inertia which makes them less vulnerable to changing environmental conditions. Thus they are not further discussed in this work.

2.1.2.1 Past Rovers

The history of roving vehicles on other celestial bodies beside Earth began with the soviet missions Lunokhod 1 & 2. They were followed by the Lunar Roving Vehicle (LRV) on board Apollo 15, 16 and 17. Since then four US rovers have been sent to Mars, with Mars Pathfinder being the first one, the Mars Exploration Rover twins Spirit and Opportunity being the ones with the longest mission duration so far and the Mars Science Laboratory, now called Curiosity, as the most recent and most complex vehicle placed on another planet.

---

[2] International competition that proposes 30 M$ to the first group that places a lander and rover on the Moon by the end of 2012; or with a reduced prize money by the end of 2014. The group must be funded privately to at least 90 %.

Figure 2-3a shows a photograph of Lunokhod 1. The soviet Lunokhod rovers 1 & 2 had dimensions of 1.35 · 2.2 · 1.6 m and masses of 756 kg and 840 kg, respectively. The Lunokhod rovers were designed to survive lunar nights. The instruments were located within the rover body. On the inside of the top hatch solar cells were mounted. During lunar day the hatch was opened occasionally to use the solar cells to charge the batteries. During lunar night the hatch remained closed, the spacecraft was in a hibernation mode and heat was created by a polonium-210 isotopic heat source. During lunar day the radioactive heat source was cooled by an open loop water cooling system. Lunokhod 1 operated for 11 lunar days (~11 months) and Lunokhod 2 was operated for 4 months. After that period the Lunokhod 2 mission was declared to be finished with western experts suspecting that the rover was unable to wake up after its 4th lunar night (Ivankov 2013a; Ivankov 2013b).
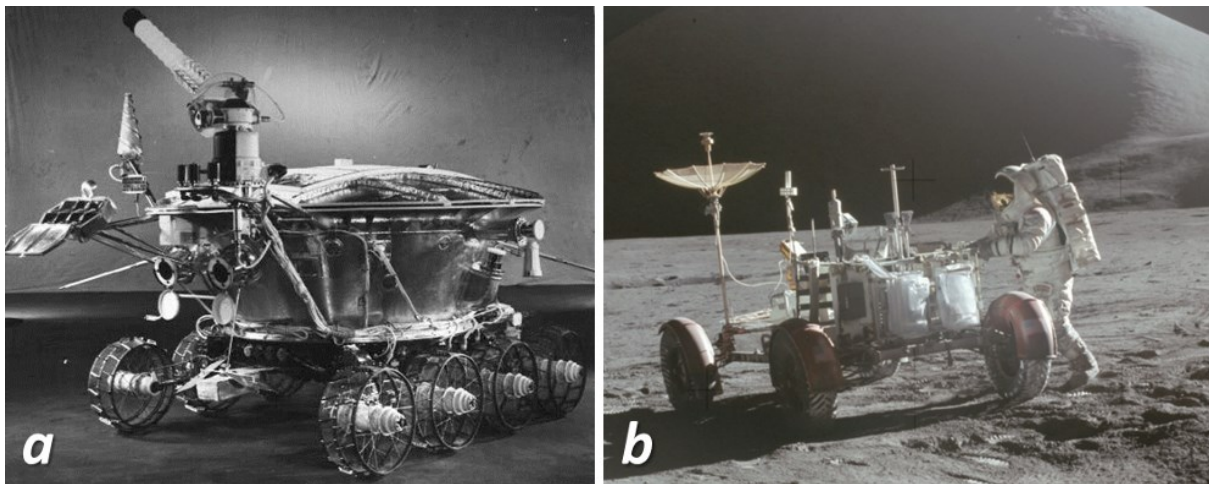
Figure 2-3: a) Photograph of the Lunokhod 1 rover (Ivankov 2013a); b) The lunar roving vehicle (LRV) with Astronaut Jim Irvine during Apollo 15 (NASA 1971b).

During Apollo 15, 16 and 17 the so called lunar roving vehicles (LRV) or short "Lunar Rover" were used to increase the mobility of the Apollo Astronauts (Figure 2-3b). The LRV batteries had an operation temperature range of 4 to 51°C and the ambient environment during the mission was between 10°C and 82°C (Gaier and Jaworske 2007). The batteries were connected to a horizontally oriented radiator. The radiators of the LRV where equipped with dust covers and it was foreseen to brush of the dust whenever possible. But the brushing of dust proofed to be inefficient. In Apollo 15, the LRV battery temperature reached 47°C after the third extravehicular activity (EVA). In case of Apollo 16 and 17 the cool-down between the EVAs was worse than encountered during Apollo 15 and exceeded expected levels predicted from the lessons learned during Apollo 15. During Apollo 16 the batteries maximum operation temperature was reached at the end of the third EVA. In case of Apollo 17 the maximum operation temperature was reached well within the third EVA. At the end of the third EVA of Apollo 17 even the batteries survival temperature was reached (Gaier and Jaworske 2007).

2.1.2.2　Current Rovers

Beside the flown rovers there is a long list of rover concepts which were and still are being discussed. These rovers range from large scale pressurized rovers to small exploration rovers. On the one side there are designs pursued by national agencies. But on the other side there are privately funded companies participating in the Google Lunar X-Prize, a commercial competition to place a rover on the Moon. This chapter focuses on past lunar rovers, their thermal design and performance. Moreover current rover designs will be introduced, as proposed by different space agencies, and rover concepts being designed and tested by private companies, or groups of individuals in the Google-Lunar-X-prize competition.

<u>Governmental funded rovers:</u>

Currently five agencies of space faring nations are proposing to place a rover on the surface of the Moon within this decade. The European Space Agency (ESA) considered sending a rover to the Moon aboard the ESA lunar lander until the program was put to a halt in November 2012. The Japan Aerospace Exploration Agency (JAXA) plans the mission SELENE-2. The Chinese space program foresees the mission Chang e3 as a predecessor mission to the Chang e1 (2007) and Chang e2 (2010) missions. NASA worked on a rover concept for robotic lunar polar exploration until the termination of the Constellation program in 2009 and since then has put further effort into landers for multiple destinations. Also India and Russia are planning to put equipment on the Moon in a joint endeavor. The Indian Space Research Organization (ISRO) plans to place a rover on the lunar surface with the second Chandrayan mission. The Russian Federal Space Agency (Roscosmos) is responsible of building the lander, whereas ISRO builds orbiter, rover and takes team leadership[3].

In the last decade several ESA missions as well as German National missions to the Moon were discussed and at some stage cancelled. The most recent concept from ESA was the ESA lunar lander, which was a combination of the earlier ESA NEXT lunar lander and German LEO mission concepts. The German Aerospace Center (DLR) planned to participate in the ESA Lunar Lander with a rover (Claasen et al. 2012) to expand the accessible region around the landing site, increase scientific output and to avoid the area contaminated by the descent stage thrusters (Carpenter et al. 2012). Though the ESA lunar lander project was put on hold in November 2012, the rover concept, under development at Kayser-Threde GmbH, is still being developed further to participate in missions of other nations and agencies.

Already in the early studies it was identified that the thermal environment had a large impact on the performance of a small rover. Due to the lighting conditions, at the envisaged landing area between Shakelton and De Gerlach crater (Carpenter et al. 2012) on the lunar South Pole the illumination played an important role. It was found that boulders could have a significant impact on the thermal layout of a small rover (Barraclough et al. 2009).
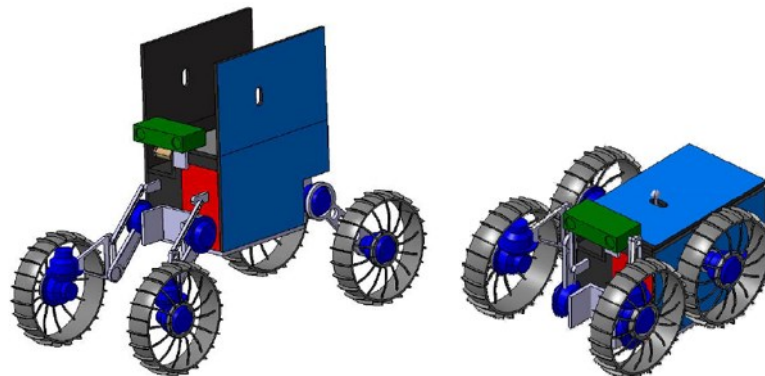
Figure 2-4: Deployed and stored configuration of the Mobile Payload Element concept (Haarmann et al. 2012).

The Mobile Payload Element (MPE) proposed by the German Aerospace Center (DLR) for the ESA Lunar Lander (LL) or other interested international partners foresees a lightweight (11-14 kg) exploration rover (Figure 2-4). It is designed to carry a small scientific payload of about 2 kg and means to sample regolith from interesting spots and carry them to the lander. It is supposed to survive short periods of darkness (~5 h) and traversing shadows (~2 h). The Mobile Payload Element (MPE) called rover shall be able to travel distances of about 1,500 m in total, traversing small craters and small boulders as well as shadowed areas. The proposed speed is 5.4 to 7 mm/s depending on the used navigation mode (Haarmann et

---

[3] As of February 2013. Roscosmos since has desided on an independent Moon program and to restart the succesfull Luna missions of the nineteen-seventieth with Luna 25.

al. 2012). The power is provided by solar cells that are mounted on the vertical sides of the rover. The lower parts are fixed and the upper parts can be deployed. In a warmth box the electronic equipment is housed including data processing systems and secondary batteries. A heat switch on the lower side allows for heat rejection during shadow phases (Claasen et al. 2012; Hofmann et al. 2011).

The SELENE-2 spacecraft is currently planned by JAXA. SELENE-2 is the successor to the successful mission SELENE-1 that orbited the Moon from 2009 to 2010. The objective of SELENE-2 is to place a lander with rover on the surface of the Moon. Beside safe and accurate landing, and surface mobility through a rover, the night survival is amongst the top three goals for JAXA. Moreover the mission shall stimulate technology development demands for lunar exploration and exploitation. Also the investigation of the surface environment is mentioned amongst the top priority scientific goals (Hashimoto et al. 2011). JAXA develops different concepts to overcome the lunar night. One of the concepts is a regenerative fuel cell with high thermal and electrical capacity to heat up and produce electrical energy during night phases. Another concept focuses on an extreme well insulated rover body with electrical heaters. Besides, hibernation is considered as a possible way of surviving the lunar nights.

The Chinese probe Chang e3 is scheduled to land and place a rover on the Moon in 2013 (Laxman 2012). In Chinas' Deep Space Exploration objectives the Moon takes up a special role. The next space probe send to the Moon shall demonstrate soft precision landing, and the capability of roving and surveying the lunar surface in order to study it thoroughly. In order to answer scientific questions China plans to make *in-situ* analysis, surveys of the lunar surface material and beside others make moon-based astronomical observations. As a long term goal, the return of Moon samples to Earth are planned (Information Office of the State Council 2011).

The Indian Space Research Organization ISRO is planning a joined mission with the Federal Space Agency of Russia (generally referred to as Roscosmos) to send an orbiter-lander-rover probe to the Moon in 2013. The main objectives of the mission are the gathering of scientific data of the composition of the Moon and the physical properties of the surface material. Launcher, Rover, and orbiter are provided by ISRO and the lander is the contribution of Roscosmos. Lander and Rover are planned to have a total wet mass of 1,260 kg. There will be five scientific instruments on board the orbiter and two on board the rover, plus further not specified instruments on the lander. The actual landing area will probably be at high latitudes (Goswami and Annadurai 2011). More recently Roscosmos, announced a set of five missions for the next decade from lander, lander plus rover, to sample return missions to the Moon. These missions will be called Luna 25 to Luna 29.

NASA planned a lunar rover until the Constellation Program was cancelled in 2009. Since then further work has been pursued with a focus on lander systems which can be used for several destinations. In 2006 an extensive study on rovers for permanently shadowed craters was performed in all NASA space centers and the Jet Propulsion Laboratory (JPL). The baseline rover concepts were in the size range of 300 to 400 kg and used either so called multi mission radioisotopic thermal generators (MMRTGs) or fuel cells to provide power. The thermal design foresaw a heat box for the electronic equipment and the use of the heat produced by either MMRTG or fuel cell. The fuel cell concept needed additional heaters but was feasible. The lunar dust impact on thermal control surfaces was neglected in the study (Graham 2007).

The ongoing efforts at NASA focus on the increase of the technology readiness level of existing technologies. Moreover the goal is to provide a flexible platform to land at and explore different landing sites on atmosphere-less celestial bodies. The environmental conditions were identified to pose a high risk especially to batteries. A high uncertainty is connected to the lack of performance data for batteries in demanding thermal environments. In order to control the heat flow for warmth boxes with electric equipment in hot and cold cases, variable conductive interfaces with a "turndown rate" of 1,500:1 were deemed necessary. Loop heat pipes and two phase heat pipes have the potential to provide this large area of applicability but currently do not have the required technology readiness level (TRL) (Cohen et al. 2012).

Another rover concept developed throughout the past years at the Carnegie Mellon University is the SCARAB rover concept (Figure 2-5). The project is conducted in collaboration with NASA. The rover was dedicated to investigate cold traps and find volatiles at the lunar poles. The rover is designed to autonomously operate in lunar craters, to traverse distances of 1,000 m between up to 25 sample sites and drill to 1 m depth. The drill is the central piece of equipment placed in the center of the rover. The rover has a total mass of 250 kg. The mass was derived from the needed force for drilling operations. The height of the chassis can be altered so the center of gravity can be lowered for drilling operations (Wettergreen et al. 2010). The rover is equipped with lithium ion batteries with 26 Ah of power which need to be recharged by an "external station" (Wettergreen et al. 2009). Earlier designs envisaged the use of RTGs (Bartlett et al. 2008). For cases of high internal and external loads the use of radiators is intended. A 1:1 scale engineering model was build. With this model, concepts to avoid slippage, overcome obstacles, and follow waypoints autonomously were tested (Wettergreen et al. 2009; Wettergreen et al. 2010; Bartlett et al. 2008). The thermal concept is not addressed sufficiently in any of the available publications and remains unresolved.

Figure 2-5: The SCARAB Rover concept. A 1:1 scale engineering model in field tests (Wettergreen et al. 2010).

The All Terrain Hex Limed Extra Terrestrial Explorer (ATHLETE) is a rover concept developed by the Jet Propulsion Laboratory. The design is a 6 legged rover, whereas wheels are placed at the end of the legs. Each leg can be steered individually allowing for rolling, climbing and walking. The second generation Tri-ATHLETE rover mock up is composed of two three-legged versions that can be combined to one ATHLETE or attached to a pallet carrying large scale base structures. In this mode it can haul base segments to heights of 3.5 m and carry up to 500 kg under 1-g conditions. The sealing against lunar dust on the driving motors take into account thermal expansion. The wheels are made by Michelin®, specifically for lunar applications. The used proprietary material is able to endure in cryogenic temperatures (40 K) and even improves material properties such as flex, fatigue, compression and tensile modulus (Haverley et al. 2010). Neither the impact of changing environmental conditions or temperature gradients along such a large structure made of aluminium was addressed. The wheels are well suited for high temperature. Their endurance was shown in long-term tests in a liquid nitrogen bath, but whether they are able to sustain multiple temperature swings was not addressed.

Privately funded rovers:

Beside missions to the Moon, planned by governmental agencies, there is a private sector of Moon missions initiated through the Google Lunar XPrize competition. In total, 33 teams, with participants from 47 countries worldwide, registered for competing in the Google Lunar XPrize competition until the deadline at the end of 2010. 25 teams currently are either in the process of fundraising, testing or building hardware as of January 2013. Little information on rover or lander design is published by the participants of the Google Lunar XPrize. This is understandable with regard to the competitive nature of the endeavor and that the participants are often private companies or some sort of public private partnership.

In the following the thermal design of four of the teams will be introduced:

Team Italia, with their Rover concept AMALIA, focuses on a 14 days operation phase during one lunar day. They neglect the possibility and optional Google-Lunar X-Prize goal to survive a lunar night, due to the additional requirements this would create. Their passive thermal design foresees a warmth box for the electronics and a radiator, mounted on the top of the rover. The rover chassis is covered with multi-layer insulation (MLI) on the lower side and with solar cells on the upper side. During the cruise phase heaters inside the warmth box are controlled and powered by the lander via an umbilical connection. Besides, the solar panels cover the radiator before deployment on the lunar surface (Della Torre et al. 2010).

The Carnegie Mellon University in collaboration with the private company Astrobotic Technology Inc. develops another concept for the Google Lunar XPrize. The thermal concept foresees an asymmetric composite structure with good lateral heat transport (see Figure 2-6 A). The basic form is that of a pyramid. The sides are covered with solar cells and one side is used as a radiator. The solar cells shall be used as additional radiators when they are not illuminated by the Sun. The concept relies on commercial-of-the-shelf components (COTS). This group also focuses on the lunar equator and mission duration of at least 14 Earth days. During the lunar night, the rover shall be set in a hibernation mode and be restarted afterwards. Whether a restart is possible after the lunar night depends on the performance of the used electronic COTS components (Gump and Thornton 2011)

White Label Space is an European/Japanese team working on a concept for the Google LunarXPrize. Their rover design (see Figure 2-6 B) does not take into consideration night survival but a warmth box is considered as a "garage" for the rover on board the lander during lunar night (Laurand 2010).

Another, mainly German, team participating in the Google Lunar XPrize is called "Part Time Scientists". Their rover, called "Asimov" (see Figure 2-6 C) is also supposed to go into hibernation during the lunar night. No special precautions seem to be foreseen to survive the lunar night. The team seems to be aware that the rover might not wake up again after the first lunar night (Part-Time-Scientists 2013).
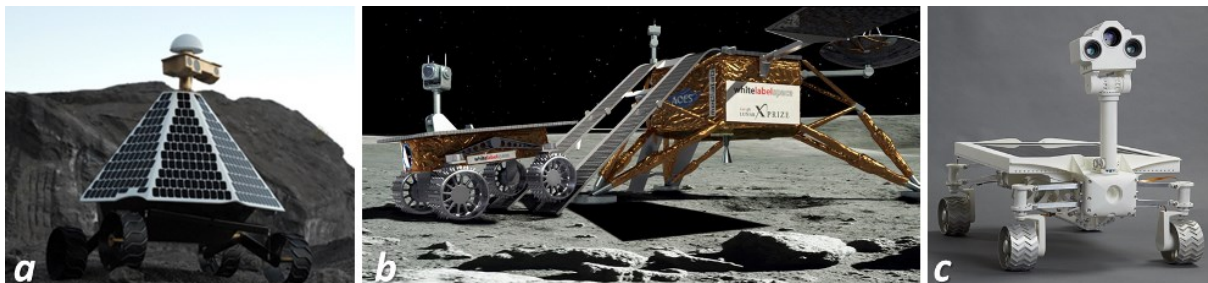
Figure 2-6: a) A photograph of the engineering model of the Astrobotic Red Rover (Astrobotic 2012); b) A computer rendering of rover and lander from WhiteLabelSpace (Bartoloni 2011); and c) A rover mock-up of the Asimov Rover designed by the PartTimeScientist Team (Part-Time-Scientists 2013).

In Table 2-1 twelve Moon and Mars rovers are compared for the volume and mass. The values for the average rover density are derived from volume and mass. The densities are averaged for all twelve rovers.

The averaged rover density value is used for thermal calculations in section 7.1.2. The averaged densities for the rovers that actually flew to Moon and Mars range from 32 kg·m^{-3} to 230 kg·m^{-3}.

Table 2-1: Comparison of Rover integration values for 12 rovers.

Name	Volume [m³]	Mass [kg]	Density [kg·m⁻³]	Source
LRV	2.14	210.00	98.18	(Zakrajsek et al. 2005)
Lunokhod	3.67	840.00	228.76	(Zakrajsek et al. 2005)
Mars Pathfinder	0.05	10.50	231.48	(Zakrajsek et al. 2005)
MER	5.52	180.00	32.61	(Zakrajsek et al. 2005)
Sojourner	0.08	10.50	124.01	(JPL and NASA 1996)
NOMAD	8.00	550.00	68.75	(Zakrajsek et al. 2005; Cabrol et al.)
Scarab	0.30	280.00	933.33	(Bartlett et al. 2008)
Nanokhod	0.03	3.00	115.38	(Bertrand et al. 2000)
Curiosity	4.50	900.00	200.00	(JPL and NASA 2012)
Selene B	0.10	60.00	576.92	(Okada et al. 2006)
Micro5	0.07	5.00	68.61	(Kubota et al. 1999)
Day/Night Lunar Rover	2.80	381.00	136.07	(Berkelman et al. 1995)
Average Value			234.51	

2.1.3 Spacesuits

The International Space Exploration Coordination Group (ISECG) foresees a combination of robotic and human efforts in order to further explore our solar system. A human is not made for space and thus faces an extremely hostile environment with temperature extremes, radiation, micrometeorites, and vacuum. A spacesuit is a small spacecraft that provides all the necessary means to keep a human being alive and to provide a comfortable protecting environment that allows for a wide variety of tasks. Emerging from the experiences made with balloons and high flying planes (Fullerton 2001), protective suits were and are an indispensable part of spaceflight. In section 2.1.3.1 the suits worn during the Apollo missions and their predecessors in the Shuttle program, the Russian space program, and the International Space Station are shortly introduced. In section 2.1.3.2, designs and technologies for future missions on Moon and Mars are presented. The thermal environment has proven to be a major challenge in the design of spacesuits.

A spacesuit consists of several subsystems. Each subsystem has a certain impact on the thermal behavior of the entire suit. The liquid cooling garment (LCG), the suit insulation, the ventilation system, and the personal life support system (PLSS) have the biggest influence on the thermal design of a suit, apart from the human. The LCG is a part of the suits active thermal control (ATC) and transports heat away from the human body by a fluid cycle with a 90-110 m long system of tubes that are woven into a suit worn by the astronauts (Flouris and Cheung 2006). The water flow is pumped through a heat exchanger inside the PLSS. From there the heat is transferred to a sublimator, in the common configuration of current suits. The PLSS is mainly responsible of providing oxygen, removing carbon dioxide, and controlling humidity and water flow rate.

2.1.3.1 Apollo, MIR, Shuttle & ISS suits

The spacesuits used in Apollo were the result of a process that can be traced back to World War II were protective clothing for fighter and bomber pilots were developed. For the Apollo program many models were designed, tested, and improved before the final design was delivered to NASA. Between Apollo11 and Apollo 17 further amendments were made to the PLSS and the suit. A long history of development is also true for the Russian ORLAN spacesuits, although it was never used on the lunar surface. The Soviets/Russians focused on space stations in low Earth orbits (LEO) and gained experiences there.

The Apollo PLSS that was used during Apollo 9, 11, 12, and 14 was able to support a total metabolic heat production of ~5,021 kJ. It had three modes for low, medium and high thermal loads. The different states could be changed manually by changing the position of the cooling water inlet. The cooling water temperature could be changed between 7°C, 15°C and 21°C. The thermal control system could either cope with heat production rates of ~464 W for three hours or ~348 W for four hours. During Apollo 15 and 17 an improved version was used which was able to support a total heat production of ~7,531 kJ in rates of either 290 W for seven hours or 261 W for eight hours. The cooling water temperatures were 7°C, 18°C and 27°C (Waligora and Horrigan 1975). During the Apollo missions the astronauts never mentioned a serious thermal problem in their suits. Yet, there were two occasions when the Astronauts were ordered to change their thermal valve setting as a precautionary measure in order to prevent the astronauts from overheating. The biggest heat loads were apparent during Lunar Module ingress and egress as well as during geological/scientific tasks (Gernhardt et al. 2009). The overall heat loads were highest during Apollo 15 and 17 (Waligora and Horrigan 1975).

On the Soviet/Russian side a lot of experience with extravehicular activities (EVA) was gathered on the MIR[4] space station (Katuntsev et al. 2004). Main stressors for the crew were caused by changed sleep cycles before EVAs, prolonged period without meals (9 to 11 h), and an accelerated feeling of fatigue due to the intensified use of arms above legs for locomotion during EVAs. The astronauts[5] often used the shadow periods of an orbit to take brakes, especially after strenuous tasks. Here often hypothermia was encountered, which lead to emotional stress, pain, fatigue and cardiac arrhythmia (Katuntsev et al. 2004). Often astronauts were reported to have a certain reluctance to take care of the manually regulated thermal control of their spacesuits (ORLAN) due to physical and psychical stress and fatigue (Barer 1991). The transient effects, when the astronaut was changing from sunlit to shadow areas, and with that a changing use of the sun shield of the helmet, lead to changing internal heat conditions with the result of visor fogging. In one case, these interactions lead to an erroneous reading of instruments which almost lead to panic and to an abort of the EVA (Barer 1991). It was also found that more experienced EVA-astronauts handle the manual thermal control of their spacesuits better (Barer 1991). Furthermore, Russian and US astronauts reported to experience cold finger in the ORLAN-M suit, when the astronauts had contact with equipment in the shadow, and were not using their fingers for longer periods of time (Abramov et al. 2001).

The manual control of the thermal subsystems of spacesuits was a major shortcoming during Apollo, Shuttle and MIR programs. Intensive hardware tests and software modeling on suit thermal control was performed in the late 1990s and early 2000s. The focus was set on automatically controlled spacesuits liquid cooling garment in combination with radiators and heat-exchangers. A result was that control algorithms which govern the LCG fluid temperature have a strong dependency with the environmental conditions.

"The robustness of this calibration is important since the environmental conditions in space are dynamic, and heat loss through the spacesuit can vary with orbit altitude, position of the space walking astronaut relative to the sun, and proximity of the astronaut to radiation surfaces on the space shuttle. This analysis was conducted to determine if the resting states defined for one set of initial conditions would be valid throughout an EVA for which there might be substantial environmental changes." (Nyberg et al. 2001). Thus, it was concluded that further work and more detailed studies including a dynamic environment were necessary. Although the work was focused on spacesuits used for EVAs on the International Space Station (ISS) the statement can be extrapolated to the Moon. *"Comparison of the two simulations shows*

---

[4] (Russian. *Peace* or *World)*, Soviet/Russian space station, operated between 1986 and 2001.

[5] In soviet/russian space flight they are called „cosmonauts". For simplicity cosmonauts are called astronauts in this work.

that a changing environment can have a large effect on the controller setting for the inlet water tempera-ture.” (Nyberg et al. 2001). The thermal modeling at that time used basic static environmental conditions.

The American EMU suits, used during the Shuttle program and now used on the ISS, are based on Apollo and Spacelab heritage. The current Shuttle EVA suit has the capacity to remove 586 W (2,000 BTU/hour) for short periods of 15 minutes, 469 W (1,600 BTU/hr) for 1 hour and 293 W (1,000 BTU/hour) for a period of 7 hours (reference to specification No. SVHS7800 by Hamilton Sundstrand in Norcross et al. 2009). The Russian pendant, the ORLAN-M suit has a long heritage throughout Soviet and Russian space station programs. Both, the EMU and Orlan-M suits were designed for the micro-gravity environment in missions to Low Earth Orbit (LEO). The suits have high masses, need constant maintenance and use inaccurate insulation materials, hence are not suited for surface operations. The used insulation materials inhibit mobility and dexterity under higher gravitational loads on planetary surfaces. Further uncertainties arise from contact times with cold rocks on planetary surfaces (Fullerton 2001).
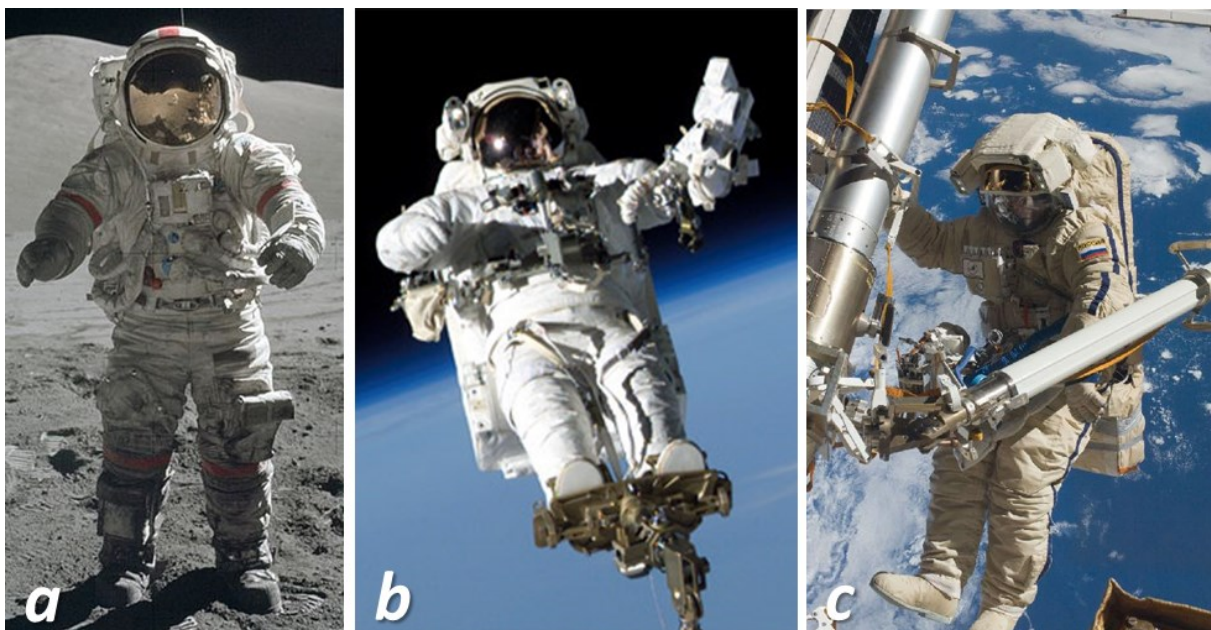

Figure 2-7: a) Apollo 17 AL-7 suit (NASA 1972a); b) ISS Extravehicular maneuvering unit (EMU) (NASA 2005); c) ISS ORLAN (NASA 2012a).

2.1.3.2   Surface Mobility Suits

In the late 1990s and early 2000s NASA put a large effort in simulation of the human and PLSS interactions (Campbell et al. 1996; Campbell et al. 1999, 2000; Nyberg et al. 2001; Fullerton 2001) on how spacesuits need to be designed to sustain future missions in planetary environments. The focus of these investigations was set on Mars, but also Moon was taken into consideration. One of the foci was the thermal interaction between the different spacesuit subsystems. It was found that there is a strong ther-mal interaction between a human and spacesuit as well as between LCG, radiators or water sublimators, and heat exchanger (Campbell et al. 2000). The (Martian) environment was considered static and no transients could be modeled. Yet, even then in a hot Martian environment only a short period with high metabolic rate can be endured by a space suit. In a cold environment a low metabolic heat production rate is not sufficient to maintain the astronauts' body temperature within a comfortable range. The body heat should not deviate from more than ±19 W·h to remain in a comfortable zone (Campbell et al. 2000). *“Many other variables of the body, such as mean skin temperature or heart rate, have faster response times to changes in LCG water temperature, activity, or environment.* […] *Whereas a steady-state model of the system should allow for preliminary component sizing, a fully integrated transient model of the entire system is needed for detailed design and to evaluate thermal comfort especially with the wide variations in*

environment (-123 to 20°C) (-190 to 70°F) and frequent changes in MR (80–600W) (273–2,046 Btu/h)." (Campbell et al. 2000). At low environment temperatures and low metabolic rates (MR), thermal designs must foresee heaters. In parallel, the insulation of the suit needs to be improved compared to a current thermal conductivity of 1.19 $W \cdot m^{-2} \cdot K^{-1}$ [Campbell et al. 1999]. A better insulation will lead to savings of consumables in cold conditions but raise their consumption in moderate environments (Campbell et al. 2000). Increasing the heater power lead to increasing mass of batteries and does not neglect the thermal imbalance during cold conditions entirely (Mays et al. 1999).

In a study with 6 male subjects, performing a 10 km walk in a spacesuit with reduced gravity, elevated metabolic rates were reported. The suited subjects were walking on a level treadmill and the reduced gravitation was simulated by a mounting suspension. The heat production rates of the subjects ranged from 562 W (1,918 BTU/hour) and 782 W (2,667 BTU/hour), averaging 695 W (2,374 BTU/hour) (Norcross et al. 2009). This average value is higher than the peak load sustained by the shuttle EMU (586 W for 15 minutes – see section 2.1.3.1). All test subjects reported insufficient cooling capacity during phases of high metabolic rate, although for most subjects the body core temperature increased by not more than 1°C. Topography, navigation tasks, geologic tasks, or construction tasks were not taken into consideration. Also the thermal environment was neither controlled nor altered: *"Lunar-like conditions including terrain, topography, and navigation could significantly alter the results, likely increasing time and/or metabolic rate needed to complete a 10-km walkback."* (Norcross et al. 2009). A field study of a 10 km traverse at a crater in the Canadian high-artic showed an increase of overall metabolic rate of 56 % compared to the average speed and grade-matched during treadmill trials in the laboratory setting under 1-g (Norcross et al. 2009).

The use of sublimators is often discussed for Moon and Mars spacesuits. It was the method of choice during Apollo, is used in current EMU and ORLAN-M suits, and is investigated for future Moon and Mars missions. Due to the different pressure levels on Moon and Mars a given sublimator design cannot be used in both environments without adaptations. Sublimators alone cannot sustain all mission envelopes (Mays et al. 1999; Sompayrac et al. 2009). Although sublimation is a very effective process to remove heat, it is problematic for long-term missions because the sublimated water is lost permanently. The resupply with water becomes paramount and expensive in remote places like the Moon, Mars or NEOs (Jones 2009; Fullerton 2001). Besides, planetary protection is an issue for missions to Mars where the contamination with waste material from Earth must be kept to an absolute minimum. A primary goal of future spacesuit concepts thus is to reduce the amount of water wasted by the thermal control system. This can be achieved by heat exchangers and the use of radiators (Fullerton 2001).

Several concepts exist concerning the shape and the technologies of radiators for the application in spaceflight. Different shapes are parabolic forms as those used on the ALSEP (Harris 1972) and proposed for an early ESA lunar rover model (Barraclough et al. 2009). Other concepts foresee terraced radiators or baby buggy shaped shields against the infrared radiation emitted by the lunar surface (Ochoa et al. 2006; Ochoa et al. 2008). Again others proposed the use of a turtle-shell like cover to protect the astronaut against high levels of incident heat flux (Klaus et al. 2007). Further technologies are digital radiators (Ganapathi et al. 2009) and materials that are able to change their emissivity and absorptivity, so called "electrochromics" (Metts et al. 2011) or "thermochromics". The use of radiators in turn demands a more detailed knowledge of the spacesuit geometry, the position of the radiator and the astronauts' metabolic rates (Jones 2009). Moreover, the thermal lunar environment needs to be known more accurately (Ochoa et al. 2006; Ochoa et al. 2008; Sompayrac et al. 2009; Metts et al. 2011). A more detailed discussion of radiators is given in section 4.3.2.3.

2.2 Modeling Thermal Conditions of the Lunar Surface

In the past, a multitude of models were developed in order to simulate the temperature behavior of the lunar surface. These models are mainly driven by scientific question on how the upper layers of the Moon are composed and behave thermally. Another group of software tools were engineered in order to simulate the illumination and lighting conditions on the lunar surface. The lighting conditions are important for the sizing of solar power arrays and the design of habitats. The backscattering of the surface is also important for instruments such as laser altimeters for the landing of spacecraft on celestial bodies. Yet another set of models focused on the survivability of equipment to be operated on the lunar surface.

2.2.1 Scientific Models of the Upper Layer Thermal Behavior of the Moon

Since the beginning of the 20th century scientists were interested in the thermal conditions of the lunar surface. Various scientific and engineering temperature models for the lunar surface have been proposed, of which only some can be discussed here. Their goal was to understand and predict the temperature behavior of the Moon, to understand its surface properties and history, gain new insights in the thermal behavior of porous media in vacuum, or to determine whether ice deposits are possible. With time, the used measurement methods matured as well as the computational possibilities of the accompanying models. Most data was obtained during the Apollo and Luna programs and adjunct precursor missions in the 1950s to 1970s. More recently new data was gathered by a fleet of probes: Kaguya (SELENE), Chang'e1, Chandrayan and the Lunar Reconnaissance Orbiter (LRO). Especially the Diviner Lunar Radiometer Experiment (DLRE)[6] aboard the LRO provided a large set of temperature data in different infrared wavelength bands (Paige et al. 2010a; Paige et al. 2010b).

The first and often cited work dates back to 1930 when Pettit and Nicholson performed infrared (IR) measurements with a telescope and came up with predictions for the thermal behavior of the Moon. They were the first to measure the change in infrared wavelengths emitted from the lunar surface before, during, and shortly after a lunar eclipse as well as during a lunation[7]. Pettit and Nicholson assumed constant values for heat capacity, conductivity, and density, and used static formulas with fixed initial temperatures (Pettit and Nicholson 1930).

In the 1940s, 1950s, and 1960s several models for the lunar surface were proposed (Wesselink 1948; Jaeger and Harper 1950; Jaeger 1953; Krotikov and Shchuko 1963; Winter 1967; Winter and Saari 1969; Linsky 1966). These models considered the lunar surface to be covered with either one homogenous layer or several layers of differing properties. The models used numerical simulations to compute the change in surface temperatures. A temperature-dependent conductivity was first proposed by Krotikov (1963) and Linsky (1966). In contrast to models with layers, Winter et al. (1969) used a particulate model to compute the lunar surface temperature. They proposed to simulate the grainy consistency of the lunar regolith as an array of cubes in several layers. The cubes were only connected through joining corners, resulting in a radiation dominated heat transfer through the regolith (Winter and Saari 1969).

Not until *in-situ* photographs were made by Surveyor 1 and Luna 9 to prove assumptions, scientists were able to forecast lunar nighttime and eclipse temperature development in a satisfactory way (Menzel 1969). These models were further improved by data gathered during the Apollo program and embedded into a scientific model by Cremers and Birkebak (Cremers et al. 1971). Experimental and simulated results indicated a large impact of radiative heat transfer in porous media.

---

[6] Within this work the DLRE is also referred to as „Diviner"

[7] One synodic lunar month is the time between two full moons. A synodic lunar month correlates with 29 (Earth) days 12 hours 44 minutes and 3 seconds (Heiken et al. 1991).

As predicted by (Krotikov and Shchuko 1963; Linsky 1966; Menzel 1969) it was found that the conductivity of the lunar dust layer depends on its temperature. As real lunar regolith samples became available, returned by the Apollo crews and the Soviet sample return missions, more accurate values were measured for the thermal conductivity (Horai et al. 1970; Horai and Fujii 1971) and heat capacity (Robie et al. 1970). Based on the *in-situ* measurements and returned samples, the scientific models were further improved (Cremers et al. 1971). But the model did not account for the internal heat flux, different regolith densities and used a solar heat flux that was too low. With increasing computational power, finite element models became available to model temperatures on a crater scale. For example, in the topographic thermal model published by (Salvail and Fanale 1994) each crater element received direct solar radiation, reflected radiation from other crater elements and emitted radiation into its environment.

With new data from the Clementine mission, the effort in thermal Moon models increased again. In 1999 Vasavada et al. established a model which characterized polar ice deposits in craters on the Moon and on Mercury (Vasavada et al. 1999). The model is in line with the scientific models produced in the nineteen-sixties and nineteen-seventies (Menzel 1969; Jaeger and Harper 1950; Jaeger 1953) as well as other models on the same topic (Salvail and Fanale 1994). Thus Vasavadas model uses two-layers. The upper layer has only a few millimeters of depths and differs in density by a factor of two and in thermal conductivity by an order of magnitude from the underlying layers. Additional a heat flow from the interior of the Moon was added. The Vasavada model from 1999 matches the values found during Apollo and modeled by Cremers and Birkebak (1971) to a high degree. The possibility of cryogenic storage of fuels at lunar polar or equatorial regions was investigated with a two layer model (Christie et al. 2008). The model is derived from the work conducted by Vasavada et al. and uses a fluff and coarse regolith layer. It takes into account a sinusoidal solar heat flux and an internal lunar heat flux. Local surface features are neglected. The model correlates with Clementine and Apollo data. A major shortcoming of that work is that no topographic data is used.

A different approach was chosen by Hale & Hapke (2002). The proposed model couples conductive heat transfer with radiative heat transfer within the upper layers of regolith. Beside the thermal inertia also used by Wesselink (1948) they introduce a value which describes the radiative contribution to the thermal conductivity. The results indicate a good agreement with the early model by Wesselink and measurements made by Pettit and Nicholson in (1930). Small temperatures difference between model and measured data were traced back to diurnal or annual changes in incident solar heat fluxes or local differences in geology, as well as to the thermal behavior of regolith itself. Thus the understanding of the regolith thermal behavior is of paramount importance in order to better understand and interpret data gathered by remote sensing satellites (Hale and Hapke 2002).

In 2009 Bauch et al. presented a model for the thermal behavior of lunar regolith and to predict regolith temperature. Predicted nighttime temperatures at the Poles were around 100 K and topographic effects were found to be of significance for the local thermal environment. The impact of local inclined slopes at $\alpha_{sl} = 20°$ lead to a time difference of about two Earth days to reach the same temperature as an undisturbed planar surface at the same position. Varying Albedo between Maria and Highland can lead to temperature differences as high as 15 K (Bauch et al. 2009).

The Clementine Long Wavelength Infrared (LWIR) Camera was unable to record temperatures smaller than 200 K and only mapped 0.4 % of the lunar surface (Paige et al. 2010a). The Diviner Lunar Radiometer Experiment (DLRE) on board the Lunar Reconnaissance Orbiter (LRO) was designed to detect temperature sink at the lunar poles lower than 200 K, to increase the thermal resolution of lunar temperature maps, and to verify the proposed thermal model (Paige et al. 2010a). The Lunar Reconnaissance Orbiter (LRO) is in orbit around the Moon since July 2009 and gathers remote sensing data in nine infrared wavelength bands. From Clementine data it was apparent that the local geology also has an important influence on local temperatures. Younger craters with fresh regolith blankets were influenced more than older craters. In case of the Aristarchus crater temperature differences of about 32 K were found compared to

the surrounding undisturbed regolith (Paige et al. 2010a). The combination of temperature data obtained by the DLRE experiment, and the cameras on board the LRO, lead to more detailed models. Local temperature anomalies on crater slopes and ridges could be traced back to high abundances of boulders (Bandfield et al. 2011). Finite element models showed that even boulders in the range of tens of centimeters store more heat. A 7 cm boulder was found to have a temperature that is higher by 25 K and a 28 cm boulder has a temperature higher by 50 K than undisturbed regolith (Williams et al. 2011). "*Superposed on the large scale trends due to latitude, time of day, and season, the surface temperature of the Moon can exhibit extreme spatial variations at length scales all the way down to that of the diurnal thermal skin depth (10 cm) due to the low thermal conductivity of the bulk of the regolith, the lack of an appreciable atmosphere, and the effects of slopes and shadowing. Further, surface temperatures are highly sensitive to the thermophysical properties within the first few meters of the surface and thus spatial variations in density, thermal conductivity, heat capacity, albedo, and emissivity, will have an influence. This significantly complicates the interpretation of lunar thermal observations (Fig. 1).*" (Williams et al. 2011)

Besides the thermal surface models presented above for the Moon and Mercury, there are models which focus on Near-Earth-Asteroids (NEA). In contrast to the lunar temperature models, these models use the measureable infrared (IR) radiation to determine the albedo and size of NEAs. These models will not be discussed further in this work, although they are considered important for future applications of a dynamic temperature model (Harris 1998).

Table 2-2: List of models for the thermal behavior of lunar regolith (not exhaustive).

Author	Year	Remarks
Pettit & Nicholson	1930	Simplified static model based on ground observations
Wesselink et al.	1948	
Jaeger et al.	1950&1953	
Krotikov et al.	1963	
Winter et al.	1963	Particulate cube model
Linsky et al.	1966	
Cremers et al.	1971	
Salvail & Farnale	1994	Finite Element Model for craters
Harris	1998	Thermal Model for Near Earth Asteroids
Vasavada et al.	1999	Finite Element Model for craters with layers of different material prop.
Hale & Hapke	2002	
Bauch et al.	2009	Different material properties
Williams et al.	2011	Finite Element Model for impact of small pebbles on local temps.

2.2.2 Thermal Modeling for Spacecraft on the Lunar Surface

The driving factors for lunar surface thermal analysis for spacecraft in the past were made for the lunar landing module, lunar exploration rovers, power plant radiators, cryogenic fuel storage, sublimator and radiator efficiency for spacesuit and advanced radiator concept performance. Besides, the lunar environment impact on orbiter thermal design was investigated.

The investigation of thermal inertia of the lunar surface during Apollo showed that it was save for Astronauts to exit the Lunar Module after 5 to 10 minutes. The temperature increase of the surface due to the Lunar Module exhaust was not deemed dangerous after that period (Menzel 1969). Horizontally oriented radiators with temperatures above 314 K and solar absorptivity of < 0.2 [-] are beneficial for post-Apollo lunar power plant designs. This was found in a thoroughly design study of lunar power plant radiators (Dallas et al. 1971), neglecting dust effects and local topography. The study of different spacesuit radiator concepts showed the vulnerability of the radiator efficiency to infrared backload from the lunar surface (Ochoa et al. 2006). The infrared back load is a driving factor for the dimensioning and orientation of

radiators (Zakrajsek et al. 2005; Dallas et al. 1971; Ochoa et al. 2006). Radiators with no means of adjusting cannot be used in a lunar hot and cold environment likewise. A radiator optimized for the hot environment will cool down the entire surface-craft in a cold environment (Ochoa et al. 2008). A turndown ratio of 1:10 is necessary for radiators used on orbiter, decent module, and landers alike (Ganapathi et al. 2009). This turndown-ratio was determined by static worst case calculations and a fixed thermal profile for the Altair lunar lander. The use of radiators is important from a cost and supply standpoint. For long-term missions with numerous extravehicular activities the use of water depleting sublimators becomes unaffordable (Jones 2009; Fullerton 2001). During an EVA on the lunar surface, the expected water loss by a sublimator ranges between 3.5 and 5 kg. The amount of water depends on environmental and metabolic heat fluxes (Jones 2009). These static worst case calculations did not take into account tasks and local heat flux changes. With a quasi-static environment model of the lunar surface, it was found that sublimators will also exceed their maximum capacities if the planning of operations is not accounted for. It is important to avoid high zenith angles inside craters or at the lunar equator (Sompayrac et al. 2009). As shown in Figure 2-8, above 70° of lunar latitude the use of radiators becomes interesting according to a long-term thermal calculation (Sompayrac et al. 2009). None of these cases take transient local effects into account, yet state that they would have an impact.

Analysis for small scale lunar exploration rovers showed that the thermal environment is a major design driver. In static worst case calculations the impact of local boulder shadows on the rover temperatures was identified for the entire moon and for the poles in particular (Barraclough et al. 2009). In the aforementioned thermal evaluations for specific components and systems transient effects due to local surface features were neglected. The covering with dust is sometimes mentioned but never addressed.

A thermal model, neglecting lunar topography and assuming perfect isolation to the interior, was used to define the thermal profile for the orbiting spacecraft SMART-1 (Racca 1995).
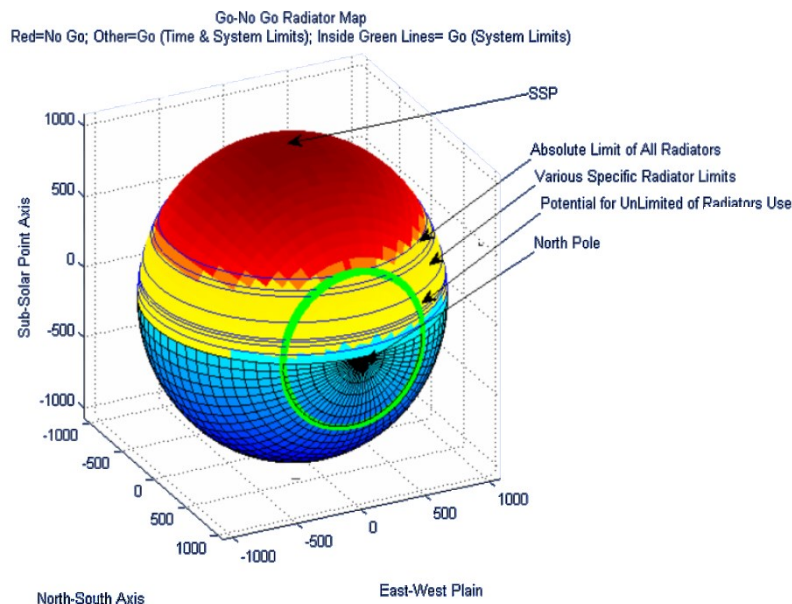

Figure 2-8: Map for "go" and "no-go" areas for radiator and sublimator controlled spacecraft [from (Sompayrac et al. 2009)].

2.2.3 Modeling the Lunar Illumination Environment

This chapter introduces work performed by other groups, concerning the modeling of the lunar surface for spaceflight applications. The models focus mainly on two fields, which are: lander descent simulations for hazard avoidance; and illumination simulations for solar array sizing and positioning.

The Planet and Asteroid Natural scene Generation Utility (PANGU) was developed at the University of Dundee in Scotland. The software is able to create maps of planetary surfaces with a focus on the Moon and asteroids. PANGU was designed to support the development of planetary landers which use some means of optical instruments for descent (Parks et al. 2010). It was developed under a number of ESA contracts. The main objective of this software package is to simulate accurately the lighting conditions for descending spacecraft for hazard avoidance in the final stage of a landing. PANGU allows the simulation of the interaction of RADAR and LIDAR systems with the surface (Rowell et al. 2009; Parks et al. 2010). The PANGU tool produces either random surface areas based on fractional Brownian motion or can import topographic maps. It can furthermore add craters and boulders. Crater size, shape and position can either be created randomly or according to literature. User defined data can be added. The boulder shape is based on an icosahedron. The software is based on OpenGL and has JAVA libraries that allow the connection to MATLAB®. PANGU can either be purchased or used freely under ESA-funded projects (Rowell et al. 2009; Parks et al. 2010).

PANGU is a sophisticated tool to produce realistic pictures of a lunar or asteroid landscape. Moreover it can be used to develop means for hazard avoidance. It does not target thermal calculations and does not incorporate any means of accounting for the thermal behavior of lunar regolith or boulders.

An interesting and potent tool recently developed at the University of Stuttgart is the so called MOON-BASE simulation. It is an extension to the work on space-station design and architectures, as well as prior work by H.H. Kölle and H.P. Eckhart. The main objective of the MOONBASE simulation-tool is to help in the positioning of habitats at the Polar Regions of the Moon. The software tool is written in C/C++ and uses other software tools for the local topography (PANGU) and orbit propagation (Spacecraft Planet Instrument C-matrix Events - SPICE). Kaguya laser altimeter (LALT) data is used for the global topography. The illumination conditions for a given base geometry, destination on the lunar surface, and for a certain time can be determined. The tool can be used mainly for the layout and sizing of solar arrays. Additionally lighting conditions for traversing surface-craft can be determined. The thermal conditions can be predicted based on steady state worst case calculations from the incident heat flux. The infrared heat flux is calculated using simplified time and latitude dependent equations. Local craters and boulders, regolith material properties and dust contamination are not accounted for in the thermal calculations, neither are transient effects for surface-craft (Schlutz 2012; Schlutz and Messerschmid 2012).

Simulations on hazard avoidance in the final decent of lunar landing spacecraft were performed by ESA. Local shadows at a given landing site must be avoided due to power constraints. Landers with solar cells and secondary batteries require constant exposure to the Sun. The batteries are discharged at the beginning of surface operations. Landing in a shadow would terminate the mission immediately. The simulations take into account different boulders down to a size of 0.5 m. Thermal aspects are of secondary importance for this illumination calculations. No thermal calculations of temperatures are taken into consideration or are addressed (De Rosa et al. 2012). ESA also used the illumination simulation and a tool for orbit propagation to analysis the availability of communication links with the Earth. The general shape of the lander was modeled down to the meter level to perform these analyses (Fisackerly et al. 2011).

3 Gap Analysis

"Equipped with his five senses, man explores the universe around him and calls this adventure Science."

- Edward Powell Hubble

Programmatic driven plans for the future exploration of the solar system (section 3.1) or questions about the development of the universe posed by scientists (section 3.2) must be realized by the use of specifically designed technology. Any technology placed on the Moon has to sustain the demanding thermal environment. The environment drives the technical implementation designed by engineers, in order to fulfill the programmatic or science driven requirements (section 3.3). The objectives of this thesis, presented in section 3.4, are a direct consequence of the programmatic and science driven engineering requirements for the future exploration of the Moon.

3.1 Programmatic Requirements

On the international as well as on the European and national German exploration roadmaps, thermal demands are recognized as design drivers for future spacecraft and sustained survivability in space.

The International Space Exploration Coordination Group is a joined endeavor of 12 space faring nations that tries to coordinate and bundle the efforts started around the world to explore space. The most recent roadmap was published in 2011. In this report technologies are categorized in 14 technological areas (TA) that need to be enhanced in order to prepare for future missions. Amongst others, the identified areas demand for (ISECG 2011):

- *enable wide operational temperature ranges for power systems and advanced power storage (TA03),*
- *advancement of modeling and simulation is proposed associated with flight and ground computing, as well as integrated software and hardware modeling (TA11),*
- *improvement of thermal management systems with a focus on **heat acquisition, transport and rejection, an increase in subsystem robustness, decrease in maintenance time** and a broader temperature range for cryogenic systems" (TA14).*

One of the main goals defined by ISECG is to develop **exploration technologies and capabilities to allow and sustain human presence in the solar system**. This also incorporates longer missions with a higher degree of autonomy. Thus, the improvement for spacesuits and their thermal control systems is mentioned. The claim is made for:

- "[…] *high performance mobility extravehicular activity, life support and habitation capabilities […]*";
- "***Develop thermal management systems**, including cryogenic fluid management capabilities (e.g. systems **that can operate at length in extreme temperature environments**, and cryogenic fluid management, storage, and distribution capabilities).*" (Suzuki et al. 2011).

The understanding of local conditions, especially on planetary surfaces, is important with regard to science objectives that allow for the sustaining presence of humans in space. This is true on one hand to decide upon the most beneficial exploration sites as well as the interaction between spacecraft and the environment

"***Characterize the*** *geology, topography, and conditions at destinations (e.g. perform surveys of geologic, topographic, atmospheric,* ***thermal,*** *lighting, and micrometeorite* ***conditions at sufficiently diverse sites to support identification of future exploration sites).*" (Suzuki et al. 2011).

Moreover the demand for highly accurate models to predict the interaction between spacecraft and environment is expressed:

"***Evaluate the impacts of the surface, near-surface, and atmospheric environment on exploration systems (e.g. Research the impact of the destination's environment on the performance of exploration systems to inform future design activities).***" (Suzuki et al. 2011).

The European Space Agency also recognizes the demand for detailed models of the thermal environment for future lunar polar missions. The ESA Lunar Lander, a mission proposed by ESA and currently on hold, is a joined European effort to primarily demonstrate the capability of soft precision landing in the lunar south-pole region. The mission shall also provide insight in surface characteristics for future missions. **Measurements on illumination conditions, the day/night cycle, the thermal environment, material properties of the regolith and the impact of boulders, craters and slopes on the temperature behavior** shall be used to improve and validate existing models (Carpenter et al. 2012).

The German Aerospace Center (Deutsches Zentrum für Luft-und Raumfahrt - DLR) steers and coordinates a number of projects with respect to the Moon, such as the proposed Mobile Payload Element (MPE) a rover for the use in future lunar landing missions, and the Small Lunar Exploration Orbiter (SLEO). Further technologies under investigation in the national program are bio-regenerative life-support systems, regenerative fuel cell and energy systems, as well as *in-situ* resource utilization (Claasen et al. 2012).

3.2 Scientific Requirements

A large number of *geologic, geochemic, geophysical, astronomy,* as well as *physiology,* and *life science,* research questions were gathered in comprehensive review papers by Jaumann (2012) and Crawford (2012). The Moon is a subject of study itself or can be used as base for science. The identified fields for science *of* the Moon, besides those mentioned above, are (Crawford et al. 2012):

-   The bombardment history of the inner solar system,
-   The structure and composition of the lunar interior,
-   The diversity of lunar crustal rocks,
-   Volatiles at the lunar poles,
-   Lunar volcanism,
-   Impact processes,
-   Regolith processes, and
-   Atmospheric and dust environment.

The scientific questions that can be addressed *on* or *from* the Moon are:

-   Life science and astrobiology,
-   Human physiology and medicine,
-   Fundamental physics, and
-   Low frequency astronomy.

Most of the research questions will require *in-situ* measurements by instruments. The instruments have to survive the lunar surface conditions. In the following, only some of the named research fields will be addressed, because of the known impact of the lunar thermal environment on the necessary equipment.

Future scientific missions will aim at the *volatile elements* that were detected in cold traps at the lunar poles (Colaprete et al. 2010) and water which was found in lunar regolith (Pieters et al. 2009; Greenwood et al. 2011). These science driven missions will have **stringent requirements on acceptable heat loads as well as spatial and temporal thermal gradients**. These requirements will depend on the energy necessary to break or disturb the binding mechanisms keeping volatiles attached to the regolith. Samples in the past were gathered with scoops (Mars Phoenix lander) on the top of manipulators. More recent concepts foresee the use of so called moles (Richter et al. 2004; Grygorczuk et al. 2009; Lange et al. 2010). Scoops and moles are often made of metal and lack insulation means that are usually used for the body of a spacecraft. The lack of insulation makes manipulators more vulnerable to the thermal impact of received solar and infrared radiation. The secondary objectives for the ESA Lunar Lander stated the demand to minimize the alteration of pristine samples with volatile elements during transport to an analysis instrument hosted on the lander.

> "*A challenge for the sampling system is to minimise alteration of the samples during the extraction and delivery process. Samples are then deposited into the payload of choice.*" (Carpenter et al. 2012)

The composition of the core of the Moon and thus its origin and development differ from the history of Earth. The lack of tectonic plates in the Moons' crust leads to an entirely different *seismic* behavior. This can only be investigated by seismic instruments placed on the surface of the Moon. The instruments are sensitive to shocks normally caused by impacts of meteorites or of moonquakes originating in the core or crust of the Moon. The change in temperature due to local shadows at the terminator, but also solely due to **large thermal variations, cause thermal moonquakes and structural loads in equipment which bias the measurements** (Sens-Schönfelder and Larose 2010).

The installation of telescopes on the lunar far side for **low frequency radio-astronomy** was proposed in long-term scenarios for the utilization of the Moon (Burns et al. 1989). Since the far side of the Moon never faces the Earth, there are no artificially generated signals that might disturb measurements.

3.3 Engineering Requirements

A good and understandable overview of future trends for spacecraft thermal design challenges for robotic missions was presented by Swanson & Birur (2003). They identified a number of design drivers that require increasingly sophisticated thermal control technologies (Swanson and Birur 2003):

- Dimensional stability of large structures.
- Deep cryogenic heat acquisition and transport (40 K and below).
- **Tight temperature control (1 °C).**
- Integrated thermal/mechanical/optical systems.
- Common thermal design for fleets of micro/nano-spacecraft.
- **High flux heat acquisition (>100 W·cm^{-2}) with tight temperature control.**
- **Challenging thermal sink situations, especially for planetary environments.**
- Minimization of mass and auxiliary power use.
- Thermal control of inflatable and gossamer space structures.
- **Thermal control of spacecraft in extreme high temperature environments.**

Some of the new thermal control technologies described in the work by Swanson & Birur has matured further. Especially technologies which use radiation as primary means of rejecting heat, lead to demanding control questions if used on the lunar surface and in conjunction with random relative movement induced by the spacecraft itself. These **new thermal control components/technologies** are advanced loop heat pipes with two phases (Nabity et al. 2008; Peters et al. 2011), digital radiators with high turn-down ratios (Ganapathi et al. 2009), self-regulated heat exchangers, and electrochromic radiators with

variable optical surface properties (Metts et al. 2011). Another possible application are phase change materials which are used to dampen the effects of short term and cyclic heat loads (Swanson and Birur 2003). The technology of thermoelectric generators (TEG) proposes to use waste heat of instruments to generate power (Cernaianu et al. 2012). This technology might also be used in conjunction with the temperature extremes on the Moon.

The *lunar dust problem* was identified by the Apollo astronauts and investigated extensively by Gaier (Gaier 2005; Gaier and Jaworske 2007; Gaier 2008; Gaier et al. 2008; Gaier et al. 2010; Gaier et al. 2011; Berkebile and Gaier 2012). The studies show that dust impact on thermal control surfaces impacts the emissivity and absorptivity of radiators. Thermal control surfaces show a linear increase of the α/ε-ratio with increasing dust accumulation over time. The α/ε-ratio doubles for coverage of 53 % with a monolayer of lunar dust simulant. The absorptivity is more sensitive to coverage with dust than the emissivity (Gaier et al. 2008). Radiators covered with dust will absorb more heat from the incident solar radiation and decrease in their ability to radiate heat. Dust mitigation techniques such as brushing have shown to be inefficient (Gaier et al. 2011). Other concepts such as an electrodynamic dust shield are promising (Calle et al. 2010). A detailed analysis of heat flux/radiator interaction, taking into account dust effects will further help in the design and determination of margins for thermal control hardware.

A set of *upcoming rover missions* (see section 2.1.2.2) on private and agency level as well as studies for further exploitation of the Moon provide yet another set of potential benefiters for the analysis method described in this work. Most of these rovers are not designed to sustain the lunar night. The proposed transient analysis method can help in answering the question how long the rovers would survive if they encounter local shadows, or how long they will survive in the lunar night. Especially at the lunar Poles the illumination conditions pose special challenges both for power as well as thermal considerations (Fisackerly et al. 2011). A German consortium of academia, scientific institutes and industry investigates *robotic lunar infrastructures*. Here a set of central stations (nodes or landers) and rovers are dedicated to work together, to install instruments and prepare future human exploration at different sides on the Moon. The transient interaction between several rover modules with different purposes, for adjustable configurations of the infrastructure and each rover, and their interaction with the lunar surface can be addressed with the proposed transient analysis method. A more detailed discussion on the engineering demands caused by rovers is given in section 3.3.1.

The development of *radioisotope thermoelectric generators (RTGs)* and sterling radioisotope generators (SRGs) is closely related to thermal design of spacecraft. RTGs and SRGs are proposed for extended stays on the surface of Moon, Mars, or Asteroids or for exploration probes in interplanetary missions traveling beyond the Earth orbit. The use of radioisotope heat sources is also proposed for rovers to the lunar poles, or rovers scheduled to survive lunar nights (see Lunokhod 1 & 2 in chapter 2.1.2.1).

In the long run *manned lunar bases* provide yet another set of transient requirements. Extravehicular Activities (EVAs) performed by astronauts in spacesuits at different locations but also at different times of the lunar day will lead to very different external heat loads. This is true for the lunar topography in general but also for shadows or reflected sunlight by the man-made infrastructures composing the base. Whether areas in and in the vicinity of the base or certain modules are accessible, or if certain paths must be chosen, body postures avoided or strenuous tasks postponed, could be addressed with a more detailed knowledge of local heat fluxes and rates of change. The same is true for geological tasks in regions of permanent or prolonged shadows and thus cold spots. A more detailed assessment of the demands created by the design of spacesuits in the context of EVAs is given in section 3.3.2. The establishment of manned lunar bases also requires a more in-depth knowledge of the regolith material properties relevant for civil engineering, such as: density, cohesion, penetration resistance, slope stability, load support, regolith thickness, regolith trafficability, as well as electrical properties (Plescia 2009).

Most past and present mission designs for extended human presence on the lunar surface foresee the use of local resources, the so called ***in-situ resource utilization (ISRU)***. The lunar surface material is composed of a multitude of oxides, minerals and ores. The most abundant element is silicon dioxide SiO_2 followed by iron oxide FeO and aluminum oxide Al_2O_3 (Heiken et al. 1991) Many different approaches to utilize the *in-situ* resources were discussed in the past (Taylor and Carrier III. 1993). The processes discussed most often are the reduction of hydrogen from Ilmenite and pyroclastic glass, carbothermal reduction of lunar silicates, and molten silicate electrolysis (Cutler and Krag 1985; Sanders et al. 2005; Gustafson et al. 2009; Braukhane et al. 2010). Other resources are volatile particles implanted by the solar wind (Sanders et al. 2005; Pfeiffer and Hager 2012). Most of the concepts require process temperatures ranging from 400°C (molten salt) to 10,000 °C (plasma torches). The most promising processes such as hydrogen reduction of Ilmenite requires temperatures between 600°C and 1,000°C. These processes must be decoupled from environmental heat fluxes to control and maintain the same process conditions at all times.

In the development process of hardware that shall be used on the Moon, several fields can be identified that benefit directly from transient thermal analysis. These "stakeholders" of the engineering branch are depicted in Figure 3-1. In the early phases of a project, transient thermal analysis can help to define the boundary conditions and environmental requirements for a mission scenario. The mission scenario serves as a basis to define load envelopes for the development of equipment and surface craft. In the development process the technologies, especially for thermal control, require detailed thermal analysis. Common worst case calculations can be enhanced by the use of transient calculations and help to design the control of active thermal control devices. The overall design and layout, the accommodation and the used materials also depend to a large extend on the thermal boundary conditions. Commercial software tools do not address all the problems that are encountered on the lunar surface. Once a piece of equipment or a surface-craft is placed on the Moon, the operations domain has to deal with the conditions at hand, handle system failures or unpredicted events. A transient thermal analysis tool thus could help in the path planning and path optimization. In this context, the schedule that describes which task has to be performed at what time of lunar day is impacted by local spatial and temporal thermal conditions.
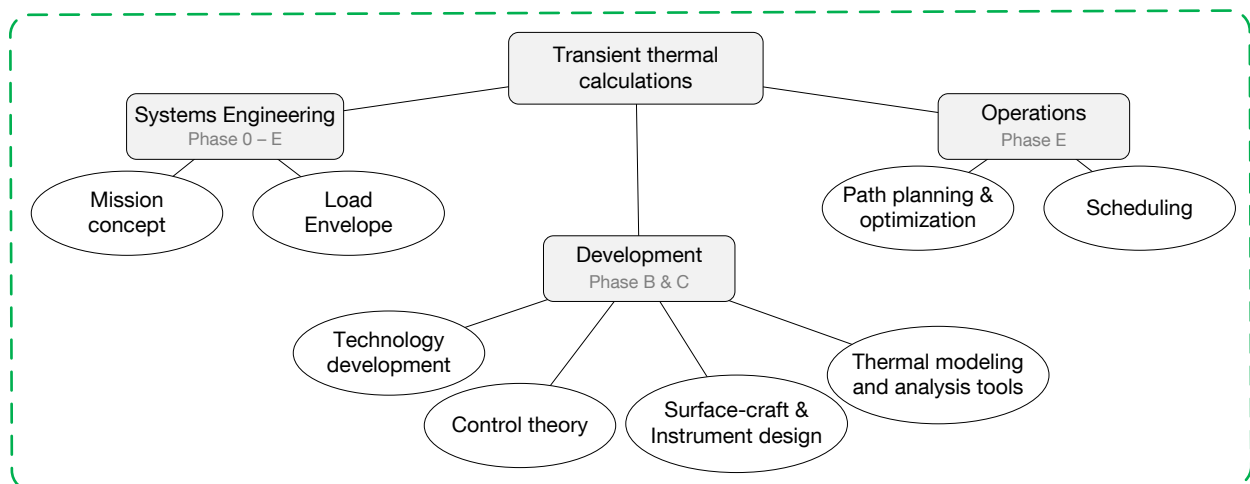

Figure 3-1: Stakeholders of transient thermal calculations for spacecraft on the Moon.

3.3.1 Thermal Analysis Requirements for Rover, Instruments, and Equipment

In this section, the main questions and design drivers regarding the thermal design of rovers, instruments, and equipment are summarized and their impact on this work is concluded, based on the investigation presented in section 2.1.1 and section 2.1.2.

The large variety in upcoming surface missions underlines the interest in the Moon. On the one hand there is the space agency's led goal to prospect scientific knowledge, human exploration of the solar system and prove technological maturity of a nation or community. On the other hand there is the competitive challenge to place and operate a rover on the lunar surface by private companies.

The survival of the lunar night was identified as special challenge. The DLR-MPE concept foresees to avoid prolonged periods of shadow and target the operation at regions with almost permanent solar illumination at the lunar poles. JAXA in contrast develops concepts to survive the lunar night. The Google Lunar XPrize offers additional prize money for the team that is able to sustain at least one lunar night. Yet, numerous teams decided to avoid the additional requirement caused by lunar night-time survival because it poses too many additional constraints on the entire spacecraft design.

The rovers currently planned for surface operations on the Moon are designed to worst case considerations which account for the hottest and coldest cases expected during the mission. The thermal control methods are thus designed to meet those static cases but are not necessarily suitable for transient effects occurring in the lunar surface environment. Often a passive design is chosen for the sake of system simplicity and with that a presumed higher safety. But that a passive design alone often is not enough to survive lunar nights or prolonged periods of darkness with resulting low temperatures was identified by most design teams. There are questions resulting from the static worst case approach that cannot be addressed without transient calculations:

- Are passive systems really unable to survive the lunar night?
- How long can such a system still operate in the lunar night environment?
- Is it possible to use local surface features to prolong or maximize this operation duration or even allow the spacecraft to survive the lunar night?

Static calculations will not be sufficient if scientific requirements for sample acquisition cause additional constraints, especially of pristine volatiles in the Polar Regions shall be sampled. These volatiles have been in cold regions for billions of years. Samples exposed to direct solar heat fluxes, infrared heat fluxes, spacecraft infrared fluxes or elevated instrument temperatures, will be lost. A thorough analysis of the transient thermal environment of the sample and its environment can help to define necessary transport times, optimized transport ways, or design of protective covers.

For static objects with an *a priory* known position on the lunar surface a passive design, based on worst case hot or cold cases, is appropriate in most occasions. Some instruments and pieces of equipment used during the Apollo program did not perform as expected due to thermal problems. Some equipment had to be redesigned. If local slopes, surface features, and possible coverage with dust were taken into account the margins could be designed accordingly. A transient assessment, taking into account local surface features and time-dependent behavior will help to answer the following questions:

- Is it possible to use a piece of equipment that was designed for particular latitude at a different location on the Moon?
- Will it perform at all or will it only perform to a certain extend?

It is noteworthy how close lunar dust contamination is connected with the thermal behavior of equipment (Gaier 2005). Lunar dust is extremely abrasive (Stubbs et al. 2007) and charged due to plasma or ultraviolet radiation (Sternovsky 2002), and thus tends to stick to the surfaces of spacecraft or spacesuits. Lunar regolith has a high absorptivity in the infrared well as in the visible wavelength spectra (sees section 4.2.2). The combination of intensive adhesion and absorptivity leads to an increased heat gain. The cause of thermal problems encountered during the Apollo program is clearly dust (Gaier 2005). The modeling of dust adhesion is not the focus of this work but its impact on thermal control surfaces can be accounted for with the proposed transient simulation approach. Whereas rover systems and instruments raise the question whether the spacecraft is able to work in a certain environment, lunar dust leads to the question:

- How well will it perform in comparison to an ideal case?

In larger rovers such as the Tri-ATHLETE concept (Heverly et al. 2010), thermal gradients can occur in parts because they have a higher view factor to the hot surface at the bottom, and a lower view factor at the top. This is further complicated by a moving spacecraft and the interaction with local surface features. Another interesting effect are high temperatures of the undercarriage of rovers due to the high lunar surface temperatures (Gump and Thornton 2011).

Dynamic thermal simulations for rovers are highly attractive for a number of cases in which mere static calculations are not sufficient.

3.3.2 Thermal Analysis Requirements for Spacesuits

An issue often encountered is the control of the liquid cooling garment. It is obvious from the abundant literature available on the subject that manual control can lead to hypothermia. The astronauts are occupied with other tasks or tired and reluctant to make the necessary adjustments (Barer 1991). Simulations relying on static worst case cold and hot environmental conditions indicated that spacesuits are unable to cope with metabolic loads in combination with extreme environmental conditions (Campbell et al. 2000). This led to the conclusion that the static consideration of metabolism and environment will result in designs that are either not feasible or must be oversized (Mays et al. 1999). Developed control algorithms did not take into account the transients in the thermal environment (Nyberg et al. 2001). The transient behavior of the environment needs to be taken into consideration when designing the control for the spacesuit thermal subsystem. Especially the control algorithms for LCG are highly dynamic (Nyberg et al. 2001). Thus, in order to design the buffers in a LCG, suit, and human thermal system, mere static environments are not sufficient. The human might not notice the changing environment as fast as the PLSS, which has to cope with it in order to maintain the astronaut in a comfortable working environment inside the suit. Furthermore, dynamic environmental conditions can help to identify if a design needs to be redone or if mission schedule recommendations are enough, even with a non-optimized system (Campbell et al. 2000). Work on the Martian surface can be used for the Moon too, since the infrared and solar heat fluxes, the overall temperatures, as well as temperature swings are more pronounced on the Moon. The movement of the astronauts during an EVAs on a planetary surface leads to a dynamic interaction with the environment, which leads to the following questions:

- Is it necessary to redesign a spacesuit because it cannot cope with worst case conditions?
- Is it possible to use buffers or other technological means to bridge situations of thermal imbalance?
- Is the LCG control algorithm able to cope with fast changing environmental conditions?
- How fast does the entire system respond to changes in the environment?
- Is it possible to overcome thermal imbalances by changes in the path of the astronauts?
- Can cases of thermal extremes be avoided by carefully planned mission schedules and by selection of regions of operation in the light of incident heat fluxes?

Thus, dynamic thermal calculations are important to accurately simulate spacesuit / external environment interactions.

As a result from the "10 km walk back test", one can conclude that the current spacesuit design would not be able to sustain the high metabolic heat during a 10 km walkback. These findings do not even account for higher heat loads due to higher metabolic production rates caused through topography or geological tasks. And it also does not account for additional environmental heat loads that might be caused by nearby slopes, boulders, or sunlit crater rims. Since the test was performed under ambient conditions, convection might have helped in cooling the spacesuit. On the other side, the space background, which serves as a cold sink, was also not present (Norcross et al. 2009). Current LCG and heat removal systems for spacecraft are not sufficient to remove elevated amounts of thermal heat loads

created by strenuous tasks, which should be expected for planetary missions (Gernhardt et al. 2009). Hence, the heat removal rates of PLSS for future missions will need significant improvements (Norcross et al. 2009).

- Does a static worst case calculation provide enough information to perform Earth based tests?

Radiators cannot replace sublimators entirely in lunar hot cases and for high metabolic loads in worst case static calculations (Jones 2009; Sompayrac et al. 2009). Yet, future concepts target the use of smaller amounts of consumables by replacing sublimators with radiators. These radiator concepts need a detailed assessment of the thermal environment in order to design appropriate control algorithms. Especially the direction and amount of incident heat flux in the infrared and solar wavelength region are important. Electrochromics or digital radiators require new control algorithms to cope with a wide variety of environmental conditions or body postures. Questions resulting from new radiator concepts are:

- How fast has the control algorithm to react to changes in the environment?
- Are there certain tasks (body postures) or areas that should be avoided?
- Which areas of the spacesuit or rover are best suited to host eletrochromatic radiators?

Static environmental cases for the design of radiators are sensible and sufficient for a landing module that remains at one position. But if the same radiator concept should be used for a (manned) rover or a spacesuit, it would see more dynamic environmental heat loads. Typical properties such as the mass flow rate have to be adopted for each environment the spacecraft-radiator encounters. Thus, even in a relatively robust spacecraft with high thermal inertia, the environment could impact the control loop of radiators. Electrochromic, thermochromic, or digital radiators show a promising potential in the thermal control of future spacesuits. But these technologies demand fast control algorithms to optimize heat rejection in connection with the astronaut's posture, velocity, and the thermal environment. A static worst case analysis can neither provide the encountered rates nor will it be able to calculate the elevated heat flux densities due to local surface features.

Another issue is the impact of dust on thermal control surfaces. Dust will alter the optical properties independent of whether the surfaces are dedicated radiators, structural parts, multi-layer insulation, or the spacesuit insulation. This effect can be taken into consideration with transient thermal models and answer the question:

- How long can a suit be exposed to the dusty environment before it needs maintenance?
- Can the thermal control system of the suit handle additional heat gains or heat losses caused by dust coverage (how large are the margins)?

Based on these findings one can conclude that it is important to have a dynamic model of the human-*LCG-Suit-PLSS-Environment* interactions to accurately predict the performance of a spacesuit for planetary missions. Extreme hot cases are deemed more difficult to handle technically than cold cases (Jones 2009; Campbell et al. 2000). In order to derive more accurate requirements to design more capable and appropriate spacesuits, the understanding of the local environment (such as thermal and local topography) is necessary (Fullerton 2001).

3.4 Thesis' Objectives

The interaction of solar heat reflected and re-emitted in the infrared range are far more complex on the surface of celestial bodies than in an orbit. In the absence of an atmosphere, which serves as a thermally inert buffer, the radiation-dominated heat exchange is even more pronounced. The local temperature and with it the local heat fluxes depend on a number of factors of the Moon-Earth system, local Moon material properties and local surface features. Such surface features are boulders or craters, riffs, and channels which are especially pronounced in geological inactive and atmosphere-less bodies such as the Moon (see chapter 4.2.2).

Man-made objects on the lunar surface are subject to this radiation-dominated thermal environment. This is true for static objects such as landers, instruments, and bases as well as moving spacecraft such as rover and astronauts in spacesuits. In the case of bases and landers, static thermal analysis will provide sufficient results. A thoroughly design of moving surface-craft in contrast will have to take into account infrared heat loads due to local features and varying direct and reflected solar heat fluxes. The use of static worst case thermal calculations leads to spacecraft that are either oversized or of which the margins for transient cool down and heat up phases have large uncertainties.

Current thermal tools like Thermal Desktop/SINDA, ESATAN-TMS or Thermica/Thermisol are well suited to account for the thermal design questions arising in orbits around the Earth or other celestial bodies. When it comes to surface operations, only simplified spherical bodies are implemented in Thermica (Sariano 2010), and were added to ESATAN-TMS in its release r5, in late 2012. This lack of detailed models shall be overcome with the simulation approach, presented in this work.

The main objective of this work thus targets moving surface-craft on the surface of the Moon, such as small exploration rover and astronauts in spacesuits. The secondary objectives focus on the implementation of an appropriate simulation approach to address the primary objectives.

Primary Objectives:

1) **Calculate time-dependent local infrared and solar heat flux**, depending on local surface features, time of lunar day and local surface temperature.

2) **Calculate dynamic infrared heat flux rates,** for characteristic movements of spacesuits.

3) **Provide a higher temporal resolution of core temperature of sample bodies,** compared to static worst case calculations, in shadow transients in a relevant lunar environment.

Secondary Objectives:

1.) Asses the feasibility of a dynamic thermal simulation method for moving spacecraft on the lunar surface.

2.) Establish the dynamic thermal simulation method and verify its results against literature and remote sensing data.

3.) Identify cases in which dynamic thermal simulations are likely to be most beneficial compared to static cases.

4.) Derive simplified equations for the thermal design in Phase 0/A studies.

5.) Provide a framework for further studies (for example on the impact of lunar dust on thermal control surfaces).

4 Fundamentals of Thermal Engineering

"There is a theory which states that if ever anyone discovers exactly what the Universe is for and why it is here, it will instantly disappear and be replaced by something even more bizarre and inexplicable. - There is another theory which states that this has already happened."

- Douglas Adams

This chapter focuses on physical, geological, engineering, and computation science fundamentals necessary to address the hypothesis. In section 4.1 the fundamentals of heat transfer are discussed with a focus on radiative heat transfer. Section 4.2 highlights the space environment with a focus on the lunar environment and its thermal characteristics. In section 4.3 the principles in thermal design and control of spacecraft are discussed with a focus on planetary surface-craft and innovative radiator concepts. In section 4.4 computational methods for thermal modeling relevant for this thesis, are presented. The mathematical basics of linear algebra and analysis, necessary for coordinate transformation and differential equations are omitted. The interested reader is referred to standard textbooks.

4.1 Fundamentals of Heat Transfer

In the following, the main mechanisms of heat transfer are shortly introduced in the light of spacecraft thermal engineering. For more detailed deduction of those equations the interested reader is referred to the textbooks on thermodynamics and heat transfer such as (Incropera and DeWitt 2002; Polifke and Kopitz 2009). Conductive and radiative heat transfer mechanisms are discussed in more detail due to their relevance for this work. Special emphasis is put on the radiative heat transport, since it plays a central role in the presented work. Convective heat transfer has heat diffusion and heat advection contributions that must be taken into account for fluids or gases. Convection is crucial for pressurized volumes or planets and moons with atmospheres. Yet, for surface-craft on atmosphere-less celestial bodies, convection can be omitted and will not be further addressed[8]. Ablation, which some textbooks consider as an independent fourth form of fundamental heat transfer, will also not be discussed here.

4.1.1 Elementary Heat Transfer

The foundation of heat transfer is the first law of thermodynamics (conservation of energy). It is often a helpful tool to understand the heat fluxes crossing boundaries and to derive the overall heat equation of a given problem. For basic heat transfer the easiest way to understand the underlying equations is to consider a control volume and balance the rate of incoming $\dot{Q}_{in}$ and outgoing $\dot{Q}_{out}$ thermal energy [J·s^{-1}] [W] with heat originating inside the control volume $\dot{Q}_g$. Figure 4-1 shows such a control volume.

$$\dot{Q}_{st} = \frac{dQ_{st}}{dt} = \dot{Q}_{in} + \dot{Q}_g - \dot{Q}_{out} \tag{1}$$

The thermal energy balanced yield the internally stored thermal energy Q_{st} of the control volume. $\dot{Q}_{in}$ and $\dot{Q}_{out}$ can occur via conductive, convective, radiative or ablative heat transfer, and are functions of temper-

---

[8] If fluid loops are modeled the free and forced convection must be accounted for, also for systems on atmosphere-less celestial bodies.

ature, position in space, and material properties. The governing functions to conductive and radiative processes will be discussed in more detail in section 4.1.2 and 4.1.3. $\dot{Q}_g$ can either be a chemical process (exogenic reactions), radioactive decay, or dissipation in electronic devices. With $\dot{w}$ being the rate of energy production per unit volume one can derive for the control volume:

$$\dot{Q}_g = \dot{w}\ dx\ dy\ dz \tag{2}$$

The change in stored thermal energy $\dot{Q}_{st}$ depends on material properties and can be written as:

$$\dot{Q}_{st} = \rho \cdot c_p \cdot \frac{\partial T}{\partial t} \cdot dx \cdot dy \cdot dz \tag{3}$$

A special case is the so called steady state. The steady state is a condition in which the time-dependent variations are assumed to advance zero:

$$\rho \cdot c_p \cdot \frac{\partial T}{\partial t} \cdot dx \cdot dy \cdot dz = 0 \tag{4}$$

Steady state is often used in order to derive first order approximations of a given problem, especially if the problem is assumed to be thermally inert. This can be the case for large volumes $dx \cdot dy \cdot dz$, material with high densities ρ or specific heat capacities c_p in comparison to the applied heat loads. This is independent of the heat source or transport mechanism.
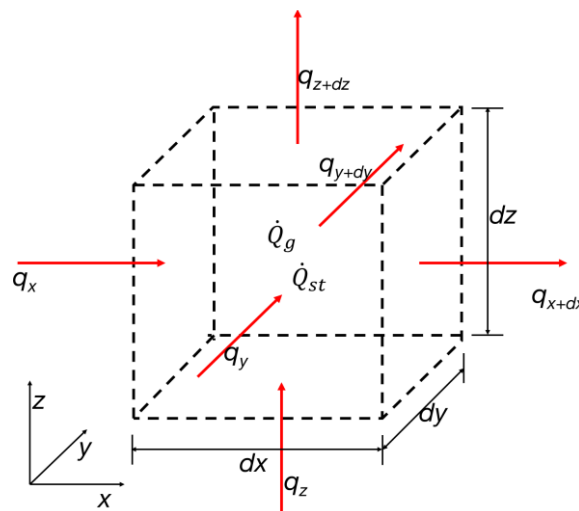
Figure 4-1: Differential control volume [reproduced from (Incropera and DeWitt 2002: 61)].

4.1.2 Conductive Heat Transfer

The conductive heat transport is a transfer of energy by changes in the vibration energy levels of atomic bonds in an atomic lattice, so called phonon-phonon interactions. In addition, free electrons carry energy in case of conductors (Modest 1993; Incropera and DeWitt 2002). The conductive heat transfer is governed by Fouriers law. Fouriers law states that heat $\dot{Q}_{cond}$ flows along a temperature gradient $\frac{\partial T}{\partial x}$ and is proportional to the area A perpendicular to the line denoting the direction of the temperature gradient. This relation is mediated by a proportionality factor, called the thermal conductivity k.

$$\dot{Q}_{cond} = -A \cdot k \cdot \frac{\partial T}{\partial x} \tag{5}$$

The thermal conductivity k depends on the material and can vary with temperature. Inside a given material inhomogeneities can also cause different values of k. These differences might even be present between different batches of the same material. In composite materials, different materials or the direction of the

webbing can cause large differences between parallel and orthogonal values of the thermal conductivity. A value often used is the thermal heat flux q_x which is defined as:

$$q_x = \frac{\dot{Q}_x}{A} = -k \cdot \frac{\partial T}{\partial x} \tag{6}$$

With regard to equation (1) it is now possible to define the conductive heat fluxes across the system boundaries of the control volume. They can now be separated into incoming:

$$\dot{Q}_{in} = q_x + q_y + q_z \tag{7}$$

and outgoing heat fluxes. The outgoing conductive heat fluxes can be approximated by a Taylor series expansion neglecting higher order terms (Incropera and DeWitt 2002):

$$\dot{Q}_{out} = q_{x+dx} + q_{y+dy} + q_{z+dz} = q_x + \frac{\partial q_x}{\partial x} dx + q_y + \frac{\partial q_y}{\partial y} dy + q_z + \frac{\partial q_z}{\partial z} dz \tag{8}$$

The conductive heat rates can be derived from Fouriers law. With the assumption that the material is at least locally homogenous $k = k_x = k_y = k_z$ and hence:

$$q_x = -k \, dy \, dz \frac{\partial T}{\partial x} \tag{9}$$

$$q_y = -k \, dx \, dz \frac{\partial T}{\partial y} \tag{10}$$

$$q_z = -k \, dx \, dy \frac{\partial T}{\partial z} \tag{11}$$

These equations can be adopted for cylindrical or polar coordinates, but will not be introduced here. Based on equations (9) to (11) it is now possible to derive the heat diffusion equation:

$$\frac{\partial}{\partial x}\left(k \frac{\partial T}{\partial x}\right) + \frac{\partial}{\partial y}\left(k \frac{\partial T}{\partial y}\right) + \frac{\partial}{\partial z}\left(k \frac{\partial T}{\partial z}\right) + \dot{u} = \rho \cdot c_p \cdot \frac{\partial T}{\partial t} \tag{12}$$

in which ρ is the material bulk density and c_p is the specific heat capacity. In order to solve this equation initial conditions for the temporal domain and boundary conditions for the spatial domain are necessary. From a physical standpoint it is necessary to know the conditions at the beginning and at the end of a given control volume in each dimension in order to determine the condition of the intermediate volume. From a mathematical point of view the spatial coordinates are of second order, two boundary conditions must be given per dimension (Incropera and DeWitt 2002). Since the temporal term is of first order one initial condition is sufficient.

There are three boundary conditions. The boundary conditions are the Dirichlet (first kind), the (van) Neumann (second kind), and the third kind of boundary conditions which has no distinct name (Incropera and DeWitt 2002). The Dirichlet boundary condition describes a boundary with a constant surface temperature:

$$T(0, t) = T_s \tag{13}$$

It is encountered in cases with bordering elements that are subject to a phase change. The van Neumann boundary condition is the one used most often. It describes a boundary with a constant finite heat flux:

$$-k \frac{\partial T}{\partial x}\bigg|_{x=0} = q_s \tag{14}$$

A special case of this condition often used for simplification is an adiabatic boundary condition:

$$\frac{\partial T}{\partial x}\bigg|_{x=0} = 0 \tag{15}$$

Finally, the third type of boundary condition is applicable if a surface is heated or cooled by convection:

$$-k \frac{\partial T}{\partial x}\bigg|_{x=0} = h \cdot [T_\infty - T(0,t)] \tag{16}$$

As can be seen from the equations above that conductive heat transfer depends on direction and material properties, as well as on boundary and initial conditions. With regard to spacecraft applications the control and understanding of material properties is important. The qualification and control processes involved are one of the reasons why spacecraft hardware is so expensive. The geometry in spaceflight is seldom composed of solid bodies but thin plate structures, leading to two dimensional heat conduction problems. With composite materials entering the spaceflight domain more and more, differences in conduction of different direction gain more importance. The conductive paths transmitting thermal energy between different parts, components, or assemblies are of utmost importance for the thermal design of a spacecraft, but often can only be determined by test.

4.1.3   Radiative Heat Transfer

In order to understand the basic principles involved in radiative heat transfer certain laws, relationships and coefficients have to be introduced. Numerous textbook exist specifically on the subject of thermal radiation. The interested reader is referred to the books of (Siegel and Howell 1992) or (Modest 1993). Only the basics are mentioned here for completeness. Radiative heat transfer or thermal radiation is a process in which heat is transferred by photons. The technical relevant wavelength spectrum is 10^{-7} m to 10^{-3} m, which is the ultraviolet, visible, and infrared portion of the wavelength spectrum (Modest 1993). Different from conductive and convective heat transfer, which both need a medium, thermal radiation also works in absolute vacuum. Hence, it is the most important heat transfer mechanism in spaceflight applications. Different from conductive and convective heat transport, heat transported via thermal radiation is equivalent to the forth power of a body's temperature. This fact is important for the understanding of transferred heat flux on the Moon and from its surface material the regolith to surface-crafts. In porous media the radiative heat transport can become the most important method of heat transfer if no gas or liquid is present and the temperatures are high enough (Winter and Saari 1969).

The central equation for radiative heat transfer q_{rad} between two surfaces, in spacecraft applications is:

$$q_{rad} = -\alpha_2 \cdot \varepsilon_1 \cdot \sigma \cdot F_{1-2} \cdot (T_2^4 - T_1^4) \tag{17}$$

In this equation the subscript *1* denotes the emitting and *2* the receiving surface. Thus T_1 and T_2 are the surface temperatures of the surfaces involved in the heat exchange, α_2 is the absorptivity coefficient of the receiving surface and ε_1 is the emissivity coefficient of the emitting surface. σ denotes the Stefan-Boltzmann constant and has a value of $\sigma = 5.6704 \cdot 10^{-8}$ W·m^{-2}·K^{-4}. The factor F_{1-2} is the view factor, and is sometimes also referred to as configuration factor (Siegel and Howell 1992).

The temperature of each surface is coupled to the material by means of conduction or convection. Material properties such as density, specific capacity, and mass will have an effect on the temporal behavior, as was mentioned in section 4.1.1 about elementary heat transfer and can be seen in Fourier's law. The temperature thus is a coupled value depending on the result of a spatial and temporal dependent differential equation.

$$T = f(c_p, \rho, m) \tag{18}$$

<u>Emissive Power:</u>

It is important to note that the quantities discussed hereafter depend on angle of incident (specular vs. diffuse) as well as wavelength (spectral, averaged, or total). For spaceflight applications and the presented work only diffuse properties averaged for a certain wavelength region are used. The starting point for the introduction to radiative heat transfer is always a black body. A black body does not reflect any incoming radiation but allows it to pass across its boundaries and attenuates all radiation (no transmission) for all wavelength and angles of incident (Siegel and Howell 1992). It serves as reference for a body that is

absorbing and emitting in an ideal way. Intensity and emissive power are only a function of the black body's temperature. The spectral emissive power $e_{\lambda,T}$ of a black body, according to Planck's law is given with:

$$e_{\lambda,T} = \frac{2 \cdot \pi \cdot h \cdot c^2}{\lambda^5 \left(e^{\frac{h \cdot c}{k_B \cdot \lambda \cdot T}} - 1 \right)}$$

(19)

With the Planck constant $h = 6.626 \cdot 10^{-34}$ J·s, the speed of light c in the surrounding medium, and the Boltzmann constant $k_B = 1.38 \cdot 10^{-23}$ J·K^{-1}. Here the wavelength is used although in literature Plank's equation can be found also written with frequency v or wavenumber η. Since the wavelength will be used more often in this work, this notation is chosen. Also here it is assumed that the radiative heat exchange takes place in vacuum, thus $c = c_0 = 299,292,458$ m·s^{-1}. For other media the refractive index n_r must be taken into account with $c = c_0/n_r$.

Integration over the entire wavelength spectrum yields the hemispherical total emissive power $E_{bb,T}$, also called the Stefan-Boltzmann law:

$$E_{bb,T} = \int_0^\infty e_{\lambda,T} \cdot d\lambda = \sigma \cdot T^4$$

(20)

with the Stefan-Boltzmann constant $\sigma = 5.6704 \cdot 10^{-8}$ W·m^{-2}·K^{-4}. This fundamental equation governs the radiative heat transport.

Emissivity and absorptivity:

Most materials are not entirely black, leading to the introduction of emissivity ε and absorptivity α. The entire spectral range of the Sun ranges from $0.2 \leq \lambda \leq 3\,\mu m$, thus ultraviolet, visible light, and near infrared (Incropera and DeWitt 2002). The distribution of the radiation of the Sun is approximately 7 % ultraviolet, 46 % visible, and 47 % near infrared. For spaceflight applications it is important to note that the infrared emitted by the Sun is in a much shorter wavelength region than the heat emitted by spacecraft near room temperature. This fact must be taken into consideration for the choice and application of surface control materials (Gilmore, ed. 2002-c2003).

The emissivity is defined as the ratio between the emitted energy by a real body and a perfect black body. This is also referred to as a grey body:

$$\varepsilon(\theta, T) = \frac{\int_0^\infty \varepsilon_{\lambda,T} \cdot e_{\lambda,T} \cdot d\lambda}{\int_0^\infty e_{bb,\lambda,T} \cdot d\lambda} < 1$$

(21)

The emissivity depends on the wavelength λ and the angle of incident θ. Thus one has to be cautious whether a given ε is diffuse or spectral, for a certain wavelength regime or the entire spectrum. In spaceflight applications it is common to use the diffuse emissivity for the infrared wavelength region (between λ = 0.78 μm and 1,000 μm).

The absorptivity in turn determines the amount of radiation really absorbed by a body in contrast to the ideal case of a black body:

$$\alpha(\theta, T) = \frac{\int_0^\infty \alpha_{\lambda,T} \cdot e_{\lambda,T} \cdot d\lambda}{\int_0^\infty e_{bb,\lambda,T} \cdot d\lambda} < 1$$

(22)

Also the absorptivity of a real or grey body can either be specular or diffusive, and an absorptivity coefficient can be defined for the entire spectrum or portions of it. For spaceflight applications it is common to use the diffuse absorptivity for the spectral range of the Sun. Besides, for a given angle of incident and a given wavelength it is:

$$\alpha(\theta, \lambda) = \varepsilon(\theta, \lambda) \; \forall \theta, \forall \lambda \tag{23}$$

This law often confuses engineering students, since in textbooks about spacecraft engineering α and ε are often given for the spectral regions mentioned above. This in turn means that α and ε are not at all equal and cannot be used as substitute for each other but must be used with care in the applicable wavelength regions.

With the Stefan-Boltzmann law and the definition for grey bodies the total emissive power E_T, a grey body for a given wavelength interval emits is:

$$E_T = \varepsilon_\lambda \cdot \sigma \cdot T^4 \tag{24}$$

The maximum in wavelength for a given temperature can be derived from Planck's law and is formulated in Wien's displacement law:

$$\lambda_{max} = \frac{b}{T_{max}} \tag{25}$$

With the factor $b = 2{,}897.8 \cdot 10^{-6}$ m·K and T_{max} the maximum temperature in [K]. In general, this law states that with higher temperatures the maximum wavelength is shorter.

The coefficients for absorptivity and emissivity depend mainly on material properties but are also dependent on temperature, angle of incident θ, and wavelength λ.

$$\alpha(T, \lambda, \theta), \varepsilon(T, \lambda, \theta) \tag{26}$$

The law for the conservation of energy demands that absorbed energy, reflected energy, and transmitted energy sum up to 1. In spaceflight applications the used materials are mostly opaque[9] which means that transmitance $\tau^k = 0$.

$$\alpha(\lambda, \theta) + \rho^k(\lambda, \theta) + \tau^k(\lambda, \theta) = 1 \tag{27}$$

The reflectance ρ^k can be either diffuse ρ_d^k or specular ρ_s^k. In this work all surfaces are considered to be of diffusive reflectance.

$$\rho^k = \rho_d^k + \rho_s^k \tag{28}$$

View factor:

The view factor gives the geometric relation between two randomly shaped and oriented surfaces. Other names are angle, shape, interchange, or configuration factor (Siegel and Howell 1992). In the present work the term "view factor" is used since it is the common term used in spaceflight applications. In order to explain the geometrical behavior of a black body's intensity it needs to be defined alongside the emitted power. The outgoing emissive power $E_{bb}(\lambda, \theta)$ and the projected surface area on a hemisphere above that surface are connected through the intensity $I_{bb}(\lambda, \theta)$:

$$E_{bb}(\lambda, \theta) = I_{bb}(\lambda, \theta) \cdot \cos\theta \cdot dA_1 \tag{29}$$

This is also called Lambert's law or cosine law (Modest 1993; Siegel and Howell 1992; Walter 2007). Analog to the emissive power, a distinction needs to be made between total and spectral, as well as diffuse and directional intensity.

Figure 4-2 depicts the general correlation between the differential elements d_1 and d_2 of surface element A_1 and A_2 [m²]. The total hemispherical emitted power $E_{bb,d1-d2}$ of the finite surface element dA_1 for a diffusive black body is:

---

[9] Complete attenuation of penetrating radiation, i.e. incoming electromagnetic waves, at the wavelength considered, do not pass the material; they are either absorbed or reflected. If none of the incoming electromagnetic waves are reflected the body is called a perfect absorber or black surface Modest (1993).

$$E_{bb,d1-d2} = I_{bb} \cdot dA_1 \cdot \cos \theta_1 \cdot d\omega_1 \tag{30}$$

where the slash between d_1 and d_2 means "to", θ_1 is the angle between surface normal of A_1, and the line connecting the center of A_1 and A_2 and $d\omega_1$ is the solid angle. The solid angle in turn is the projection of area dA_1 on the distance d between the centers of surface A_1 and A_2 (Siegel and Howell 1992):

$$d\omega_1 = \frac{dA_2 \cdot \cos \theta_2}{d^2} \tag{31}$$

$$E_{bb,d1-d2} = \frac{I_{bb} \cdot dA_1 \cdot \cos \theta_1 \cdot d\omega_1 \cdot dA_2 \cdot \cos \theta_2}{d^2} \tag{32}$$
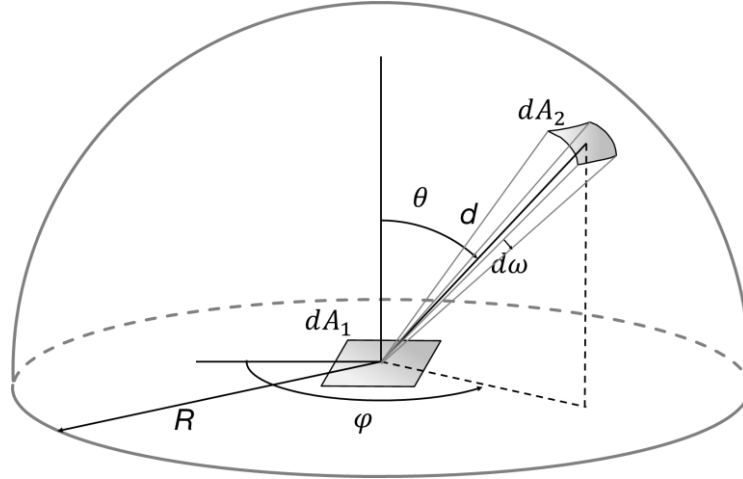
Figure 4-2: Solid angle $d\omega$; view factor between dA_1 and dA_2. (reproduced from Siegel and Howell 1992).

The view factor is defined as the ratio between the directional emitted power of A_1 and A_2 to the total hemispherical emissive power:

$$F_{d1-d2} = \frac{I_{bb} \cdot dA_1 \cdot \cos \theta_1 \cdot dA_2 \cdot \cos \theta_2}{d^2} \cdot \frac{1}{\pi \cdot I_{bb} \cdot dA_1} = \frac{\cos \theta_1 \cdot \cos \theta_2}{\pi \cdot d^2} \cdot dA_2 \tag{33}$$

This also shows that the view factor is always between 0 and 1. It is important to note that in general:

$$F_{1-2} \neq F_{2-1} \tag{34}$$

But for the view factor between two finite surfaces one can derive the law of reciprocity (Siegel and Howell 1992):

$$A_1 \cdot F_{1-2} = A_2 \cdot F_{2-1} \tag{35}$$

Only four view factors will be introduced here, since they are used in the calculation of simplified cases in section 4.2.2 and section 6.2. The interested reader is referred to the exhaustive textbook by Siegel and Howell (1992) and its online supplement with a rich database of view factors.

As the first example, the view factor from an element in the Earth orbit (1) facing the Sun (2) is calculated and shown in Figure 4-3a. With the assumption that angles θ_1 and θ_2 approaching 0°, the radius of the Sun R_{Sun} ~700,000 km and the distance between Sun and Earth $d_{Sun-Earth} = 1.49 \cdot 10^6$ km (= 1 AU) the view factor becomes:

$$F_{Earth-Sun} = \frac{dA_{Sun}}{\pi \cdot d_{Sun-Earth}^2} = \frac{\pi \cdot R_{Sun}^2}{\pi \cdot d_{Sun-Earth}^2} = \left(\frac{R_{Sun}}{d_{Sun-Earth}}\right)^2 \tag{36}$$

From this calculation and the simplification $\cos \theta_1 \approx 1$ for small values of θ_1, one can also derive that the radiation coming from the Sun is parallel at the distance of the Earth. The second example, shown in

Figure 4-3b, represents the view factor from a perpendicular surface element on a disc. This correlation can be used for orbiting spacecraft:

$$F_{1-2} = \frac{1}{\pi} \cdot \left(\tan^{-1} \frac{1}{\sqrt{r_F^2 - 1}} - \frac{\sqrt{r_F^2 - 1}}{r_F^2} \right), \qquad r_F = \frac{d}{R} \tag{37}$$

The third view factor (Figure 4-4a) refers to a finite rectangular surface element placed above an infinite plane. It can be used for small elements, such as spacecraft, on planetary surfaces.

$$F_{d1-2} = \frac{1}{r_F^2 + 1}, \qquad r_F = \frac{d}{R} \tag{38}$$

The fourth view factor (Figure 4-4b) introduced here is between two orthogonal rectangular surfaces with a common edge. In a first order approximation, and the assumption that $d \ll w$, it can be used for the vertical sides of spacecraft on planetary surfaces.

$$F_{1-2} = \frac{1}{2} \cdot \left(1 + r_F - \sqrt{1 + r_F^2} \right), \qquad r_F = \frac{d}{w} \tag{39}$$
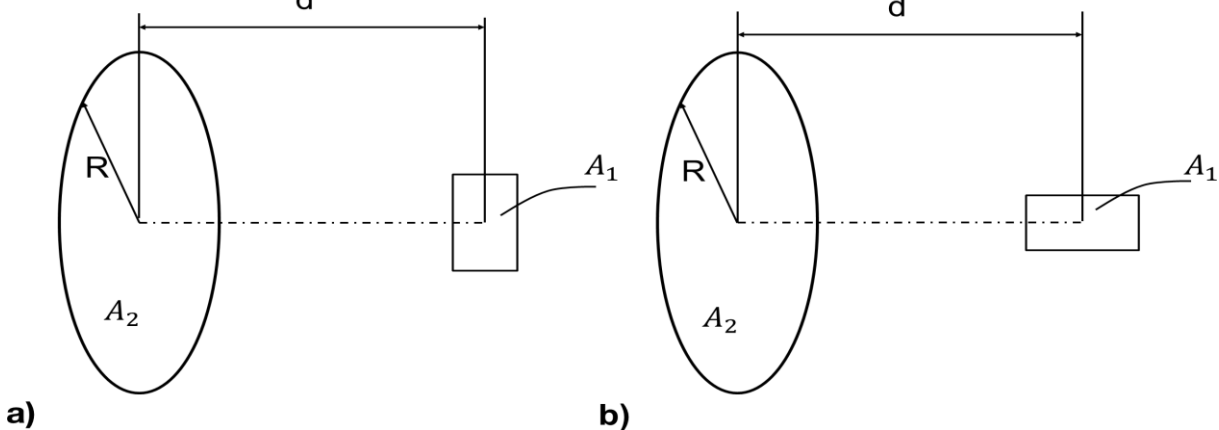
Figure 4-3: View factors a) of a square element parallel, and b) of a square perpendicular to a disc with coaxial center lines.
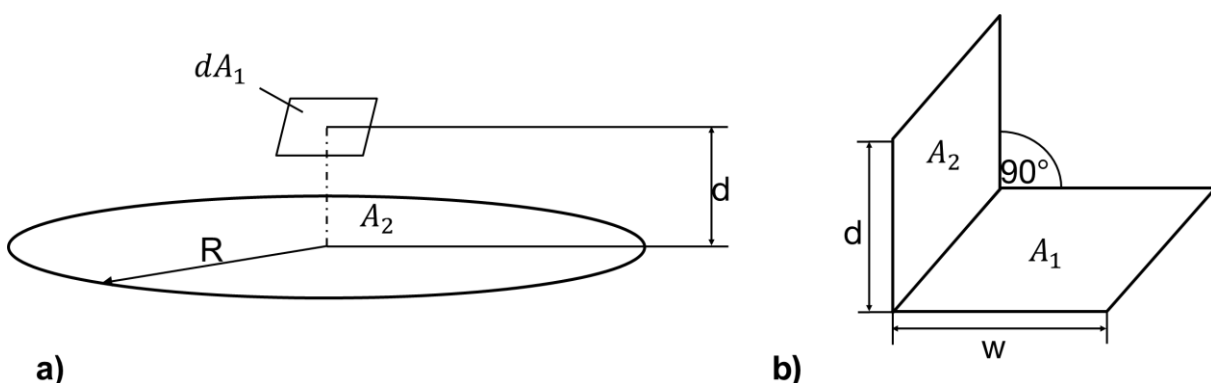
Figure 4-4: View factors a) of a finite rectangular surface element placed above an infinite plane, and b) between two orthogonal rectangular surfaces with a common edge.

4.2 The Space Environment

In the following section the thermal space environment will be discussed in more detail for various regions: the immanent vicinity of the Earth with the orbits used for most of the spacecraft currently send to space (section 4.2.1), for interplanetary voyages (section 4.2.3), as well as for spacecraft on atmosphereless celestial bodies such as the Moon, Mercury or Asteroids. A separate section is dedicated to the lunar environment (section 4.2.2).

4.2.1 Near Earth Space

The Earth has a mean radius of 6,378 km. The border to space is defined at 100 km altitude above this mean radius. There is no distinct line that separates the Earth atmosphere from space but a gradual change in environmental conditions. The decrease in pressure follows an exponential decay with altitude and is the most obvious change with increasing altitude. The space environment encountered beyond 100 km poses a number of challenges to man and equipment. The most apparent differences to the environmental conditions on the surface of the Earth are the lack of an atmosphere and the effects of weightlessness. Other problems trace back to these fundamental differences.

The values for the atmospheric density stretch from 1.2 [kg·m^{-3}] at the surface of the Earth, to 6.98·10^{-12} kg·m^{-3} in a 350 km orbit, and 5.21·10^{-16} kg·m^{-3} in a 1,500 km orbit (Wertz and Larson 1999). The ambient gas density diminishes further with increasing distance to a gas source. The reduced gas density and therewith reduced gas pressure is called vacuum once the total pressure drops below 300 mbar. The lack of gaseous molecules in turn disables convective heat transfer and causes off-gassing of materials. Off-gassing occurs if the gas-pressure inside of a given material is higher than the surrounding total gas pressure. This is mostly true for organic materials (Wertz and Larson 1999). The molecules freed in this way, are a contamination on optics and thermal control surfaces. Such an artificial coating decreases the functionality of the subsystem. Furthermore, with respect to human spaceflight a pressure vessel must be provided to keep the humans' body fluids from boiling, oxygen must be provided, and carbon dioxide needs to be removed. The lack of atmosphere also exposes a spacecraft to the full sun spectrum. Ultraviolet-rays in the solar spectrum cause the degradation of surface materials. The protective effect of the atmosphere also takes its toll on the exposure to micrometeorites and radiation. Both are harmful to spacecraft and humans in different ways. Especially in LEOs[10] the remaining neutral atmospheric particles can cause mechanical degradation of surfaces due to their relative kinetic velocity, but also by reacting with the surface. A part of the atoms in LEO are ionized by the solar irradiation. This so called plasma environment leads to spacecraft charging and is hazardous for instruments, as well as optical and thermal surfaces (Tribble 2003).

For spacecraft in an orbit around the center of the Earth, the gravitational force decreases proportional to the inverse of the second power of distance between the spacecraft and the center of the Earth. The gravitational force in LEO is around 90 % of that at the Earth surface (Wertz and Larson 1999). Thus weightlessness does not describe lack of gravitational force but equilibrium of gravitational pull and mass inertia. This effect mainly impacts the behavior of fluids because the natural free convection due to density gradients does not apply. This has consequences for organic or technical systems that contain liquids or gases. Further, more subtle effects such as feeling of remoteness or constriction are of psychical nature and will not be discussed in this work any further. With increasing distance to the Earth and depending on the orbit inclination, charged particles from our Sun, or other active celestial bodies can cause severe harm to human tissue as well as electronic circuits. In the vicinity of the Earth, spacecraft are protected by the magnetic field.

---

[10] Spacecraft with an orbit perigee below 1000 km are said to be in a Low Earth Orbit (LEO). Most spacecraft in this orbit have a low eccentricity, often with high inclinations, in order to cover most of the Earth's surface.

The most important impact, related to this work, is a combination of lack of convection paired with the exposure to the entire solar spectrum. Due to these effects thermal radiation becomes the main means of heat transfer for spacecraft.

A spacecraft is subject to heat fluxes directly from the Sun, reflected from the surface of nearby planets or moons, as well as the emitted infrared radiation from planets and moons. Inside the spacecraft thermal energy comes from electronic devices, chemical processes, or atomic decay. All energy used in electronic devices eventually is converted into thermal energy with the exception of electric energy transformed in high frequency electromagnetic waves for communication, spacecraft control, and data transmission. The human metabolism also creates heat depending on load level (oxygen consumption) and individual fitness and constitution. Figure 4-5 depicts the different heat fluxes impinging on a spacecraft. In contrast to the heat sources mentioned above, deep space is an infinite radiative heat sink. It has an absolute temperature of $T_\infty = 2.7$ K (Gilmore, ed. 2002-c2003; Ley et al. 2009).
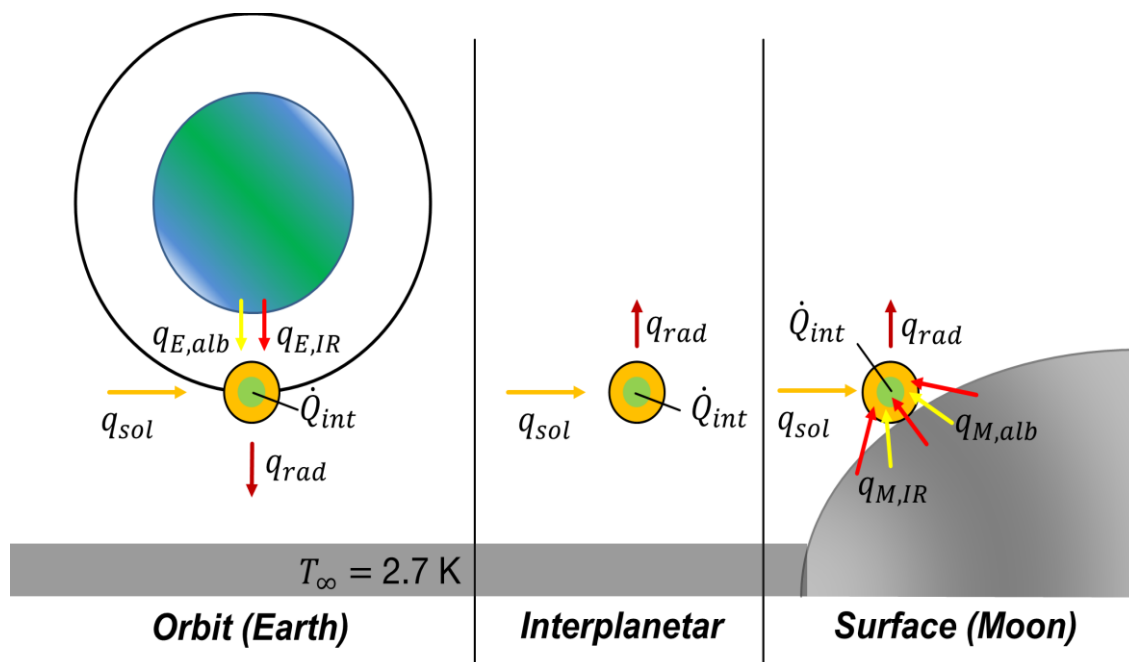
Figure 4-5: Heat fluxes for spacecraft in an orbit around Earth, in interplanetary space, and on the surface of the Moon.

The direct solar heat load covers the wavelength spectrum from 0.2 μm to 2.6 μm (Gilmore, ed. 2002-c2003) with its maximum at around $\lambda \approx 501$ nm (Siegel and Howell 1992). Whereas on the surface of Earth certain parts of the spectrum are dampened by the atmosphere, in space the full solar spectrum impinges on the spacecraft. Assuming the Sun to be a blackbody that emits uniformly in every direction, and taking into account the maximum wavelength, an effective surface temperature of 5,780 K (Siegel and Howell 1992) can be calculated. Based on the effective surface temperature of the Sun T_{sol}, the distance to the Sun R_{Sol}, the heat flux of Sun radiation q_{sol} [W·m^{-2}] can be calculated for any distance d_{sol} [km] from the Sun (Walter 2007). The radius of the Sun is given with 6.96·10^5 km (Ley et al. 2009).

$$q_{sol} = \sigma \cdot \left(T_{sol} \cdot \sqrt{\frac{R_{sol}}{d_{sol}}} \right)^4 \qquad (40)$$

For 1 astronomical unit (AU) the heat flux thus yields $q_{sol} = 1,369.4$ W·m^{-2}. In literature the so-called solar constant at 1 AU is often given with 1367 W·m^{-2} and is denoted with S. The distance between Sun and Earth is not constant but changes due to the eccentricity of the Earth orbit. This change in the distance between Sun and Earth leads to a fluctuation of about ±3.5 % throughout one year with a minimum of

1,322 W·m⁻² during summer solstice and a maximum of 1,414 W·m⁻² at winter solstice. The 11-year cycle of the Sun only has minor impact on the overall heat flux of less than 1 % (Gilmore, ed. 2002-c2003). Figure 4-6a depicts the decline of the overall heat flux with distance to the Sun.
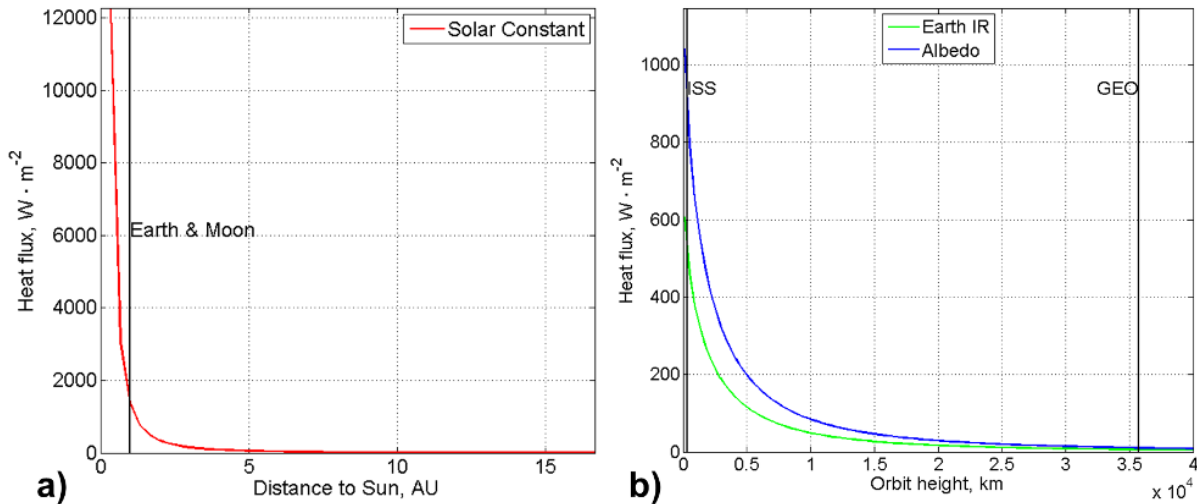
Figure 4-6: a) Decrease of the solar constant with distance from the Sun; b) decrease of infrared and albedo heat fluxes with orbit height, [based on (Ley et al. 2009)].

The central body emits heat in the infrared wavelength according to its mean surface temperature. Wavelength and temperature are connected through Plancks law (see section 4.1.3). In case of Earth, the effective medium temperature is 255 K (-18°C) (Gilmore, ed. 2002-c2003). The infrared heat flux originating from a planet decreases in the same manner as the solar heat flux decreases by the inverse of the distance between spacecraft and Sun. For Earth, the decline in infrared heat flux with orbit altitude is depicted in Figure 4-6b.

The reflected solar heat flux, the so-called Albedo is a ratio between incoming and outgoing heat flux of a celestial body. The Albedo heat flux depends on the surface of the celestial body as seen from the spacecraft. For celestial bodies with an atmosphere, such as Earth, the Albedo is influenced by clouds which reflect large amounts of sunlight. Ice fields are also highly reflective to the light in the solar spectrum and thus have an Albedo of 0.8-0.85. Oceans have an Albedo of 0.08, forests of 0.05-0.1 and deserts of 0.3 (Gurdeau et al. 2004). In general, an average Albedo for Earth is given with 0.3 for first order calculations (Wertz and Larson 1999; Ley et al. 2009). Albedo is not a diffuse but a specular quantity, depending on the surface properties. Thus the distribution of the Albedo is not necessarily hemispherical. Furthermore the Albedo changes continuously as the spacecraft orbits Earth, Earth turns underneath the satellite path and the weather changes. Yet, for first order approximations it is often assumed that Albedo decreases with increasing orbit altitude. The farther a spacecraft moves away from a planet or moon, the lower the Albedo gets. In Figure 4-6b the decay of Albedo heat flux with increasing orbit height above the Earth and an average Albedo of 0.3 is shown.

There are two things one has to bear in mind when treating with the reflected solar heat flux. On one hand the Albedo is not uniform but depends on the incident solar angle, the angular reflectivity of the reflecting material (clouds, water, soil) as well as the nadir point of the orbiting spacecraft. On the other hand it is important to note that the reflected heat flux represents the entire solar spectrum. The alpha and epsilon values used in spaceflight mostly refer to an alpha value averaged over the entire solar spectrum whereas the epsilon value is only valid for the infrared spectrum.

Yet another value important for thermal analysis and layout of orbiting spacecraft is the so-called β-angle. The β-angle describes the minimum angle between the orbit-plane and the solar vector, i.e. the vector directing towards Sun. The β-angle varies between -90° and +90°. If the β-angle approaches 0° the orbit

is edgewise as seen from the Sun, and the eclipse period is at its maximum. Moreover, the spacecraft crosses the sub solar point which leads to the largest Albedo value. In the extreme cases of -90° or +90° there is no eclipse, the spacecraft is subject to the solar radiation throughout the entire orbit. The β-angle changes continuously due to relative position of the orbit in space and its regression throughout the year. Since orbiting spacecraft play no role in this work, the β-angle will not be discussed or described in more detail here. A detailed introduction to the use of β-angle especially in low Earth orbits is given in Gilmore (Gilmore, ed. 2002-c2003).

4.2.2 The Lunar Surface Environment

"The fundamental purpose of activity involving the Moon is to enable humanity to do there permanently what we already value doing on Earth: science, to pursue new knowledge; exploration, to discover and reach new territories; commerce, to create wealth that satisfies human needs; settlement, to enable people to live out their lives there; and security, to guarantee peace and safety, both for settlers and for the home planet." - (Ehrenfreund et al. 2012)

The lunar thermal environment is characterized by an ultra-high vacuum, full exposure to the solar spectrum, and the surface material regolith. The thermal environment was subject to research for almost 80 years, as was elaborated in chapter 2.2.2. Further environmental conditions, not discussed in detail here, are micro meteorite bombardment, the solar magnetic field, electrostatic charges, moon-quakes, and radiation. The factors and the conclusion for the lunar thermal environment can also be applied to Asteroids, Mercury and further inactive, atmosphere-less moons or dwarf-planets in the solar system.

On the lunar surface the atmosphere is extremely thin and varies between $1.3 \cdot 10^{-12}$ and $1.3 \cdot 10^{-14}$ mbar [Johnson & Carroll] during lunar night and day respectively. Since gases are not present in significant amounts, the solar influx is as high as 1,367 W·m^{-2} (Clawson et al. 2002-c2003). As in Earth orbit the incident solar heat flux varies around 3.5 % throughout one Earth year and less than 1 % for the 11-year solar cycle.

One full revolution of the Moon, with respect to the stars, takes 27.32 days and is called sidereal month. The time between two new Moons, the so called synodic month, is 29.53 Earth days. The synodic month denotes two successive alignments of Moon and Sun as seen from the Earth (Heiken et al. 1991). The revolution of the Moon also leads to long times of "day" and "night", compared to Earth standards. A full synodic month is often called a "lunation". The Moons orbit is inclined with 5.145° towards the ecliptic. The Moons rotation axis, also called obliquity, is tilted at an angle of 6.68° to the orbit. Figure 4-7 depicts the angles in the Earth-Moon-Sun system. The distances and sizes are not to scale. The obliquity and the orbit inclination are in opposite directions, resulting in a total angle of 1.54° between Moons' axis of rotation and the ecliptic. This condition determines the angle of incident from the Sun. In this way there are almost no "seasons" on the Moon (Tattusch 2011).

In a first order perception the lunar surface can be distinguished in *mare* and *highlands*. The highlands are regions consisting predominantly of granite that are mainly 4.3 billion years of age. The darker mare regions consist mainly of basaltic minerals and are 3.8 billion years of age. The lunar topography is dominated by millions of *craters* of different sizes. The overlay of craters throughout billions of years led to structures that look like structures on the Earth although on the Earth the mechanism that form the topography are not dominated by impact cratering. Still due to the similar appearance the structures on the Moon are ordered in mountain ranges, sees, lakes, rills, canyons, bays, and domes. On an even closer look numerous rocks, so called *boulders*, scatter the surface of the Moon, mainly in the vicinity of craters. Finally, the lunar surface is covered by a layer of fine grained stones, the so called regolith. All these features with different material properties play a role in the thermal environment, relevant for past and future spacecraft, on the surface of the Moon.
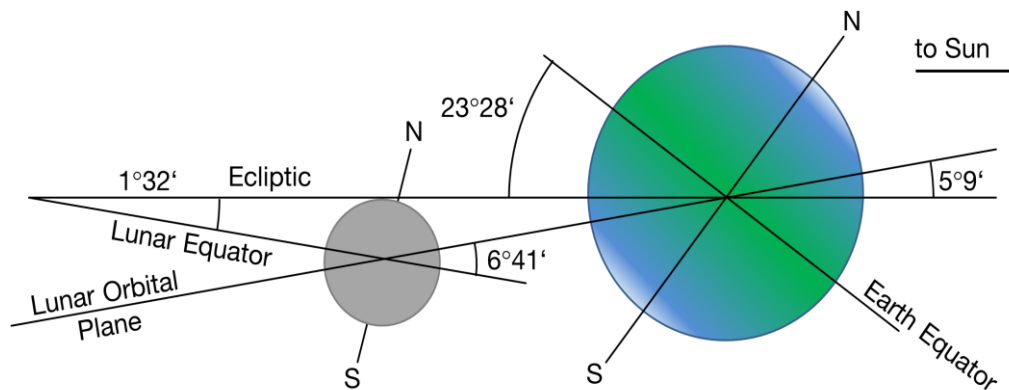
Figure 4-7: Geometric Relationship between the orbit planes and rotation axis in the Earth-Moon-Sun system [reproduced from (Heiken et al. 1991: 58)]. Sizes, distances, and angular values are not to scale.

Lunar regolith:

The regolith (from ancient Greek: *regma* = brake; *lithos* = stone) is a porous media of rocks grained down to submicron size. The regolith covers the entire lunar surface. In the younger *mare* regions the regolith has a depth of 4-5 m and in the ancient highland regions of 10 to 15 m with a maximum at 20 m in rare locations (Heiken et al. 1991). The regoliths' material properties have a large impact on the overall temperature behavior. The material properties of lunar regolith important for thermal calculations are density, thermal conductivity, and heat capacity. The fine grained "unconsolidated" material in the subcentimeter fraction of regolith is often referred to as lunar soil (Heiken et al. 1991) or "fluff" (Christie et al. 2008). The size distribution of regolith is known for the samples and drill cores returned by the manned and unmanned missions in the 60s and 70s of the 20th century. 90 % of the regolith sample material is of a size <1mm (Heiken et al. 1991). The composition of regolith varies largely throughout the Moon and depends predominantly on the local bedrock material. Regolith is created by a constant bombardment with meteorites. Large meteorites break up the bedrock material and displace large boulders and small grain sands into the surrounding. Depending on impactor size, angle, and velocity as well as bedrock material, the displaced material covers from few hundred meters to a couple of hundred kilometers. The impact processes also create glass melts. In contrast, micrometeorites that constantly hit the lunar surface break down smaller rocks. This process eventually leads to the fine grained regolith. The regolith material itself can be compared to porous media found on Earth, as for example dry clay or pumice. The particles often have an elongated shape with numerous holes and cavities [Figure 4-8]. Paired with its sharp-edged shape the resulting high inner surface leads to a high reactivity of regolith with man-made surfaces and provides significant health risks to humans (Cain 2010).

The density of lunar regolith varies between 1,000 and 2,000 kg·m^{-3} (Mitchell et al. 1972; Heiken et al. 1991). The density increases with depth. The fine grained portion of lunar soil that makes-up the upper 1-2 centimeters of the regolith has generally the lowest densities because this layer suffers no compression by overlaying material. An empirical equation for a depth dependent density profile of lunar regolith for level areas on the Moon, undisturbed from surface features was measured during Apollo 15 and is given with (Heiken et al. 1991):

$$\rho_{Reg} = 1.89 \cdot \left(\frac{z + 1.69}{z + 2.9}\right) \tag{41}$$

The density ρ_{reg} is given in [g·cm^{-3}] and the depth z in [cm]. This empirical equation is valid for a depth of up to 0.7 meters. The relative density of the lunar regolith increases with depths from as low as 30 % close to the surface to about 92 % at depths of 30 cm (Heiken et al. 1991). According to (Hovland and Mitchell 1972) and (Mitchell et al. 1972) the angle of repose is between 35° and 37°. Above this angle regolith will slide down slopes and reveal the underlying bedrock.
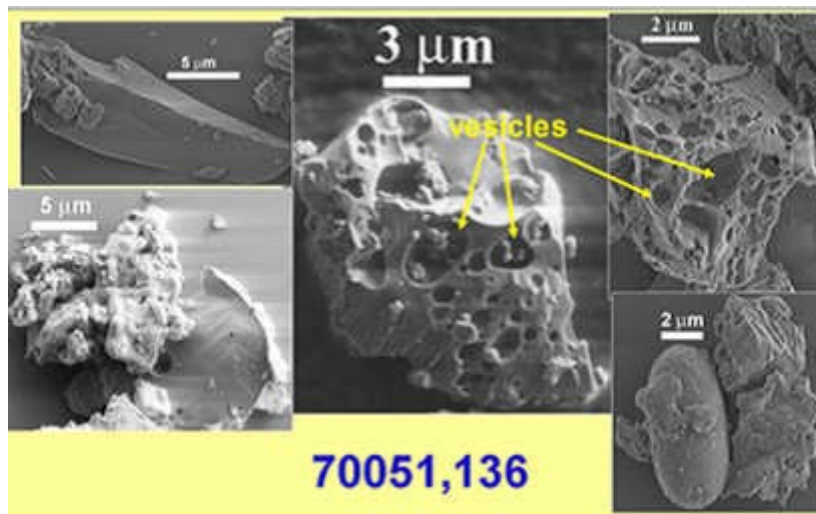
Figure 4-8: Morphology of lunar dust with particles in the micron range. The swampy and rugged structure can be seen [from (Gustafson and White 2009)].

Thermal and Optical Material Properties of regolith:

Thermal conductivity values of lunar dust k_{dust} and soil k_{soil} vary between 0.009 W·m^{-1}·K^{-1} and 0.035 W·m^{-1}·K^{-1} (Keihm et al. 1973; Horai et al. 1970; Cremers and Birkebak 1971). The low conductivity can be explained by the high inner surface of the lunar regolith grains and a high porosity. In porous media the radiative heat transfer becomes predominant for higher temperatures, especially under vacuum conditions. The thermal conductivity of regolith follows a T^3 function. At lower temperatures the thermal conductivity is governed by the conductive interfaces between individual grains. The sharp edged and jagged regolith grains have only small points of contact. The regolith porosity changes with depth, as can be seen from the increase in density. Tests with evacuated regolith powders lead to an empirical equation for k_{dust} [W·m^{-1}·K^{-1}] and k_{soil} [W·m^{-1}·K^{-1}] that takes into account different densities: The values base on the Apollo 12 sample 12001.19, a lunar fine with a bulk density of 1,300 kg·m^{-3}. The temperature T is assumed in K and the empirical relations are valid in the range from 160 K $< T <$ 430 K (Cremers and Birkebak 1971).

$$k_{dust} = 9.22 \cdot 10^{-4} \cdot \left[1 + 1.48 \cdot \left(\frac{T}{350 \text{ K}} \right)^3 \right] \qquad (42)$$

The second equation for coarse lunar soil with higher densities was taken from Vasavada et al. (1999) and references therein:

$$k_{soil} = 9.30 \cdot 10^{-3} \cdot \left[1 + 0.073 \cdot \left(\frac{T}{350 \text{ K}} \right)^3 \right] \qquad (43)$$

The heat capacity of regolith $c_{p,reg}$ ranges from 250 J·kg^{-1}·K^{-1} to 825 J·kg^{-1}·K^{-1} (Robie et al. 1970). It was measured in Apollo 10 sample 10084.

$$c_{p,reg}(T) = -34 \cdot T^{1/2} + 8 \cdot T - 0.2 \cdot T^{3/2} \qquad (44)$$

The temperature T is assumed in K. The empirical equation is valid in the range 90 K $< T <$ 360 K (Robie et al. 1970).

The optical properties of regolith are a low reflectivity to solar illumination, no transmissivity and with that a high absorptivity throughout the solar spectrum. It was found that the reflectance depends on the angle of incident, material composition, density, and temperature (Birkebak and Dawson 1973). The density dependency might be traced back to differences in particle size distribution of the examined samples. The Albedo as a ratio between reflected and total incident heat flux, varies for Apollo 11, 12, and 14

samples in the range of 0.076 to 0.297 (Birkebak and Dawson 1973). The albedo varies largely with local mineralogy. The brightest features on the Moon are ejecta blankets originating from younger craters in a ray pattern. In general, the highlands are brighter than the mare (Heiken et al. 1991). With equation (27) the absorptivity is 1 minus the spectral reflectivity and thus $\alpha_{reg,spec}$ = 0.703 – 0.924.

The spectral infrared emissivity ε for regolith with a temperature between 90 and 400 K was measured to be from 0.972 and 0.927 in an Apollo 11 sample with a bulk density of 1,910 kg·m^{-3} and 0.976 to 0.925 for an Apollo 14 sample with a density of 1,600 kg·m^{-3}. Based on these data the spectral emissivity was curve fitted to a third order polynomial (Birkebak and Cremers 1974):

$$\varepsilon(T) = 0.9696 + 0.9664 \cdot 10^{-4} \cdot T - 0.31674 \cdot 10^{-6} \cdot T^2 - 0.50691 \cdot 10^{-9} \cdot T^3 \qquad (45)$$

The upper layers of regolith on the lunar surface are packed less densely resulting in cavities which absorb more radiation. Increasing temperature leads to a decrease in emissivity. Thus, close to the terminator, or for low angles of incident caused by topography, the amount of reflected sunlight is higher. In a nutshell, the high absorptivity in the solar wavelength region and the high emittance in the infrared region give the Moon the properties of an almost perfect black body.

<u>Surface Temperatures on the Moon:</u>

The thermal properties presented above lead to a change in temperature throughout one lunar day. The diurnal temperature variations occur mainly in the upper centimeters of the lunar surface. Figure 4-9 shows the daytime temperatures measured over the course of one lunar day in October 2009. The temperatures can be as high as 400 K at the lunar equator on a sub-solar point (Cremers et al. 1971; Heiken et al. 1991; Paige et al. 2010b). Without insulating atmosphere, the heat is radiated to space during the lunar night, which causes surface temperatures to drop to values of 100 to 120 K (Cremers et al. 1971; Heiken et al. 1991) at the lunar equator and around 70 K on average at the lunar poles.

Figure 4-12 shows the progress of temperature for one lunar day at the lunar equator. There are also regions at high selenographic[11] latitudes (i.e. low solar angles of incident) that are enveloped in longer periods of shadows due to the local topography. Some crater floors are even permanently casted in shadow. In these "cold spots" the temperature can drop as low as 25 K (Paige et al. 2010b) as depicted in Figure 4-11. From the results of the artificial impact of the Lunar Crater Observation and Sensing Satellite (LCROSS), the presence of water ice in the regolith at permanently shadowed craters at the lunar Poles was measured (Hayne et al. 2010).

Due to the extremely low conductivity, spatial temperature difference of 200 K (Gaier and Sechkar 2007) is possible in the length scale of the lunar diurnal temperature changes in depths, i.e. ~ 0.1 m (Williams et al. 2011). During Apollo 15 and 17 heat flow measurement were performed in order to measure local surface and subsurface temperatures, the heat flow from the core of the Moon, and the thermal conductivity. In those experiments the heat flux from the lunar interior was measured to be between 0.021 and 0.016 W/m² with an uncertainty of 15 %, at the Apollo 15 and 17 landing sites and in regolith of densities from ~1,750 to 1,900 [kg·m^{-3}] (Langseth et al. 1972; Langseth et al. 1976; Keihm et al. 1973).

A study of lunar surface photographs in the 1970s revealed more than 300 temperature anomalies on the lunar near side. Boulder fields and crater rims were suspected to be the source of these anomalies (Allen 1971a, 1971b). More recent work on temperature anomalies in the vicinity of lunar craters found that local surface features, mainly boulder and clusters of boulders along crater rims, have a large impact on the local regolith temperatures. These findings base on the comparison of temperature data with high resolu-

---

[11] Selenography is the study of the physical features of the surface of the Moon. It is equivalent to Geography for the Earth

tion cameras on board the LRO (Bandfield et al. 2011). Even small rocks in the size of 28 cm can have a temperature that is 50 K higher than undisturbed rock-free regolith (Williams et al. 2011).
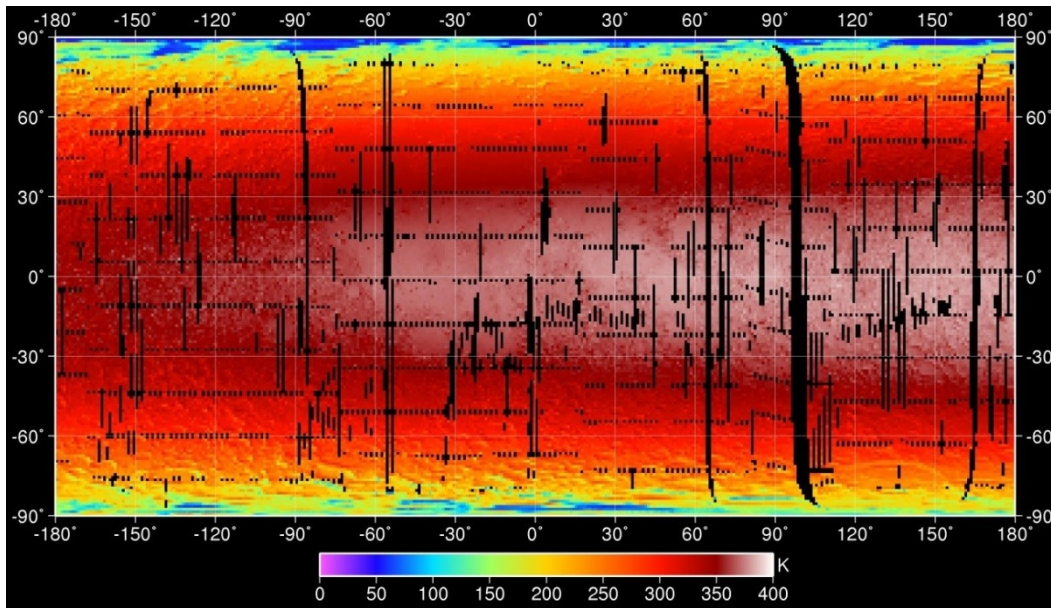

Figure 4-9: Lunar daytime temperature measured during October 2009 by the DLRE instrument on board the Lunar Reconnaissance Orbiter (LRO), shown is the brightness temperature [from: (Paige 2012)].
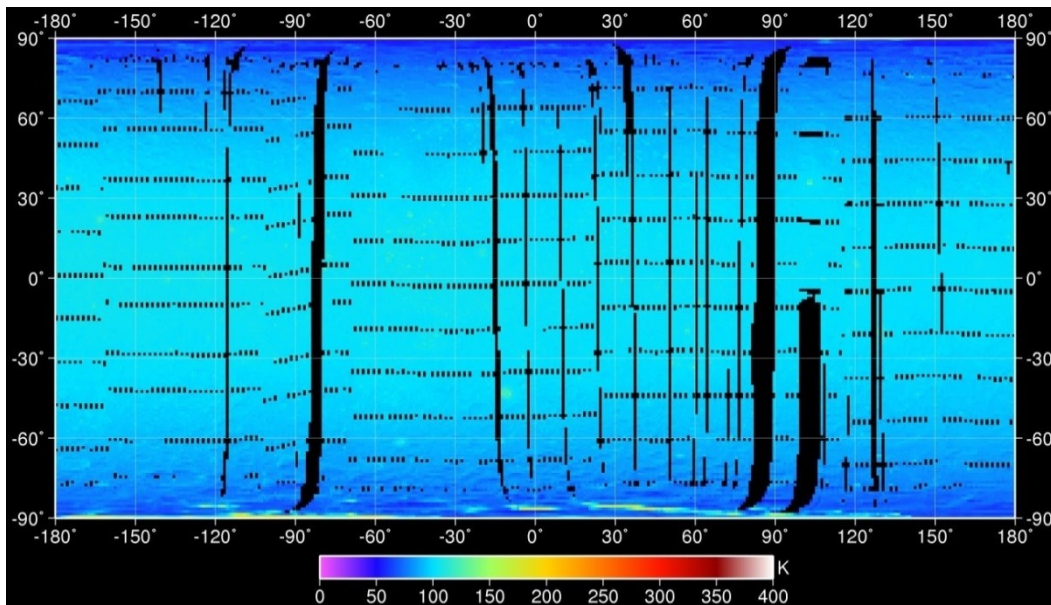

Figure 4-10: Lunar nighttime temperature measured during October 2009 by the DLRE instrument on board the Lunar Reconnaissance Orbiter (LRO), shown is the brightness temperature [from: (Paige 2012)].

Further impacts on lunar surface thermal conditions are the sunlight reflected by the Earth, so called "Earthshine", and micrometeorites (Head 2006). The maximum heat flux for Earthshine is 0.111 $W \cdot m^{-2}$ for full illumination of the Earth and at a "sub-Earth" point. Due to the tilt of the Moon axes towards the ecliptic the sub-Earth point is close to the Moons equator. The Earthshine at the Poles reaches values between 0.019 $W \cdot m^{-2}$ and 0.071 $W \cdot m^{-2}$. This value is in the same order of magnitude as the heat flux from the Moon interior. The impact of micrometeorites as source of heat flux was calculated to be in the order of $4.1 \cdot 10^{-6}$ $mW \cdot m^{-2}$, which is a negligible value (Head 2006).
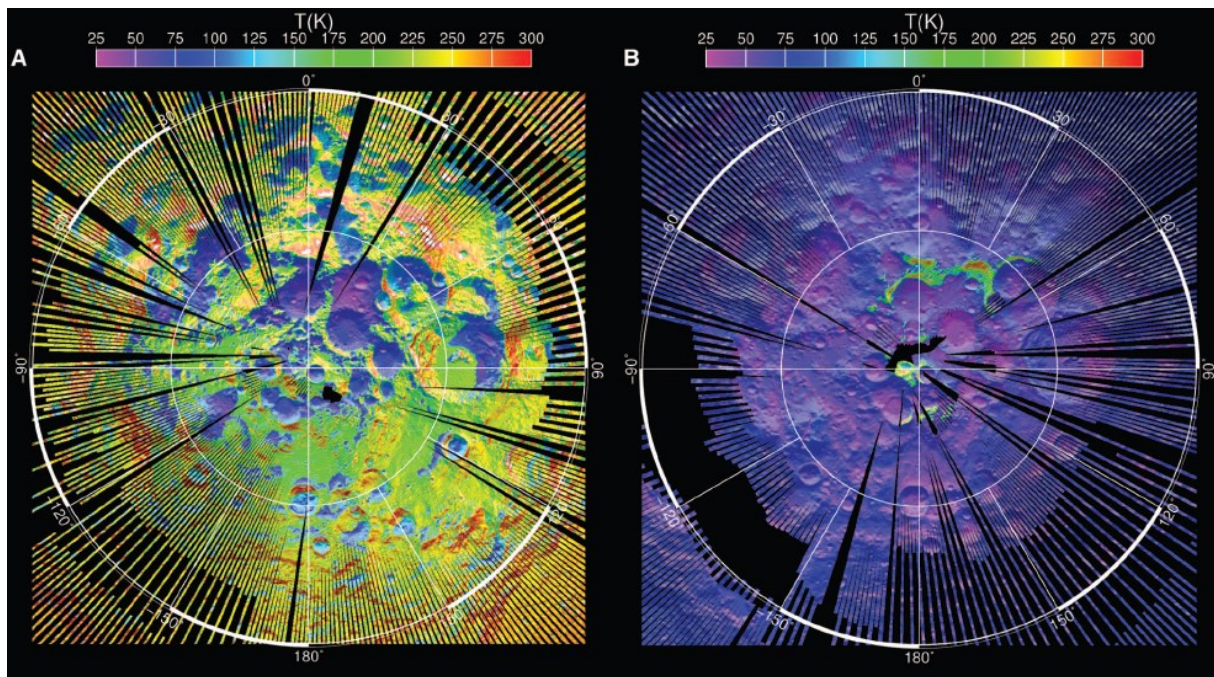
Figure 4-11: Lunar south pole temperature data for A) daytime and B) nighttime; Measured with the DLRE instrument on board the Lunar Reconnaissance Orbiter (LRO) (Paige et al. 2010b)).
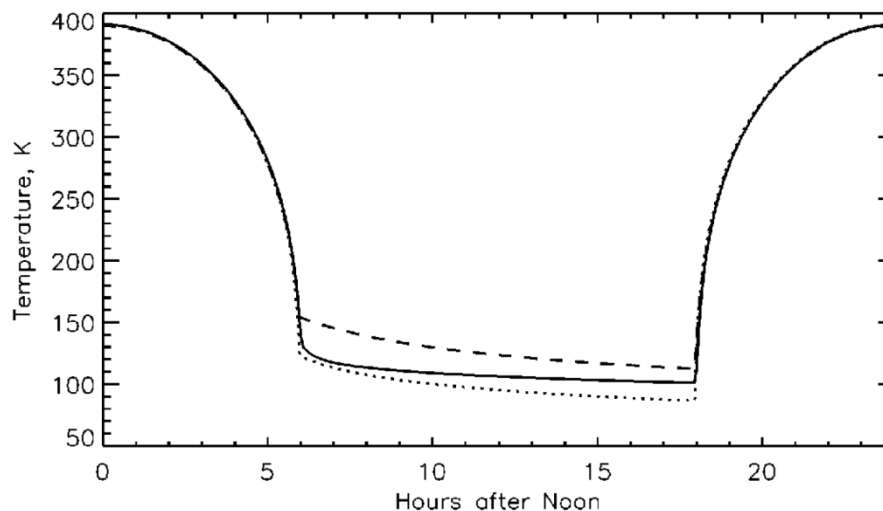
Figure 4-12: Progression of temperature for one lunar day at the lunar equator in a two layer regolith model. The time is given for a 24 hours normalized with the lunar 29.15 Earth days (Vasavada et al. 1999). The dashed line gives the temperature in a subsurface layer and the dotted line in the uppermost layer.

Lunar Craters:

Beside the darker colored *mare* terrains, craters are the most characteristic features on the lunar surface. The lunar surface is covered with craters of different sizes, as can be seen easily from Earth with binoculars or small telescopes. Craters are created by particles that travel through interplanetary space and cross the lunar orbit at high velocities and impact on the lunar surface. The craters can be as large as the South Pole Aitken Basin with a diameter of 2,400 km and a depth of more than 8 km (Hiesinger and Head 2004). On the other side of the scale, the craters reach down to diameters of < 0.1 μm (Heiken et al. 1991). For even smaller particles the cratering becomes sputtering. The bombardment of the lunar surface took place throughout the last 4.3 billion years and still goes on today. The largest and biggest number of craters where created in a time called the "Late Heavy Bombardment" 4.1 to 3.8 billion years ago (Jau-

mann et al. 2012). Figure 4-13 shows the three general shapes of craters that are distinguished for the majority of lunar craters. The most basic type is a small bowl shaped crater with a lens of small rocks in its center, also called a simple crater. Simple craters typically have a size of maximal 20 km. Larger craters are characterized by a more complex structure, with a more shallow floor, central peaks, and rings.
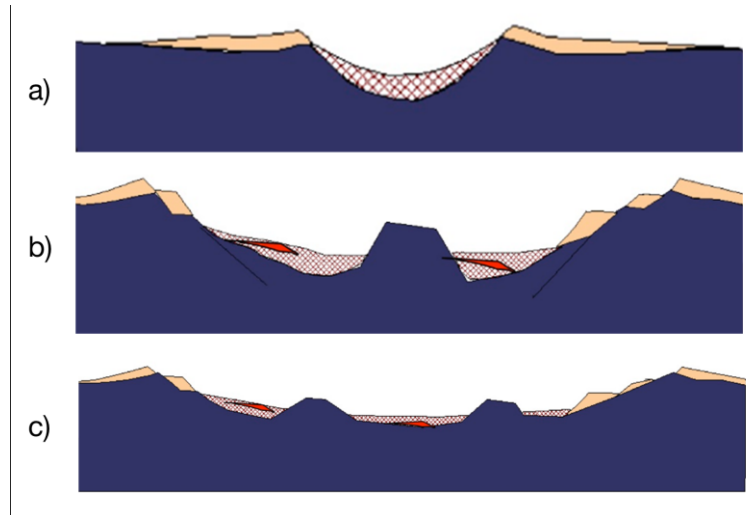
Figure 4-13: Crater shapes from A) simple crater, B) complex crater with central peak, and C) complex crater with ring a structure, also called basins [from (Ernstson and Claudin 2012)].

Craters with diameters up to 100 km often contain central peaks or terraced floors. Craters with diameters larger than 100 km often have one or multiple mountain rings (Hörz and Cintala 1997), giving the crater the appearance of a frozen wave-ring. Craters can also be distinguished in primary and secondary craters. Primary craters are created by impactors from interplanetary space with impact velocities in the range of v_{imp} = 15-20 km·s^{-1}. In contrast, secondary craters are caused by impactors which were created during primary impact events. The impactors of secondary craters have impact velocities of v_{imp}< 2 km·s^{-1} (Bart and Melosh 2007). Equations related to craters on the Moon can be described by empirical correlations of the form:

$$y = a \cdot D_c^b \tag{46}$$

where y is the crater characteristic, for example depth or rim height in units [km], D_c is the crater diameter in km and a and b are given coefficients (Heiken et al. 1991). The coefficients were determined by the study of photographs from the lunar surface in the decades since the Apollo landings.

The crater density is the number of craters per unit area. It depends on the age of the lunar region. The ancient highlands on the Moon have a crater density of 1,758·10^{-4} km^{-2} for craters with D_c > 1 km (arithmetic average). The lunar mare regions are younger and thus show a smaller crater density which ranges from only 30·10^{-4} to 90·10^{-4} km^{-2} for craters with D_c > 1 km (Neukum et al. 1975).

Lunar Boulders

Boulders are created during impact events on the lunar surface. The impactor itself evaporates to the most part but the impact event excavates chunks of bedrock material, which are the boulders. Boulder size, position, and bulk material depend on the parent crater and with that on impact velocity and bedrock material. During the crater formation process 5 % of the crater mass disperses around the crater as boulders (Cintala et al. 1982). The remaining material forms the regolith and granular material of coarse pebbles. Boulders are constantly subject to micrometeorite impacts as well as thermal weathering caused by thermal stresses (Molaro and Byrne 2011). The level of degradation depends on the boulder age. Approximately 0.15 % of the lunar surface is covered with boulders of a wide variety of sizes (Allen 1971a). The boulders have a high frequency around craters (e.g. 7,000 boulders in the diameter range D_B

= 1 m to 14 m around a crater of diameter 300 m) (Bart and Melosh 2005; Cameron and Coyle 1971). The maximum boulder diameter $D_{B,max}$ [km] depends on crater size D_C [km] and is given by (Bart and Melosh 2005; Moore 1970):

$$D_{B,max} = 0.1 \cdot K \cdot D_C^{2/3} \tag{47}$$

where D_C is the crater diameter [km] and K [-] is a correlation factor. The correlation factor depends on the crater type. Primary craters have $K = 0.29$ and secondary craters have $K = 0.46$ (Bart and Melosh 2007). The bedrock material determines boulder distribution around craters. In highland regions 65 % of the boulders lie within the crater. In the mare regions only 10 % lie inside the crater, for craters in the range $D_C = 0.2$ to 3.5 km. The bedrock material has no influence on the maximum boulder size $D_{B,max}$ (Bart and Melosh 2007; Lee et al. 1986). In both cases most of the boulders are within an area up to 2 crater radii away from the crater center (Lee et al. 1986). The penetration depth of a crater is approximately 31 %. The penetration depth was determined by investigation of boulder tracks (Hovland and Mitchell 1972). Figure 4-14 shows a boulder with $D_B = 1.5$ m during Apollo 14. Some parts of the boulder are covered with patches of regolith or finer grained material.
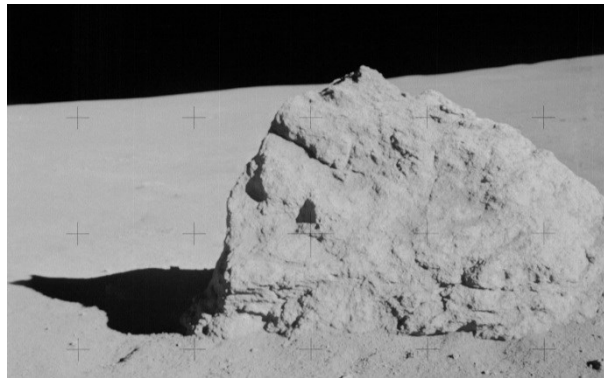
Figure 4-14: Image of a 1.5 meter diameter boulder taken by astronaut Allen Shepard during Apollo 14 [NASA].

The temperature of a boulder is different from the surrounding regolith. A boulder receives direct solar illumination and it radiates heat to deep space. Depending on the boulder surface temperature in contrast to the lunar regolith temperature heat is either radiated to or received from the surrounding in the infrared wavelength regime. Due to the extremely low thermal conductivity of lunar dust, the conductive interface between boulder and ground can be neglected for thermal calculations (Roelof 1968). Figure 4-15 shows the temperature behavior for a cubical boulder with an edge length of 3 m at a lunar equatorial position throughout one lunar day (lunation).

The temperature in Figure 4-15 was calculated based on a finite element approach, assuming a homogenous basaltic material. The vertical walls facing east and west heat up to the black body temperature when illuminated for prolonged periods of time during sunrise and sunset respectively. The core temperature is dampened and never reaches the extreme hot and cold temperatures of the boulder surfaces. Besides, the core temperature has a certain phase lag, especially during lunar night. While the surface temperature decreases very fast and drastically, the boulder core temperature changes more benign and never reaches the regolith temperature.
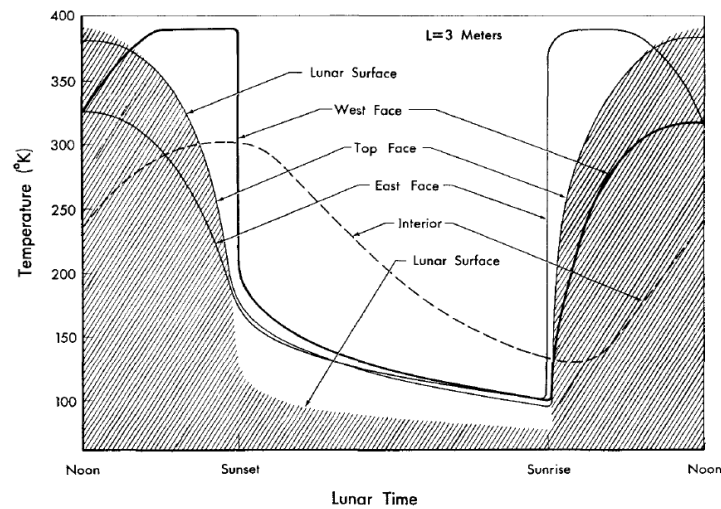
Figure 4-15: Progression of temperature for a boulder of 3 m diameter at the lunar equator (Roelof 1968). The outline of the hatched area is the lunar (regolith) surface temperature.

Further Aspects of the Lunar Surface:

Lunar dust can either be displaced by anthropogenic or naturally occurring forces. Dust was kicked up by lunar rovers and the Apollo astronauts, or distributed by rocket motors of descending and ascending spacecraft. Natural transport phenomena include movement of electrostatic charged particles along electrostatic gradients on the lunar surface, as well as impact events (Colwell et al. 2007). Mainly triboelectric charging, but also non-electrostatic (chemical) charging can lead to the adhesion of dust particles to optical elements, thermal control surfaces, structural elements or spacesuit fabrics. The tribocharging effects are several orders of magnitude larger than those caused by non-electrostatic forces (Berkebile and Gaier 2012). The Lunar Ejecta and Meteorites (LEAM) instrument registered a flux mainly of highly charged, slowly moving lunar surface fines. The enhancement of registered elements was traced back to the movement of dust around the lunar terminator due to electrostatic forces (Berg et al. 1976).

The so called 'mascons' are region on the lunar surface which have a higher density that is a higher concentration of mass than other regions. This is not of relevance for the thermal model but has an impact on orbiting spacecraft. In this context it is important to note that the measured topographic maps rely on the orbit altitude to calculate the distance with the surface. Thus the mascons bias the measurements of the lunar topography.

4.2.3 Planetary and Interplanetary Space

A first order approximation of the temperatures for other bodies in the solar system can be calculated by considering black bodies at the appropriate distance to the Sun and applying equation (40). Table 4-1 lists the orbit semi major axis, mean equator, mean solar illumination, planetary infrared and the steady state temperatures of reference black bodies at that position in the solar system. Depending on the composition of the planets' atmosphere, the cloud composition and atmosphere densities are different, having yet another impact on the Albedo. This is of special interest in the case of Venus and Mars as well as the giant gas planets beyond the asteroid belt.

Table 4-1: Planetary first order reference temperatures and heat fluxes [based on (Gilmore, ed. 2002-c2003)].

Planet	Orbit Semi Major Axis [AU]	Mean Equatorial Radius [km]	Mean solar illumination [W·m⁻²]	Planetary IR [W·m⁻²] ‡	Reference sphere temperature [K] †
Mercury	0.387	2,425	9155.1	8,000-12,700	634
Venus	0.723	6,070	2623.1	153	464
Earth	1.000	6,378	1371.2	180-332	394
Mars	1.524	3,397	590.4	30-470	319
Jupiter	5.200	71,300	50.7	13.60	173
Saturn	9.540	60,100	15.1	4.60	128
Uranus	19.180	24,500	3.7	0.63	90
Neptune	30.060	25,100	1.5	0.52	72
Pluto/Charon	39.440	3,200	0.9	0.50	63
Moon	1.000	1,738	1,371.2	5.2 - 1,314	394

‡ IR values depend on the orbit additional to the central body

† black body, without planetary heat flux and Albedo.

4.3 Thermal Engineering in Spacecraft Design

The space environment discussed in the previous section provides a number of challenges for the thermal engineer. These challenges are different for a) an orbiting spacecraft, b) an interplanetary probe, and c) a surface-craft on the surface of planets or moons. For a) and c) the central body is of utmost importance, its surface or atmospheric properties and its distance to the Sun are important, for orbiting spacecraft the orbit altitude and the β-angle are important and for interplanetary probes the cold sink of space is the main design driver. Any electrical power eventually is transformed into thermal energy. Since spacecraft are more electronics than mechanics and due to the absence of convective cooling, the operation mode of a spacecraft influences the thermal behavior to a large extent. The spacecraft layout, its material and optical properties govern the temporal behavior, controlling the absorbed and emitted heat and dampening temperature fluctuations.

In section 4.3.1 the general approach for the thermal design of spacecraft and typical requirements are shown for orbiting spacecraft as well as for surface-crafts. In section 4.3.2 the components necessary to conserve, transport, and exchange or reject heat are classified in passive and active thermal control components.

4.3.1 Thermal Design Principles & Requirements

Space programs and therewith the spacecraft design follows a specific development process. This process is separated into different phases. Figure 4-15 shows the development phases of ESA and NASA projects. In this figure the phases are not to scale concerning their duration and only the major reviews at the end of each phase are shown. The phases are separated from each other by formal reviews. Analysis or tests must be performed and documented prior to these reviews. Special emphasis is put on reviews that mark the transition into a new phase.
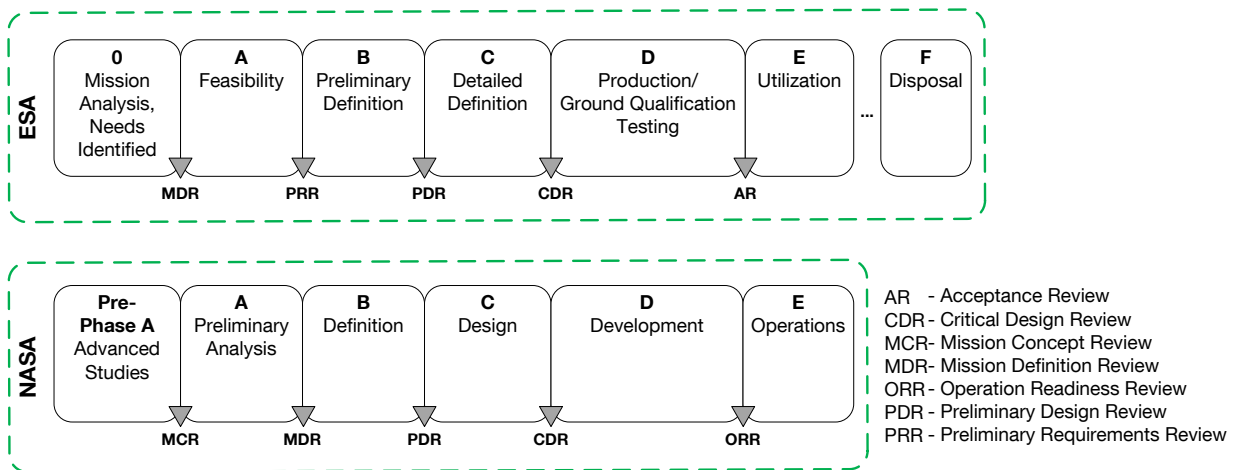
Figure 4-15: Spacecraft development process in ESA and NASA projects. The phases are not to scale and only major reviews are show [reproduced from (Wertz and Larson 1999)].

The subsystem development matures as the overall program proceeds. During phase 0 (pre-phase A in the US) the process starts with simplified first order analysis. For the thermal engineer this means that the performance envelope is being defined, thus the general heat fluxes or temperatures are determined. Due to high uncertainties large margins are still applied during this phase. The thermal design is build up around basic mainly passive, components. Different design possibilities are compared to each other through parametric studies and are governed by the thermal engineers' experience. During phase A parts of the entire system which are expected to be most critical are being designed to a higher level. This in turn requires more detailed analysis, manual calculations or numerical models in the different engineering

domains. Many parametric studies based on a simple model often can produce more valuable information than single point studies with large scale and detailed models. Also the reuse of models created for similar projects can be adopted and reused instead of creating entirely new models (Gilmore, ed. 2002-c2003). With respect to the temperature requirements and an increasing knowledge of the entire system, the mathematical models (described in more detail in chapter 4.4) get more and more elaborated simultaneously throughout phase B. In phase C subsystem analysis are performed for critical elements with detailed models and hardware-tests. In phase D the flight hardware is manufactured and tested in relevant environments. For the thermal engineer the thermal-vacuum, thermal-cycle, and thermal-balance test are the most important environmental tests. In the thermal-vacuum and thermal-cycle tests the functionality of the thermal control concept is tested and with the results of the thermal-balance test the correlation of the thermal model is conducted.

In the thermal branch minimum and maximum analysis are mostly used to cover the extreme cases in which a spacecraft or component will be operated during its lifespan. This worst case approach is explicitly demanded in ESA ECSS-E-ST-31C (ESA - ESTEC 2008) and US MIL-STD 1540D standards (DOD 1994). The worst case approach created envelope values evolve throughout the development process. With a more detailed knowledge of orbit, attitude and operation modes the minimum and maximum cases can be redefined more accurately. The minimum maximum worst case approach is well suited for spacecraft in deep space missions with a slowly changing thermal environment and/or a high thermal inertia. Also in the case of Earth orbiting spacecraft, a robust design based on worst case considerations will survive the space environment and perform as designed. But even for orbiting spacecraft this worst case approach does not take into account transient effects which appear during the entrance in and exit out of the eclipse or due to shadowing effects created by satellite extension and spacecraft attitude towards the Sun. Here the transient effects become important. This is even more pronounced for spacecraft in close vicinity, such as spacecraft that perform docking or berthing, astronauts in spacesuits around the ISS or – surface craft moving on the lunar surface.

Time marching numerical models (discussed in more detail in chapter 4.4) are used to determine the thermal behavior of a spacecraft. The thermal models are compared with tests in a relevant environment. In case of the thermal domain typically a thermal-vacuum, a thermal-cycle, and a thermal-balance test are being conducted towards the end of phase D. Critical elements are tested beforehand during Phase B and C to get a higher understanding of the thermal components or its interaction with other subsystems.

Thermal Requirements:

> *"The purpose of a thermal-control system is to maintain all of the spacecraft's components within the allowable temperature limits for all operating modes of the vehicle, in all of the thermal environments it may be exposed to"* - (Gilmore, ed. 2002-c2003).

The central purpose of thermal control in spacecraft design is to maintain its components within certain temperature limits. As long as the component is in use, these limits are referred to as *operational limits*. The component is qualified and its functionality is guaranteed by the vendor only for this temperature region. If the component is switched-off the limits are called *survival limits* and are less stringent than the operational limits. If the survival temperature is exceeded a permanent damage of the component is almost certain. The same is true if the components exceed its operational limits during its operative mode. Values for typical components and subsystems are gathered in Table 4-2.

Beside absolute values for temperatures there are spatial and temporal gradients and stability criteria to be met. The spatial temperature gradients can lead to distortions in structural components which in turn can lead to misalignment in optics or antennas. The temporal gradients refer to a change in temperature over time which can cause fatigue and even failure in structural components or electronic parts. Typical spatial temperature gradients are $\Delta T / \Delta x$ < 5K·min^{-1} across optical instruments or between

monomethylhydrazine (MMO) and nitrogen tetroxide (NTO) tanks, and $\Delta T/\Delta x < 2\,\text{K·min}^{-1}$ for structural elements (Poinas 2004).

Table 4-2: Temperature requirements for common satellite components [based on (Wertz and Larson 1999), (Gilmore, ed. 2002-c2003)].

Component	Operational [K]		Survival [K]		Source
	min.	max.	min.	max.	
Batteries	0	15	-10	25	Wertz
Data management unit	-40	35	-50	55	Gilmore
Reaction Wheels	-10	40	-20	50	Wertz
Sun sensor	-40	38	-67	120	Gilmore
Hydrazine Tanks & Lines	15	40	5	50	Wertz
Solar panels	-150	110	-200	130	Wertz
Antennas	-100	100	-120	120	Wertz
Deployment Mechanism	-10	25	-55	80	Gilmore
Inactive Structure	-100	100	-	-	Gilmore

Temporal stable Temperature gradients are $\Delta T/\Delta t < 5\,\text{K·h}^{-1}$ for common electronic units, $< 0.1\,\text{K·min}^{-1}$ for charged coupled device (CCD) cameras, and down to $< 100\,\text{K·min}^{-1}$ for cryogenic telescopes. Critical temperature gradients often occur in structural elements with a large exposed area and low specific mass (Karam 1998). The temperature stability describes the ability to maintain an operational temperature within a certain narrow temperature range. Stability requirements guarantee the performance of sensors. Temperature stability requirements in the range of 1 K are routine. More narrow gradients were achieved in the 80s and 90s of the 20th century for optical systems e.g. Hubble with 21.1°C ± 0.1°C (Pecson et al. 2002-c2003). Future telescopes such as the proposed International X-ray Observatory (IXO) have temperature requirements of 20°C ± 0.5°C (Choi 2010). There are even more stringent requirements in the range of mK for actual and upcoming missions with optical telescopes (Pecson et al. 2002-c2003).

4.3.2 Thermal Control

In order to design a spacecraft, a subsystem or a component so it remains within the required temperature limits and gradients, the thermal engineer can choose from a large palette of control mechanisms. These mechanisms are commonly divided into *passive* (section 4.3.2.1) and *active* thermal control (section 4.3.2.2).

Commonly, the use of passive thermal control (PTC) technology is considered to be easier in its application and more robust in contrast the active thermal control (ATC). Passive thermal control relies on heat rejection via radiators, the use of surface finishes and paints to control the α/ε, the use of insulating material and phase change material to conserve heat and dampen changes in the environment and fillers, doublers, heat pipes or the structure itself to distribute heat. Passive components that generate heat continuously are radioisotope thermoelectric generators (RTGs) or their derivatives.

In general, designing systems with stringent requirements on thermal stability or gradients will require decoupling sensitive components or subsystems from the rest of the spacecraft. The thermal control then changes from a mere passive to an active design. This in turn means that not the temperature is controlled anymore, but the heat flux that is exchanged between parts of a subsystem (Pecson et al. 2002-c2003). The active components often need electronic power and a certain computational logic for control. ATC mechanisms are louvers which shade radiators, heaters, pumped fluid loops, cryostats, and heat exchangers (Wertz and Larson 1999; Gilmore, ed. 2002-c2003; Karam 1998). Some radiators must also be considered active for example electrochromatic or digital radiators which require a control that reacts to the environment and the internal heat loads.

4.3.2.1 Passive Thermal Control Mechanisms

There are numerous passive thermal control mechanisms. This chapter shortly introduces radiators, surface finishes, heat pipes, multi-layer-insulation, and phase change material. Only the PTC technologies with relevance to this work are introduced. The interested reader is referred to the exhaustive textbooks by (Gilmore, ed. 2002-c2003; Wertz and Larson 1999; Ley et al. 2009).

Radiators:

Radiators are a technology often used in spacecraft. Every spacecraft thermal design takes into account the rejection of heat via thermal radiation. Dedicated radiators are often the primary means of rejecting heat in spacecraft. The principle is governed by Plank's law. The higher the radiator temperature and the lower the sink temperature, the more heat can be rejected per surface area. In orbiting spacecraft and interplanetary probes the space background temperature of ~3 K serves as cold sink. Generally materials with high infrared emissivity ($\varepsilon > 0.8$) values and low solar absorptivity ($\alpha < 0.2$) values are used as radiator surface finish. Typical radiator finishes are quartz mirrors, silvered or aluminized Teflon, and white paint. Radiators are able to reject between 100 to 350 W per square meter, under the assumption of a 3 K cold sink (Gilmore, ed. 2002-c2003).

Figure 4-16: Radiators with ammonium working fluid, on the International Space Station (NASA 2012b).

The spacecraft structure itself can be used as radiating surface, if covered with a favorable coating. Electronic devices which form the heat sources are often mounted directly to the inside of the structure. An improvement of heat transport between the heat source and radiator are achieved by the use of doublers. If the heat source cannot be mounted to the structure, or of doing so is not appropriate due to other requirement, decoupling of the radiator position and location of the heat source can be achieved by the use of loop heat pipes, pumped fluid loops, or capillary pumped loops. The heat can be spread across a radiator by conductive materials or heat pipes. In case of large spacecraft with high levels of heat dissipation, the spacecraft body might not provide enough surface area to allow for heat rejection or might be used for power generation with solar arrays. In this case deployable radiators must be used (e.g. ISS). Deployable radiators are connected with the heat source by fluid loops. The fluids for heat transport are ammonium or Freon in case of ISS (Figure 4-16) and Space Shuttle Orbiter, respectively. Water is used on the inside of man-rated spacecraft. The use of ammonium and Freon is restricted to the outside due to their toxicity. Between inner and outer fluid loops heat exchangers (HX) are used to shift heat from the water loop to the external working fluid.

In situations of low internal heat load (e.g. safe mode) or extreme cold phases, the fluids used for heat transport in radiators are subject to phase changes. When the radiator temperature drops the used fluids freeze. As soon as the radiator temperature rises again the fluids thaw. This effect is dangerous due to the expansion of freezing water and expansion during melting for most other fluids. Ways to address this problem are a) the use of different radiator material, b) increasing tubing yield stress, or c) adding phase change material for increased thermal inertia (Gilmore, ed. 2002-c2003). Instruments on cryogenic tele-

scopes such as the Herschel telescope have instruments that are kept around 3 K (Hohn et al. 2004). Radiators for these cryogenic devices are especially sensitive to heat leaks.

A value often used with regard to radiators is the turndown ration r_{td} [-]; it is defined as the ratio between the maximum and minimum heat rejection level of a radiator.

$$r_{td} = \frac{q_{rad,min}}{q_{rad,max}} \tag{48}$$

This value helps in the design bandwidth in which a radiator design has to be able to work. It depends to a large extend on environmental conditions, thus the sink temperature.

Radiator design becomes even more complicated when the environmental or internal conditions change. In case of changing environmental conditions, the cold sink can change its temperature which has an impact on the radiators ability to reject heat. If the environmental sink temperature rises above the radiator surface temperature the radiator will gain heat. This is due to the fact that the high infrared emissivity of a radiator equals also a high infrared absorptivity. A high internally dissipated heat, will also impact the radiator size. Fluctuating heat loads must either be buffered or accounted for in a controllable radiator. In current thermal spacecraft design this is most often realized with louvers. Louvers decrease the view factor between radiator and cold sink. Other concepts foresee to decrease the flow rate of the pumped fluid loops, or to change the emissivity of the radiating surface.

Surface Finishes:

All surfaces of a physical body are thermal control surfaces since each body exchanges heat in form of radiation with its environment. Surface finishes are passive thermal means to control this radiative heat exchange and with that to achieve the desired temperature of a component. The performance of surface finishes is wavelength-dependent. One can distinguish between solar absorbers, solar reflectors, flat absorber, and flat reflectors. Solar reflectors are radiating surfaces of spacecraft that require high emissivity in the infrared spectrum to emit heat efficiently to deep space. Ideally this pairs with a high reflectivity in the visible-spectrum. The solar reflector group includes second surface mirrors white paints and silver- or aluminum backed Teflon (Gilmore, ed. 2002-c2003). It is important to note that the color of a finish, in the visible spectrum, may give a hint of the absorptivity in the visible spectrum but provides no information about its absorptivity and emissivity in the infrared spectrum. Solar absorbers are finishes that absorb in the solar spectrum but emit almost nothing in the infrared region. Here selective black paints are used. Other solar absorbers are bulk (unpolished) metals. Flat reflectors reflect throughout the entire spectrum. This group is represented by polished metals or special dielectric films. The group of flat absorbers is characterized by good absorption and emission coefficients in the visible as well as the infrared spectrum. Here "normal" black, grey, or pastel paints are used (Gilmore, ed. 2002-c2003). Electronic boxes as well as the internal structure are often painted to achieve a high emissivity to facilitate heat dissipation. It is common to use black paints although most paints would work due to their high infrared emissivity.

All paints or foils need to meet the requirements of low outgassing, in-space stability, and mechanical adhesion (Gilmore, ed. 2002-c2003). The absorptivity and emissivity are often given with beginn of life (BOL) and end-of-life (EOL) values, since especially paints and polymer films degrade in the space environment. Sources for degradation are charged particles, ultraviolet radiation, high vacuum or the outgassing residuals of polymers and adhesives. Metals can degrade before the launch by oxidation which also has an impact on their optical properties. But the effect of oxidation can also be used to alter the optical properties in a beneficial way, for example to decrease the α/ε ratio of copper (Roos et al. 1983). Due to the potential build-up of electric charges in spacecraft the finishes either have to be electrically conductive themselves or be covered with thin layers of conductive materials.

Heat pipes (HP):

Heat pipes are passive, self-regulated and closed containers which allow the transport of heat between a heat source and a heat sink. The most basic form of a heat pipe consists of condenser, evaporator, reservoir, wick, capillaries, and working fluid. The heat pipe uses the vaporization and condensation as working principle. At the evaporator heat is input in the system. The fluid in the wick evaporates at the evaporator, expands and moves to the cooler condenser. At the condenser the vapor condenses and is soaked back into the reservoir through small capillaries. The reservoir in turn feeds the wick (Gilmore, ed. 2002-c2003). The heat pipe principle is robust, flight proven in many mission and the technology is well-known. Many different concepts are available. Special forms often mentioned separately are loop heat pipes (LHP), which were traditionally developed and used in Russia and Europe, and pumped fluid loops (PFL), which were implanted in spacecraft manufactured in the USA (Gilmore, ed. 2002-c2003). Heat pipes are less effective under gravitational influence, which makes them less attractive and more complicated for the implementation in surface-craft on other celestial bodies. Another form of heat pipes are so called variable conductance heat pipes. They operate at higher ΔT temperatures than other heat pipes (Anderson et al. 2009). A further description and discussion of HP, LHP, and PFL is beyond the scope of this work.

Multi-layer insulation (MLI):

The term multi-layer insulation (MLI) describes a passive thermal insulation blanket. It uses multiple layers of foil, scarcely connected to each other, using the insulating effect of vacuum. The foils can only exchange heat by radiation. By the combination of reflective and emissive surface finishes, the number of foil layers and the material and shape of the spacer material, the overall insulation or effective emissivity can be designed. In Figure 4-17 on the left, the general layup of a multi-insulation-blanket is sketched. The design of MLI has many analogies with the textile industry. MLI best is used for large areas. Edges and inlays are thermal shortcuts that diminish the insulating capabilities of MLI, especially for small patches. The overall performance is better for large MLI blankets (Gilmore, ed. 2002-c2003).

Figure 4-17: left) principle layout of a MLI blanket and right) MLI blanket of a cubesat.

MLI is sensitive to handling because any wrinkle might also cause heat paths, thus its handling and integration into a spacecraft must follow certain guidelines, e.g. (Finckenor and Doolling 1999). Organic components such as hair or grease as well as many chemicals can degrade surface properties of MLI blankets. Another risk is so called ballooning which happens if gas is trapped between the different layers and cannot ventilate during ascent. This poses the danger of blanket rupture, thus venting holes (perforation) must be accounted for in MLI layout. Electrostatic discharge must also be taken into account to protect sensitive electronic equipment. This can be done by the use of conductive cover layers (Finckenor and Doolling 1999).

Outer covers have the objective to protect the reflective surfaces from atomic oxygen (in LEO) and from UV radiation (typical materials for the outer covers are beta cloth, Tedlar®, Kapton®, or Teflon®); the reflective inner layers are made of alumized or goldized Kapton®, aluminized Mylar®, polyester, or Teflon®; the

layer facing the spacecraft hardware must be compatible with the spacecraft material (corrosion, off-gassing, electric conductivity, flammability, etc.). The spacers which separate the layers should not conduct heat, have a low mass, but still provide sufficient stiffness and strength to maintain a dedicated offset between the different layers. Moreover the spacer material should be porous for gas (typical are Dacron® or Nomex®) (Gilmore, ed. 2002-c2003).

Phase change material (PCM):

The phase change materials (PCM) use the change in enthalpy of a material when heat transforms the materials' state from one phase to the other. The phase change of a material is used to buffer transient heat transfer processes. Most systems use solid to liquid phase change (melting and freezing), but also liquid to gas (vaporization) or solid to gas (sublimation) are used. PCM are used in applications with short term high thermal loads, such as in launch and reentry vehicles. It is also used for fluctuating internal heat loads in devices that are often switched on and off. Moreover PCM can be used to soften the impact of environmental heat loads, which is of special interest in case of atmosphere-less celestial bodies. For example a paraffin-based PCM was used during Apollo 15 around the batteries. In between sorties the PCM solidified because it was connected to a radiator which was exposed to the space background.

Examples for common PCM are a) inorganic salt hydrates, b) organic compounds (e.g. paraffin), c) eutectics of organic materials and natural inorganic elements (e.g. sulfur), and d) water (Bledjian et al. 2002-c2003). PCM materials can be used in a wide variety of geometries, for example around pipes.

An important use case for PCMs is in the design and sizing of radiators. Radiators combined with the dampening effects of PCMs can be designed to mean values instead of maximum and minimum heat levels. Compared to solid heat sinks (such as beryllium or aluminium) PCM are often better in terms of mass but not as beneficial with respect to system complexity and development risk. The trade-off between a pure radiator system and a PCM buffered radiator system can be calculated according to the following equations [from Bledjian (2002-c2003) funding on the original work by Busby & Mertersdorf (1987)]:

$$r_{m,rad} = \frac{(q_{pulse} \cdot r_{rad})}{q_{rad}} \tag{49}$$

$$r_{m,rad,PCM} = \frac{\beta^* \cdot (q_{pulse} \cdot r_{rad})}{q_{rad}} + \frac{\beta^* \cdot \Delta t_{cycle} \cdot (q_{pulse} - \beta \cdot q_{pulse})}{e_{PCM}} \tag{50}$$

With $r_{m,rad}$ [kg·m⁻²] being the area specific radiator mass without phase change materials, and $r_{m,rad,PCM}$ [kg·m⁻²] being the area specific mass of the radiator combined with a PCM. q_{pulse} is the periodic heat dissipation flux [W·m⁻²], q_{rad} the net heat flux the radiator can reject [W·m⁻²], r_{rad} [kg·m⁻²] the mass per radiator area, and e_{PCM} [W·s·kg⁻¹] is the mass specific stored energy in the used PCM. β denotes the duty cycle [-], which is the fraction of the total cycle time Δt_{cycle} [s], the pulse q_{pulse} occurs. The value β^* is neither defined in Bledjian (2002-c2003), nor in Busby & Mertersdorf (1987). It appears to be a factor to average q_{pulse} over the entire cycle time.

The draw backs of phase change materials are their housing and interaction with other materials. A phase change material needs to be housed, especially when the liquid phase is used. Most phase change materials will also expand. This in turn must be accounted for in the design phase. The room for expansion decreases the contact area between PCM and the device of application, leading to uncertainties in heat transfer. The material pairs used in combination with phase change materials must be chosen and tested with great care. Material interaction can lead to corrosion or the production of gases which in turn impact the phase change behavior, also increasing heat transfer related uncertainties (Gilmore, ed. 2002-c2003).

4.3.2.2 Active Thermal Control Mechanisms

Similar to the section about the passive thermal control a not exhaustive overview of active control Mechanisms, relevant for this work, is presented. In the following heaters, louvers, and pumped fluid loops (PFL) are shortly introduced.

Heaters:

The most common way of actively controlling the temperature of spacecraft or surface-craft is to place electric heaters on the device of interest. Electric heaters are made of thermally insulating material with good off-gassing properties, such as for example Kapton®. Copper wires are worked into the Kapton®. The wires serve as electronic resistor in an electronic circuit. The heater foil often has an adhesive side which can be attached directly to the dedicated part of equipment. The benefits of heaters are that they can be made in numerous geometric shapes (Figure 4-18), even custom made to the desired instrument geometry. Moreover they have a small mass and are relatively easy to integrate into a thermal design. They can be controlled to operate when necessary and appropriate. The downsides of this type of adhesive heaters are numerous cables which add to overall mass and system complexity and can provide unwanted heat paths (Gilmore et al. 2002-c2003).
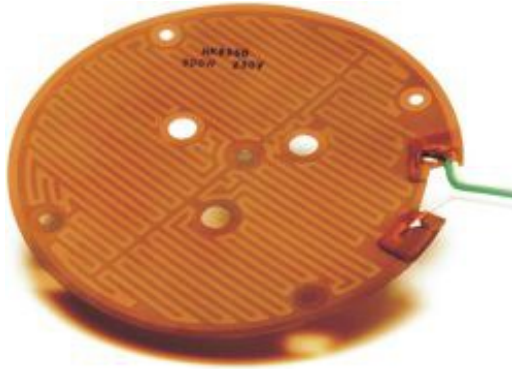
Figure 4-18: Polyimide (Kapton®) heaters (Minco 2012).

Other means of heaters are so called radioisotope thermoelectric radiators (RTGs). RTGs provide mainly heat by radioactive decay. RTGs are used in regions with lower or no solar heat flux. They were used mainly for deep space missions beyond the Earths' orbit (Voyager I&II, Pioneer) and missions to the surface of other celestial bodies in the solar system (Mars Science Laboratory). Spacecraft departing from the Sun receive less power from the Sun and have to rely on other means to maintain an appropriate temperature. Until 2007[12] the USA had flown 23 RTGs in interplanetary missions. All of them used Plutonium Pu238 as fuel. The RTG is also used to produce power for the spacecraft, but RTGs have low efficiency in terms of thermal to electronic energy conversion (only 6-7 % - Shaltens 2007). Although more advanced versions foresee the use of a combination of RTG and sterling motors, so called SRGs, the efficiency is not better than 20-25 %. In SRGs noble gases are used, for example Helium or Xenon (Shaltens 2007). Further concepts (shown in Table 4-3) are the multi-mission radioisotope thermoelectric generator (MMRTG), advanced radioisotope thermoelectric generator (ARTG) and the general purpose heat source radioisotope thermoelectric generator (GPHS-RTG) (Vining and Bennett 2010).

---

[12] In the meantime at least the Mars rover „Curiosity" was equipped with two RTGs

Table 4-3: Overview of existing radioisotope thermoelectric generators concepts (reproduced from Vining and Bennett 2010).

Radioisotope power source	Power (BOL) [W]	Mass [kg]	Specific Power (BOL) [W·kg⁻¹]	Efficiency [%]	Estimated TRL [-]
MMRTG	125	44.0	2.9	6.3	6
(A)SRG	143	20.2	7.0	28.0	5
ARTG	250	40.0	7.0	8.3	3
GPHS-RTG	300	55.9	5.3	6.8	9

The benefit of RTGs and SRGs is that they operate at any time, independent on the distance or view factor to the Sun. Significant drawbacks of RTGs and SRGs concerning the thermal design are high internal temperature (500-1,000°C), and the need to provide enough radiator area to continuously reject excess heat. An SRG might be controlled in certain narrow confines but an RTG will always provide its maximum heat load. Besides, the handling of radioactive material is dangerous and the safety require-ments are high – demanding for example that RTGs must be contained to survive a launcher failure or a reentry in the atmosphere. This leads to a large mass penalty. Furthermore, the radioactive decay of the fuel declines over time, yielding less thermal and electric power with progression mission time. A more direct use of the thermal energy freed by the radioactive decay process is the use of radioisotope heater units (RHU) and variable radioisotope heater units (VRHU). RHUs and VRHUs are small pallets of plutoni-um in a solid containment. The heat produced by these units can be applied directly to the appropriate position on the spacecraft. RHUs and VRHUs have no inefficient conversion from heat to electronic energy and back, compared to conventional heaters. On the other hand there is no way to switch the heater unit off, only to redirect the emitted heat flux with MLI and white paints (Gilmore et al. 2002-c2003). The use of RTGs, RHUs, and VRHUs is often restricted out of political reasons and the availability of plutonium Pu238.

Pumped fluid loops:

A pumped fluid loop basically consists of pipes, a pump, a working fluid and a radiator. The working fluid is forced by the mechanical pump to transport the heat away from a heat source to some device to re-move the heat. The adjunct heat removal can either be done via radiation or sublimation. In human rated spacecraft, two different working fluids are used for the interior and exterior. Different working fluids are used due to toxicity and temperature ranges. For systems with two working fluids an additional heat exchanger is mandatory between the fluid loops (Lam et al. 2002-c2003). As for all flow systems pressure, Reynolds number, Nusselt number, pipe diameter, and resistances are important beside numerous other parameters. The ability of a working fluid to transport heat depends on the fluids material properties and flow properties. Detailed information about the layout of cooling fluid loops can be found for example in (Incropera and DeWitt 2002; Polifke and Kopitz 2009; Glück 1990). Pumped fluid loops are advantageous compared to heat pipes in cases of high thermal loads or on planetary surfaces where the functionality of heat pipes is diminished or ceases entirely due to gravitation. The ability to remove large quantities of heat generated by atomic decay in MMRTGs lead to the use of mechanically pumped fluid loops in the NASA Mars Exploration Rovers (Lam et al. 2002-c2003) and Mars Science Laboratory (MSL = Curiosity) (Mastropietro et al. 2010). Figure 4-19 shows the rover heat recovery and rejection system of the MSL rover.
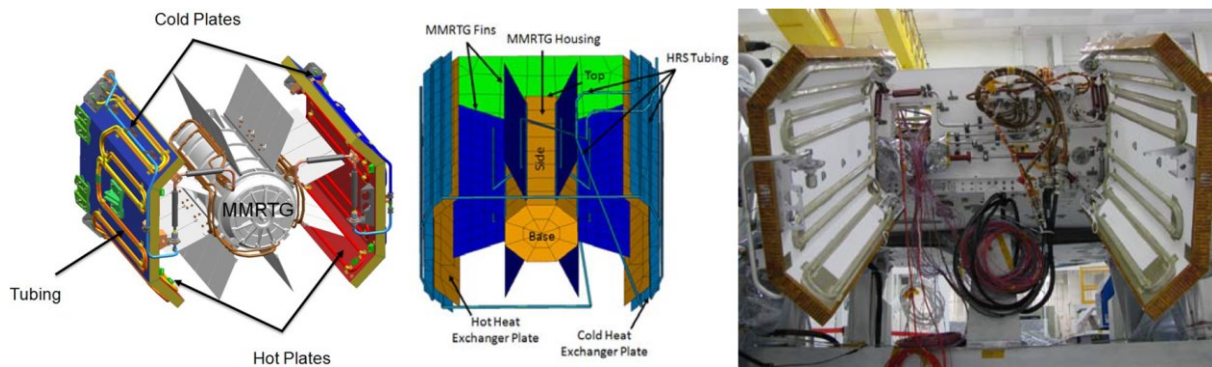
Figure 4-19: Structural and thermal models and flight hardware of the MSL pumped fluid loop in conjunction with the used multi-mission radioisotope thermoelectric generator (Mastropietro et al. 2010).

Louvers:

A louver is an assembly of blades that can be opened and closed in order to allow or to prohibit radiative heat exchange of the shaded surface with the environment. In most cases louvers are used in combination with external radiators facing deep space. Louvers have either bimetallic actuators, electrical actuators or hydraulic actuators. The bimetallic actuators can either be entirely passive but with uncertainties concerning their actuation or be controlled by heater/controller assemblies. Hydraulic and electronic actuators are more complex but allow a better control of the louver blades (Hardt et al. 2002-c2003).

4.3.2.3 Emerging Technologies for Thermal Control

A number of heat control concepts were developed and designed over the years. It would fill shelves to name and describe them all. Some concepts with relevance for planetary surfaces, proposed in recent years, will be introduced shortly in the following.

- Electrochromic radiators
- Digital radiators
- 2 phase heat exchangers

For a more elaborated summary of concepts under investigation the interested reader is referred to the work of (Swanson and Birur 2003).

Electrochromic radiators (Metts et al. 2011; Bannon et al. 2010):

Electrochromatic thin films change their transparence for electromagnetic waves if subject to a voltage. The voltage causes ions to move in or out of the electrochromatic (EC) substrate, respectively. This is a reversible process. The range of emissivity can be adjusted depending on the EC manufacturing process and the materials used. The change in optical properties can either be applied to the visible part of the solar spectrum or to the infrared regime. EC technology for use in the visible- spectrum is already commercially available and is being used in windows or automotive rear mirrors. The technology for a broadband modulation in the infrared wavelength region is less mature (Metts et al. 2011). Materials used for ECs designed for space applications must have low off-gassing values. The EC devices are produced in small patches of different sizes. They also can be integrated into flexible substrates, such as Kapton®. A concept to implement EC directly into the fabric of spacesuits was proposed in (Metts and Klaus 2009). By using the ECs properties of controllable emissivity, this approach would allow to actively control the heat rejected to, or absorbed from, the environment. The turndown ratio for electronic driven devices $r_{td,EC}$ is given in (Metts et al. 2011) is defined as the ratio between maximum heat rejection $q_{rad,max}$ to minimum heat load $q_{env,min}$:

$$r_{td,EC} = \frac{q_{rad,max}}{q_{env,min}}$$

(51)

For EC devices a maximum turndown-ratio of ~1:5 was calculated. Tests with EC test coupons in a relevant environemtn showed turndown ratios of 1:2 (Bannon et al. 2010). The control of the EC radiators needs to take into account changes in metabolic rate, internally dissipated heat from electronic devices, and environmental conditions. Body posture and fast movements can lead to a dynamic metabolic behavior which must be addressed by the EC control (Metts et al. 2011).

Digital Radiators (Ganapathi et al. 2009):

The concept of digital radiators foresees the ability to switch-off certain branches of a radiator to control the heat rejection. The driving factor for the development of digital radiator is the turn-down ratio. Different from a spacesuit that might be stored inside another spacecraft a lunar lander has to survive not only the thermal environment on the lunar surface but also during cruise phase between Earth and Moon and descent to the lunar surface. The day-night cycles are demanding for the radiator sizing. Large spacecraft also have higher overall power which needs to be radiated. Digital radiators were developed for the Altair lunar lander (Ganapathi et al. 2009).

The working principle of digital radiators bases on the principle of the stagnation radiators used during Apollo. The Apollo stagnation radiators had self-regulating flow rates by a change of cooling fluid viscosity. The stagnation approach was well suited for the benign thermal environment encountered during the Apollo missions. The turn-down ratio of this concept was only 1:1.6. Digital radiators propose a turndown ratio of 1:10 (Ganapathi et al. 2009). The ability to control heat rejection would be beneficial for concepts with varying environmental and internal heat loads. Freezing and thawing of the cooling fluid in the radiator branches not used are still a concern for this concept. The proposed countermeasure is to evacuate the branches that are not used.

2 phase heat exchangers

In a 2-phase heat exchanger the cooling fluid is allowed to freeze. The freezing process reduces the cooling fluids thermal conductivity creating an automatic control mechanism that passively governs the heat exchange. If internal or external loads are higher, the cooling fluid will melt and heat transfer will be simplified, thus transporting more heat towards the radiator where it can be rejected eventually. If the heat loads decrease, the water will start to freeze and the flow will decrease accordingly. One such concept of a freezable heat exchanger for spacesuit applications uses water as cooling fluid and reaches a theoretical turndown ratio of 1:7 (Nabity et al. 2008).

4.4 Thermal Modeling

The modeling of thermal problems has a long tradition in spaceflight applications. The first step are still the modeling of a spacecraft concept as cube or sphere and manually calculating the temperature based on the first law of thermodynamics. Throughout a space project, as the design gets more and more elaborated, manual calculations reach their limitations. Complex shapes, narrow temperature tolerances, temperature dependent material properties, and time-dependent boundary conditions lead to the development of numeric methods to support the thermal analysis. In the established approach, spacecraft components are discretized into smaller units which are called nodes. Each node is a finite representation of a segment of the entire component. There are several finite methods which will be introduced in section 4.4.1. The nodes or capacitors are connected through conductive, convective, or radiative heat transfer paths and form a thermal network. This thermal network is a model of a mathematical system of differential equations. The conductive interfaces depend on a number of parameters on the boundary between materials. They must be calculated manually or determined experimentally. The knowledge about simple connections can be found in textbooks, but in most cases the information is proprietary due to the costs and know-how involved in determining them. The radiative heat transfer can be determined analytically as shown in chapter 4.1.3 with the use of view factors or with numerical ray tracing methods. Such methods will be addressed in section 4.4.2.

4.4.1 Finite Methods

Numerical methods are widely used for solving problems in fluid dynamics, heat and mass transfer problems and other physical or economical processes that can be described with partial differential equations (Özişik 1994; Bungartz 2009). The most common methods are the finite-element-method (FEM), finite-difference-method (FDM) and finite-volume-method (FVM). The numerical methods are used when the problems cannot be solved by analytical mathematics. This might be due to nonlinearities, complex geometries and complex boundary conditions (Özişik 1994). Which method is used strongly depends on the nature of the basic physic problem. In general the FDM is often used for thermal problems in solids, the FEM is used in structural mechanics, and the FVM is used for flows in gases or liquids. Although in recent years the FEM has also found its way into the thermal analysis, the spaceflight thermal domain still relies on the FDM method. The FEM provides more elements and with that a higher accuracy can be reached. The radiative boundary conditions dominant in space make the FEM not attractive yet. In case of a FEM mesh for each surface node the radiative exchange would have to be calculated individually.

Lumped parameter method:

In case of thermal engineering a somewhat adopted FVM approach is used. A component made up of a continuous medium is discretized into nodes. Each node represents a small part of the real component. The thermal mass is concentrated or "lumped" in the node. The node is placed in the geometrical center or center of mass of the modeled volume. This method is called the *lumped parameter method* (LPM). Good introductions to this method can be found in (Gilmore and Collins 2002-c2003; ITP Engines 2010). The LPM has its origin in the analogy between electric and thermal networks. It is assumed that the temperature is homogenous for the lumped volume.

In a lumped parameter network the "lumped" volumes represented by nodes are also called capacitors C [J·kg^{-1}]. The interfaces between the nodes are called conductors G [W·K^{-1}]. Depending on the type of conductive interface the conductors are divided into conductive G_L, convective G_F, and radiative G_R. The capacitor is a function of the material properties and geometry of the volume it is representing:

$$C = \rho \cdot c_p \cdot V \tag{52}$$

In the lumped parameter method the volume V [m^3] and density ρ [kg·m^{-3}] are kept constant throughout the simulation. The specific heat capacity c_p [J·kg^{-1}·K^{-1}] in turn is a temperature dependent value that can

vary in the course of a simulation run. In order to allow a simplified matrix notation the conductive and radiative heat $\dot{Q}_{cond_{ij}}$ and $\dot{Q}_{rad_{ij}}$ exchanged between two capacitors i and j are given with:

$$\dot{Q}_{cond} = G_{L_{ij}} \cdot (T_i - T_j) \tag{53}$$

$$\dot{Q}_{rad} = G_{R_{ij}} \cdot (T_i^4 - T_j^4) \tag{54}$$

The direction of heat flux depends on the temperature gradient T. As a convention the heat flux leads from i to j. In case that the temperature of node j is higher, the heat flux has a negative sign. The conductor for conductive heat exchange G_L [W·K] is defined as the rate between the thermal conductivity k multiplied with the cross-sectional area A, divided by the distance dx between the capacitors:

$$G_L = \frac{k \cdot A}{dx} \tag{55}$$

The conductor for radiative heat transfer between an emitter i and a receiver j, is the product of geometrical and optical properties. The geometrical properties are the cross-sectional area of the receiving capacitor A_i and the view factor between the two capacitors F_{ij} [-]. Besides, the receivers' absorptivity α_j [-] and the emitters' emissivity ε_i [-] have to be accounted for. σ is the Stefan-Boltzmann constant.

$$G_{R_{ij}} = A_i \cdot F_{ij} \cdot \varepsilon_i \cdot \alpha_j \cdot \sigma \tag{56}$$

The radiative conductor $G_{R_{ij}}$ [W·K^{-4}] relies on the determination of view factors. It can be replaced if the heat transfer is calculated with a ray tracing approach. In the latter case $\dot{Q}_{rad_{ij}}$ is just another heat load.
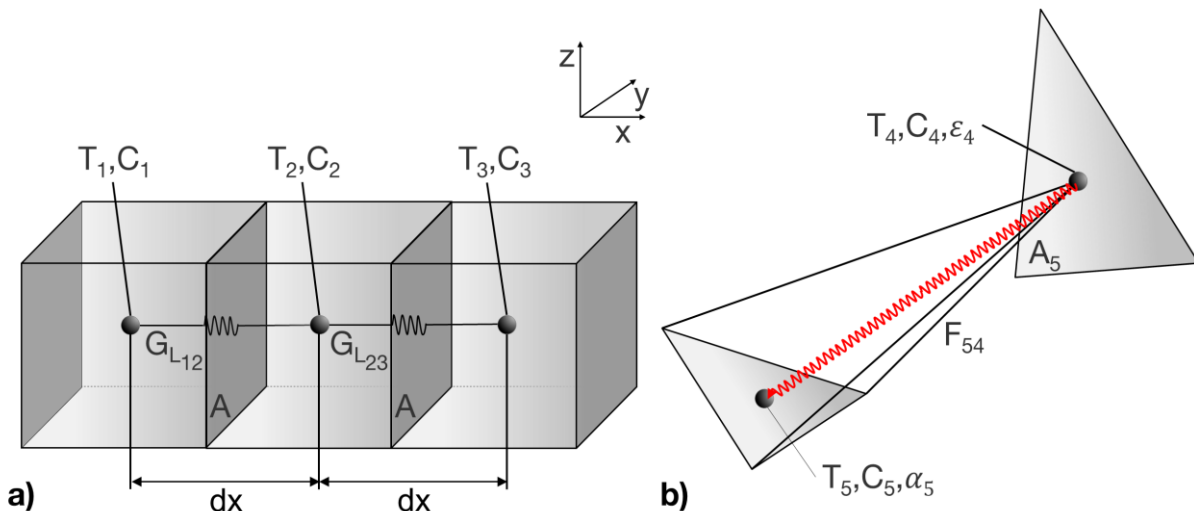
Figure 4-20: a) Conductive path through a solid material, simplified as cubes with the same volume. b) Radiative exchange between two surfaces [reproduced from (Gilmore and Collins 2002-c2003)].

4.4.2 Ray tracing for Radiative Heat Transport

To determine the view factors analytically becomes more and more complex with increasing complexity of the geometry until it gets impossible. Ray tracing simulations are often used in order to statistically determine view factors or to bypass them altogether. Monte-Carlo ray tracing is a statistical method and the most common approach used as replacement for view factors in complex geometries, and denotes a statistical method with inherent uncertainties. It is not possible to define when a Monte-Carlo method becomes more efficient in terms of computational demand than the conventional techniques. Moreover Monte-Carlo poses the danger of statistical errors much like errors inherent in experimental measurements (Modest 1993). Ray tracing allows the determination of the heat that is exchanged by approximating the radiated energy bundles as discrete rays. This approach is mainly used for computer games, the

visualization of realistic lighting effects and scenes, but also in scientific computation. A multitude of tools and approaches exist. One tool to create photo-realistic graphical pictures is the OptiX® framework, a specialized language distributed by NVIDIA®. OptiX® is a derivative of the language CUDA C (Robinson 2009). With OptiX® code can be written that is executable directly by NVIDIA® graphic boards. It is possible to set up geometries, light sources, and cameras or observers, and to calculate the lighting conditions seen from the position of the observer. Forward and backward ray tracing are two different approaches. Forward ray tracing is the more realistic way of one or several light sources which emit light and a pinhole camera that receives a portion of the light. This approach is realistic but demanding. In the backward ray tracing approach the rays are emitted by the camera, thus inversely determining which rays are important for the observer. The second approach is less time consuming but cannot be used for calculations were the rays carry scientific information. This information is independent of the rays that reach the "observer".

In the forward ray tracing approach, depending on the type of light source, the rays can either be emitted parallel or from a point source. The surface is made up of a set of triangular elements connecting a cloud of data points. Each surface can be attributed with optical properties, mainly reflectivity and transmissivity. Additionally, each ray carries information about a) what it shall do when it hits a certain optical surface and b) the number of times it was reflected. Each ray is terminated after a predefined number of reflections or if it misses the geometry. To accelerate the processing of rays, the geometry can be divided into "acceleration structures". Acceleration structures are primitive shells that are placed around parts of the geometry. Each newly emitted ray is checked against an intersection with the "acceleration structures". Subsequently, if it intersects the structure, the intersection with the contained geometry is tested (Parker et al. 2010).
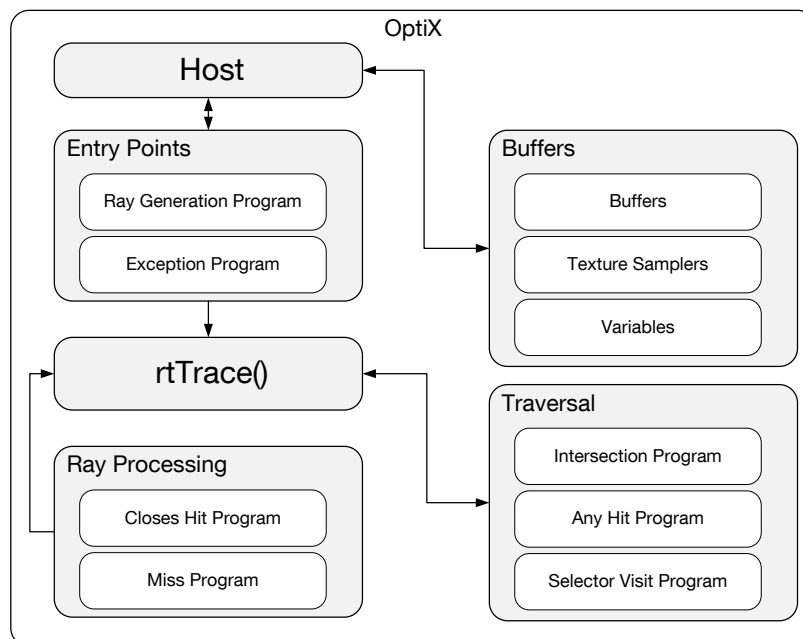
Figure 4-21: Interaction inside the OptiX Framework [reproduced from (Robinson 2009)].

NVIDIA® OptiX® is a framework which provides building blocks to construct and implement a ray tracing algorithm tailored to the problems at hand. The main abstractions in the OptiX® Framework are Context, Ray, Geometry, Material, and Program. The context contains all OptiX® resources such as textures, geometry and user defined programs. The context also is the interface to control the setup and launch of the ray tracing engine. A ray is the central element of any ray tracing algorithm. A ray is defined by origin, direction, and payload. The payload is a user defined set of information, also called *Per Ray Data*. This set of information determines the behavior of the ray if it intersects a surface element. The Material contains information on the shading of rays. Certain Optix® specific programs can be called or be defined by the

user. With these programs reflections shadows or other behaviors can be implemented (Nogina 2012; NVIDIA 2008)].

As can be seen from Figure 4-21 an Optix® application can have a number of programs. The programs handle the ray properties on their way through the 3D geometry, thus for example annihilating rays if they miss all objects or add to their reflection counter, once they hit a part of the geometry (NVIDIA 2008).

4.4.3 Thermal Software

The available computational methods reach from basic spread-sheet based calculations to complex software tools. Spread-sheet tools, often created in Microsoft Excel, can be used to keep track of components, material properties, and simplified conductive and radiative heat exchange. These tools are unable to give a geometrical representation to solve differential equations. The view factor calculations can be stored in libraries but are restricted to relatively simple shapes that still can be solved analytically.

Complex software tools are able to solve thermal networks (section4.4.1) and use ray tracing methods (section 4.4.2) to determine view factors and radiative heat transfer, respectively. Advanced tools allow the use of materials with changing properties, implementation of heat sources, display and manipulation of graphical representations of the spacecraft as well as the import and export to computer aided design (CAD) tools. Furthermore the tools provide general user interfaces (GUI) to simplify their handling. Examples for such complex software are ESATAN-TMS used in Europe and Thermal Desktop in combination with SINDA/FLUINT used in the US. Both software packages are written in the programming language FORTRAN. These software packages are the standards and their application is demanded in ESA and NASA projects, respectively. Large aerospace companies have developed their own, internal tools to either compete with the agencies' standard tools or to help in the thermal analysis of specialized problems such as cryogenics and optics. Table 4-4 shows a (not exhaustive) overview of thermal analysis software. The allowable temperature limits for components and subsystems are provided by each system authority. Accuracies of uncorrelated models have to be better than ± 10 K for the specified temperatures in order to gain preliminary acceptance. After thermal tests the correlated models have to be tuned to be accurate within a range of ± 3 K (Welsh 2002-c2003).

Table 4-4: Overview thermal analysis software used in space projects (not exhaustive).

Thermal preprocessor	Solver	Manufacturer, Country
Thermal Desktop (FLUINT/RadCAD/FloCAD/EZ-XY)	SINDA	C & R Technologies, USA
Sinaps		
Thermica	Thermisol	ASTRIUM, France
ESATAN-TMS	ESATAN	ITP Engines, United Kingdom
ThermXL		
NX Space Systems Thermal	NX Nastran	
FEMAP		Siemens, Germany
Thermal Synthesizer Systems (TSS)		Spacedesign, USA

Approach in ESATAN

The general approach to set up a model in ESATAN is depicted in Figure 4-22. The approach is used exemplarily for other commercial thermal tools for spaceflight applications. In the first step, the geometry of interest is either imported from other computer aided design tools or created directly in the ESATAN GUI. The CAD part of group has to be subdivided into triangular or quad-elements. This step normaly is performed in a different meshing tool (e.g. Hypermesh, FEMAP). Subsequently, materials are defined and optical sets are generated. Material properties and optical sets are then assigned to the geometry. If

applicable, the rotation of appendices is realized, such as antennae or solar arrays. In the next step an orbit and a number of positions in this orbit are defined. Based on orbit cases geometry and optical properties a Monte-Carlo ray tracing is performed that determines the heat fluxes from the environment for each of the defined points in the orbit. Moreover, the ray tracing determines the view factors between the components of the spacecraft, the elements of the so called G_R-matrix. These radiative conductors are important to calculate the radiative heat exchange between different parts of the spacecraft during the numeric calculations. By determining the G_R values first and storing them in a matrix, it is possible to treat them like a matrix of conductive interfaces and avoid the need of a raytracing in every time step. The data set is stored and rerun for a predefined number of orbit cases. After the dataset for the environmental heat flux throughout one orbit is generated, the next step is to set the conductive interfaces of the geometric parts. ESATAN-TMS is able to find conductive paths, but not all of it. Especially in complex geometries the user has to add many conductive paths manually. In addition, the user has to define the initial and boundary conditions that are necessary to solve the thermal network. The information can either be input through the graphical user interface or with code files. From this second data set the numeric calculation can be launched.
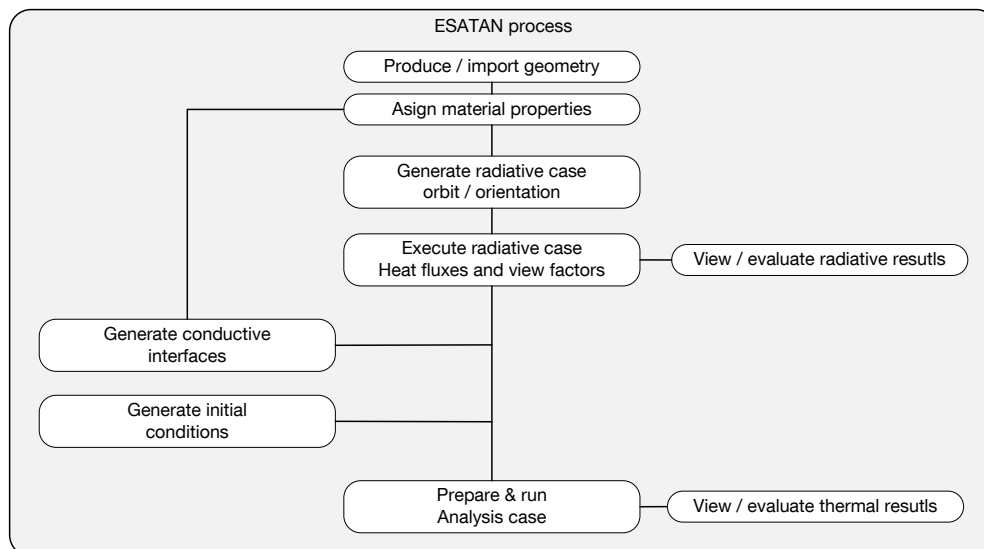
Figure 4-22: The process behind a thermal analysis of a spacecraft with ESATAN-TMS.

5 The *Thermal Moon Simulator - TherMoS*

To invent, you need a good imagination and a pile of junk.

- Thomas A. Edison

In this chapter the methods are described to meet the objectives and answer the hypothesis. The used methods base on common thermal analysis software tools from the engineering domain and methods to calculate lunar surface temperatures established from the field of planetology. The combination of the different fields leads to a new method that enables the dynamic prediction of radiative heat fluxes on the outer surface of a spacecraft and subsequent calculations for the spacecraft temperatures. The developed tool is called the *Thermal Moon Simulator (TherMoS)*. In section 5.1 the general approach is introduced and the overall building blocks of the simulation and its core structure are presented. In section 5.2 the different modules that make up the simulation are described in more detail. The verification of the model against remote sensing data and other models from literature is presented in section 5.3.

5.1 A Dynamic Thermal Modeling Approach

In section 4.4.1 the common method to calculate heat fluxes and temperatures for orbiting spacecraft was introduced. The method consists of a model of lumped parameter nodes. The capacitors represent the nodes. They are connected by conductors of different type. Capacitors and conductors form a thermal mesh which can be solved numerically with appropriate initial and boundary conditions. Radiative heat exchange is calculated with a ray tracing algorithm. The ray tracing algorithm calculates heat fluxes and view factors. The left side of Figure 5-1 depicts the common approach how it is implemented for example in ESATAN-TMS. The *TherMoS* approach, shown on the right side of Figure 5-1, differs slightly but significantly from the common approach. The main differences between the common approach and the approach implemented in this work are:

a) it is new to determine heat solar and infrared fluxes for each time step (red line),
b) to decouple thermal calculations of the surface-craft from environmental conditions (red dashed line), and
c) to allow for a predefined relative path in a lunar landscape.

In commercial spacecraft thermal tools there is no necessity to recalculate the heat fluxes in each time step. In general it is sufficient to calculate the heat fluxes caused by Earth infrared, Earth Albedo, and Sun for several steps in the orbit and interpolate in between. In order to determine the heat fluxes between components of the spacecraft the view factors are determined once and stored in a radiative conductor matrix. This approach is not applicable to spacecraft that have a relative movement towards a complex environment as on the surface of the Moon. Thus in each time step the ray tracing is repeated.

In the common approach, the radiative cases are run first and then are stored. The numerical thermal calculation is performed based on the radiative cases. The optical coatings of the components must be added beforehand. If the optical properties are changed, all radiative cases have to be repeated and with that all thermal cases have to be rerun. The *TherMoS* approach in turn determines the solar and infrared heat fluxes for each time step based on the outer shell of the spacecraft, considering it to be a black

body. Thus a multitude of optical coatings and internal thermal combinations can be run after the ray tracing was performed.

In current thermal software tools relative movement of components is enabled. In this case, view factors for several positions are determined and stored. The relative movement of a spacecraft towards its environment is not implemented at all. Recently, some software tools (Thermica 4.4 & ESATAN-TMS r5) added static planetary bodies. With planetary bodies, the long time day-night cycle for static objects such as landers and bases can be calculated to a certain degree. Neither the surface properties nor surface features are accounted for. The *TherMoS* tool in contrast takes into account the material properties of the surface as well as boulders and craters. Together with a way to represent relative movement along this artificial surface, the hypothesis set up in section 1.2 and the objectives pointed out in 3.4 can be addressed.

Yet another difference is the computer language in which the simulation is programmed. Whereas ESATAN® and Thermal Desktop rely on FORTRAN, the *TherMoS* tool is written in MATLAB®[13]. MATLAB® uses matrix operations to process the calculations. Matrix operations are beneficial for large networks. Moreover it is a common language in the engineering domain.
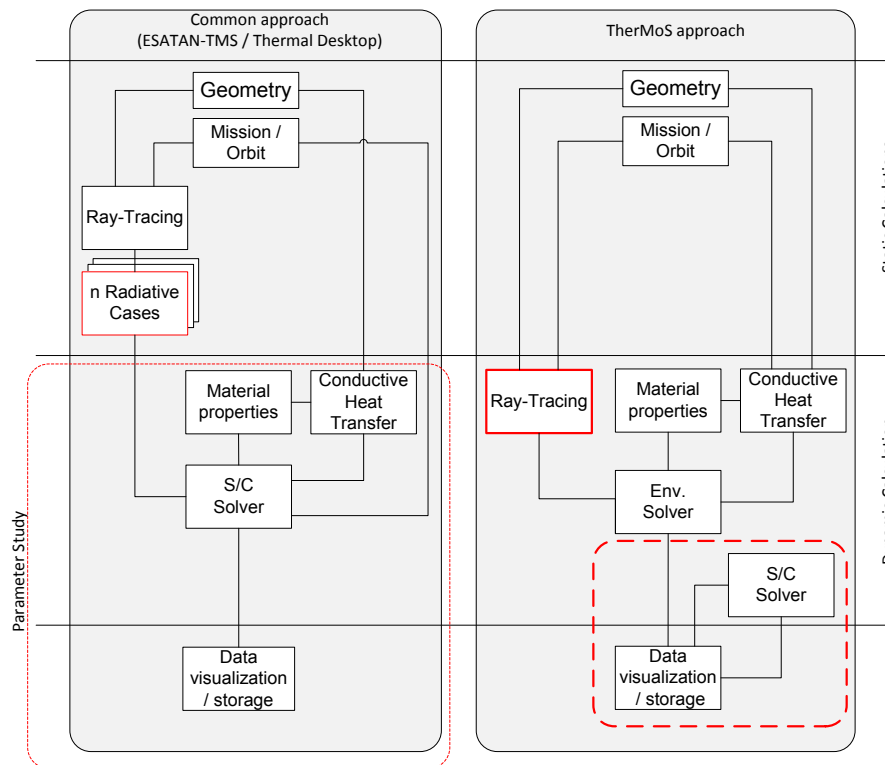
Figure 5-1: Differences between the common approach in thermal analysis tools in the space flight domain (left) and the *TherMoS* approach (right).

---

[13] MATLAB is not a programming language in its classical sense. Here this term is used to underline the contrast between FORTRAN and MATLAB.

5.2 *TherMoS* Modules

Figure 5-2 depicts the internal structure of the *TherMoS* tool. The *Spacecraft* and *Environmental modules* generate geometries. The *Spacecraft Module* also creates a path, based on predefined waypoints. The *Environmental Module* provides a calculation of the directions towards the Sun and the thermal properties of the lunar surface. The resulting data is stored in MATLAB® *structs*, defined as global variables. They are accessible for all other modules. The *Thermal Solver Module* prepares the capacitors and conductors, includes the incoming and outgoing heat fluxes, and calculates the temperature for each time step. The *Movement* function continuously alters the geometry of the spacecraft during the transient calculations. The *Data I/O Module* provides an interface to stored data. It also provides an interface to interchange data with the ray tracer based on text files. Stored data is for example the geometry of a spacecraft. Exchanged data are the current temperatures and balanced solar and infrared heat fluxes for each surface element. Only the modules enclosed in the orange field with the dash dotted line are processed in MATLAB®. The ray tracer is implemented in OptiX® and not in MATLAB®. The text files are either standard text files (.txt) or comma separated values files (.csv). The *Postprocessing Module* uses the stored data from text files or global variables stored in MATLAB® to visualize temperatures and heat fluxes.
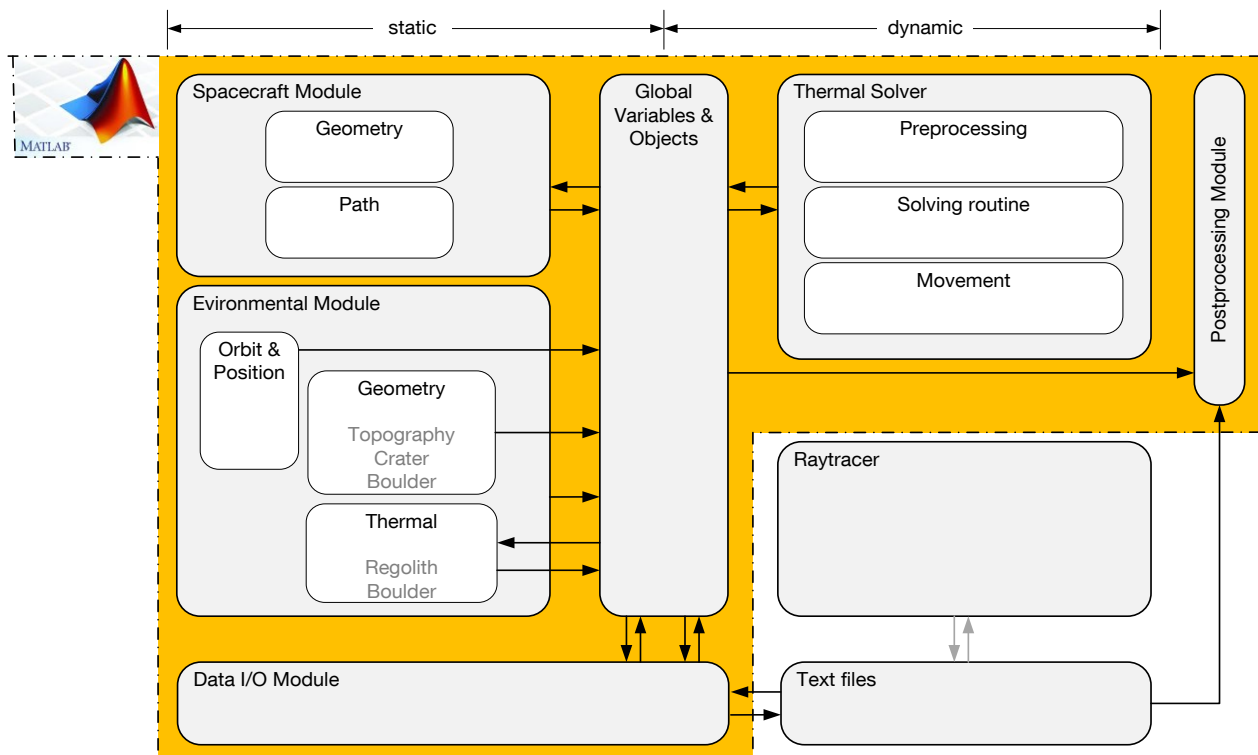
Figure 5-2: Overview of the internal structure of the *TherMoS* tool.

The properties created by the modules are stored in MATLAB® structures (-*structs*). These structures allow the combination of different data types in a single containment. In the *TherMoS* tool the *structs* are used like objects in an object oriented computer programming approach. Their contents and hierarchy is shown in Figure 5-4. The landscape objects are a large or a small scaled topography, one or several boulder objects, or a crater object. Each landscape object contains properties relevant for geometric representation and calculations as well as properties for the thermal calculations. The geometric properties are the x-, y-, and z- coordinates, the point combinations that form the triangles (TRI), the area, the center of gravity of the area, the distance to the center of the scene, the normal vector, and the slope angle. The thermal properties are the capacitors and the conductors. For each *landscape object*, apart from boulder objects, additional properties are stored in the *structs*: density, mass, and a static value for the conductors. In case of the *spacecraft object,* the geometric properties are the same as for the land-

scape objects. In the *spacecraft object* no thermal properties are stored during the heat flux determination phase and the absorptivity and emissivity values of the spacecraft object are set to 1. The thermal properties and conductors and capacitors are added in a subsequent step when the temperatures of the surface-craft elements are being calculated.
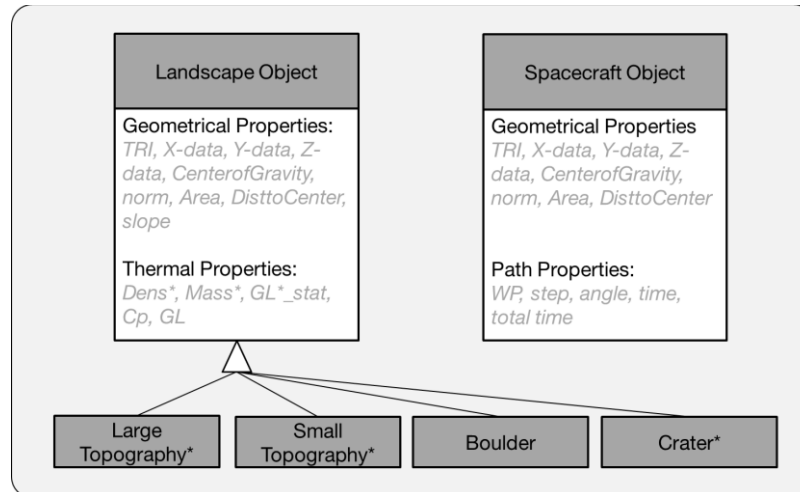
Figure 5-3: Objects represented as *MATLAB –structs*. The objects contain the geometric and thermal properties.

5.2.1 Environment Module

The *Environment Module* is the backbone of the *TherMoS* tool. It provides the thermal environment for objects put in a lunar environment, such as spacesuits and rovers. The top level objective of the *Environment Module* is to provide the geometrical and thermal representation of a lunar landscape. Thus the environmental modules has to provide a representative set of geometric objects to account for view factors and shadowing effects, as well as to provide correct material models to account for time, temperature, and density dependent material properties. In order to represent appropriate view factors, the geometry has to reproduce large scale topography as well as small scale surface features. Hence, the environmental module consists of a *Regolith Model*, a *Topography Model*, a *Boulder,* and a *Crater Model*. Figure 5-4 shows the basic hierarchy of the *Environment Module*. Topography, Crater, and *Boulder Models* reproduce the geometry of the lunar surface, based on published remote sensing data. The thermal properties of the lunar surface and boulders are accounted for in two models with nodes in a FVM net. The geometries are constructed of triangular elements because MATLAB® provides functions for so called 'delaunay triangulations' and because triangles are plane elements without curvature. The latter fact simplifies the determination of geometrical properties such as area, normal vector, or center of gravity.

<u>Assumptions and Restrictions:</u>

The values used for the geometric and thermal models of the lunar surface are based on literature data. The data was either obtained by remote sensing instruments or by the measurements performed *in-situ* during the Apollo and Luna missions. From orbit the global topography was measured in recent years with light detection and ranging (LIDAR) instruments. The material properties for regolith and rocks were only measured at a few sides on the Moon. As on Earth the geology, the *selenology* on the Moon varies from region to region. Due to the lack of other material data, the Apollo and Lunar data are extrapolated to the entire Moon.
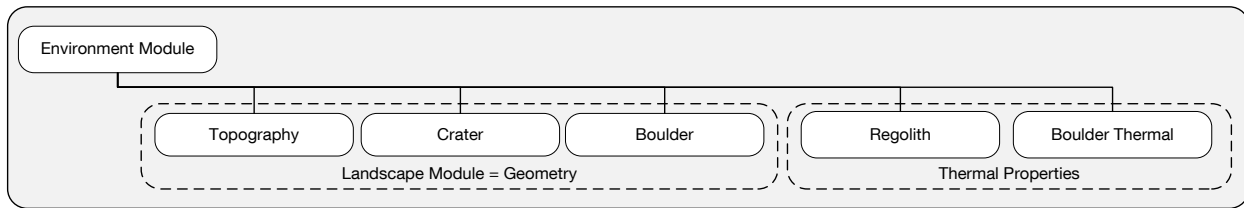
Figure 5-4: Hierarchy of the Environment Module.

5.2.1.1 The *Landscape Module*:

The *Landscape Module* is the integrating element for the preparation of the lunar surface geometry. In this module the topographic geometries, derived from the remote sensing data, are combined with the crater and boulder geometries. The generated geometry is then used for thermal calculations and for the ray tracing. Figure 5-5 shows the input and outputs of the *Landscape Module*. The user decides upon the position on the lunar surface by entering latitude and longitude. Furthermore, the user enters the size of the presented landscape and the resolution of the surface elements. Landscape size and resolution determines the number of surface elements. The user can also add information whether the landscape is a highland or mare region. In addition, the user can decide upon the number and position of boulders or leave it to a randomized routine. The *Landscape Module* uses the Kaguya remote sensing data set as part of the *Topography Module* as well as the crater and boulder modules to generate a mesh of the demanded landscape. Each model calculates the geometrical properties of area, center of area, normal vector, and slope angle. The generated landscape is visualized at once for the user to check the outcome of the inputs. The main set of data is stored as global variables in MATLAB® structures. Global topography, boulders and crater are stored in different variables.
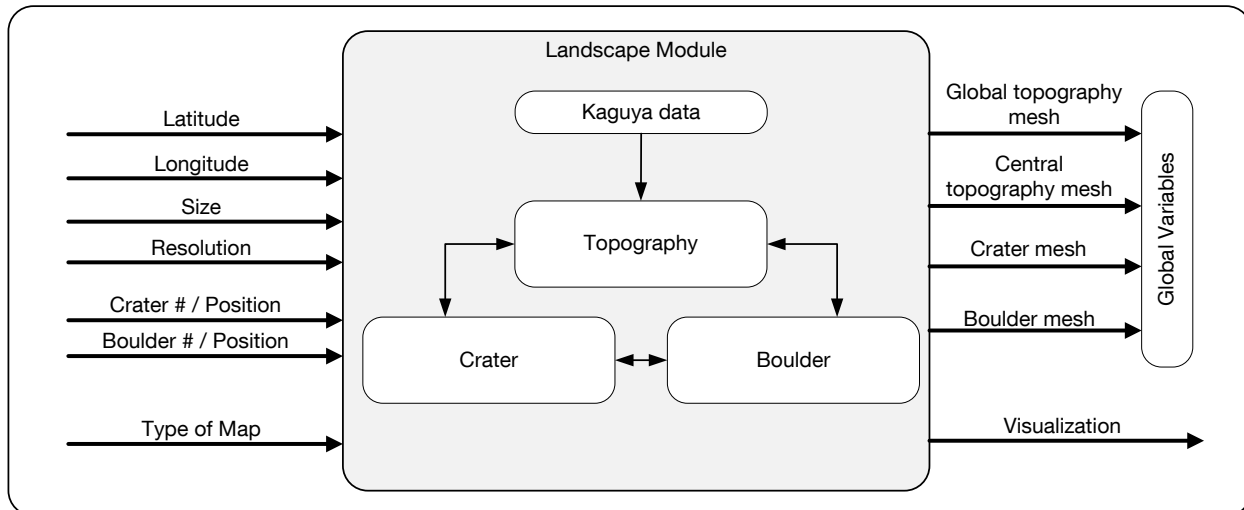
Figure 5-5: In- and outputs of the landscape module.

The *Landscape Module* allows building a multitude of combinations from a level surface with no features to a Kaguya topography superimposed by large and small craters and numerous boulders. In the center of the scene an area with a higher resolution of surface elements is included. Boulders, small craters, and the surface-craft are placed in this region of higher resolution. The higher the resolution of the topography the more accurate are the heat flux results. The regions further away from the spacecraft have a lower resolution than the central part. Figure 5-6 gives an overview over the possible landscape configurations currently implemented in the *TherMoS Landscape Module*. On a global level either *a)* a rectangular grid based on Kaguya data, *b)* a level terrain with an area of higher resolution in its center, or *c)* a large crater on a level terrain with an area of higher resolution in its center can be created. In the central area with a higher resolution, surface features can be integrated. These surface features are *d)* a small crater, *e)* a

crater with a fitting set of small boulders (see also section 5.2.1.4), or *f)* a single set of boulders that are placed manually.
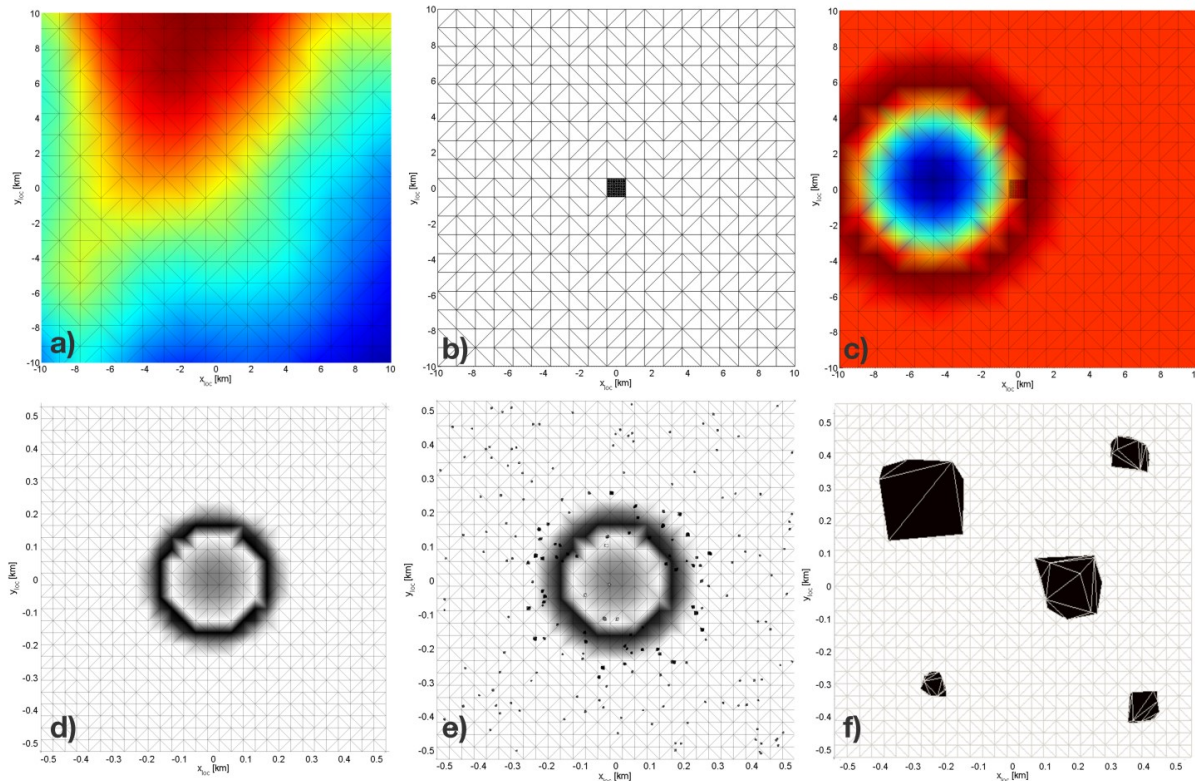
Figure 5-6: Overview of the possible configurations with the *Landscape Module*.

5.2.1.2   The Topography Module:

The *Topography Module* for the *TherMoS* tool is based on a publicly available dataset measured by the LALT (Laser ALTimeter) instrument onboard the Japanese probe Kaguya. The instrument measured 16,588,800 points on the lunar surface. The distance between two measured points is 1/16°. This means that values for 5,760 longitudes and 2,880 latitudes were obtained by LALT (Araki et al. 2009; Vogel 2010; Lechner 2011). Depending on the latitude, the data points are closer together or more scattered. At the lunar poles the topographic features are well represented because the probe passed the poles during each orbit and thus the density of data points is higher. Along the equator, where passes of the probe occured less often, the resolution of data points is not better than 1.895 km in East-West direction. Closer to the poles this value decreases for the latitude. The distance of 1.895 km between two data points remains constant along the meridians. Thus features in the range of the spatial resolution of the instrument appear to have smoother slopes than in reality. Features with a size <1.9 km such as small craters, boulders, and steep cliffs could not be measured by the LALT instrument at all. The overall vertical resolution is better than 5 m (Araki et al. 2009). The altitude of the Kaguya probe was not constant due to the influence of the inhomogeneity of the lunar gravitational fields that is called by so called mascons. Hence, the LALT data is subject to measurement errors. The changing orbit altitude biases the measured distance between spacecraft and surface. The measurements were repeated several times during the operational phase of the Kaguya probe.

Several assumptions were made to implement the *Topography Module*.

-   The *Topography Module* relies on the lunar reference radius of R_m = 1,737.4 km (Sullivan and Paige 2011; Araki et al. 2009) which is used by Kaguya and LRO.

- The lunar surface does not change over time. The simulations are extremely short compared to the timescales in which the surface of the Moon changes by impact events of different magnitudes.

As mentioned before, the grid in which the Kaguya data is stored has an increment of 1/16°. Each data point is represented in longitude, latitude, and altitude above the reference radius. The native format of the Kaguya LALT data set were comma separated value (*.csv*) files. Because of limitations inherent to programs such as MS EXCEL®, the data was distributed over 262 files. The data thus was transformed into a MATLAB® matrix and stored in a *.mat* file. This format can be accessed by MATLAB® more easily (Vogel 2010; Lechner 2011).

Figure 5-7 shows a flowchart of the *Topography Module*. At first the input values are adapted, the fitting data is extracted from the Kaguya data set, the data is transformed into the local coordinate frame and a triangular mesh is created based on the data points. The following steps depend on whether a central region with a higher resolution, and if craters or boulders shall be included. In the next step, geometric properties of each surface element are calculated. At first, the area and the center of gravity are calculated, followed by the normal vector and the distance to the topographies local center of origin. Each geometry element created by the topography model represents a patch of the lunar surface. Depending on the size of the entire landscape and the chosen resolution, the size of the surface element varies. Especially if a small resolution is chosen, the points in the data set will have a coarser resolution than the topographic representation produced by *TherMoS*. In this case the intermediate points are interpolated. Prior to visualizing the topography all geometric properties are stored in vertices and matrices and combined in a MATLAB® *struct*.
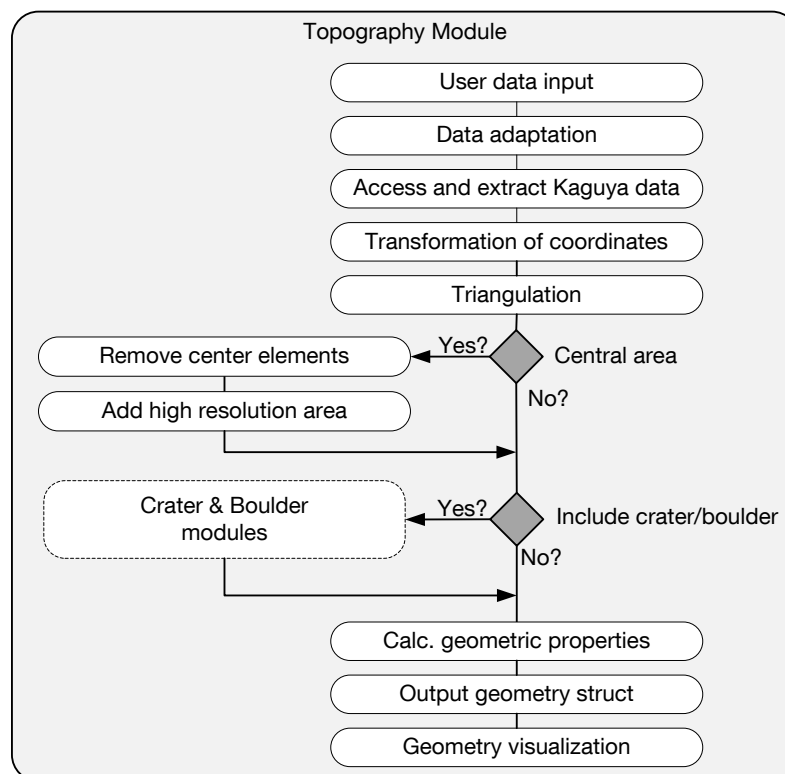
Figure 5-7: Flowchart for the topography module.

The current implementation for the *Topography Module* in *TherMoS* allows to decide between flat square representation for small patches (<100 km), as well as convex circular elements for larger regions. Additional a panoramic view calculated from the center of a given spot can be created. In Figure 5-8 the Apollo 15 landing site was used as an example to show the capabilities of the *TherMoS Topography*

Module. The diagram in the left upper corner of Figure 5-8a) shows a rectangular patch with an edge length of 36 km. This is the standard view used for the case studies. In Figure 5-8b) a circular topographic map of the same region is shown. The diameter of the spherical shell segment is 300 km. The circular map is superimposed with grid lines showing meridians and parallels of latitude in order to simplify the understanding. In Figure 5-8c a panorama of the same position is shown. The depth of the panorama is 25 km. r_{lok} is the distance from the center and φ_{lok} represents the circumference. In Figure 5-8a) and c) the height represents the distance to the center of the Moon, and in b) towards the lunar reference radius.
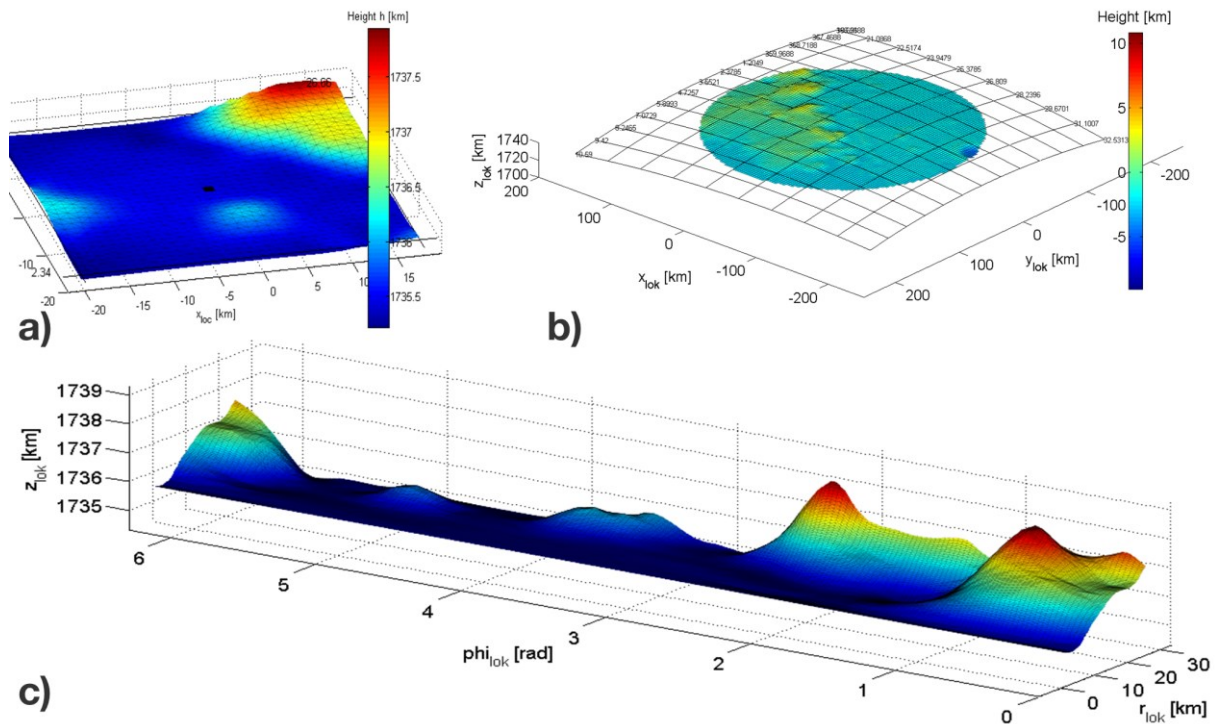
Figure 5-8: Different representations of the lunar topography at the Apollo 15 landing site [adapted from (Vogel 2010; Lechner 2011)].

5.2.1.3   Regolith Model

A central part of any thermal simulation for the lunar surface is a model of the lunar regolith, with its unique and extreme thermal properties. The thermal properties of regolith were described in chapter 4.2.2. A multitude of models for lunar regolith have been proposed in the past (see chapter 2.2.1). Most of these models focus on flat planes and average temperatures on the Moon. The authors of the models agree in that the temperature variation on the Moon mainly depends on the thermal conductivity k_{reg} [W·m^{-2}·K^{-1}], the density ρ_{reg} [kg·m^{-3}], and the specific heat $c_{p,reg}$ [J·kg^{-1}·K^{-1}] of lunar regolith. The temperature also depends on the lunar infrared emissivity $\varepsilon_{IR,reg}$ [-], its solar absorptivity $\alpha_{sol,reg}$ [-], the albedo $\alpha_{alb,reg}$ [-], the solar constant S [W·m^{-2}], and its angle of incident θ [°].

The used approach in this work bases on the two layer model approach that was introduced by (Cremers et al. 1971) and later improved by (Vasavada et al. 1999). This type of regolith layer models considers the lunar surface to be made up of two layers of different material properties. The upper layer is the so called "*fluff*" or lunar soil. The soil layer has a thickness of only two millimeters and has a lower density, heat capacity, and thermal conductivity than the layer underneath. The implemented *TherMoS Regolith Model* differs from the one proposed by (Cremers et al. 1971) since it a) includes an internal heat flux as proposed in Vasavada et al. and b) uses time, temperature, and density dependent material properties as opposed to static values.
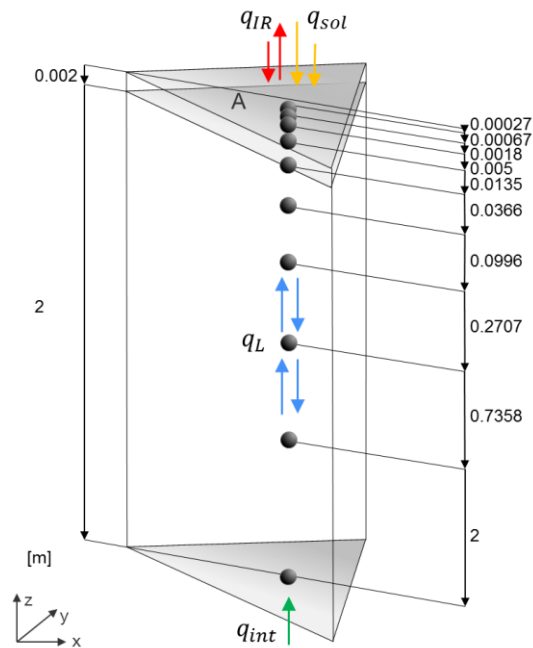
Figure 5-9: Thermal structure of each triangle. Values are given in [m]. Distances are not to scale.

In the regolith model used in the *TherMoS* simulation, the density increases according to the empiric law discussed in chapter 4.2.2. In earlier works it was determined that the heat wave does not penetrate the lunar surface more than 0.5 m during one lunation (Winter and Saari 1969; Cremers et al. 1971). The regolith is modeled with 10 nodes to a depth of 2 meters. The nodes are spaced in a logarithmic fashion with increasing distances towards two meters and a higher frequency close to the surface. The regolith elements have a triangular base, since they are derived from the *Topography Module*. It is assumed that the cross sectional area does not change with depth. This assumption is valid for level areas but becomes erroneous for inclined slopes on crater rims and walls. The temperature at 2 m depth was measured during Apollo 15 and 17 and found to be 255 K (Langseth et al. 1972). This value is used as initial condition. The internal heat flux q_{int} was set to 0.019 W·m^{-2} (see chapter 4.2.2). The values for heat capacity and thermal conductivity are temperature dependent. They can be recalculated in each time step. Based on the geometry stored in the MATLAB® *struct*, the thermal preprocessing is used to calculate the capacitors C_{reg} and conductors $G_{L,reg}$. In this way, each surface element is thermally represented by 10 thermal nodes. The conductivity of the lunar fines is extremely low, with several mW·m^{-1}·K^{-1}. Because the surface elements have diameters of several meters, horizontal heat exchange was neglected in the *TherMoS Regolith Model*. Each surface element, consisting of its 10 thermal nodes, thus is adiabatic to the bordering surface elements. In Figure 5-9, the thermal structure for each regolith triangle is depicted. The 10 thermal nodes are depicted with dark points. The values on the right side represent the distances between lunar surface and node. On the left side of Figure 5-9 the thickness of the layers is shown. Thus, the first three nodes still lie within the soil layer and the remaining seven nodes lie in the region with coarser regolith. Additionally, the heat fluxes are integrated to Figure 5-9. The infrared heat fluxes, depicted in red, are incoming and outgoing fluxes. The incoming fluxes are caused by nearby areas. The outgoing infrared fluxes are governed by the temperature of the uppermost node. The solar heat flux, represented in yellow, consists to a large extent of the solar rays incident directly from the Sun. A smaller portion results from reflected solar rays from nearby surface elements. Two vertically neighboring nodes in one surface element exchange heat by means of thermal conduction. In Figure 5-9 the thermal conduction is depicted in blue. The lowest node is subject to the lunar internal heat flux. In Figure 5-9 the internal heat flux is depicted in green. The conductors G_L and the capacitors C for every node are important for the thermal calculations in the *Solver Module* (section 5.2.3). The layer in which a node is places, dictates

the thermal conductivity of the node. The heat capacity of each node is a function of its volume V_{reg} [m³], the local density ρ_{reg} [kg·m⁻³], and the local specific heat $c_{p,reg}$ [J·kg⁻¹·K⁻¹]. According to equation (52) the capacitor can be described with:

$$C_{reg} = \rho_{reg}(z) \cdot V_{reg}(z) \cdot c_{p,reg}(T) \tag{57}$$

regolith density is a function of depth, the volume depends on the size of each layer, and due to the log distribution of the nodes consequently is also depth dependent. The heat capacity is a function of temperature. The area A [m²] of each surface element is available from the topography variables. Based on the log distribution of the nodes, the distances between the boundary of two layers d_1, the distance between a node and the surface d_2, the distance between two adjacent nodes d_3, and the height of a layer d_4, can be computed. For m surface elements and n depth nodes per surface element the volume of each node thus is a matrix $V_{reg,m,n}$:

$$V_{reg,m,n} = \begin{bmatrix} A_1 \\ A_2 \\ \vdots \\ A_m \end{bmatrix} \cdot [d_{4,1}, \quad d_{4,2}, \quad \cdots, \quad d_{4,n}] = \begin{bmatrix} A_1 \cdot d_{4,1} & A_1 \cdot d_{4,2} & \cdots & A_1 \cdot d_{4,n} \\ A_2 \cdot d_{4,1} & \ddots & & \vdots \\ \vdots & & \ddots & \vdots \\ A_m \cdot d_{4,1} & \cdots & \cdots & A_m \cdot d_{4,n} \end{bmatrix} \tag{58}$$

regolith depth and slope dependency of the regolith density and the temperature dependence of the regolith heat capacity was presented in section 4.2.2. For the first iteration, an initial temperature of 300 K is used to calculate the first capacitor value C_{reg} [J·K⁻¹]:

$$C_{reg,m,n} = V_{reg,k,n} \cdot \rho_{reg,n} \cdot c_{p,reg,n} = \begin{bmatrix} C_{1,1} & C_{1,2} & \cdots & C_{1,n} \\ C_{2,1} & \ddots & & \vdots \\ \vdots & & \ddots & \vdots \\ C_{m,1} & \cdots & \cdots & C_{m,n} \end{bmatrix} \tag{59}$$

In order to simplify the calculation in the *Solver Module*, the capacity is stored in a vector of size $j = m \times n$. The column, which represent the different layers, are placed in one row, which yields:

$$C_{reg,j} = [C_{1,1} \quad \cdots \quad C_{1,n} \quad C_{2,1} \quad \dots \quad C_{m,2} \quad \cdots \quad C_{1,n} \quad \dots \quad C_{m,n}]^T \tag{60}$$

The conductive interface $G_{L,reg}$ can be separated into a static part and a transient part. The static part depends on the Area A [m²] and distance between two nodes d_3 [m]. The static part of the conductive connection $G_{L,reg,stat,k,n}$ can be calculated with:

$$G_{L,reg,stat,m,n} = \begin{bmatrix} A_1 \\ A_2 \\ \vdots \\ A_m \end{bmatrix} \cdot \left[\frac{1}{d_{3,1}}, \frac{1}{d_{3,2}}, \dots, \frac{1}{d_{3,n}} \right] = \begin{bmatrix} A_1 \cdot \dfrac{1}{d_{3,1}} & A_1 \cdot \dfrac{1}{d_{3,2}} & \cdots & A_1 \cdot \dfrac{1}{d_{3,n}} \\ A_2 \cdot \dfrac{1}{d_{3,1}} & \ddots & & \vdots \\ \vdots & & \ddots & \vdots \\ A_m \cdot \dfrac{1}{d_{4,1}} & \cdots & \cdots & A_m \cdot \dfrac{1}{d_{3,n}} \end{bmatrix} \tag{61}$$

The transient part depends on the thermal conductivity k_{reg} [W·m⁻²·K⁻¹] which in turn is a function of temperature and depth (see section 4.2.2). For the first calculation of the $G_{L,reg}$ values [W·K⁻¹] a temperature of 300 K is assumed. The depth nodes $n = 1 \dots 3$ are calculated with thermal conductivity values for regolith soil k_{soil}, and depth node $n = 4 \dots 10$ with coarse regolith k_{reg}. Hence, the temperature-dependent part $G_{L,reg,temp,m,n}$ [W·K⁻¹] is:

$$G_{L,reg,temp,m,n} = \begin{bmatrix} k_{soil,1,1} & k_{soil,1,2} & \cdots & k_{reg,1,n} \\ k_{soil,2,1} & \ddots & & \vdots \\ \vdots & & \ddots & \vdots \\ k_{soil,m,1} & \cdots & \cdots & k_{reg,m,n} \end{bmatrix} \tag{62}$$

In order to simplify the computation demand both matrices are converted into vectors, similar to the conductor matrix.

$$G_{L,reg,stat,m,n} = (G_{L,reg,stat,1,1} \quad \cdots \quad G_{L,reg,stat,m,n})^T \tag{63}$$

$$G_{L,reg,temp,m,n} = (G_{L,reg,temp,1,1} \quad \cdots \quad G_{L,reg,temp,m,n})^T \tag{64}$$

In addition to the empirical relation for plain surfaces (equation (41), section 4.2.2), the regolith density can also be expressed as a function of slope angle. Densities at different slope angles were measured during Apollo 15 and 17. According to (Mitchell et al. 1972) and (Houston et al. 1974) the slope dependency can be represented by the following equations:

$$\rho_{reg} = \rho_0 + \rho^* \cdot ln(z + 1) \tag{65}$$

In this empirical equation z is the depth in [cm]. In Table 5-1 slope angle depend values for ρ_0 and ρ^*, are given. The values in the first row are mean values for all measurements during Apollo 15 to 17. The values in the second row were gathered on the slopes of the Apennine front (Apollo 15), at Station 2. According to the Apollo 15 Mission Handbook the slope angle at this station was approximately $\alpha_{sl} = 13°$ (Jones et al. 1995-2012).

Table 5-1: Characteristic values for regolith **depending on slope angle α_{sl} (Mitchell et al. 1972; Houston et al. 1974), *unit is not given in original text.**

ρ_0 [g·cm⁻³]	ρ^* [g·cm⁻³]*	Remarks	Source
1.27	0.121	Apollo 15 – 17	(Houston et al. 1974)
0.80	0.225	Apollo 15, Apennine front ($\alpha_{sl} = 13°$)	(Mitchell et al. 1972)

Under the assumption that density follows an exponential law, the values for ρ_0 and ρ^*, can be calculated with respect to the slope angle α_{sl} with:

$$\rho_0 = exp(-0.0356 \cdot \alpha_{sl} + 0.239) \tag{66}$$

$$\rho^* = exp(0.0478 \cdot \alpha_{sl} + 2.112) \tag{67}$$

Equations (66) and (67) can only be used in a slope angle range between 0° and 13°. All surface elements with slope angles $\alpha_{sl} > 13°$ are assumed to have the same density distribution as a slope with $\alpha_{sl} = 13°$. Regolith will slide down a slope and reveal the underlying bedrock at angles of repose between 35° and 37° (Hovland and Mitchell 1972; Mitchell et al. 1972).

5.2.1.4 Boulder Model

Boulders are chunks of bedrock material excavated by impact events on the Moon (see section 4.2.2). An impactor creates a crater and excavates material that is either dispersed as small grained regolith or as boulders of different sizes. Boulders have very rough shapes due to their process of creation. The "erosion" caused by micrometeorites or thermal cycling is very slow and not enough to take the edges of the boulders. A boulder of 1 kg mass has survival time of 10 million years on the lunar surface (Jaumann et al. 2012). The coverage with regolith is currently not part of the *TherMoS* simulation.

In the *TherMoS Boulder Model* the diameter of a boulder D_B depends on the crater diameter D_C according to equation (46). It is also possible to enter D_B manually. The boulders are created from a cloud of random numbers. A MATLAB® function envelopes the random numbers and creates a convex body consisting of triangular surfaces. The user can either create boulders by entering the maximum boulder diameter $D_{B,max}$ and its position on the topography, or let them be created randomly. The translation of a boulder to its dedicated position takes into account the local surface. The lowest points of the boulder are level with the surface. In this way no gaps and no overlapping of regolith elements and boulder elements occur, even if the boulder is placed on slopes. The boulder elements facing the regolith are automatically cut away. The

surface normal vectors point towards the inside of the boulder by convention of the MATLAB® function. In the ray tracing algorithm the intersection is determined based on normal vectors. Thus the normal vectors are switched to point outwards. The volume of the enclosed space is calculated automatically. The random placement of boulders is related to bedrock material and parent crater size. 5 % of the crater volume is dispersed as boulders (Cintala et al. 1982). Thus the number of boulders increases as long as the total volume of boulders is smaller than 5 % of the crater volume. In general, 65 % of all boulders lie inside the crater in highland regions and 90 % of all boulders are within 1.5 radii. In mare craters 10 % of all boulders lie within the crater, 65 % of all boulders lie within 2 radii, and 90 % lie within 5 radii. Larger boulders lie closer to the crater center. Figure 5-10a shows the implemented distribution of boulders around highland (left) and mare (right) crater in the *TherMoS Boulder Model* (Sievers 2012). It was assumed that no crater smaller than $0.4 \cdot D_{B,max}$ should be used in the *Boulder Model*. Boulders larger than 0.5 $D_{B,max}$ are inside the crater, boulders between 0.4 and 0.9 $D_{B,max}$ are on the slopes outside the crater rim within 2 radii. The boulders within 5 radii encountered around mare crater are assumed to be in a narrow size range between 0.4 and $0.5 \cdot D_{B,max}$.

In parallel to the regolith surface elements, the geometric properties of the boulder are calculated and stored in a MATLAB *struct* as a global variable. The geometric properties are area, center of area, distance to the center of the boulder, normal vector, and slope angle.

In Figure 5-10b the thermal node model of a random boulder is depicted. D_B is the maximum boulder diameter and d_A is the distance between the center of area of the surface and the geometrical boulder center. The thermal nodes are marked as dark points. The absorbed solar heat flux depends on the incident angle. The emitted infrared heat flux is only a function of the temperature of the emitting surface element. The absorbed infrared heat flux depends on the view factor between boulder surface element and nearby regolith surface elements. Work performed by (Roelof 1968) showed that the conductive connection between boulder and regolith can be neglected for boulders with $D_B > 1$m.
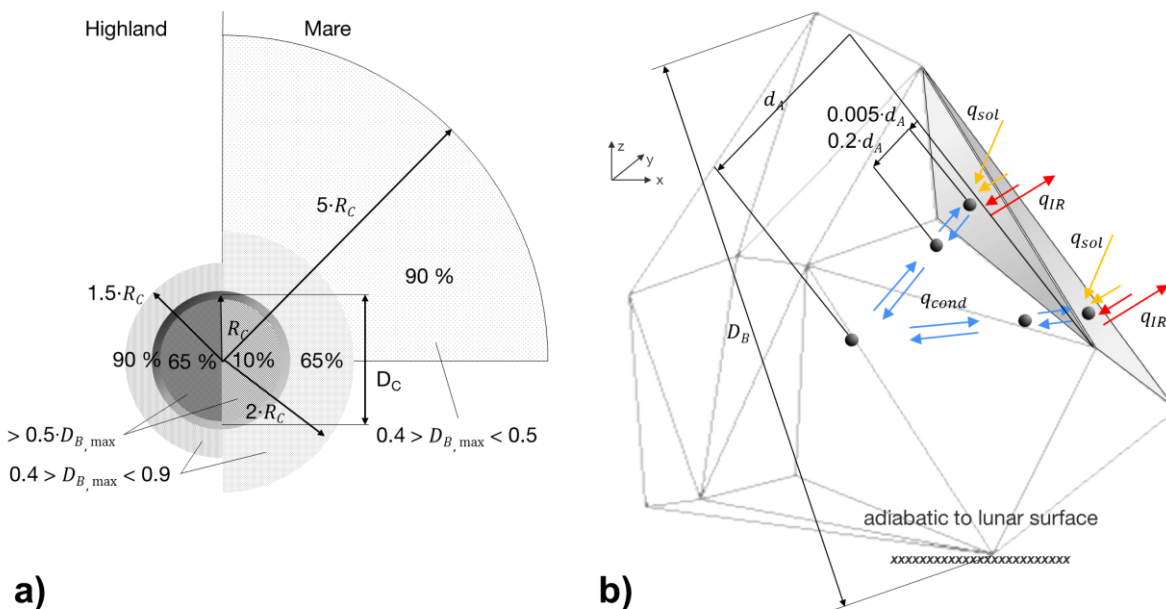
Figure 5-10: a) Distribution of boulders around craters in highland and mare regions, and b) Thermal node model for a random boulder. Only two surface nodes and their subsequent nodes are shown.

The *Boulder Model* prepares the conductors and capacitors for the processing in the *Solver Module*. Different from the *Regolith Model* thermal conductivity, density, and heat capacity do not depend on the distance to the surface but on the local material. In Table 5-2, the used generic values for lunar *mare* and

highlands are presented. Because each boulder is created from random numbers, the number of surface elements differs. The general procedure is the same for each boulder.

The layer thickness for the lumped parameter is fixed to 0.005 m for the surface node and $0.2 \cdot d_A$ for the intermittent node. The volume for the nodes are calculated under the assumption that the cross sectional area is equal to the surface element area for the upper node and 80 % of the surface elements area for the intermittent node. The volume of the core is the difference between the entire boulder volume minus the sum of all surface and intermittent nodes. Thus, for i boulder surface elements the conductive interface between surface node and intermittent node $G_{L,B,1}$ and between intermittent and core node $G_{L,B,2}$ are given with

$$G_{L,B,1,i} = \left(A_{B,i} \cdot \lambda_B\right)/d_{B,1} \tag{68}$$

$$G_{L,B,2,i} = \left(0.8 \cdot A_{B,i} \cdot \lambda_B\right)/d_{B,2} \tag{69}$$

With $d_{bould,1}$ and $d_{bould,1}$ [m] representing the distances between surface node and intermittent node and intermittent node and core, respectively. The conductors are rearranged in a single vector in the same manner as in the *Regolith Model*:

$$G_{L,B} = \left(G_{L,B,1,1} \quad \cdots \quad G_{L,B,1,i} \quad G_{L,B,2,1} \quad \cdots \quad G_{L,B,2,i} \quad 0\right)^T \tag{70}$$

The last element is zero since the vectors of capacitor and conductor must have the same length. The capacitor for boulder surface nodes, for intermittent nodes and the core are calculated and stored in one single vector:

$$C_{B,1,i} = A_{B,i} \cdot 0.005 \cdot \rho_B \cdot c_p \tag{71}$$

$$C_{B,2,i} = 0.8 \cdot A_{B,i} \cdot 0.2 \cdot d_A \cdot \rho_B \cdot c_p \tag{72}$$

$$C_{B,core} = V_B - \left(\sum_{n=1}^{i} V_{B,1,i} + \sum_{n=1}^{i} V_{B,2i}\right) \cdot \rho_B \cdot c_p \tag{73}$$

$$C_B = \left(C_{B,1,1} \quad \cdots \quad C_{B,1,i} \quad C_{B,2,1} \quad \cdots \quad C_{B,2,i} \quad C_{B,core}\right)^T \tag{74}$$

In equations (73) and (74), $V_{bould,1}$ is the volume for the surface nodes and $V_{bould,2}$ is the volume for the intermittent nodes.

Table 5-2: Material properties used for *mare* and *highland* boulders [values taken from (Ahrens op. 1995) for terrestrial basalt and granite].

Value	*Material*	ρ_{bould} [kg·m⁻³]	$c_{p,bould}$ [J·kg⁻¹·K⁻¹]	k_{bould} [W·m⁻¹·K⁻¹]
Mare Boulder	Basalt	2,990	1,000	1
Highland Boulder	Granite	2,640	890	5

The last step in the process is to combine all created boulders in one capacitor and one conductor vector. The elements are finally stored in the sequence: surface nodes; depth nodes; core nodes.

5.2.1.5 *Crater Model*

In section 4.2.2 crater shapes and their origination process was presented. Large craters of several tens to hundreds kilometer of diameter are represented in the used Kaguya data set. Thus the *Crater Model* only accounts for bowl shaped primary craters with a diameter $D_C \leq 20$ km. The crater nomenclature is depicted in figure Figure 5-11. The crater morphology can be described by the empirical equations given by (Hörz and Cintala 1997):

$$h_c = 0.196 \cdot D_C{}^{1.01} \tag{75}$$

$$h_r = 0.036 \cdot D_C{}^{1.014} \tag{76}$$

$$w_r = 0.257 \cdot D_C{}^{1.011} \tag{77}$$

The applicability of equations (75) to (77) is restricted to bowl shaped craters with $D_C \leq 20$ km. D_C [km] is the crater diameter, h_C [km] is the height of the crater from the bottom to the rim, h_r [km] is the crater rim height above the undisturbed plain surface and w_r is the width of the regolith layer displaced around the crater rim during the impact event.
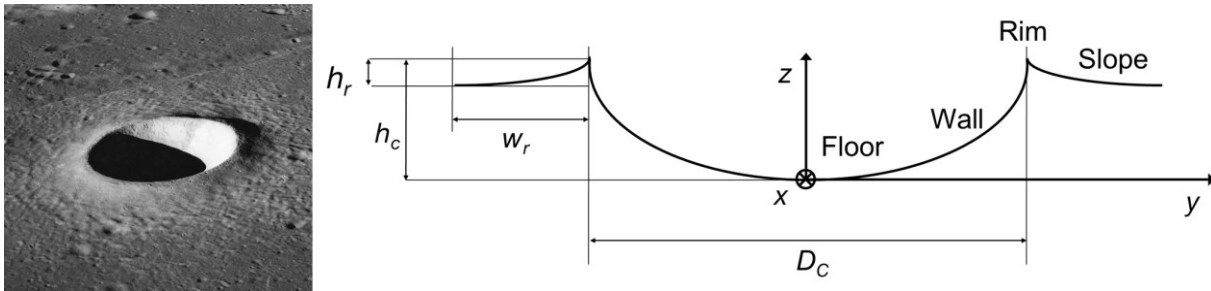
Figure 5-11: Left) Photograph taken during Apollo 10 shows Hypatia, a typical bowl shaped crater on the Moon (NASA), and Right) nomenclature for the parts of a rover used for the Crater Model [based on (Houston et al. 1974), reproduced from (Hager et al. 2011)].

The bowl shaped primary craters have an almost parabolic wall and crater slope (Neukum et al. 1975) at the end of the cratering process. The floor is filled with regolith, pebbles and breccias. Crater floor, wall, rim and slope are covered with boulders of different sizes. Based on the empirical equations (75) to (77) the z-coordinate can be modeled by the following equations:

$$z_{C,w} = 0.784 \cdot D_C{}^{-0.99} \cdot y_{C,w}{}^2 \tag{78}$$

$$z_{C,sl} = 0.545 \cdot D_C{}^{-1.08} \cdot y_{C,sl}{}^2 \tag{79}$$

with $z_{C,w}$ and $z_{C,sl}$ being the z-coordinates of the points along the radiating axes. The radiating axes are y- and x- axis in Figure 5-11. The indices sl = slope and w = wall indicate whether the z-coordinates are inside or outside the crater rim according to the nomenclature in Figure 5-11.
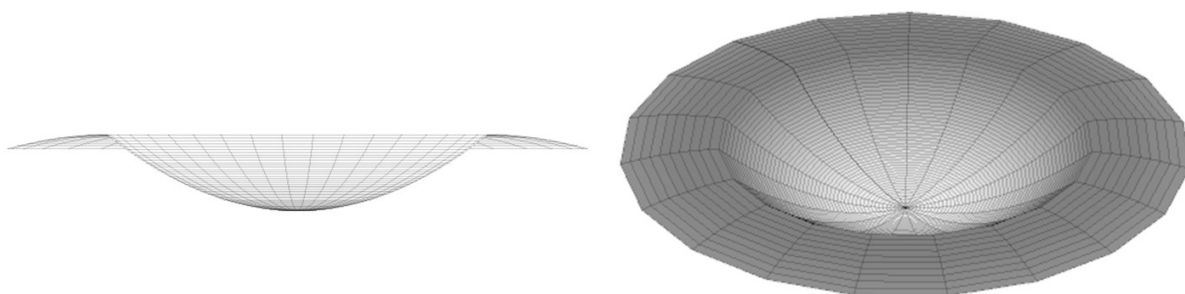
Figure 5-12: Cross sectional and isometric view of a crater generated with the *TherMoS Crater Model*.

The thermal properties of the crater elements are calculated in the same manner as those for regular regolith surface elements. The geometric and thermal properties of the craters' surface elements are combined in a MATLAB® *struct* and stored as global variable.

Besides superimposing boulders and craters, it is also possible to model the overlay of craters. A simulation approach for the overlay of craters was created and included into *TherMoS*. Its implementation and results can be found in (Sievers 2012). Because the functionality was not used for the results created in this work, it is not discussed further.

5.2.1.6   Orbit & Position Module

The angle of incident for the incoming solar heat fluxes governs the temperatures of the lunar surface. It is crucial to determine azimuth and elevation of the Sun throughout a lunar day for the location of interest. In addition, the local slope angle will alter the incoming heat fluxes. In order to predict heat fluxes for any given mission scenario the celestial dates were integrated into the *Orbit & Position Model*.

The lunar orbit is not symmetric and so its orbital parameters – inclination, semi-major axis, eccentricity, argument of perigee, and right ascension of the ascending node – are not constant but are subject to a number of perturbations. The largest impact has the Suns' gravitation. It has slightly more than twice the Earth's gravitational influence, and thus is responsible for change in orbital parameters (Weigert et al. 2009). The gravitational pull of the Sun leads to a constant perturbing acceleration acting on the Moon towards the Sun at all times. The Moon is in a synchronous rotation with Earth, it nearly always keeps the same side faced towards the Earth, but because of the optical and physical libration approximately 59 % of the lunar surface can be observed from Earth (Tattusch 2011).

In Figure 5-13 the three coordinate systems, important for the calculation of the Moons' position vector, are shown. All are right handed coordinate systems. The heliocentric coordinate system *XYZ* is defined with the *X*-axis pointing at the vernal equinox Υ, the *Z*-axis is normal to the ecliptic plane pointing towards the northern hemisphere. The *Y*-axis completes the right handed coordinate system. The geocentric coordinate system is also defined with *I* pointing towards the vernal equinox, *K* pointing north and normal to the ecliptic plane. *J* completes the right handed coordinate system. The selenocentric coordinate system *xyz* rotates with the Moons' orbit. The z-axis points normal to the Moons' orbital plane, the y-axis points in the direction of motion in the orbit plane and the x-axis points towards the intersection of the lunar equator and 0-meridian of the Moon. This intersection also marks the mean center of the Moons' disk visible from Earth.The vector between the Moons' center to the intersection of lunar equator and 0-meirdian does not always point at the same position in the Earth-Moon system, the Moon liberates.
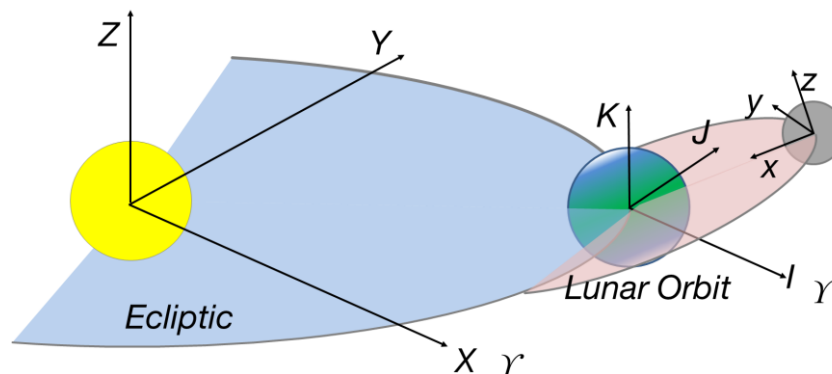
Figure 5-13: The heliocentric coordinate system *XYZ*, the geocentric coordinate system *IJK* and the seleno-centric coordinate system *xyz*.

In Figure 5-14 the topocentric selenographic coordinate system *N'W'Z'* is depicted. On the left the *N'W'Z'* coordinate system is shown relative to the selenographic coordinate system. The selenographic latitude λ_{lat} is the angle between the lunar equator and the circle of latitude. As on Earth, there are +90° of latitude north and -90° of latitude south. The longitude λ_l is counted from the 0'-meridian. In east-west direction there are 360°, with 180° to the east and 180° to the west. On the right side of Figure 5-14, the azimuth and elevation angles are shown in the topographic selenographic coordinate system. The azimuth α_{az} is the angle between north and the projected sun angle counted eastward. The elevation ε_{el} is the angle between the sun angle and its projection into the local horizon, that means the *W'-N'* plane.
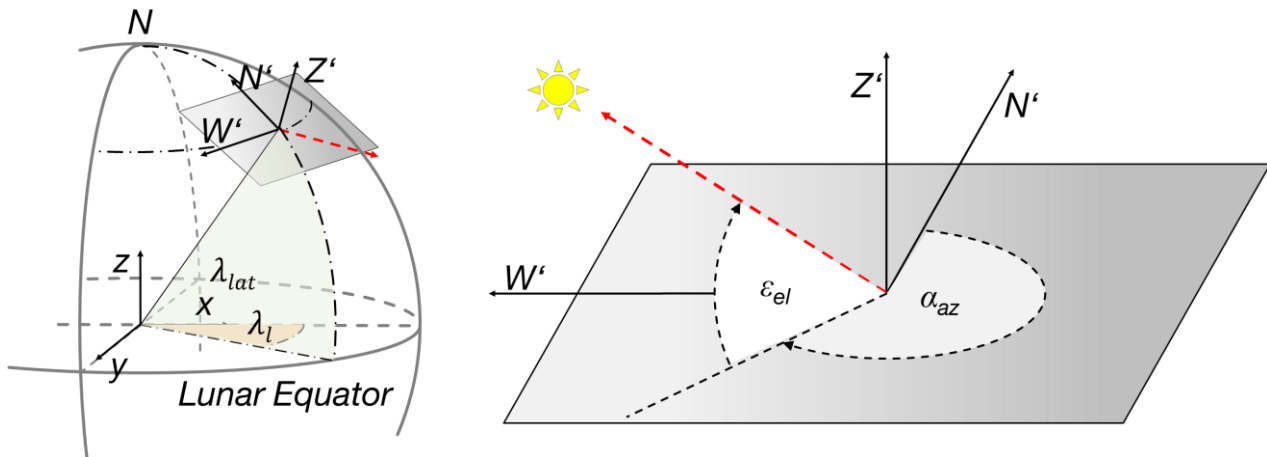
Figure 5-14: Left) Position of the local selenographic coordinate system in the Moon coordinate system, and Right) Azimuth and Elevation in the local selenographic coordinate system.

The model implemented in *TherMoS* is based on the '*Variations Séculaires des Orbites Planétaires 2000*' version A (VSOP2000A) (Moisson and Bretagnon 2001). VSOP2000A was developed at the Institute de mécanique céleste des Observatoire de Paris. It is a planetary model which is used to calculate the heliocentric position of the Earths' center and the geocentric position of the Moons' center at any given time. This model is complemented by the calculation of the optical libration angle [Taylor et al. 2010] and an algorithm to determine the visibility of the Sun in percent. The VSOP2000A has an offset of less than 500 m compared to the DE403 which is the standard theory developed by the Jet Propulsion Laboratory (JPL) and used in the satellite tool kit (STK®). Other than for DE403 the VSOP2000A raw data are openly available through the Systèmes de Référence Temps-Espace (SYRTE) (Dimarc 2009). The VSOP2000A contains the series terms for all planets of the solar system, the Moon and the Earth-Moon-barycenter. The calculation of planet positions is based on a series expansion. For example, in case of the *X*-coordinate of a planet in the heliocentric coordinate system the expression is:

$$X = \sum_{i=0}^{8} t_{bar}^{i} \cdot (A \cdot \sin \phi_{VSOP} + B \cdot \cos \phi_{VSOP}) \tag{80}$$

Here t_{bar} is the current barycentric dynamic time in Julian years based on J2000.0, i is the number of series terms taken into account. It stretches from 0 to 6 for Earth and 0 to 8 for the Moon. A and B are coefficients given in the VSOP2000A data set. ϕ is the sum of perturbations caused by the planets, the Moon and certain asteroids and minor planets (Tattusch 2011). The *Orbit & Position Model* also takes into account the optical libration of the Moon (see for example Taylor et al. 2010).

Beside the Suns' azimuth and elevation, the *Orbit & Position Model* calculates its topmost and lowermost point, the percentage of the visible solar disc, and the azimuth and elevation of the Earths' center.

Some simplifications were made in the *TherMoS Orbit & Position Model*. The physical libration is neglected due to its very small amplitude (Weigert et al. 2009) and the Moon is approximated by a sphere with a constant radius and not modeled as the ellipsoid it truly is. The planets velocity in three dimensions was simplified to two dimensions and solved with the *Vis-Viva* equation (Tattusch 2011).

The current implementation allows calculating azimuth and elevation for any time interval, beginning with seconds. Since the series expansion is demanding in terms of computation power, the supporting points are calculated for every hour. The values in between the supporting points are interpolated to match the solver time step. This adaptation is performed in the *Solver Module*.
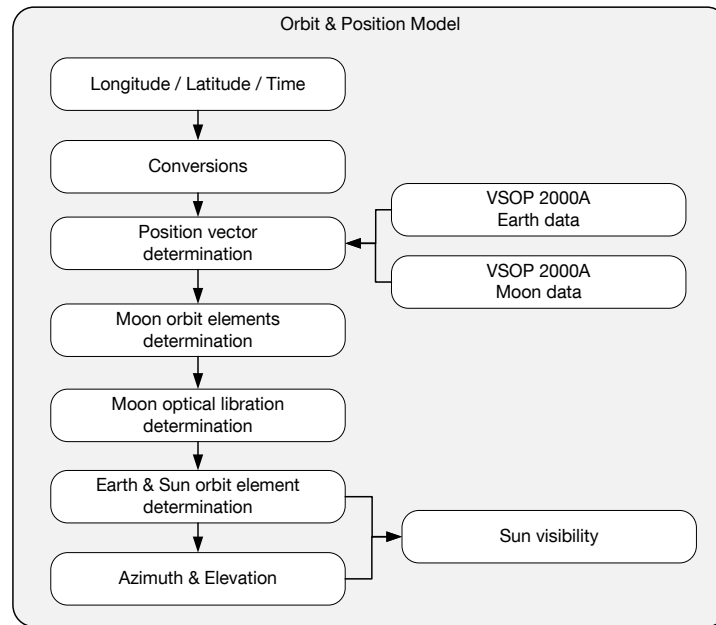
Figure 5-15: Flow diagram of the process that leads to the calculation of azimuth and elevation for a given longitude, latitude and time on the lunar surface.

Verification:

The calculation of the position of the Moon with respect to the Sun produced a maximum error of 47.24 km total compared to data calculated with online tools from the Jet Propulsion Laboratory (JPL) and the Institut de Méchanique Céleste et de Calcul des Éphemerides (IMCCE).

The azimuth and elevation results were compared to data obtained with the Satellite Tool Kit 9® (STK). The differences between the calculated and the STK data are smaller than 0.5 % for azimuth and elevation angles. Figure 5-16 shows the deviation of azimuth between STK and the *TherMoS Orbit & Position Model.* For the course of the year 2011 the deviation is not more than 1.15° (Tattusch 2011).
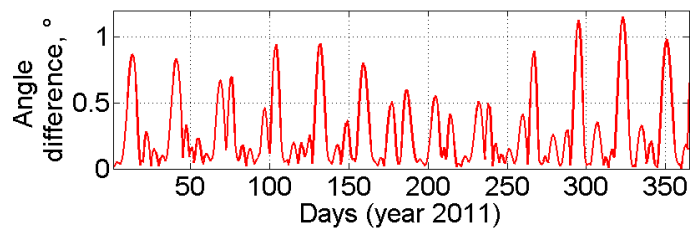
Figure 5-16: Difference of azimuth angle between *TherMoS Orbit & Position Model* and the Satellite Tool Kit 9 (Tattusch 2011).

5.2.2 Spacecraft Module

The purpose of the *Spacecraft Module* is to provide the geometrical representation of a spacecraft and to prepare its path along a given topography. The geometrical representation follows the same way as in the *Landscape Module*. The geometry is composed of a cluster of nodes which are connected by triangular surface elements. The nodes are a representation of each grid point in a body fixed coordinate system. The points for each direction in the coordinate system are stored in a vector. The triangular surface elements are produced by a Delaunay triangulation and stored in a matrix. Each surface element of an object represents an individual data point and possesses a unique number for indexing. If more than one object is present, the newest will yield to the numeration of the previous, i.e. surface-counting continues progressively.

In Figure 5-17 the structure of the *Spacecraft Module* is depicted. Two ways for the integration of space-craft geometries are currently integrated. It is possible to either create new spacecraft structures from primitive shapes or to load stored geometries. The primitive shapes are planes, cubes, spheres, and cylinders. The primitive shapes can be combined, parts can be cut away, and the shapes can be translated and rotated to form new objects. The primitive shapes are composed of points and triangular surface elements, which are stored in vectors and matrices. The last step in the creation process of primitive bodies is to check the direction of normal vectors. The normal vectors must point outward for the ray tracing algorithm (see section 5.2.4). Finally, the generated geometry is saved as comma separated value (.csv) or MATLAB® .mat files. Other formats such as .erg files, as exchange format with ESATAN-TMS®, are also possible. The primitive shapes can be created in *TherMoS*, more complex shapes must be produced in appropriate CAD software.
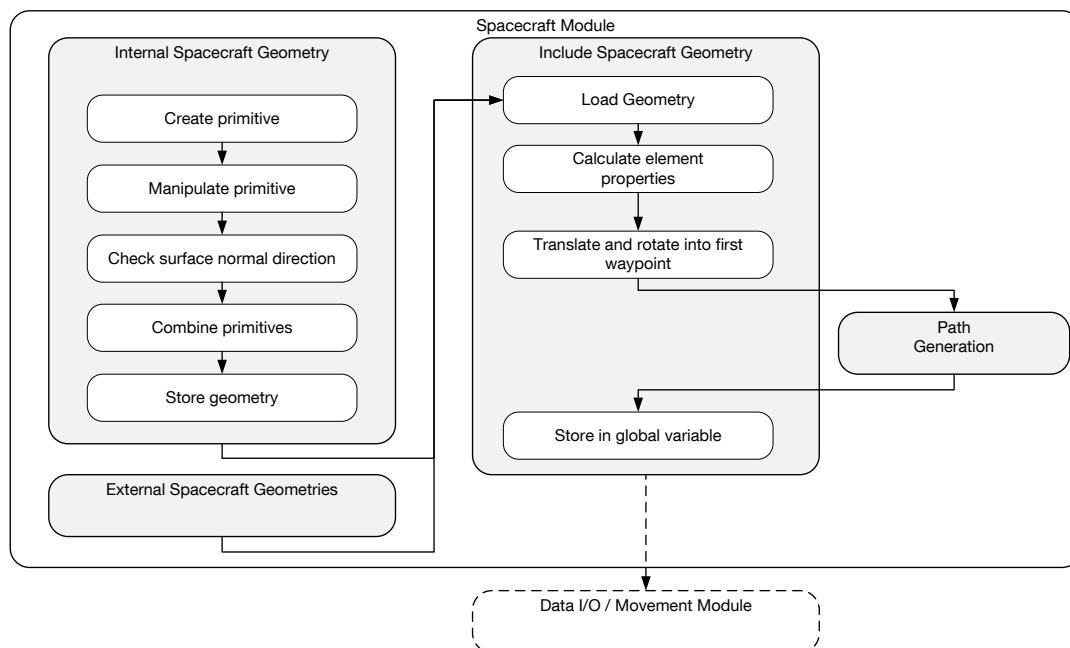
Figure 5-17: Structure of the *Spacecraft Module*.

Independent of the way the geometry was created, it needs to be extracted from saved data and transferred into the *TherMoS Spacecraft Module*. The supported data types are .bdf (NASTRAN), .iges (from computer aided design tools such as CATIA®), .erg (from ESATAN-TMS®) as well as .csv and .mat. The data consisting of points and triangular surfaces is transformed into a MATLAB® *struct*. Once the data is transferred to MATLAB®, element properties are calculated for each surface element and stored to the MATLAB® *struct*. The properties are area, center of area, normal vector, and the distance to the origin of the body fixed coordinate system. In a last step, the geometry is rotated and translated depending on the used path and the local topography.

The path is a combination of waypoints and actions performed at the waypoints. The flow diagram in Figure 5-18 depicts the preparation of a path. In case of static calculations, the first waypoint represents the position of the sample body for the entire simulation. For each further waypoint a velocity needs to be entered. With the position of the last and the new waypoint the vector between both waypoints is calculated. Together with the velocity the increment per time step is calculated. Additionally, the rotation angle for the geometry is determined.
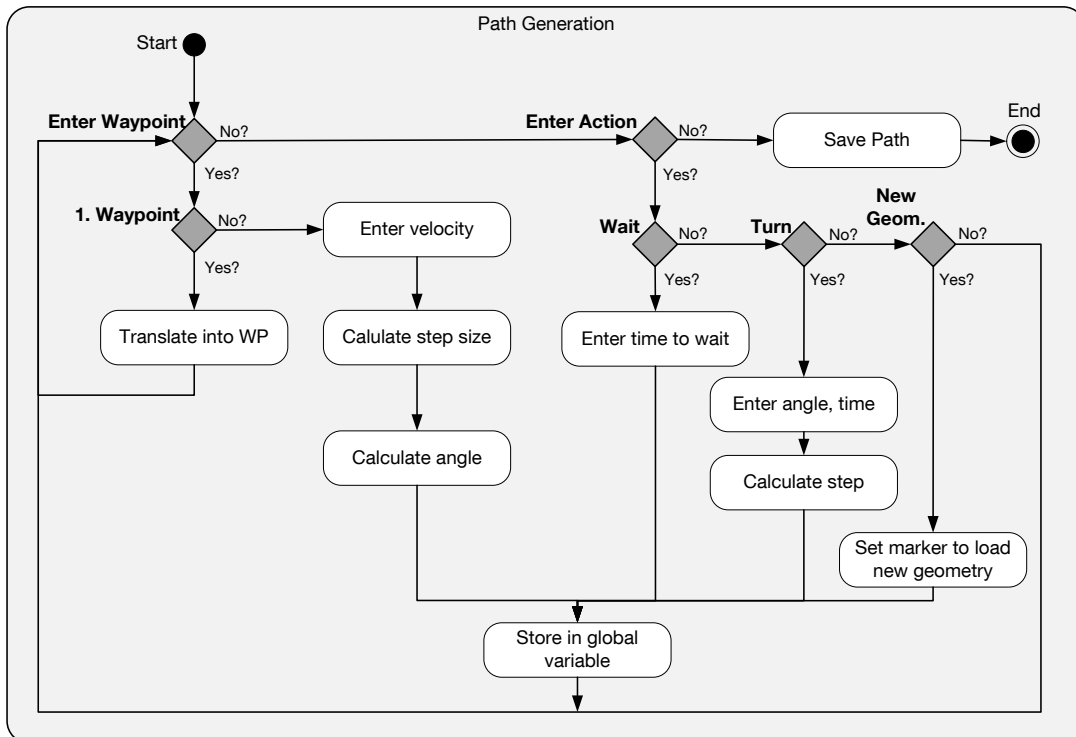
Figure 5-18: Flow diagram for the generation of a path in the *TherMoS Spacecraft Module*.

If a certain task shall be performed at a given waypoint, one can distinguish between waiting, turning, and a change in body posture. The 'wait' command requires the sample body to remain at a certain position without moving any further. The 'turn' command requires an angle and a time input. This γ-angle is the amount of degree the rover shall be rotated around the body fixed *z*-axes. Based on angle and time, the step width for the rotation per time step is calculated. The last possible command option is to load a different geometry. This otpion is applied if mere rotations or translations of the entire geometry are not sufficient to represent the action, such as the bending and erecting of the spacesuit model (see 6.1.2 and 6.1.3). In all cases, the time for each step is added to a time vector which is necessary for the *Movement* function. Finally, the information about entire time, duration between two waypoints or actions, the *x,y,z* translations and γ rotation are stored in the global spacecraft variable.

The global spacecraft variable is accessible for the *Movement* function. The thermal properties for the sample body are entered and adjusted after the heat fluxes were determined based on geometry, path, and ray tracing.

5.2.3 Solver Module

The *Solver Module* is the backbone of the entire simulation. The *Solver Module* prepares the heat balance for each thermal node in the landscape module, calculates the temperature for each time step and manages the exchange of temperature and heat fluxes with the ray tracer. In Figure 5-19 the structure and basic data exchanges of the *Solver Module* are shown. The static pre- and post-processing enclose the transient solution. Before the transient solution is started, the static calculations in the preprocessing section are performed. In the next step, the transient processing performs all steps from *a)* to *f)* in each loop. Mainly the numerical calculations and the call to the ray tracer are prepared and executed. The post-processing section stores the final data and calls the visualization.
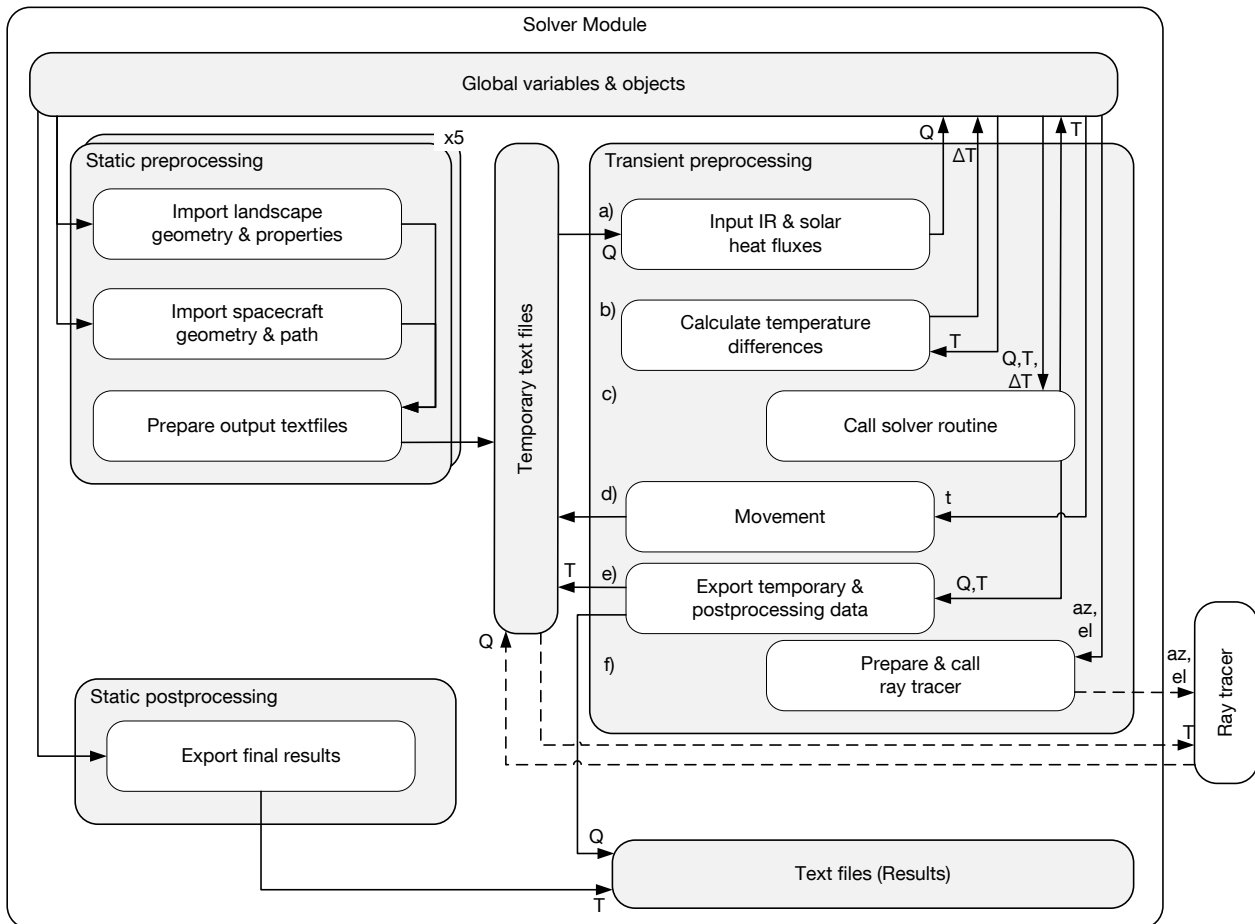
Figure 5-19: Internal relations of the *TherMoS Solver Module*.

5.2.3.1 Preprocessing

The *Static Preprocessing* has five different possible cases. The case is defined by the configuration of the *Landscape Module* chosen by the user. The different cases are 1) Kaguya data, 2) plane landscape, 3) crater without boulders, 4) crater with boulders, and 5) manually placed boulders. At first the landscape geometry is included. This means vectors for initial and current temperature, for temperature differences and heat fluxes are prepared, and memory is allocated. For a landscape with m surface nodes and n depth nodes each, the vectors have a size of $(m \cdot n, 1)$. The same happens subsequently with the sample body. Finally, the variables are used to generate empty text files with appropriate size. The text files can be accessed by the transient processing and the ray tracing.

In Figure 5-20 the nomenclature for the landscape module is shown as an example. Each layer of nodes is written as a vector. The vectors are combined to form one large vector. In this way the heat load terms $\vec{Q}_{IR}, \vec{Q}_{sol}, \vec{Q}_{L,1}, \vec{Q}_{L,2}, \vec{Q}_{int}$, the capacitor C and the conductors G_L are vectors that have the format $\vec{v} = (v_1, v_2, ..., v_m)$ with $j = m \times n$. The surface nodes are the only ones to receive heat from the environment by radiation $(\vec{Q}_{IR}, \vec{Q}_{sol})$ and only the lowermost set of nodes receive heat from the interior of the Moon $(\vec{Q}_{int})$. The intermediate nodes pass heat via conduction to their neighbors. Per definition the conductive heat that is passed in –z-direction is called $Q_{L,1}$ [W] and the heat in +z-direction is $Q_{L,2}$ [W]. The heat balance equation for each node has the form:

$$\Delta T = \left(\vec{Q}_{sol} + \vec{Q}_{IR} + \vec{Q}_{int} + \vec{Q}_{L,1} + \vec{Q}_{L,2} \right) \cdot \frac{1}{\vec{C}_{reg}} \tag{81}$$

This form based on the fundamental heat transfer equation, and the approach to use lumped parameter nodes with capacitors and conductors. In this way, only vectors have to be summed up and be divided element-wise by the capacitor. This nomenclature, and the abilities of MATLAB® to calculated vectors and matrices in an efficient way, is beneficial for the computation time of the *TherMoS* simulation.
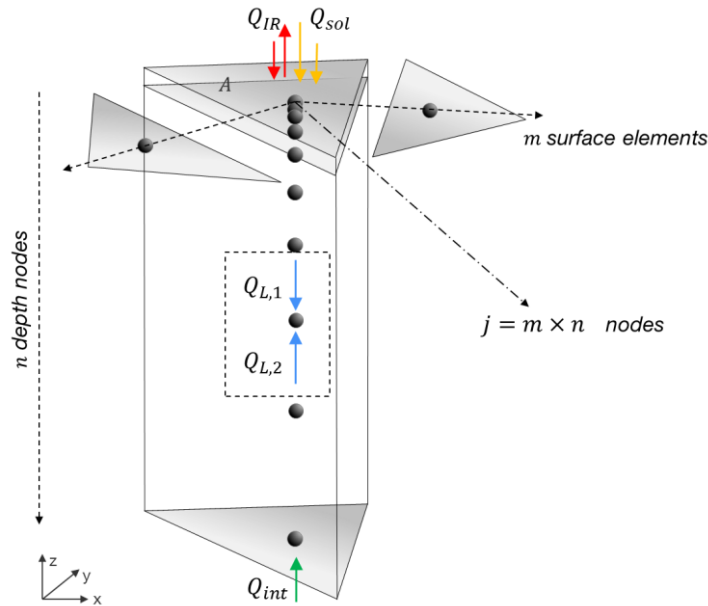
Figure 5-20: Nomenclature for the preparation of nodes in the solver preprocessing part of the Solver Module.

The following equations show the allocation of values and zeros to the heat vectors.

$$\left.\begin{array}{l} \vec{Q}_{sol,i} \\ \vec{Q}_{IR,i} \end{array}\right\} \begin{array}{l} = 0 \\ \neq 0 \end{array} \quad for \quad \begin{array}{l} i = m + 1 \dots j \\ i = 1 \dots m \end{array} \tag{82}$$

$$\left.\vec{Q}_{int,i} \right\} \begin{array}{l} = 0 \\ \neq 0 \end{array} \quad for \quad \begin{array}{l} i = 1 \dots (n-1) \cdot m \\ i = 1 \dots [(n-1) \cdot m] + 1 \dots j \end{array} \tag{83}$$

$$\left.\vec{Q}_{L,1,i} \right\} \begin{array}{l} = 0 \\ \neq 0 \end{array} \quad for \quad \begin{array}{l} i = 1 \dots [(n-1) \cdot m] + 1 \dots j \\ i = 1 \dots (n-1) \cdot m \end{array} \tag{84}$$

$$\left.\vec{Q}_{L,2,i} \right\} \begin{array}{l} = 0 \\ \neq 0 \end{array} \quad for \quad \begin{array}{l} i = 1 \dots m \\ i = m + 1 \dots j \end{array} \tag{85}$$

The determination of $\vec{Q}_{IR}, \vec{Q}_{sol}$ will be discussed in section 5.2.4. The process to calculate the conductive heat transfer is part of the *Solver Module*.

The thermal preprocessing of each node is performed in the *Regolith Model* and in the *Boulder Thermal Model*, respectively. The values for the static conductor for regolith $G_{L,reg,stat,m,n}$, the transient conductor $G_{L,reg,temp,m,n}$ and the capacitor C_{reg} can be obtained from the topography *structs*. In the static preprocessing part the static and transient conductors are combined to have the total conductor for the first time step. Since both values are stored in vectors with m elements, the product must be calculated element-wise:

$$G_{L,reg,m,n} = G_{L,reg,stat,m,n} \cdot G_{L,reg,temp,m,n} \tag{86}$$

Another important step performed during the preprocessing is the adaptation of azimuth and elevation angles. The time step from hours has to be matched with the solver time step in seconds. Thus the values are interpolated.

5.2.3.2 Solving routine

The *Solving Routine* hosts the operations and calculations that are performed in each time step. The final outcome of the solving routine in each time step is to calculate the temperature, balanced infrared, and accumulated solar heat flux for each thermal node. The temperature T [K] and the temperature difference to the prior step ΔT [K] is calculated by balancing the heat that is going in and out through the lumped parameter node boundaries. Calculating T and ΔT for each node also involves calling the ray tracer and feed it with the necessary data. Since the ray tracer also relies on text files, the content of the text files has to be updated in every time step, too. Some of the parameters that are used to determine heat fluxes are temperature dependent thus must also be adopted in each time step. Futhermore, the geometry has to be updated according to the path and activities performed along its way. As depicted in Figure 5-19 the solving routine follows six consecutive steps:

a) In the first step, the radiative heat fluxes determined by the ray tracer are loaded from text files. The ray tracer writes the results to these text files at the end of its processing. Because the ray tracer outputs heat flux densities q_{sol}, q_{IR} [W·m⁻²] the heat energy Q_{sol}, Q_{IR} [W] are calculated by an element-wise calculation:

$$\vec{Q}_{sol,k} = \dot{Q}_{sol,k} \cdot A_m \tag{87}$$

This calculation is performed for solar as well as infrared rays, for the topography as well as the sample body. The optical properties α and ε can be multiplied with the incoming heat flux, if appropriate.

b) Based on the prior time step, the temperature difference between adjacent nodes is calculated. In case of the first time step, the initial temperatures are used. The temperature is loaded from the MATLAB® global variables. Depending on the topographic scene, different calculations are performed. In any case, the principle behind the calculation is the same. Heat fluxes, conductors and capacitors were stored in vectors to simplify their summation. Thus the temperature differences are calculated and stored in the same way:

$$\Delta \vec{T}_L = \begin{bmatrix} T_{m+1} \\ T_{m+2} \\ \vdots \\ T_{2m+1} \\ \vdots \\ T_{m \times n} \end{bmatrix} - \begin{bmatrix} T_1 \\ T_2 \\ \vdots \\ T_{2m} \\ \vdots \\ T_{m \times (n-1)} \end{bmatrix} \tag{88}$$

In this notation ΔT_{cond} represents the temperature differences for heat fluxes directed into the –z direction. According to Figure 5-20, this relies to the conductive heat flux $\dot{Q}_{cond,1}$, which can be calculated with the element-wise calculation:

$$\vec{Q}_{L,1} = G_{L,reg,m,n} \cdot \Delta \vec{T}_{L,m,n} \tag{89}$$

Due to the chosen structure of the topography nodes, the counterpart, meaning the outgoing heat fluxes directed in +z-direction, can be obtained by displacing the values in $\dot{Q}_{cond,1}$ about k elements and inverting their mathematical sign. In this way $\dot{Q}_{cond,2}$ can be obtained with:

$$\vec{Q}_{L,2} = \vec{Q}_{L,2,m+1+i} = -\vec{Q}_{L,1,i} \tag{90}$$

Because there is no further node above the surface elements the first m elements of $\dot{Q}_{Ld,2}$ are 0.

A slightly different approach has to be used for boulders. The number of surface elements is based on random numbers and thus is individual for each boulder. The routine used to determine the $\Delta T_{L,B}$ accounts for this unknown. The temperature difference $\Delta T_{L,B}$ is calculated between boulder surface elements and intermittent nodes, as well as between intermittent nodes and boulder core for each boulder. All $\Delta T_{L,B}$ values are stores in one large vector for all boulders. The first part of this vector stores the tem-

perature difference $\Delta T_{L,B}$ for all surface elements to intermittent node paths and the second part for all intermittent to core paths. u is the total number of surface nodes accumulated over all boulders. The last part of this vector is occupied by zeros in order to have a vector of the same size as the conductor and capacitor vectors.

$$\Delta T_B = (\Delta T_{B,1,1} \quad \cdots \quad \Delta T_{B,1,u} \quad \Delta T_{B,2,1} \quad \cdots \quad \Delta T_{B,2,u} \quad 0 \quad \cdots \quad 0) \tag{91}$$

c) The solving routine uses the heat fluxes calculated and prepared by the preprocessor and calculated in steps a and b, the boundary heat flux from the interior of the Moon and the capacitor. The heat fluxes are summarized and divided element-wise with the capacitor according to equation (81). An ordinary differential equation (ODE) solver with variable step width is used. MATLAB® provides several ODE solvers. Here the *ode23* is used, which is an explicit Runge-Kutta pair.

d) In this step the geometry of the sample body is moved or changed. The relevant values for this part of the *Solver Module* come from the path values stored in the global spacecraft *struct*, as described in section 5.2.2. The possible operations are to follow a path, meet a waypoint, to turn, to wait, and to load a different geometry. The current time step determines which operation is executed:

- *Step)* The current sample object geometry is shifted along the *x*- and *y*- coordinates in a prede-fined time and velocity dependent step. The *z*-coordinate than is interpolated from the local to-pography values.
- *Waypoint)* The initial sample object geometry is reloaded and rotated around the *z*-axes to meet the new heading. Afterwards the sample body geometry is translated into the new waypoint.
- *Turn)* The initial sample object is reloaded, rotated around the *z*-axes and moved into the actual position.
- *Load)* A new sample object geometry is loaded and replaces the former geometry.
- *Wait)* The sample object geometry is not altered.

e) The temperature vector is updated in each time step. One version of the updated temperature vector is stored as global variable to be accessible for MATLAB® files, and a second version is written into a text file that can be accessed by the ray tracer. In user defined intervals the temperatures are appended to a second text file and stored on the hard drive.

f) In the last step, the ray tracing algorithm is called (see section 5.2.4) based on the new values for temperature, geometry, Sun azimuth, and elevation.

5.2.4 Ray Tracing Module

The *TherMoS Ray Tracing Module* is implemented in the NVIDIA OptiX® framework, which provides the background for ray tracing computations on a NVIDIA® graphics processing unit (GPU) (see section 4.4.2). In the forward ray tracing approach, used in TherMoS, the rays are generated in the radiation sources and propagated towards the geometry that is prepared and altered in MATLAB®. It is possible to estimate the incoming and outgoing heat fluxes for each surface element by determining and processing all intersec-tions of the rays with the geometric objects. Figure 5-21 shows the data exchange between the NVIDIA OptiX® framework and MATLAB® for each time step. The ray tracer is initialized by a command from the MATLAB® script. This command also contains azimuth and elevation of the Sun for the current time step. The ray tracer then assembles internally the geometry based on landscape and sample body geometry, loaded from *.csv* files. The landscape and sample body geometries are discretized in OptiX® as triangle meshes, in parallel to the geometry representation described in section 5.2.1. Subsequently, the solar parallelogram is computed, the rays are launched, and their paths are traced. In a second step, the cur-rent temperatures of the surface elements are loaded from the temporary *.csv* files created in MATLAB®, their (infrared) heat flux per surface element is computed and the rays are launched. The hits for solar and infrared rays are stored separately and outputted to *.csv* files.
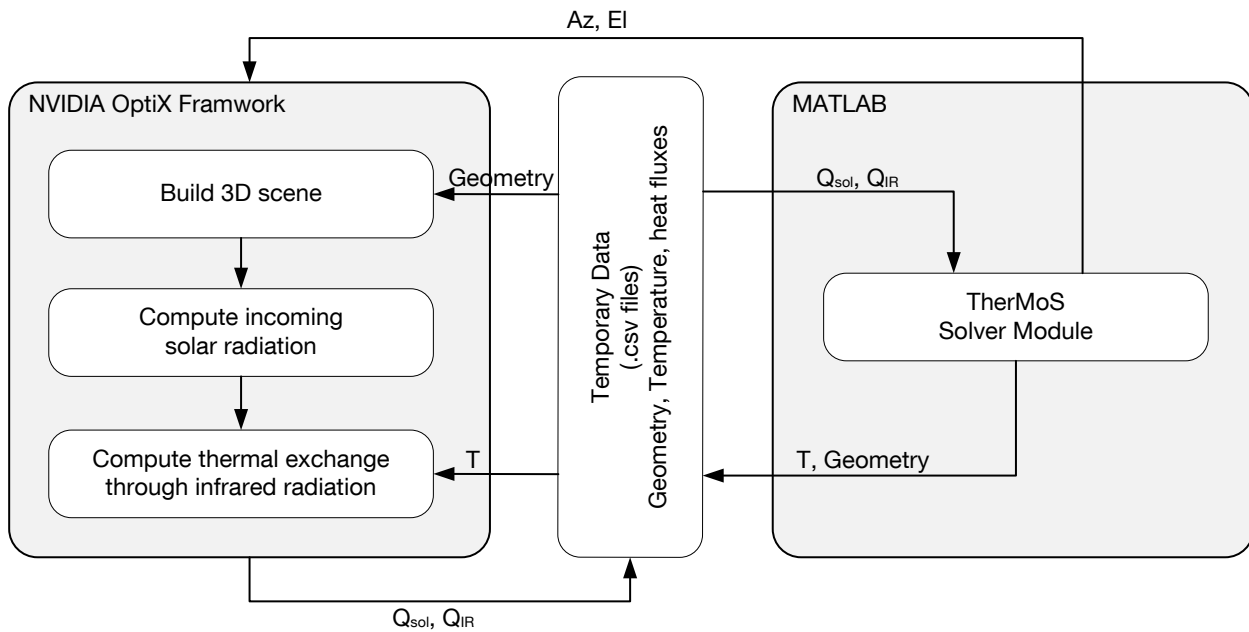
Figure 5-21: Interaction between NVIDIA OptiX® Framework and MATLAB® [based on (Nogina 2012)].

The implemented algorithm distinguishes between solar rays, and infrared rays. The term 'solar rays' is used for rays representing direct light incoming from the Sun parallelogram as well as rays reflected from the landscape geometry. As pointed out in section 4.2.2 the solar constant has a mean value of 1367 [W·m⁻²], and represents an integral over all wavelengths, emitted from the Sun. Hence, each ray represents a portion of the power emitted from the Sun independent of its wavelength. The infrared rays represent "thermal" radiation emitted by lunar surface and spacecraft objects in the infrared range of the spectrum. In the *TherMoS* simulation this means infrared rays for objects with temperatures between 40 and 450 K according to the Stephan-Boltzmann law. The objects are considered to have Lambertian surfaces, as they reflect equally and uniformly in all directions. Every ray hitting the landscape surface elements is partly absorbed and partly reflected diffusely in random directions. The incident point of a ray serves as the origin for reflected rays. This process continues until the incoming ray has either reached its maximum number of reflections or is directed towards space. Depending on the surface that is hit, the power carried by a ray diminishes until a certain threshold is reached and the ray progression is terminated by the algorithm. Solar rays are terminated after the third reflection and infrared rays after the first reflection. Solar rays hitting the spacecraft object are absorbed entirely in the current implementation (Nogina 2012).

The albedo of the lunar surface is in the range of 0.076 to 0.297 (Birkebak and Dawson 1973) for samples from Apollo 11, 12, and 14, as described in section 4.2.2. In the current simulation a solar Albedo of 0.12 is used for all Moon surface elements. The infrared emissivity of the lunar surface is set to 0.97 as a fixed value for the temperature range from 102 K to 384 K (Racca 1995).

Common for both ray types is that each ray carries information about its power – power per ray Q_{ray} [W]. The power per ray is calculated based on the area of its originating element A_0 [m⁻²], the number of rays n_{ray} and the solar constant S [W·m⁻²] for the Moon

$$Q_{ray} = \frac{A_O \cdot S}{n_{ray}}$$

(92)

The powers of all rays intersecting a surface element are accumulated for solar rays and infrared rays individually.

Solar Rays:

The Sun emits energy radial in all directions. Due to the large distance to the Sun, and the fact that the incident angle has a cosine dependency, the solar rays can be considered to be parallel on the surface of the Moon. For a ray tracing simulation it is not practical to have a real size Sun and a real Earth-Sun distance of 1 AU. The general approach for ray tracers to have a point source is not applicable either, if the Sun-Earth distance is too small. A Sun parallelogram (Figure 5-22 on the left) was introduced that mimics the parallel nature of the solar rays close to the lunar topography (Nogina 2012). The solar parallelogram is created based on azimuth, elevation and an arbitrary distance of the "Sun plane". Rays emitted from the parallelogram are all parallel but have different origins. The origin of each ray is random for both directions *x'* and *y'* on the solar parallelogram. In the current implementation the number of rays per solar parallelogram was restricted to 2,800 x 2,800 rays. Because the landscape scale lengths vary from a few to several tens of kilometers a second solar parallelogram was introduced in the center. This parallelogram highlights the central region of the landscape, hosting surface features and the sample body. In this way a higher number of rays per surface area is possible and with it a smaller resolution for the surface elements used on the sample body.
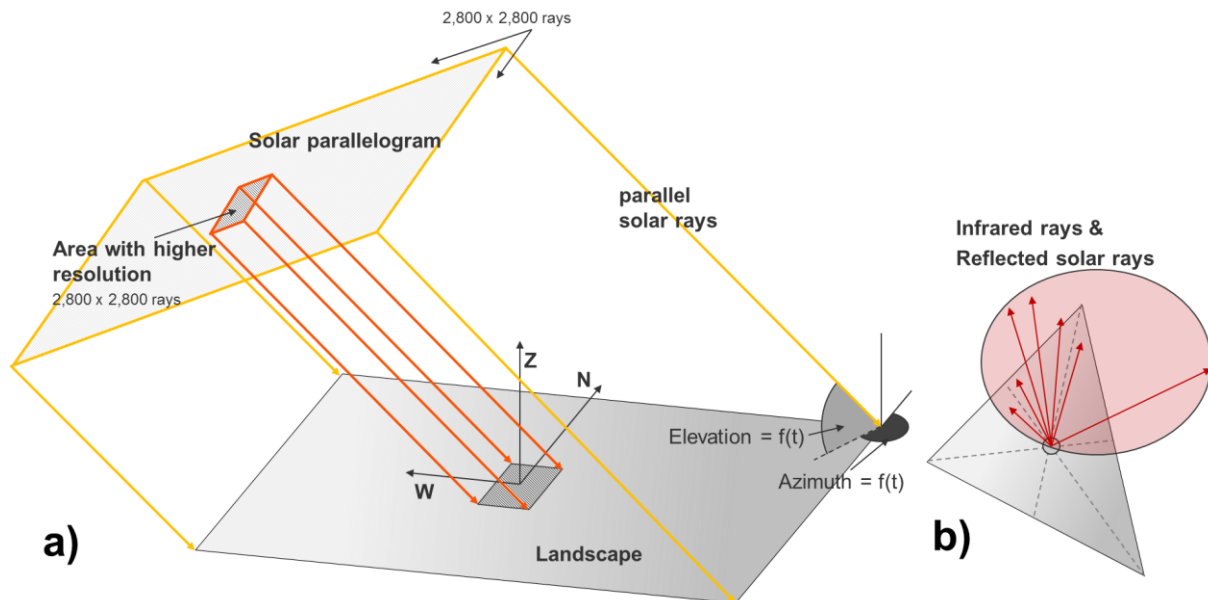
Figure 5-22: a) Representation of the solar parallelogram with low and high resolution for the parallel solar rays; b) cosine weighted IR ray emittance on a hemisphere.

Infrared Rays:

The infrared rays are emitted from each surface element depending on its temperature. The surface element temperature are calculated in the *Solver Module* and passed on with *.csv* files. The emitted power carried by infrared rays is computed for every face of the mesh using the Stefan-Boltzmann law. In Figure 5-22 on the right, the principle of the infrared ray emittance is displayed. Infrared rays are sampled randomly over a unit hemisphere in a cosine-weighted fashion. The number of infrared rays per surface element can be adjusted by the user. The number of infrared rays impacts the total simulation time. The more rays are emitted the higher is the accuracy of the results and the longer is the calculation time. The ray tracing algorithm keeps track of the number of infrared rays and the amount of power hitting one surface element. A balanced value for the infrared power per surface element is calculated with the knowledge about the emitted power, and is outputted in *.csv* files for the lunar surface and the sample object, respectively.

5.2.5 Data Exchange Module

The data exchange module takes care of the input and output of data stored for the *TherMoS* tool. Currently mainly the import and export of *.csv* and *.mat* files is implemented in the overall structure. In separate building blocks the input also of *.bdf* and *.iges* files and the output to *.erg* files is realized. The *.bdf* exchange format is used for tools using NASTRAN® routines, for example FEMAP®. The *.iges* format is used by computer aided design tools, such as for example CATIA v5® or Pro Engineer®. The *.erg* file format is a format used by ESATAN-TMS®. The *.mat* format is part of MATLAB®. In either case the principle structure of the data file is to have values separated by commas, semi colons, or tab stops. Each line contains a set of information. In case of the *.csv* files the information for the coordinates of a point (or vertex) is a set of information in a single line. In a second *.csv* file the combination of the points to triangles is stored. In case of *.bdf* files information about points and triangles are stored in one single file with coordinates in the beginning and triangles at the end of the file. Additional metadata is stored in a header. In *.erg* files, used for the data exchange with ESATAN-TMS®, each type of information is introduced in a structured way. The coordinates are introduced as points and the triangles are defined by the points. Additional information about material properties and surface coating are necessary to complete an output readable for ESATAN-TMS®. In reading data from an existing *.erg* file, only the geometric information can be extracted and the material data be omitted.

5.2.6 Post-Processing module

The post processing module contains MATLAB® functions to visualize the simulation results. Moreover this part also contains the calculations necessary to determine temperatures on- and inside the sample object. If the position is changed by the *Movement* function, the visualization adopts to it. The visualization takes into account surface temperatures, solar and infrared heat fluxes. Inherent to MATLAB®, figures and visualizations are operations to change colors of surfaces and grid lines, to alter fond size and style, to zoom and to pan the view, beside many other functions. The information data points and triangle elements from landscape and sample object geometry files is overlaid with temperature, solar or infrared heat flux data. The latter were stored in the result folder in *.txt* files through the *Solver Module*. Temperature, solar or infrared heat fluxes are loaded and mapped to the triangular surface elements with different values represented by different colors. The color coding was adapted to temperature, solar and infrared heat flux. The scale of the color coding conforms to maximum and minimum values of the calculated case. The visualization can be done step by step or be run as a continuous sequence. Moreover it is possible to create a movie from the sequence for ease of understanding. The movie format is *.mov*.

Sample-Object post-processing:

The calculations for the temperatures of the sample body are more complex. As of now this part of the simulation is not generic yet. In a first step, the sample objects geometry is reloaded and the number of surface elements is determined. A number of actions must be performed manually: the surface material properties, groups of surface elements, surface element thickness, core volume, and conductive interfaces to the core must be entered. Each surface element is a thermal node and the core is an additional thermal node. If a more detailed model of the sample object is available, further nodes can be placed between core and surface elements. The conductors for any additional node must also be entered manually, in the present state of the tool.

Additionally, it is necessary to set initial temperatures for the sample objects manually. The boundary conditions of solar and infrared heat fluxes are extracted from the results of the TherMoS *Solver Module* in each time step. Subsequently, the temperatures are calculated in the same manner as in the *Solver Module*. A heat balance of all incoming and outgoing heat fluxes, radiative and conductive, is established. All values are ordered in vectors, summarized and divided element-wise by the capacitor vector. In this way, the temperature of all nodes is determined for each time step.

Whereas the calculations in *TherMoS* take hours, the calculations of the sample body temperatures can be performed in a matter of minutes. Optical and thermal properties can be adopted quickly and the sample object post processing can be repeated. In this way numerous parametric studies for the same sample body geometry can be repeated.

5.3 Model Verification

In this chapter the verification of the implemented models is presented and discussed. Topography, regolith, boulder, and crater models are compared to remote sensing data and to literature values. The model verification is performed on model level (regolith, boulder) as well as on module level (*Landscape Module*). The discrepancies between the *TherMoS* models and measurement data or literature data are presented and explained. New models were verified against literature data from remote sensing or laboratory measurement. Not before a model was verified, was it connected to other parts of the simulation. The verification approach, described in Figure 1-3, was used throughout this work.

5.3.1 Regolith Temperature

The *Regolith Model* was derived from older models, mainly those presented by Cremers and Vasavada, described in section 5.2.1.3. In the following, the verification of the *TherMoS Regolith Model* for a simplified case is shown. The computation approach in MATLAB® is verified against a calculation in the commercial software ESATAN-TMS r4®. Additionally, the results are compared against the models of (Cremers et al. 1971; Vasavada et al. 1999; Vasavada et al. 2012; Hale and Hapke 2002). For verification a lunar surface patch is modeled with and area of 1 m², the material properties and node distribution explained in section 5.2.1.3. The boundary conditions at the top node are an incident solar heat flux and an emitted infrared heat flux. At the lowermost node, a lunar core heat flux of 0.033 W·m^{-2} is used as constant boundary condition. The solar constant was assumed to be constant with 1,367 W·m^{-2} and the deep space sink temperature to be 3 K [Clawson 2003]. A simplified approximation for the solar heat flux was used to bypass the time consuming ray-tracing for long time calculations. The simplification can be described with:

$$T_M = 70 + ([30 + 290 \cdot \sin(\Omega \cdot t)] \cdot \cos\lambda_{lat}) \qquad for \qquad 0 < t < \frac{\tau_{syn}}{2} \qquad (93)$$

$$T_M = 70 + 30 \cdot \cos\lambda_{lat} \qquad for \qquad \frac{\tau_{syn}}{2} < t < \tau_{syn} \qquad (94)$$

Here T_M is the lunar surface temperature [K], λ_{lat} [°] is the local selenographic latitude, Ω [s^{-1}] is the idealized angular velocity of the Moon, defined by $\Omega = (2 \cdot \pi) / \tau_{syn}$. The value τ_{syn} [s] represents the duration of a synodic day in seconds.

In Figure 5-23a, the verification results of the *TherMoS Regolith Model* are shown for the period of one lunation at the lunar equator. The diurnal temperature fluctuations penetrate the regolith only to a depth of 0.5 m. In Figure 5-23b, the deviation of temperatures between calculations with MATLAB® and ESATAN-TMS® r4 are shown. The deviation is about 1 % throughout the entire lunar day. Different from Figure 5-23a, the diagram in Figure 5-23b starts with the local sunrise. The steps in Figure 5-23b between 0 and 0.5 lunations can be explained with the ray-tracing method used in ESATAN-TMS®. The incident solar heat flux is calculated for several positions in the orbit and the values in between are interpolated. In the presented ESATAN-TMS® simulation (Figure 5-23b) 11 positions around the orbit of the Moon were used as supporting points.
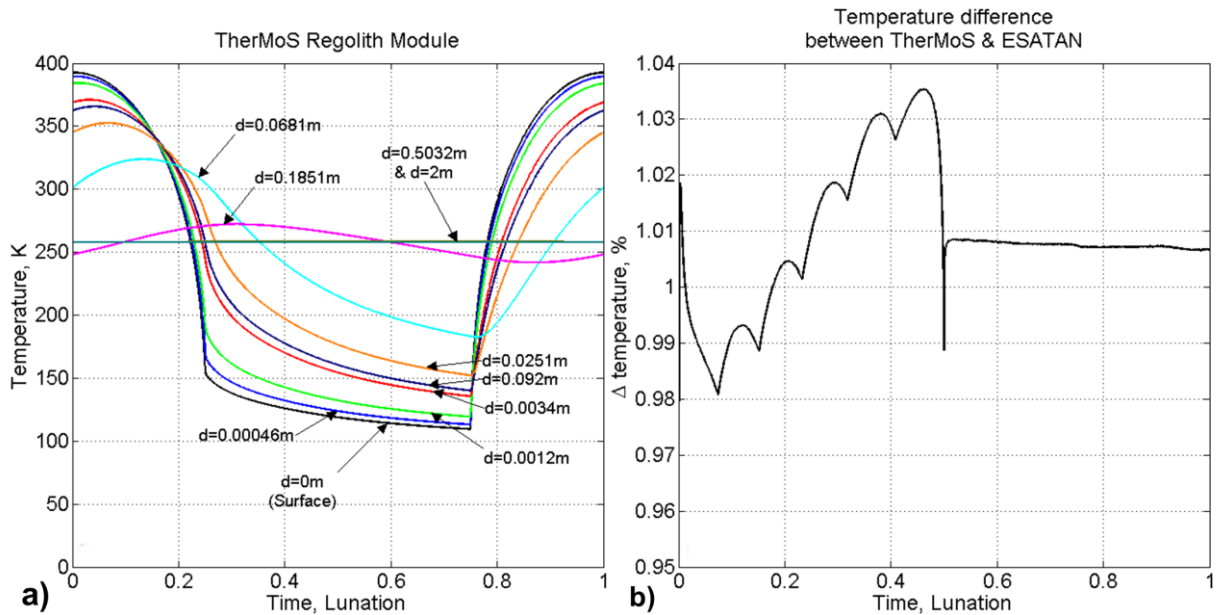
Figure 5-23: a) Results of the *TherMoS Regolith Module* for one lunation; b) deviation of MATLAB® solver and ESATAN solver for one lunation.
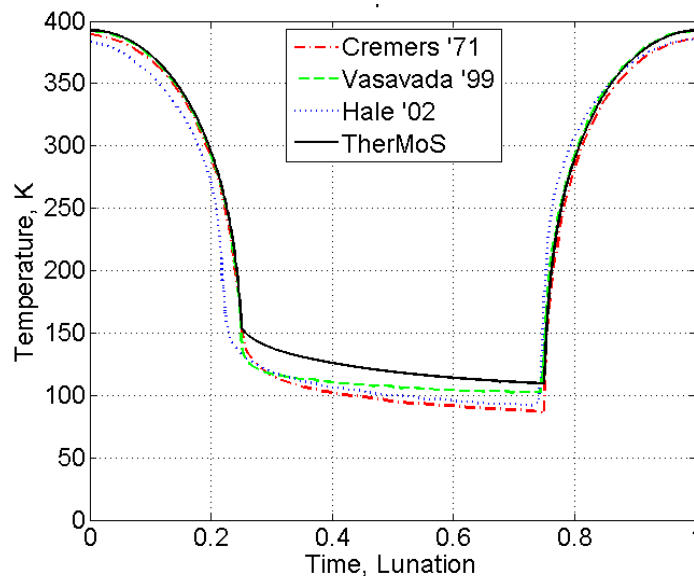
Figure 5-24: Comparison of lunar surface models with the *TherMoS Regolith Model*.

The depth profile reflects findings noted by numerous authors (Cremers et al. 1971; Winter and Saari 1969; Vasavada et al. 1999; Hale and Hapke 2002). The comparison with ESATAN-TMS r4® indicates the numerical finite volume approach yields temperatures comparable to established models. In Figure 5-24 the results of the *Thermos Regolith Model* (full black line) for one lunation at the lunar poles are compared with the results of the models presented by Cremers et al. (1971) (dash-dotted red line), Vasavada et al. (1999) (dashed green line), and Hale and Hapke (2002) (dotted blue line). The values of the models were obtained from the diagrams shown in papers with a curve fitting tool (Engauge digitizer). The curve fitting tool digitizes the data with an accuracy that depends on the resolution of the image, thus inaccuracies cannot be avoided. In Table 5-3 the temperatures at noon, sunset, midnight, and sunrise for the 4 models of Cremers, Vasavada, and Hale shown in Figure 5-24 are compared to the results from the *TherMoS Regolith Model*. For the lunar daytime the *TherMoS Regolith Model* is in good agreement with the

Vasavada model. The model by Cremers has a slightly lower maximum temperature which can be traced back to a lower solar constant used in Cremers model. At lunar nighttime, the *TherMoS Regolith Model* remains at temperatures higher than other models. A list of the results of older models can be found in (Cremers et al. 1971). The model of Vasavada was verified against LRO Diviner Lunar Radiometer Experiment data and the results were presented in Vasavada et al. (2012). Thus, the Vasavada model can be considered as the most accurate model. Several reasons might lead to the temperature differences between the *TherMoS Regolith Model* and the model presented by Vasavada et al.

Table 5-3: Comparison of temperatures at distinguished points in time during a lunation. The values have an uncertainty of about 5 % due to the way of their acquisition.

Value	Noon [K]	Sunset [K]	Midnight [K]	Sunrise [K]
Cremers et al 1971	395	152	101	93
Vasavada et al. 1999 & 2011	392	148	107	102
Hale et al 2002	383	131	100	92
TherMoS Regolith Model	393	156	119	109

Figure 5-25a shows the temperature depth profile of the *TherMoS Regolith Model* and Figure 5-25b the comparison to the models of Cremers and Vasavada. The dash dotted lines represent the conditions at lunar noon, the dashed lines at sunset, the dotted lines at midnight, and the full line at sunrise. Black lines denote the *TherMoS Regolith Model*, blue lines the Vasavada Model and red the Cremers model. Due to the discrete number of nodes in the *TherMoS* model, the black lines are more rugged than the red and blue lines. The higher temperatures during lunar night time in the *TherMoS Regolith Model* can be traced back to different material properties and a higher regolith core temperature. Whereas *TherMoS* uses 255 K the Vasavada model uses 250 K as boundary condition for the lowermost node. Additionally, Vasavada et al. used constant material properties for regolith in the model from 1999. Furthermore, in the model of Vasavada, the material properties for regolith at a temperature of 350 K are used and the density is not increasing with depth but constant for the top layer (1,300 kg·m^{-3}) and the bottom layer (1,800 kg·m^{-3}). Thus the material properties which impact the heat propagation differ between Vasavadas' and the *TherMoS* regolith models.
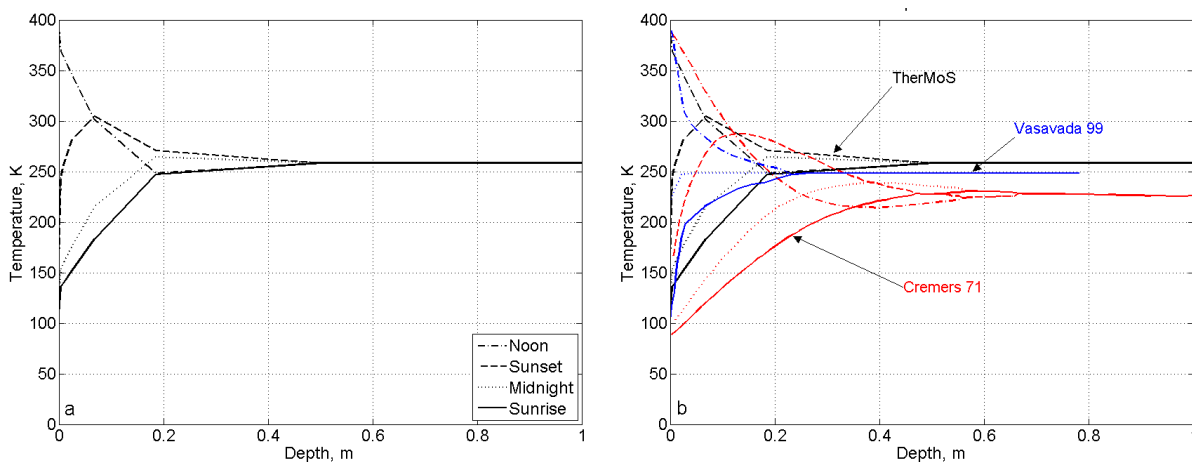
Figure 5-25: a) Temperature depth profile for Noon, Sunset, Midnight and Sunrise calculated with *TherMoS* and b) compared to results of the models created by Vasavada (1999) and Cremers (1971).

5.3.2   Boulder Temperature

In this section the *TherMoS Boulder Model*, described in section 5.2.1.4, is compared to a model presented by Roelof (1968). In parallel to the approach used in section 5.3.1, the lunar surface temperature was simplified with equations (93) and (94). The incident solar and infrared heat fluxes for each boulder surface element were calculated with view factors. The view factor method has the benefit to avoid the

time consuming ray tracing algorithm. In this way, several lunar days can be simulated in relatively short time to achieve periodic temperatures, independent of the initial conditions. The view factors to the Sun F_{sol} [-] and to the lunar surface $F_{lun,surf}$ (Siegel and Howell 1992) are given with equations (95) and (96):

$$F_{sol} = \vec{n}_\psi \cdot \vec{n}_{sol} \tag{95}$$

$$F_{lun,surf} = \frac{1}{2} \cdot (1 - cos\,\psi) \tag{96}$$

Here $\vec{n}_\psi$ [-] is the local surface normal vector and $\vec{n}_{sol}$ the vector to the sun. ψ [°] is the angle between the local zenith vector and the surface normal. The simplified sun vector $\vec{n}_{sol}$ depends on time and lunar latitude. The sun vector $\vec{n}_{sol}$ is defined in a right handed coordinate system, with the x-axes pointing towards local west, the y-axes pointing towards local north and the z-axes pointing towards local zenith:

$$\vec{n}_{sol} = [-sin(\lambda_{lat}),\quad -cos(\Omega \cdot t),\quad sin(\Omega \cdot t) \cdot cos(\lambda_{lat})]^T \tag{97}$$

As in equations (97), Ω [rad·s⁻¹] is the idealized angular velocity of the Moon and λ_{lat} [°] is the lunar latitude. Based on these values the time and latitude dependent heat flux densities can be calculated from the lunar surface q_{lun} and from the Sun q_{sun}. Solar albedo was neglected for the simplified calculations.

$$q_{lun} = T_M{}^4(t, \lambda_{lat}) \cdot \varepsilon_{IR} \cdot \sigma \cdot F_{M,surf}(\psi) \tag{98}$$

$$q_{sol} = S \cdot \alpha_{sol} \cdot F_{sol}(t, \psi) \tag{99}$$

The evaluated shapes were a cube, a hemisphere, and an arbitrary shaped boulder. Only the results for the cube and half sphere are shown here. The results for the arbitrary shaped boulder can be found in the Appendix A.3). Figure 5-26 shows the temperatures calculated for a) a cuboid boulder and b) a hemisphere boulder shape for the last of ten simulated lunations. The red line denotes the lunar surface temperature, the dash-dotted line represents the western side of the boulder, the dotted line the eastern side, the dashed line the top side, and the full black line is the core temperature. From Figure 5-26 one can see how the temperatures of the surface elements in western and eastern direction respond fast to direct solar illumination. The development of the core elements temperature is more benign which is understandable since the core node contains the biggest part of the volume and hence has a high thermal inertia. As mentioned in section 5.2.1.4 and can be seen by the values in Table 5-2, the thermal conductivity inside boulders is low with k_{bould} = 1 to 5 W·m⁻¹·K⁻¹. Although this value is high compared to the lunar regolith, the temperature wave travels slowly into the center of the boulder.
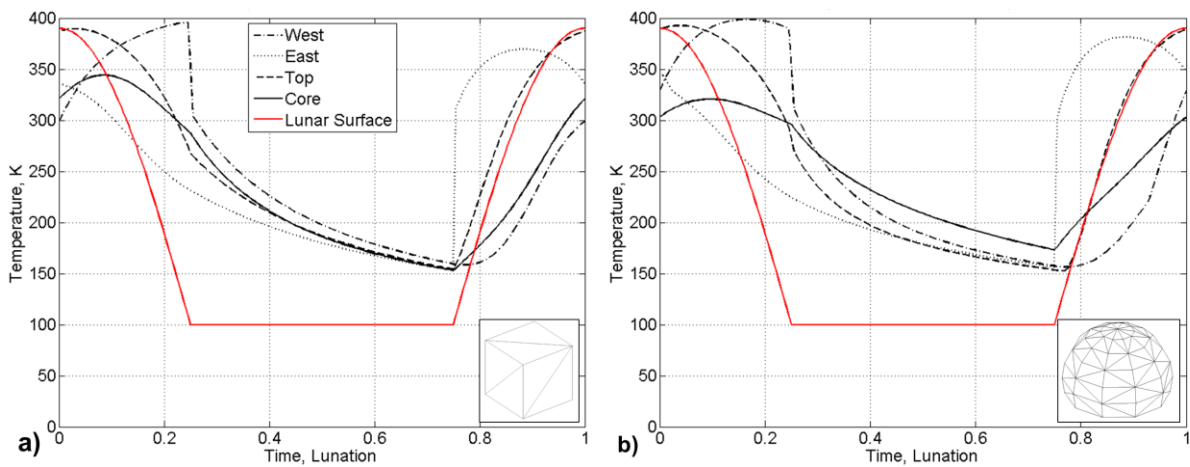
Figure 5-26: Temperatures for *TherMoS* boulders with 3m diameter and a basic shape of a) a cube and b) a hemisphere.

Roelof (1968) used a model of finite differences for 1 m and 3 m cuboid boulders. His model had meshes with 10x10x10 nodes per boulder. The higher resolution of the mesh increases accuracy and computa-

tional demand. In parallel to the *Regolith Models* in section 5.3.1, the model by Roelof was extracted from the original paper figures with a data digitizer tool. In Figure 5-27 the results of Roelofs' 3 m cuboid model (red lines) are compared with the *TherMoS Boulder Model* (black lines) for a 3 m diameter hemisphere. The compared values were those of the western side (dash dotted line) and the core (full line). Also the modeled lunar temperature was included (dashed line). In the two models, the lunar surface temperatures are different which impacts the infrared heat flux calculations. Besides, the results of Roelof's model indicate an even faster response to the incident solar heat flux. In contrast to the *TherMoS Boulder Model* the model by Reolof has more nodes. The *TherMoS Boulder Model* has three nodes, one on the surface, one intermittent and one core node.
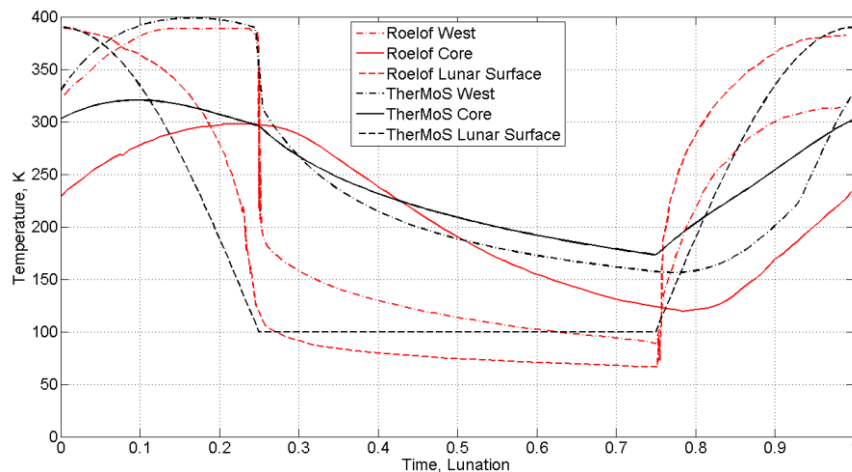
Figure 5-27: The results from the model presented by Roelof (1968), for temperatures on the west side, the core, and the lunar surface for the Roleof model superimposed with the *TherMoS Boulder Model* results.

5.3.3 Crater Geometry & Boulder Distribution

In this section qualitative comparisons are shown to depict to capabilities of the *TherMoS Crater Model* and the distribution of boulders around craters. A quantitative comparison of real and modeled crater shape is beyond the scope of this thesis and not appropriate in the light of the objectives. As mentioned before, the crater model follows a parabolic shape that can only be applied to craters smaller 20 km in diameter. Figure 5-28 shows the crater Cauchy B (NASA) with a diameter of 5 km compared to the crater model in *TherMoS* shown on the right. More recent studies showed that a truncated cone might be an even better approximation of simple crater shapes (Jaumann et al. 2012).
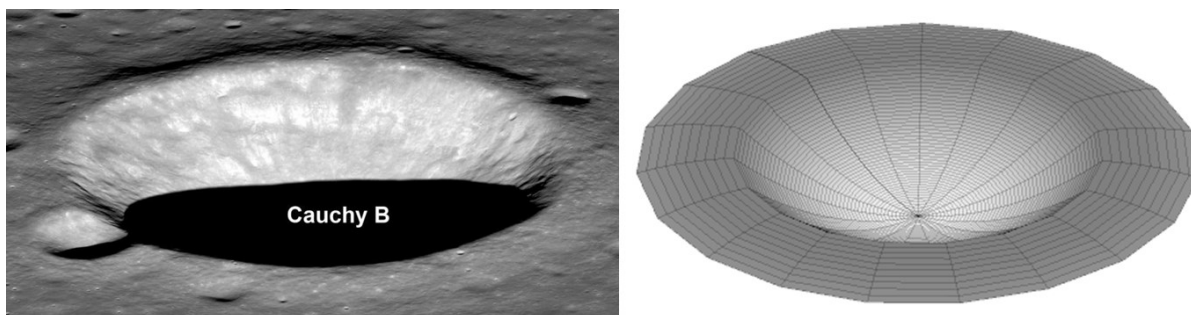
Figure 5-28: Qualitative comparison of the crater Cauchy B (NASA) and the crater model used in *TherMoS*.

Figure 5-29a shows a photograph of a nameless crater with 550 m diameter (NASA 2011). Two versions of the same photograph at different brightness levels were superimposed to also show the boulders in the shadowed region (NASA 2011). As comparison, two *TherMoS* versions are depicted with the boulder size and spatial distribution for b) a lunar *mare* and c) a lunar *highland* region. The boulder distribution is according to the values presented in section 5.2.1.5. The chosen modeling approach brings forward

larger boulders and neglects smaller boulders. Thus, especially in Figure 5-28c fewer but larger boulders are modeled on the crater slopes, walls, and floor of the highland crater.
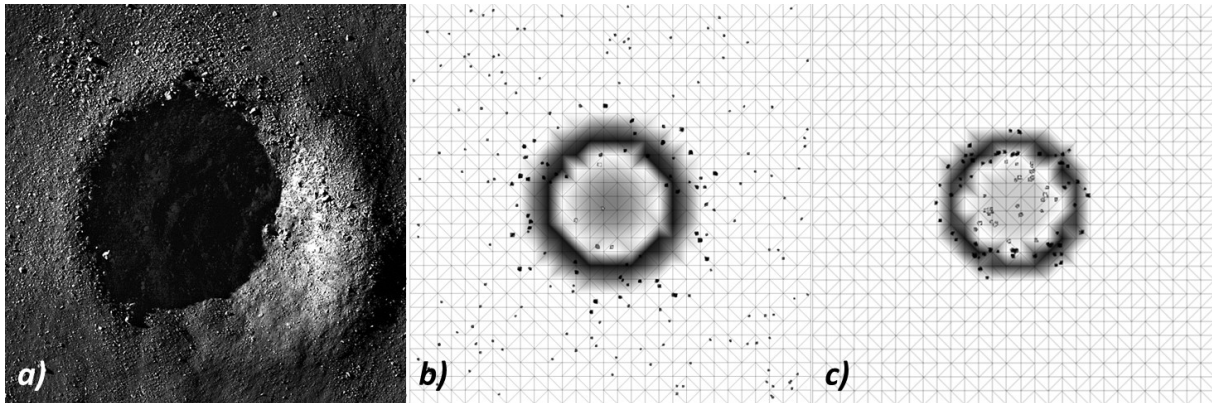
Figure 5-29: Qualitative comparison of a 550 m diameter crater (NASA 2011) with a mare crater (middle) and a highland crater (right) produced by the *TherMoS Boulder Module*. Darker colors mark higher regions of the crater and boulders lying at elevated positions.

5.3.4 Global Topography

In the past, models of the lunar topography were created from Apollo photographs, Clementine data, and Kaguya LALT data. More recently new maps from the Lunar Reconnaissance Orbiter 'Lunar Orbiter Laser Altimeter' (LOLA) instrument are available. The LOLA dataset is constantly growing as long as the LRO is in orbit around the Moon and operational. In this section, the reproduced lunar topography in the *TherMoS Landscape Model*, based on Kaguya LALT data is compared with photographs made during the Apollo program, by the Clementine probe, or by the Lunar Reconnaissance Orbiter. The photographs are available from the US National Geographical Survey or directly from the LRO LROC camera team homepage. In the following, three examples are shown. The scenes in Figure 5-30 to Figure 5-33 represent regions that are used in the verification of the thermal conditions of which some are shown in section 5.3.5. Further examples can be found in (Vogel 2010) and (Lechner 2011).
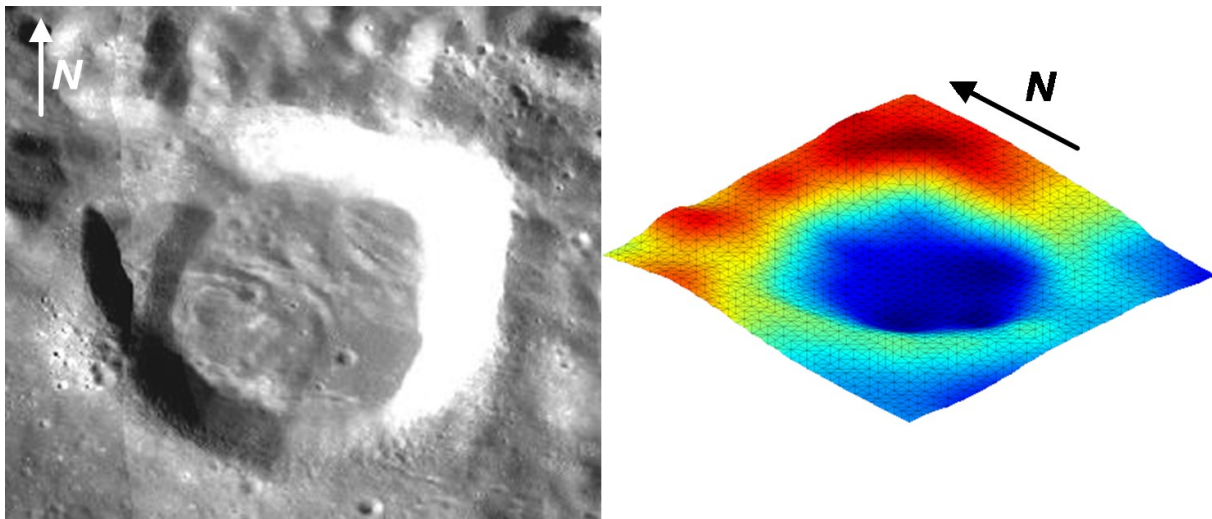
Figure 5-30: Crater Calippus photograph (left) (NASA/GSFC/Arizona State University 2011) and TherMoS landscape based on Kaguya data (right).

Blue regions have a lower altitude than red colored regions. The color scale is relative for each landscape model with dark blue being the lowest point and dark red being the highest point of the depicted landscape patch.

Figure 5-30 shows the crater Calippus at 38.9° N lunar latitude and 10.7° E lunar longitude. The crater has a diameter of approximately 32 km. The presented photograph shows a surface patch of approximately 40 km. The corresponding *TherMoS Landscape Model* derived from Kaguya LALT data has a resolution of about 0.5 km.
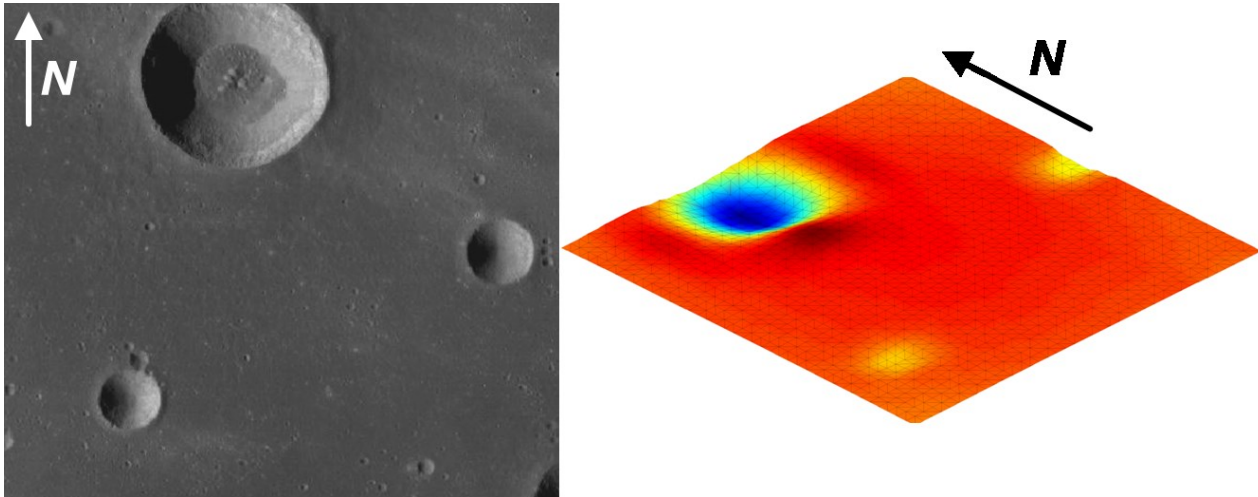
Figure 5-31: Crater Marius A (top) and Marius F (right) (USGS 2006) as well as an unnamed crater on a photograph (left) and TherMoS landscape based on Kaguya data (right).

Figure 5-31 shows several craters in the *Oceanus Procellarum*. The large crater on the northern rim of the photograph is Marius A at 12.5° N and 46° W with a diameter of 15 km. On the right of the photograph Marius F is shown, with a diameter of 6 km. The crater on the lower left side of the photograph is unnamed. The surface patch has a diameter of approximately 40 km.
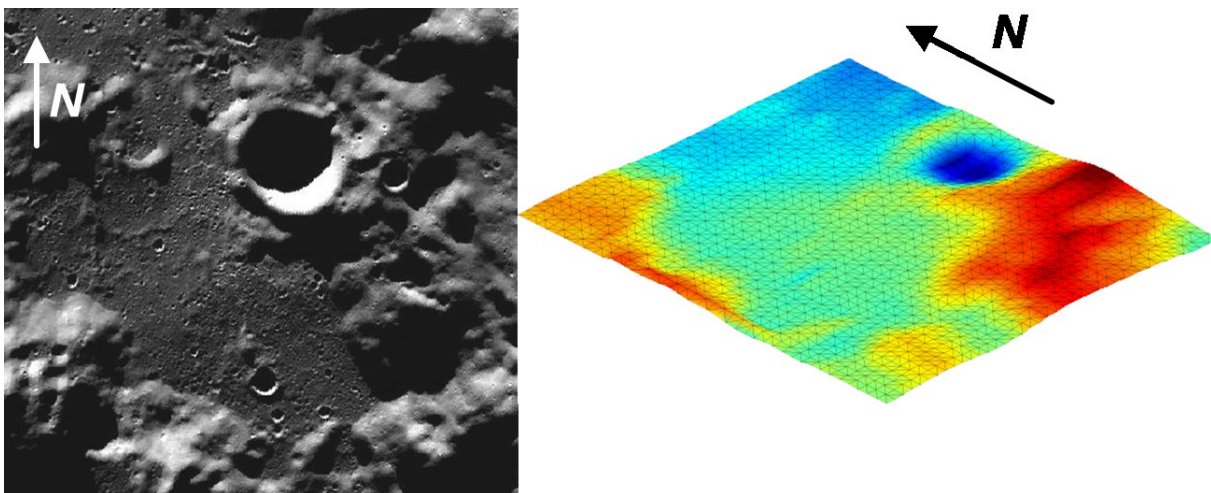
Figure 5-32: Crater Ibn Bajja photograph (left) (USGS 2009) and *TherMoS* landscape based on Kaguya data (right).

Figure 5-32 shows the crater Ibn Bajja at 86.4° S lunar latitude and 86.75° W lunar longitude. The crater is inside the Aitken Basin and close to the lunar South Pole. The crater has a diameter of approximately 12 km and the photograph shows a surface patch of 40 to 45 km diameter. The *TherMoS* landscape has a resolution of 0.5 km.

Figure 5-33 shows the Apollo 15 landing site at 26.1° N lunar latitude and 25.95° E lunar longitude. The size of the photograph is approximately 40 km.
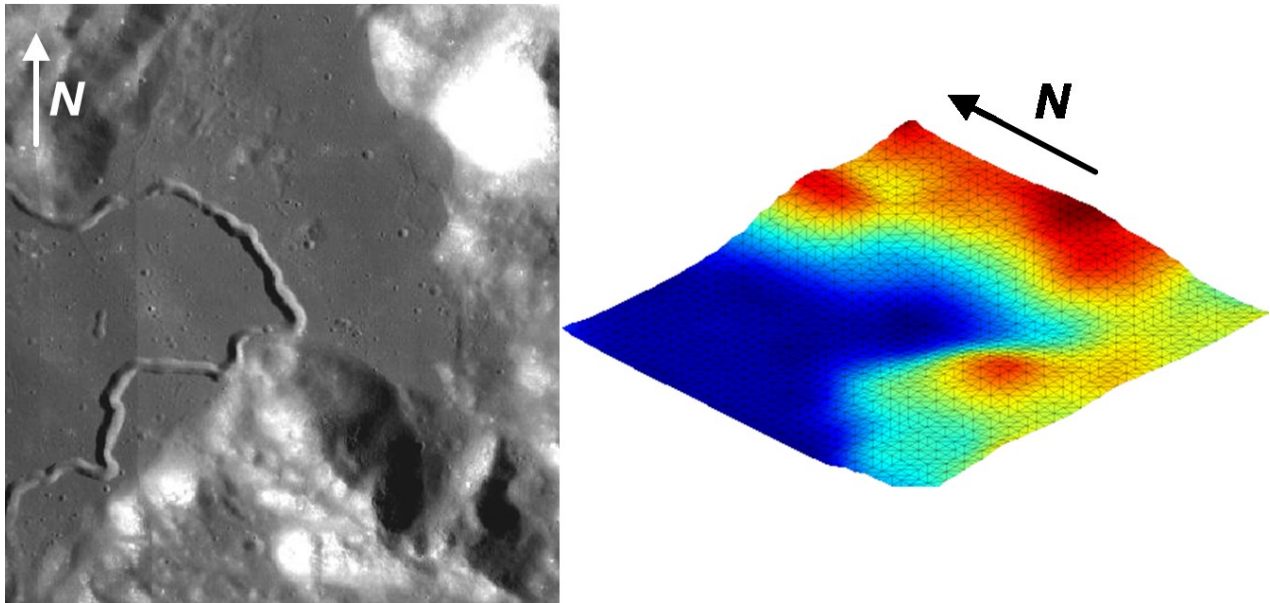
Figure 5-33: Apollo 15 landing site with Hardley Rille as photopgraph (left) (USGS 1964) and TherMoS landscape based on Kaguya data (right).

The resolution of the Kaguya LALT surface data is well suited to represent large scale structures but not surface features with dimensions in the range of several km. Small craters as can be seen in all four photographs are omitted in the landscape model. Even the Ibn Bajja crater and the Calippus crater seem to have more benign crater walls and crater rims than apparent on the photographs. Also the mountains visible in Figure 5-32 and Figure 5-33 are smoothed in the landscape model compared to the real landscape visible in the photographs. The Hadley Rille, a geological interesting feature that was investigated during the Apollo 15 landing, is not visible on the *TherMoS Landscape Model* at all*.* The Hadley Rille has an average width of 1.2 km, which is not enough for the achievable resolution with Kaguya data.

5.3.5 Ray Tracing Verification

In this section the qualitative and quantitative verification of the ray tracing algorithm are presented. Figure 5-34 shows temperatures, solar and infrared heat flux densities around a boulder at a solar angle of incidence of 10°. The temperatures are shown for comparison and to understand the infrared heat flux densities. The temperatures, given in the uppermost image of Figure 5-34, are calculated with the *TherMoS* solver module based on the incoming fluxes. The mean temperature of the undisturbed lunar surface is about 250 K. The Sun facing side of the boulder reaches temperatures of about 400 K. This is close to the black body temperature at 1 AU. The central image of Figure 5-34 shows the solar heat flux. The depicted values represent the sum of direct and reflected solar rays hitting each surface. The highest values equal or slightly above the solar constant are found for the surface elements facing the Sun. The surface elements behind the boulder do not receive solar rays at all or only few reflected rays. The lowermost image of Figure 5-34 shows the infrared flux density balance. The balance is the combination of emitted and absorbed infrared rays. Regions with a negative sign indicate elements that emit more heat in the infrared region than they receive. The lunar surface in the vicinity of the boulder is influenced by the infrared heat flux originating and the solar heat flux reflected from the boulder. This is most obvious west of the boulder were the temperature of the lunar surface reaches values approximately 100 K higher than the undisturbed soil. In contrast, the shadow casted by the boulder leads to lower lunar surface temperatures on the boulders' eastern side. Close to the boulder the shadowed soil still receives infrared heat from the boulder, leading to temperatures of about 180 K. Further away the impact of boulder infrared declines and the temperature approaches lunar night time temperatures of approximately 120 K. In general, close to the boulder the lunar surface reaches higher temperatures. The images for solar and infrared

heat flux shown in Figure 5-34 are a qualitative verification of the ray tracing algorithm. The finding of elevated temperatures close to boulders is in agreement with recent findings by (Bandfield et al. 2011; Williams et al. 2011).
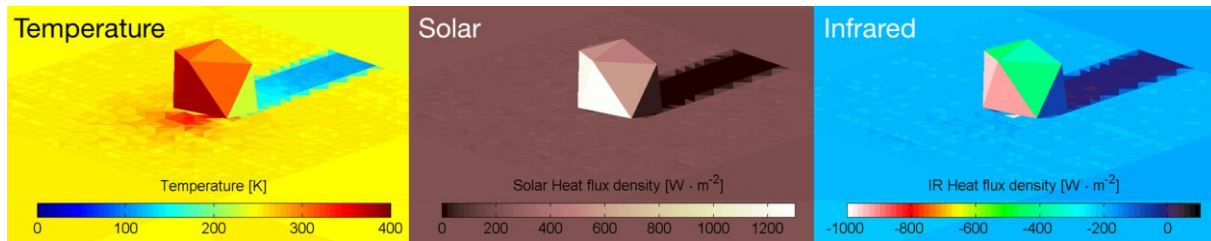
Figure 5-34: Results of the *TherMoS* ray tracing: top) temperature overlay from *TherMoS* solver results; middle) sum of solar heat fluxes and bottom) infrared heat flux balance.

In Figure 5-35 and Figure 5-36 the standard deviation for 1,920 repetitions of the ray tracing algorithm are shown for infrared and solar rays, respectively. A cuboid sample body traverses a plain at lunar equator noon surface temperature and solar elevation conditions. Figure 5-35a shows the standard deviation for infrared rays and 1920 repetitions comparing their results to the mean value. The *x*-axis represents the 12 sides of the cube. Figure 5-35b shows the standard deviation for the infrared rays compared to manual values based on view factor calculations. For the surface facing sides (1&2) a view factor of 1, for the vertical sides (3-10) a view factor of ~0.5 and for the top (11&12) a view factor of 0 was derived from the equations in section 4.1.3. The repetition deviation of the infrared rays is < 10 %. Compared with manual values, the accuracy is also < 10 %. The sides of the cube have a deviation of 4-8 % and the bottom of the cube shows the highest inaccuracy of about 9 %. Figure 5-36 shows the repetition accuracy of the solar rays accordingly. The view factors in the manual calculations are 0 for elements facing the lunar surface, ~0.5 for the sides and 1 for the top. The repetition deviation of solar rays is < 2 % and the comparison to manual values shows a deviation < 8 %. A permanent outlier was found for element 11 on the top of the cube. The solar heat flux for element 11 was beyond physically possible values. The reason was traced back to a truncation error in random number creation. If values were above a threshold value q_{thresh} [W·m^{-2}] of:

$$q_{thresh} = 1.05 \cdot S \cdot (1 + \alpha_{alb}) \tag{100}$$

they were reset to the threshold value. S is the solar constant, α_{alb} the albedo of the lunar surface. A factor of safety of 1.05 accounts for the inaccuracies of the entire ray tracing algorithm.

The source of most of the deviations, especially of the infrared rays, is the statistical nature of random numbers used for the generation of rays in the ray tracing algorithm. The infrared rays are generated in a random fashion and originate from the center of a triangular surface element. The triangular surface elements have a diameter of ~0.5 m. If a sample object is closer than half of this diameter and the sample objects surface elements are smaller than the lunar surface element, this results in fluctuations of received rays. The deviations can be omitted by a) more rays and b) smaller lunar surface elements. Both methods are accompanied by a higher computation demand and longer simulation times. The same reason leads to the deviation of reflected solar rays, obvious from Figure 5-36b. The reflected solar rays originate from the hit point of the primary rays but are launched in the same hemisphere weighted random fashion. Yet another reason for deviations of the solar rays are numeric round-off errors (see section 7.1.6). The solar parallelogram has a large distance to the landscape and sample body. Small errors in the solar ray direction lead to not-parallel rays and a deviation at the receiving surface elements. This round-off error can be omitted by reducing the distance between solar parallelogram and landscape.
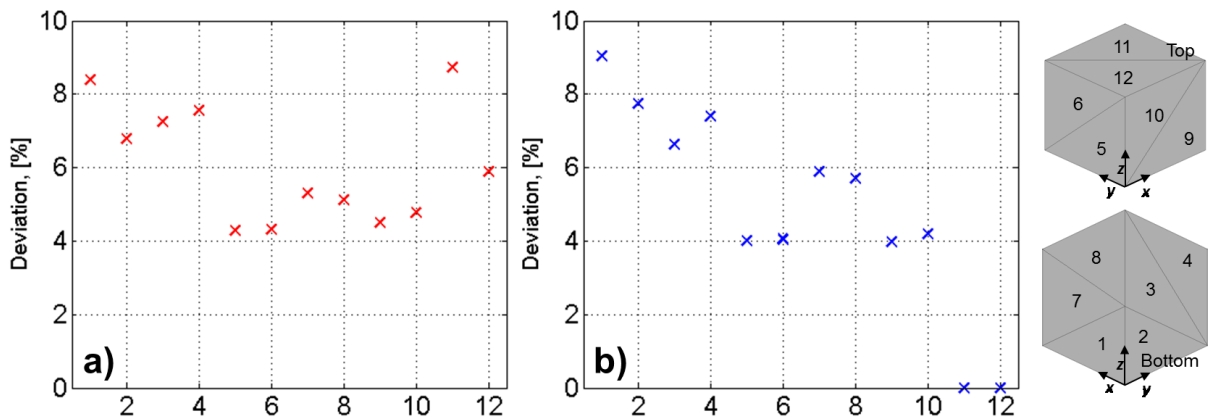
Figure 5-35: Infrared ray accuracy on a cubes' sides for 1,920 repetitions; a) standard deviation b) compared to manual view factor calculations.
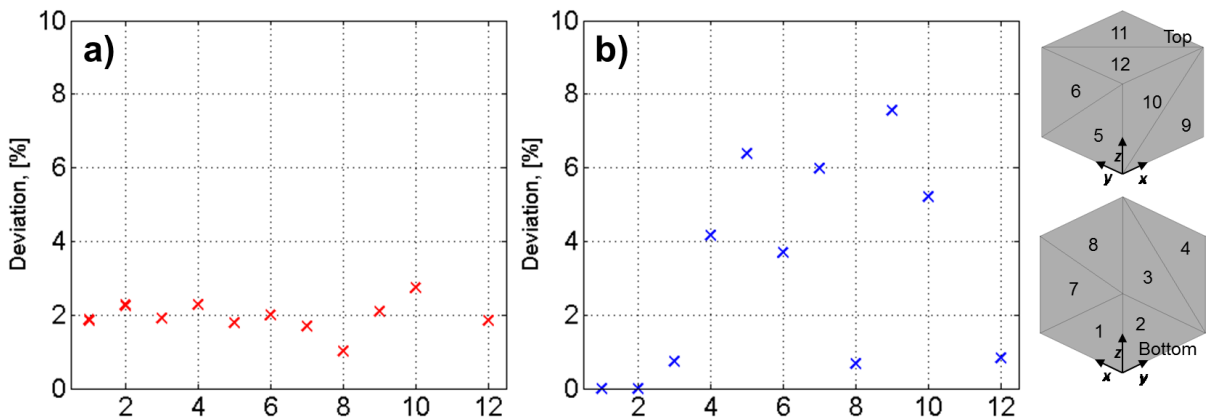
Figure 5-36: Solar ray accuracy on a cubes' sides for 1,920 repetitions; a) standard deviation b) compared to manual view factor calculations.

5.3.6 Landscape Module Global Verification Temperatures

In this section the simulation results for a large landscape are presented. The landscape is created with the *Landscape Model* based on Kaguya data, each surface element has 10 regolith depth nodes and the ray tracing algorithm calculates solar and infrared heat fluxes. The solver module calculates the surface temperatures for each time step. In total, the simulation was performed for 4 regions and 8 points in time. In the following, the simulation results for two regions are presented and their consistency with LRO Diviner Lunar Radiometer Experiment (DLRE) measurement data is evaluated in detail. The remaining cases can be found in the Appendix B.

Figure 5-37 has 6 different subplots. Figure 5-37a to c show Crater Calippus and Figure 5-37d to f show several craters with the largest being Marius A at the northern rim of the surface patch. The first row (*a* and *d*) show photographs of the lunar surface which were superimposed with LRO DLRE brightness temperature data. The second row show landscape models for the same region produced in *TherMoS*, from Kaguya LALT data. The color scale represents the temperatures calculated in *TherMoS*. The comparison of measured Diviner Lunar Radiometer Experiment data and the simulated *TherMoS* data are shown in the last row (c and f) of Figure 5-37.

The Diviner Lunar Radiometer Experiment data is accessible as raw data via the Geosciences Node of NASA's Planetary Data System (PDS). The DLRE instrument is a channel infrared radiometer measuring electromagnet waves between 0.35 and 400 µm. For this work the measurements taken with channel 6 to 9 are important since they represent wavelength between 13 and 400 µm which corresponds to the brightness temperature. The instrument is operated in a nadir pointing pushbroom mapping mode. A

signal is obtained every 0.128 s. The ground field of view depends on the spacecraft altitude but can be as low as 320 m for a 50 km orbit (Sullivan and Paige 2011).

The data from the Planetary Data System (PDS) are available in a comma separated value (*.csv*) file format. Each row contains 33 entries with information about the spacecraft, the instrument and the measured position on the Moon. Due to the rotation of the Moon, the LRO orbit, its progression, and the detection width of the instrument, each spot on the lunar surface is measured at different local times. Different times mean different lighting conditions and hence different temperatures. Not necessarily a spot is visited twice and almost never at the same sun angle conditions. The LRO is in a polar orbit around the Moon. Hence, the revisit time is higher at the poles compared to the lunar equator. As a consequence, the resolution and repetition of measurements at the poles is far higher than at the equator. The number of temperature measurements decreases the closer the point of interest is to the equator. To obtain data from the PDS one has to define a region of interest first. Subsequently different channels of the instrument, local lunar time or time in Earth based Unified Time Coordination (UTC) can be chosen. Depending on the input values and the available data points the PDS output can reach from millions to a couple of thousand data points.

Crater Calippus: In Figure 5-37a the temperature data points extracted from the PDS were restricted to a local lunar time between 8.30 am and 9.30 am. The restriction to the local morning resulted in five measurements of comparable temperatures at 5 different dates between 2009 and 2011 for the chosen 40 km surface patch. The data set of the 16th of November 2010 was used, in order to compare the *TherMoS* results with the Diviner Lunar Radiometer Experiment measurements. On the 16th of November 2010 LRO had two flyovers at the selected 40 km surface patch around crater Calippus to measure the brightness temperatures with DLRE. The same date, and thus solar elevation angle, was used for the simulations performed in *TherMoS*. The simplified temperature equation presented in 5.3.1 was used as initial condition for the simulation. The simulation used all models and functions of the *TherMoS* tool. The heat exchange was determined with the ray tracing algorithm and the temperatures were calculated with the numeric solver. The simulation started 2 hours prior to the targeted date and time. It took 10 hours in real time to calculate the 2 hours in *TherMoS*, based on the initial conditions. Figure 5-37b shows the simulated temperatures results for Crater Calippus on the 16th of November 2010 at 12:52 UTC (blue slice) and 14:45 UTC (green slice). These Earth time values correspond to local lunar times of approximately 8:50 a.m. and 8:51 a.m., respectively. Figure 5-37c superimposes the DLRE measurements, marked in green and blue, with the corresponding *TherMoS* simulation results, marked with black triangles and circles. The DLRE values represent the surface brightness temperatures (channel 6 to 9) measured along a meridian. The DLRE data colored in blue correspond to the *TherMoS* simulations with black circles and the green DLRE values correspond to the black triangles from *TherMoS*.

Crater Marius: In Figure 5-37d, e and f the DLRE remote sensing surface brightness temperature for Marius A is compared to *TherMoS* simulation results. The temperatures at crater Marius A are compared for the 28th of January 2011 at 3:08 UTC. The used criteria to obtain appropriate data from the PDS systems were: number of data points for the selected area; time interval in local lunar time between 2:30 p.m. and 4:00 p.m. This input yielded five different points in time during the lunar day, more data points for the same surface patch, but diverging temperature profiles. The same simulation approach as for crater Calippus was chosen, with initial conditions, active ray tracing, and the appropriate solar incident angle in the *TherMoS* tool. The simulation was run for 2 lunar hours (10 hours simulation time). Again values colored in blue represent the DLRE surface brightness temperature measurements and the black circles the results of the *TherMoS* simulation.
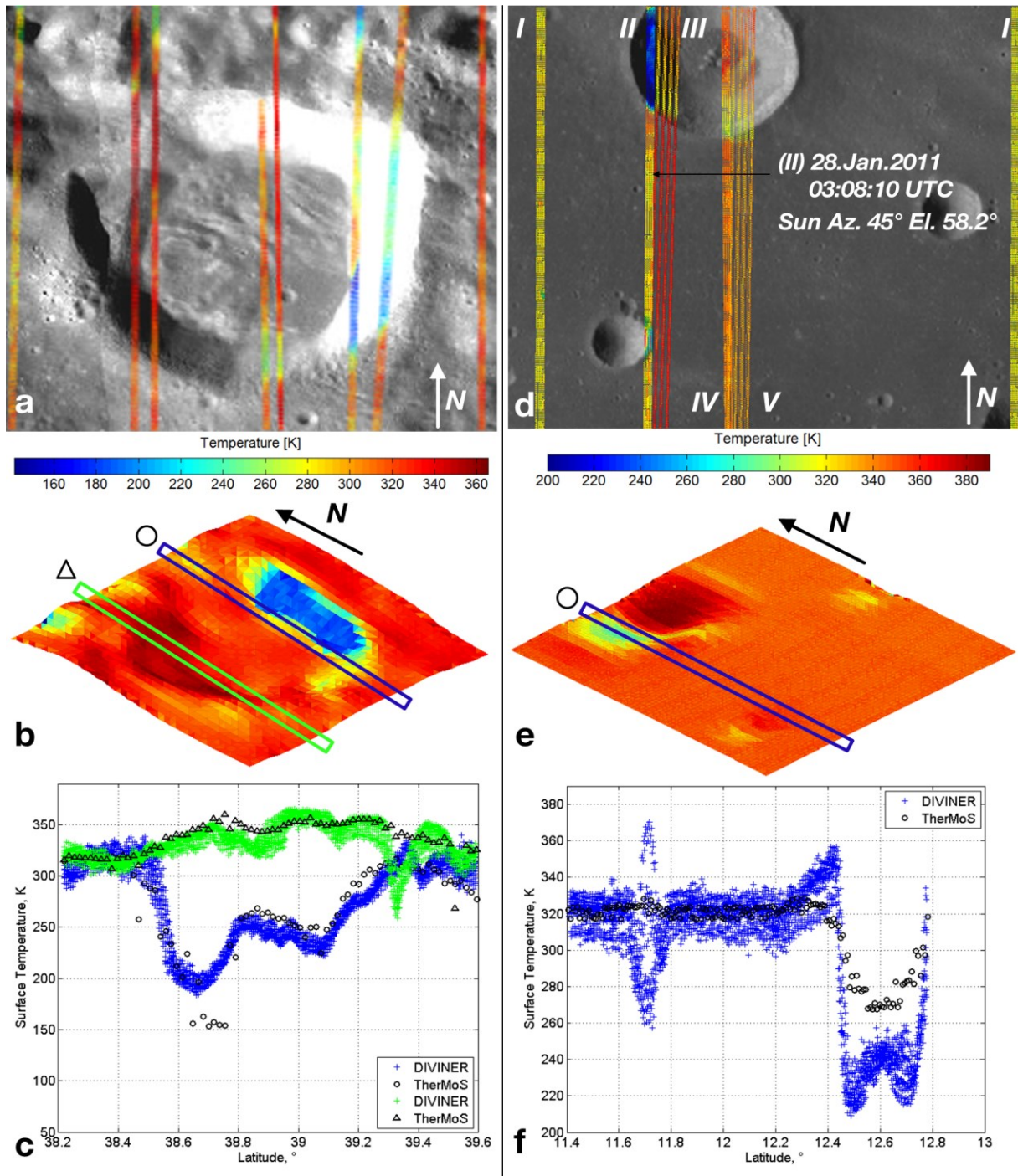
Figure 5-37: Photograph superimposed with DLRE data (Washington University 2012b, 2012a), Kaguya LALT landscape superimposed with TherMoS temperature calculations and comparison of DLRE and TherMoS temperature data for crater Calippus (a,b,c) and Crater Marius A (d,e,f).

By comparing the measurements and the *TherMoS* simulation values several conclusions can be drawn. As mentioned before, the resolution of the Diviner Lunar Radiometer Experiment is far higher than that of the Kaguya LALT instrument. Hence, small features such as small craters are not included in the *TherMoS* model. This is apparent for example in Figure 5-37c for the green data points at 39.3° N latitude. The DLRE measurement show a temperature decrease of almost 100 K for a relatively short distance of less than 3 km. The discrepancy can be explained by a small crater or rill not apparent in the Kaguya data. The resolution difference also causes the temperature differences on crater slopes and walls. In Figure 5-37e at 12.2° to 12.5° N and at 12.7° N the overall slopes of crater Marius A are too shallow from the Kaguya

data compared to the DLRE measurements. Also the *TherMoS* model is too warm in case of cold regions. This is in agreement with the observations made in the verification of the *TherMoS Regolith Model* in section 5.3.1. As mentioned before, the data point density for the Marius A surface patch (right column of Figure 5-37 is higher than for the Calippus crater patch. Hence, more data points are used in Figure 5-37e. By comparing Figure 5-37d and e one can see that at 11.7° N latitude the rim of a smaller crater is measured. This leads to high temperatures on the sun facing inside crater wall as well as low temperatures on the shadowed eastern crater slope. The resolution in *TherMoS* is too small to model all these effects correctly. In all other cases the simulated temperatures are within 30 K or 10 % of measured values.

5.3.7   Summary of the Model Verification

The *TherMoS* environment module mainly serves the purpose to represent lunar temperatures in order to determine and evaluate the infrared heat flux on a sample object. For high temperatures, the *Regolith Model* shows a good agreement with the regolith model presented by Vasavada et al. (1999, 2012). At lunar night times the *TherMoS Regolith Model* produces temperatures that are higher than those calculated by the Vasavada model and measured with the DLRE. A difference in surface temperate between 102 K and 110 K changes the heat flux at about 35 % in relative numbers and 2.1 W·m^{-2} in absolute numbers. The investigated cases in this work are during lunar day time. But for low sun angles and long shadows the model discrepancy leads to the aforementioned errors. Future work must focus on the improvement of the *Regolith Model* for low temperatures. An integrated test for a lunar landscape showed agreement with DLRE data < 10 % for temperatures beyond 300 K. At lower temperatures the discrepancy increases. The resolution of the used Kaguya LALT data is well suited to represent large scale features but is not adequate to represent steep angle crater walls, small rills, or small craters. These features also lead to a deviation between *TherMoS* results and Diviner Lunar Radiometer Experiment surface brightness temperature measurements. Future work should focus on integrating LRO Lunar Orbiter Laser Altimeter (LOLA) data to improve the resolution and with it the *TherMoS* validity.

Boulder store heat throughout the lunar day and will slowly radiate the heat via infrared radiation during the lunar night. In general, there is a phase lag between core and outer surfaces of a boulder and between the lunar surface regolith and a boulder. It is postulated that Boulders can be used as heat sources during lunar night if the Sun elevation is low. On the other side, the high temperatures of the surface elements, even at high latitudes, make boulders to a source of infrared heat flux that should not be underestimated in the thermal design of surface-craft. The verification method against the results created by Roelof (1968) is questionable. Both models were not verified against real measurements. Further improvement on the core temperature development of boulders of different sizes will be necessary. Current work focuses more on the effect of small scale boulders on the regolith environment (Williams et al. 2011), and the global impact of ejecta blankets of inhomogeneous size distribution on the regolith temperature in the vicinity of craters (see Bandfield et al. 2011).

6 Case Studies & Results

The results section follows the transition from static to fully transient simulations and is shown in Figure 6-1. In section 6.1 the simulation matrix and the parameters that define the different cases are presented. Moreover in section 6.1 the sample objects placed in the lunar landscapes are described. In section 6.2 to section 6.5 the results from simulations and calculations are presented. Section 6.2 focuses on static worst-case calculations. The static calculations in section 6.2 also form the reference for the semi-transient and fully transient cases discussed subsequently. The semi-transient cases, discussed in section 6.3, focus on static objects in a slowly changing, but already transient environment. The results in section 6.5 resemble the final stage of the simulation capabilities with *TherMoS*. Here short duration cases for moving objects in a transient lunar environment are presented that address the objectives and problem statement derived in chapter 1 and 3. Section 6.5 is divided in results for exploration rovers and spacesuit applications due to different conclusions drawn subsequently in chapter 7.

The main questions addressed with the four simulation parts A-D, shown in Figure 6-1, are:

A) Determine reference values for the comparison with the semi transient and transient cases,
B) Determine reference values in the light of the transient regolith environment for static objects,
C) Determine temperature differences inside sample objects in a transient lunar environment; Compare unobstructed to obstructed cases; for static objects throughout an entire lunar day,
D) Determine heat fluxes and temperatures for a moving object in a transient lunar environment for short term transits through obstructed landscapes.

The focus for the exploration rover cases is set on the total received heat flux from local surface features as compared to unobstructed cases. The spacesuit cases focus on the rates of change of solar and infrared heat fluxes for the different parts of the spacesuit.
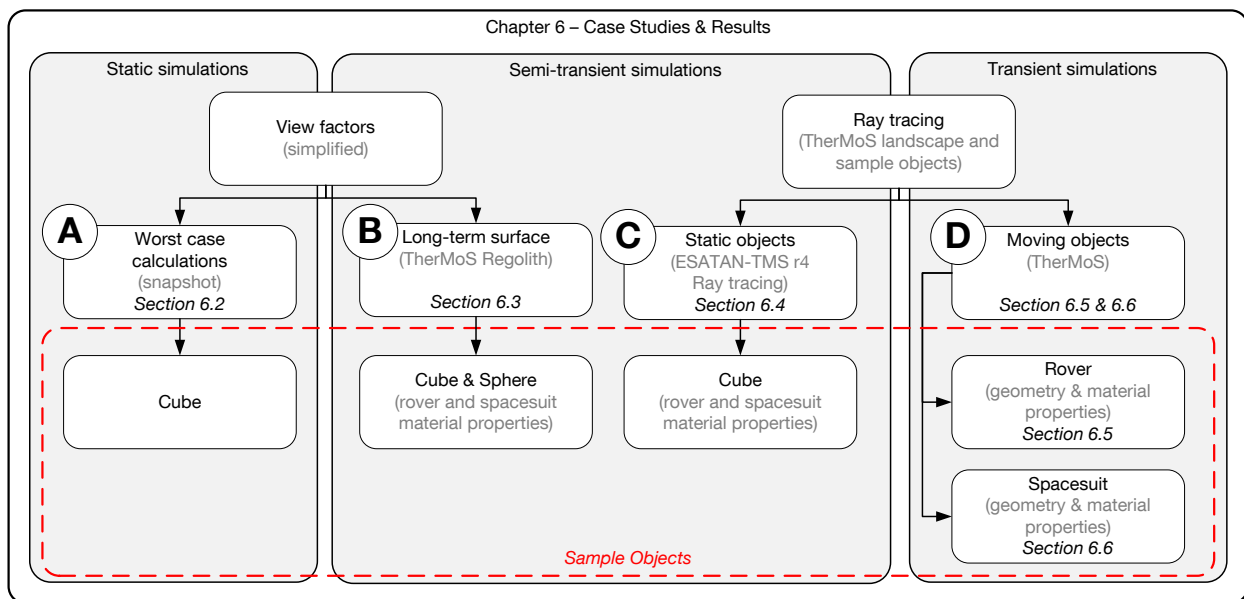
Figure 6-1: Schematic of the approach used in the results section.

6.1 Case Description and Simulation Matrix

The simulated cases span a wide variety of combinations. The cases range from static to dynamic, from simple to complex sample bodies, from plane surfaces at the lunar equator to boulders and craters at the lunar Poles. The varied parameters for the cases are: *lunar latitude, time of lunar day, surface feature, and sample body*. An additional parameter for the static and semi-dynamic cases is the normal vector of the sample object surface element. The possible combinations from these parameters are limitless. In order to reduce the number of cases for each parameter several characteristic variants were selected. The variants represent extreme conditions. Still a large number of possible combinations remain as can be seen from the simulation matrix shown in Table 6-1.

Table 6-1: Simulation matrix showing all parameters and their variants. The highlighted letters are used for the case nomenclature.

Location	Time	Surface Feature	Sample Body	Path description
Equator	**N**oon	**n**one	**n**one	**In**itial
Poles	**Du**sk	**Bo**ulder	**Cu**be	Transit (**Tr**)
	(**Da**wn)	**5 Bo**ulders	**Sp**here	Transit (**TrW**)
	(**M**idnight)	**Cr**ater	Rover 1 (**Rov1**)	
		Crater**L**	Rover 2 (**Rov2**)	
		Slope	Detailed Rover (**KT**)	
			Suit	

Each case gets an individual name, made-up of its parameter variants. The bold and underline letters are used to describe a case. For example Case_E_Du_Bo_Rov1_Tr would describe the <u>tr</u>averse of the <u>rov</u>er type <u>1</u> on the eastern side of a single <u>bo</u>ulder at the lunar <u>e</u>quator around local <u>du</u>sk. In the following, each parameter and its variants is rationalized and described. Colors and symbols (Figure 6-2) were used to simplify the orientation in the complex scenes of the transient short time cases in section 6.5 and 6.6.
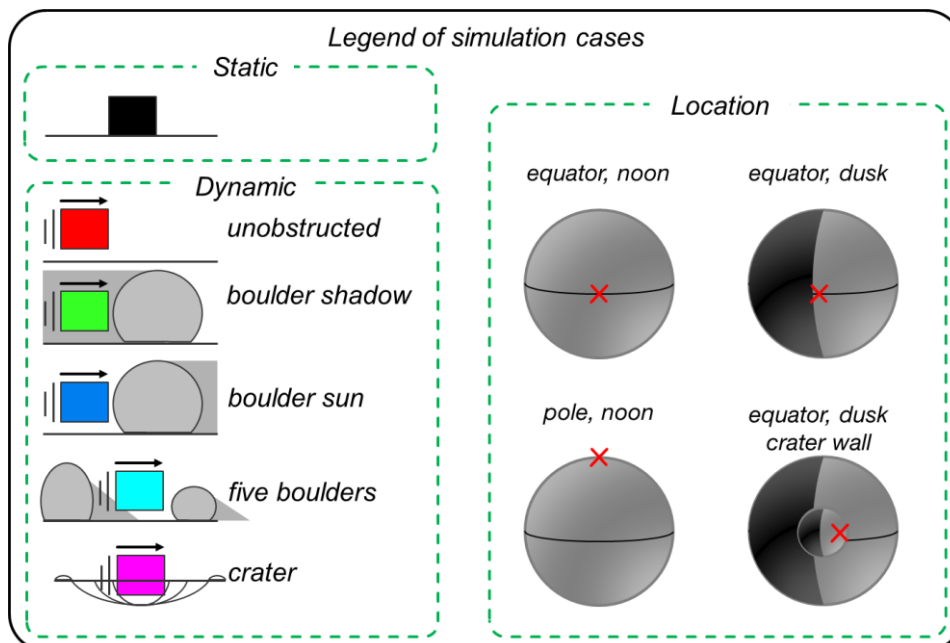
Figure 6-2: Introduction of symbols used to describe the environment case settings for the transient cases.

6.1.1 Location and Time

The latitude determines the maximum solar elevation angle ε_{el} [°]. The solar elevation angle in turn governs the maximum temperatures and this in turn the minimum temperatures encountered on an undisturbed lunar plane. The maximum temperature range of the undisturbed plane provides the surface background temperature for the simulation, in contrast to the deep space background of 3 K. The most extreme latitude is the lunar equator and the lunar poles. Whereas the location determines the maximum solar elevation angle, the local time determines the current elevation angle together with the azimuth. The angle of incident is important for surface features of any kind. Whether only inclined slopes, simple boulders, or complex crater structures are illuminated by the Sun, the local temperature mainly depends on the angle of incident. The chosen variants are local noon, dusk, dawn, and midnight. The local noon has an elevation angle of 90° at the lunar equator and of 2° at the lunar Poles (taking into account and approximating the tilt of the lunar axes of rotation to the ecliptic wit 1.54°). Dusk and dawn were chosen to be around local times 5:30 p.m. and 6:30 a.m., respectively. The solar angles were set to azimuth = 90° (dawn) and = 270° (dusk) and the elevation angle to be 10°. Lunar North and South Pole are not distinguished, because this work focuses on the general understanding of the impact of environmental heat loads on moving objects and not on the conditions at dedicated locations. Introducing a concrete landscape would have added yet another level of complexity to the results at hand.

6.1.2 Surface Feature and Path Description

Local temperature depends on the view factor to the Sun. The view factor is influenced by the angle between the surface normal and the sun angle. Thus inclined slopes can have a higher or lower view factor to the sun than unobstructed planes. The view factor can also be inhibited by other objects. The amount of incident heat on the other hand changes local temperature which in turn determines the emitted infrared. In case of surface features, emitted infrared can be absorbed changing the temperature further. The *'Location'* and *'Time'* parameters alone produce a homogenous temperature for a given scene. Hence, for each location and time combination an unobstructed plane was simulated as reference case. Figure 6-3 a) shows the reference plane with a side length of 2.5 km and a resolution of 100x100 squares. Apart from the central square, each square is further divided into two triangles. The central square has a side length of 50 m and is divided into 30x30 square elements which are further divided into two triangles.
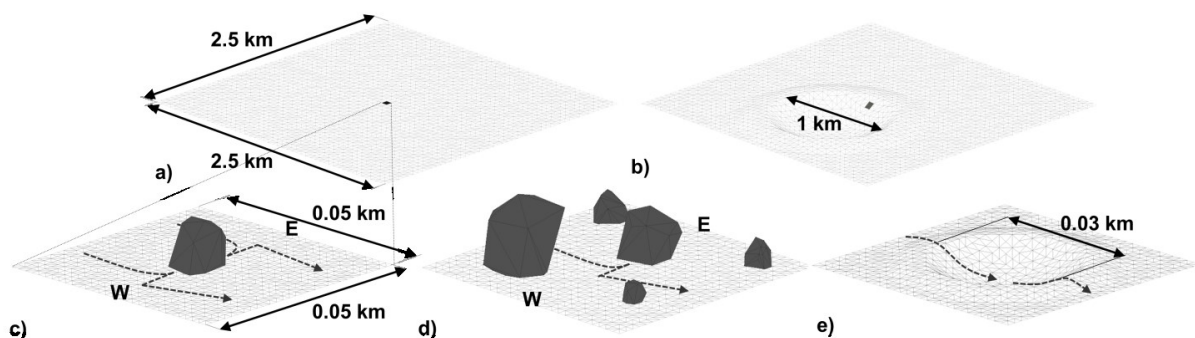
Figure 6-3: Large scale environment with unobstructed plane (a), crater with 1 km diameter (b), and small scale environment with a single boulder (c), a set of 5 boulders (d), and a small crater with 0.03 km diameter (e).

The use of surface features changes local temperatures and view factors to the Sun significantly and with it the heat fluxes received by a sample body. Beside the unobstructed plane a variant with a 1 km diameter crater (Figure 6-3 b) was used. The central element was additionally altered to contain a single boulder (Figure 6-3c) or 5 boulders (Figure 6-3 d). The single boulder has a diameter of 12 m. It was placed in the center of the central square, thus allowing transits on either side. The different sides were marked with

east (E) and west (W) in Figure 6-3c), and with '*shadow*' and '*sun*' in the diagrams of section 6.5 and 6.6. Figure 6-3 d) shows the *5 boulder* variant. The boulder diameters vary from D_B = 5 m to D_B =18.5 m. The five boulders were placed in a pattern that allows the sample object to pass through its center. A small crater, later solely referred to as '*crater*' with a diameter of D_C = 0.03 km, is depicted in Figure 6-3e. In the 1 km crater variant (Figure 6-3b) the central square with none, one, or five boulders was placed on the inclined crater wall or slope. In general the paths lead through the center square of an unobstructed plane, the eastern and western side of the single boulder, and through the center of the 5 boulder variant. The path has a maximum length of 45 m. The rover and spacesuit variants also contain additional stops, turns and change of directions. Thus, the paths that were used differ between primitive sample bodies, rovers, and the spacesuit. Their peculiarities are described in the respective sections.

6.1.3 Sample Object Description

Six sample objects were modeled and integrated into the case studies. In Figure 6-4 an overview of all six sample objects is given. The primitives, a cube, and a sphere of arbitrary size, were used to verify the outcome of the ray tracing algorithm, and for static and semi-transient calculations with view factors. The simplified models depicted in the central column of Figure 6-4 represent typical rover designs used for polar rovers (Rov1) and equatorial rovers (Rov2). In the right column of Figure 6-4 detailed models are shown. Simplified and detailed models are used for the transient calculations. The detailed models represent a current rover design of the German Aerospace Center (DLR) and the Apollo AS7 spacesuit. The rover, called the Mobile Payload element (MPE), was designed by the Kayser-Threde GmbH under a contract of the German Aerospace Center (see section 2.1.2.2). The Apollo AS7 spacesuit bases on a mock-up located at the University of Boulder, Colorado. The dimensions of the simplified and detailed sample bodies are documented in Appendix A.4). The triangular surface elements of the sample bodies vary in size. If more infrared or solar rays hit one single element, the accuracy of the ray tracing algorithm increases and vice versa.
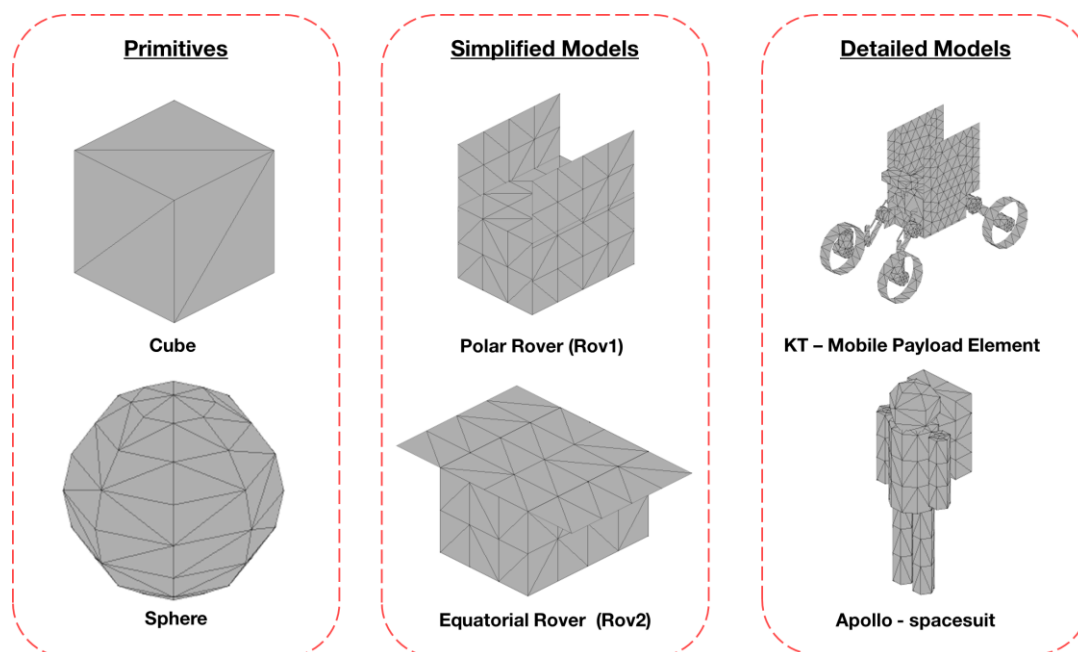
Figure 6-4: Overview of the modeled sample objects.

In addition to the geometrical representation that is necessary to define the heat fluxes, thermal properties are necessary to calculate time-dependent temperatures of rover and spacesuit sample bodies. The heat capacity, thermal conductivity, density, and optical surface properties are individual for each surface-craft.

Rovers: Especially for the large number of rover designs discussed in section 2.1.2 the thermal properties are diverse. The mean density $\rho_{rov,mean}$ [kg·m^{-3}] ranges from 68.61 kg·m^{-3} to about 933.33 kg·m^{-3} for 12 rovers and rover concepts (see Table 2-1). The lowest density was found for the small scale Micro 5 rover, and the highest density for the Scarab rover concept with its high level of integration. The value for the average density of the compared rovers is $\rho_{rov,avg}$ = 234.5 kg·m^{-3}. The modeled mean heat capacity and internal thermal conductivity are $c_{p,rov}$ = 996.4 J·kg^{-1}·K^{-1} and k = 171.8 W·m^{-1}·K^{-1}. The "rover bulk material" properties were obtained by using the relative subsystem masses of the Day/Night Rover concept [Berkelmann et al. 1995]. Table 4 gives the mass ratios r_m of the different subsystems.

Table 6-2: Averaged percentage of rover hardware [based on (Berkelman et al. 1995)].

	r_m [%]	c_p [J·kg^{-1}·K^{-1}]	k [W·m^{-1}·K^{-1}]
Structure & Locomotion	42.1	961.2	121.2
Structure CFK	-	-	-
Power	39.6	712.8	148.9
Thermal	2.5	1,004.4	0.2
Harness*	-	-	-
GNC, CCCT, Imagery	15.8	1,800.0	391.2
"Rover Bulk Material"		996.4	171.8

Spacesuit: In the same way "bulk material" properties for the spacesuit and the human within, were modeled. The thermal behavior of a spacesuit depends to a large extend on the thermal inertia of, and the heat from, the astronaut protected by the suit. The human sample body was modeled according to a standard human with a mass of 70 kg and a body height of 1.8 m. For the space suit outer area, an EMU surface area of approximately 3.9 m² was used (Metts et al. 2011). The thermal inertia was modeled as a weighted mean from skeletal muscles, adipose tissue, bones, and organs (Wang et al. 1999; Fiala et al. 1999). The heat capacity, thermal conductivity and density of the human body materials are gathered in Table 6-3. The mean density is 1,110.3 kg·m^{-3}, the mean specific capacity is 3,230 J·kg^{-1}·K^{-1} and the thermal conductivity k_{hum} = 0.43 W·m^{-1}·K^{-1}.

Table 6-3: Values used for the standard human (Wang et al. 1999; Fiala et al. 1999), with r_m = ratio of the overall body mass, ρ = density, c_p = heat capacity and k = thermal conductivity.

	r_m [%]	ρ [kg·m^{-3}]	c_p [J·kg^{-1}·K^{-1}]	k [W·m^{-1}·K^{-1}]
Skeletal muscles	44.7	1,085.0	3,750	0.42
Adipose tissue (fat)	15.0	850.0	2,300	0.16
Bones	14.9	1,500.0	1,700	0.75
Organs + remnants	25.4	1,080.0	3,680	0.47
"Astronaut bulk material"		1,110.3	3,230	0.43

Based on [Bailey & Briars 1996], the surface area of a human with the above mentioned mass and height is 1.87 m². The material properties and values of the spacesuit are those of beta-cloth fabric and the personal life support system (PLSS). The spacesuit beta-cloth cover sheet was assumed to have a thickness of 0.02 m. The optical properties are α_{suit} = 0.25 and ε_{suit} = 0.837 (Jones 2009; Campbell et al. 2000). The values were derived from the extra-vehicular mobility unit (EMU) cover material. For the thermal calculations in the transient long-time simulation cases (section 6.4) the thermal inertia and properties of the personal life support system (PLSS) were neglected. The geometry of the PLSS was accounted for in the transient short time calculations presented in section 6.5.

6.2 Static Reference Cases

In this section the results for simplified static view factor calculations are presented. The view factors are calculated based on the equations presented in the fundamentals of radiative heat exchange (section 4.1.3). The sample object is a black body cube. For Earth and Moon, albedo values of 0.3 and 0.12 were used, respectively. The absorptivity of regolith for the infrared wavelength was assumed to be 0.97. Table 6-4 summarizes the results for four cases. The view factors are the sides of a cube oriented vertical ∥ and horizontal ⊥, facing Earth (index E) and Moon (index M). The values for a low Earth orbit (LEO) at 400 km altitude and a geostationary orbit (GEO)[14] are given for comparison. The Moon cases are a worst case cold and a worst case hot. In the cold case there is a view factor neither to Earth nor Sun, and the sample object is in a region with 70 K lunar surface temperature at the lunar Poles. In the hot case the sample body receives infrared heat from Earth and Moon and direct solar heat as well as moon albedo. The lunar surface temperature is set to 390 K in the worst case hot, which represents a position at the lunar equator at the sub-solar point.

Table 6-4: View factors and the according static solar and infrared heat flux densities for a cube in LEO, GEO and on the Moon. All values are given in [W·m⁻²].

	$F_{E,\perp}$ [-]	$F_{E,\parallel}$ [-]	$F_{M,\perp}$ [-]	$F_{M,\parallel}$ [-]	Earth IR [W·m⁻²]	Earth Albedo [W·m⁻²]	Moon IR [W·m⁻²]	Moon Albedo [W·m⁻²]	Sun [W·m⁻²]
LEO	0.886	0.289	1.9e⁻⁵	1.8e⁻⁸	490.42	842.94	0.03	0.003	1,367.00
GEO	0.023	7.4e⁻⁴	2.4e⁻⁵	2.5e⁻⁸	6.23	10.72	0.03	0.004	1,367.00
Moon (cold)	0.000	0.000	1.000	0.500	0.00	0.00	4.09	0.000	0.00
Moon (hot)	2.5e⁻⁴	8.2e⁻⁷	1.000	0.500	0.06	0.10	3,823.80	495.360	1,367.00

The highest infrared heat fluxes are encountered in the lunar worst case hot. The infrared heat flux is 7.8 times higher compared to a spacecraft in a 400 km LEO. The albedo values are smaller by a factor of 0.59 compared to the 400 km LEO. The infrared heat flux caused by the lunar surface in the worst case cold conditions is 3 orders of magnitude smaller than in the extreme hot case. The infrared and albedo heat flux densities from Earth for a cube on the Moon are negligible. In the same way a cube in LEO and GEO receives almost no heat flux from the Moon. Figure 6-5 a) shows the development of infrared heat flux for a black body cube over all temperatures that can be encountered on the lunar surface. The bottom of the cube has a view factor of $F_{M,\perp} = 1$ and the circumferential sides have a view factor of $F_{M,\parallel} = 0.5$ to the lunar surface. The sum of the heat flux (red line) is the four circumferential sides plus the heat on the bottom side. The values are compared to sum of infrared and albedo heat flux for a black body cube in a worst case hot 400 km LEO. Figure 6-5b) shows the change in total infrared heat flux with increasing view factors of the circumferential sides from $F_{M,\parallel} = 0.50$ [-] to $F_{M,\parallel} = 0.90$ [-] to the ground. An increased view factor to the lunar surface can be caused by mountain ranges, nearby inclined slopes, or inside a crater.

Figure 6-6 shows the results of a parameter analysis for a change in optical properties and view factors. Figure 6-6a) shows the impact of altered ε_{IR} and α_{IR} on the total received infrared heat flux of a cube in a lunar worst case hot. A reduction of ε_{IR} has the largest impact. Figure 6-6b) shows the impact of a change in the view factors between circumferential sides and the lunar surface for a cube in a lunar worst case hot.

---

[14] The geostationary orbit (GEO) is a circular orbit, without inclination, at an altitude of 35.768 km above the Earths' radius. Satellites in GEO have an orbit period of 24 h and are placed in the Earths' equatorial plane. The main applications for GEO satellites are weather prediction, telecommunication relay links and surveillance Wertz and Larson (1999).
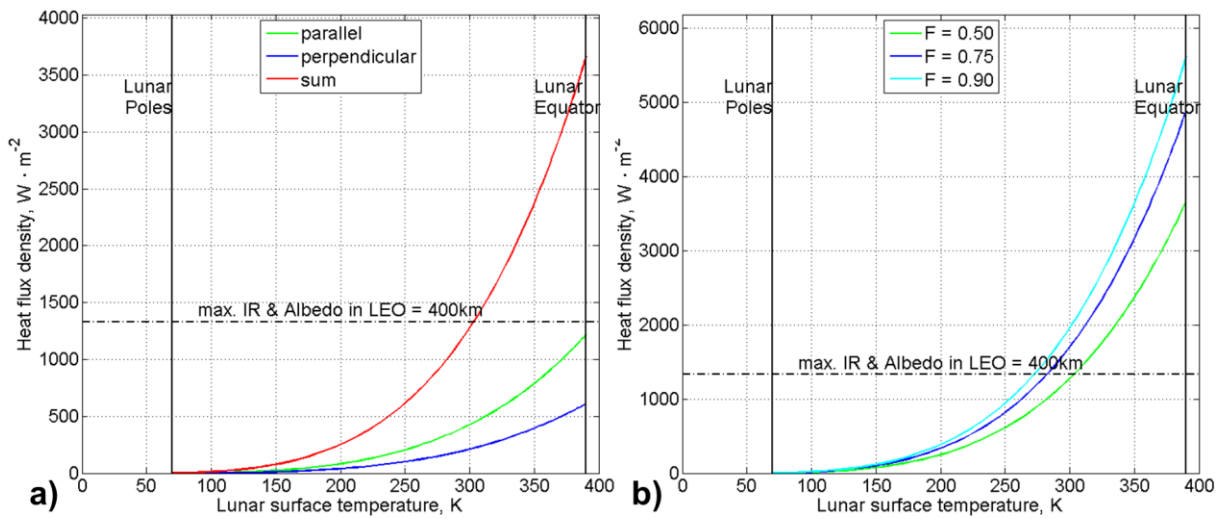
Figure 6-5: a) increase of infrared heat flux from 70 K to 390 K for a black body cube on the Moon and b) change in absorbed infrared heat flux with increasing view factor to the ground.
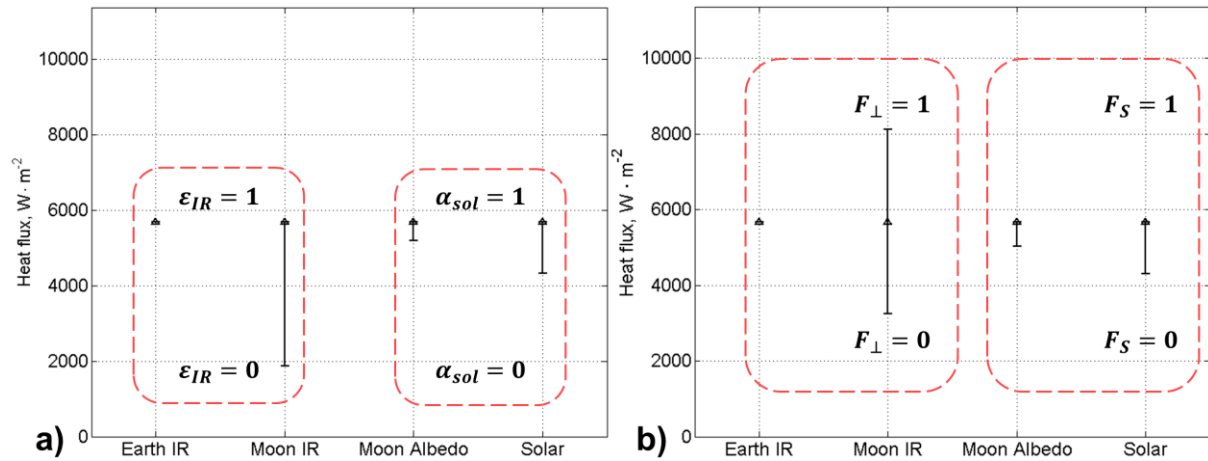
Figure 6-6: Parameter analysis for a) impact of altered ε_{IR} and α_{sol} of the sample body and b) of the view factor to the surface and Sun, in a worst case hot.

6.3 Semi-Transient Cases

Figure 6-7 shows the comparison of static and semi-transient calculations for cube temperature on the lunar surface. The cube has an edge length of 1 m. The view factors to the ground are $F_{M,\perp} = 1$ for the bottom side and $F_{M,\parallel} = 0.5$ for the circumferential sides. The cube is assumed to be a homogenous black body, modeled as one single lumped thermal node. 100 semi-transient time steps are calculated. The worst case hot assumes full exposure to the Sun, an albedo of 0.12 [-] a lunar surface temperature or 390 K and an emissivity of the lunar surface of 0.97 [-].In the worst case cold, the lunar surface temperature is 70 K and no solar heat flux is absorbed. The black body cube reaches a maximum temperature of $T_{hot,min}$ = 360 K and minimum temperature of $T_{cold,min}$ = 58 K for the worst case hot and cold respectively. In the semi-transient case the simplified regolith surface temperature from section 5.3.1 is used. The incident solar heat flux depends on changes of solar elevation angle over time, and for different lunar latitudes. The cubes' black body static equilibrium temperature is calculated for each time step, as a balance of incident solar and infrared heat flux. The black body equilibrium temperature of the cube is always lower than the lunar surface temperature because it can also radiate to deep space. The maximum temperature decreases with increasing latitude.
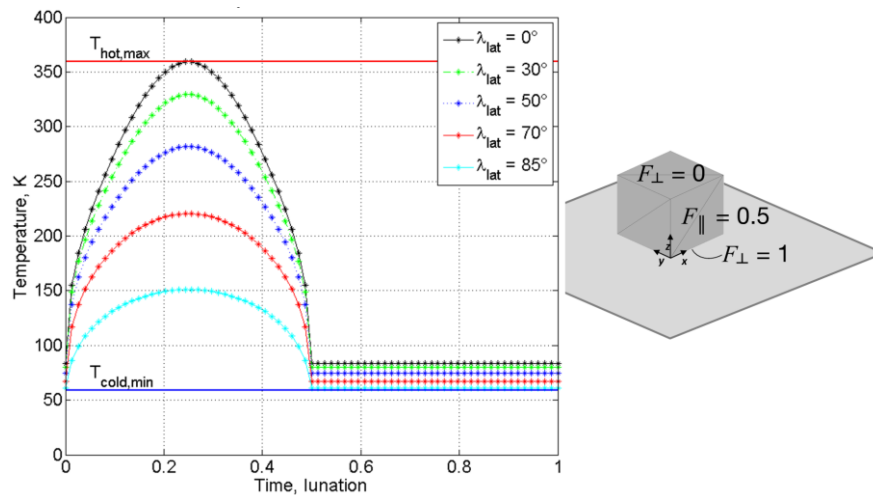
Figure 6-7: Comparison of static and semi-transient calculation for a cube at different latitudes on the lunar surface.

The transient cool down of a sample body can be calculated with an equation derived from Fouriers law. It is a simplification for the nonlinear, nonhomogeneous, ordinary differential equation that allows no analytical solution (Incropera and DeWitt 2002; Karam 1998). The equation can only be applied to perfect cooling without external or internal heat loads.

$$T(t) = \left[\left(\frac{3 \cdot \varepsilon \cdot A \cdot \sigma \cdot t}{C} + \frac{1}{T_0{}^3} \right)^{-1} \right]^{1/3} \tag{101}$$

T [-] is the temperature after time t [s], A [m²] is the surface and C the capacity of the of the sample body, ε [-] its emissivity, T_0 its initial temperature, σ the Stefan-Boltzmann constant, and t the time [s]. Figure 6-8 shows a transient cool down for the black body for a period of 20 min. The higher the capacity the lower is the change in temperature over time, which is a trivial finding.
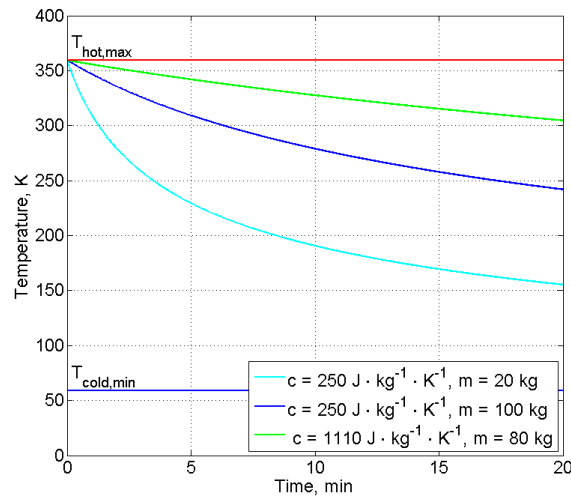
Figure 6-8: Transient cool down for sample bodies of different capacity.
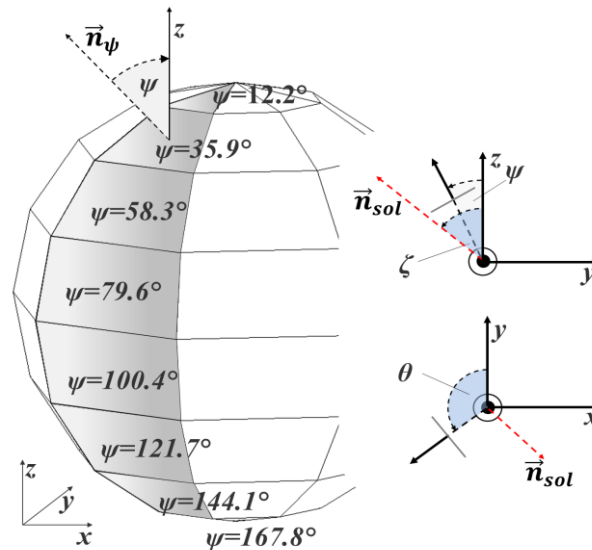
Figure 6-9: Definition of angles for the sample body.

In the following, the results of a parametric study for the total received heat flux on the sides of a facetted sphere are presented. The total received heat flux is a combination of infrared, direct and reflected solar heat flux. The lunar surface emissivity is 0.97 [-] and the albedo is 0.12 [-]. The surface temperature is calculated according to equation (93) and (94) in section 5.3.1. Figure 6-9 shows the sample body and introduces the used angles. The *xyz*-coordinate system is a topocentric selenographic coordinate system with *z* pointing towards local zenith, *y* to local north and *x* completing the right-handed coordinate system. ψ [°] is the angle between local zenith and the surface element normal vector $\vec{n}_\psi$ [-]. θ [°] is the longitude on the sample object sphere, i.e. the angle between local north and the direction of one slice of elements (a 'slice' is colored in grey in Figure 6-9) and ζ [°] is the angle between local zenith and the vector pointing to the Sun $\vec{n}_{sol}$ [-].

The static model that is used to calculate the solar and infrared heat fluxes on the sample body has the benefit of a) using simple view factors, and b) calculating one or several lunar days (lunations) in a short simulation time. The view factors to the Sun F_{Sol} [-] and to the lunar surface $F_{M,surf}$ [-](Siegel and Howell 1992) are given by the following equations:

$$F_{sol} = \vec{n}_\psi \cdot \vec{n}_{sol} \qquad (102)$$

$$F_{M,surf} = \frac{1}{2} \cdot (1 - cos\,\psi) \tag{103}$$

The local surface normal vector $\vec{n}_\psi$ [-] and vector to the sun $\vec{n}_{sol}$ [-] are used (see Figure 6-9 for definitions). The Sun angle is time-dependent with the local surface temperature according to:

$$\vec{n}_{sol} = \left[sin\left(\frac{\pi}{2} - \lambda_{lat}\right) \cdot cos(\Omega \cdot t), \quad cos\left(\frac{\pi}{2} - \lambda_{lat}\right), \quad sin\left(\frac{\pi}{2} - \lambda_{lat}\right) \cdot sin(\Omega \cdot t) \right]^T \tag{104}$$

Hence, the heat flux densities from the lunar surface $\dot{Q}_M$ [W·m^{-2}], from the Sun directly $\dot{Q}_{sol}$ [W·m^{-2}], as well as via reflection $\dot{Q}_{alb}$ [W·m^{-2}], can be calculated:

$$q_M = T_M^4(t, \lambda_{lat}) \cdot \varepsilon_{IR} \cdot \sigma \cdot F_{M,surf}(\psi) \tag{105}$$

$$q_{sol} = S \cdot F_{sol}(t, \psi) \tag{106}$$

$$q_{alb} = S \cdot \alpha_{sol} \cdot sin(\zeta(t)) \cdot F_{sol}(\psi) \tag{107}$$

Figure 6-10 shows the total heat flux on the facetted spherical sample object at the lunar equator during lunar day. Depicted are the surface elements inclined at different angles. The full lines are used for elements with a higher view factor to space, and the dashed lines have a higher view factor to the lunar surface. The full black line marks a reference heat load. The reference heat load is the theoretical amount of heat flux emitted by a radiator at an operation temperature of 300 K. The difference between the reference value and one of the colored lines is the heat flux that can either be rejected or is accumulated. If lines are above the reference heat flux the difference is the amount of heat accumulating on the radiator and if the line is underneath the reference line, the difference marks the amount of heat that can be emitted or rejected.
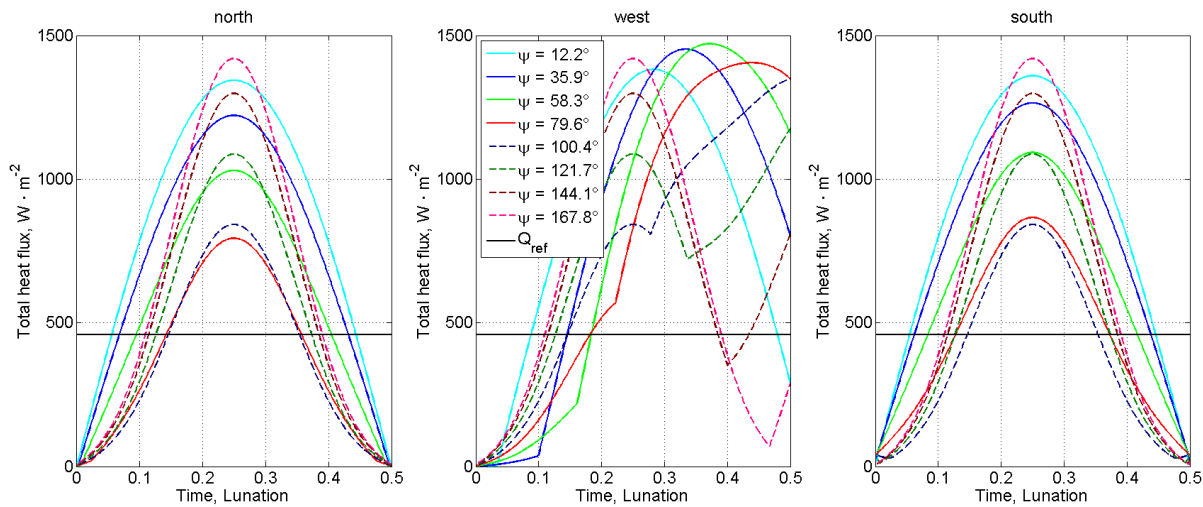
Figure 6-10: Heat flux combined for solar and IR for a static black body at the lunar equator. Left) north facing Middle) west facing, and Right) south facing part of the sample object.

Figure 6-11 and Figure 6-12 show the same surface elements at $\lambda_{lat} = 50°$ and $\lambda_{lat} = 85°$, respectively. This approach can be used to evaluate radiator efficiency at different locations on the Moon, and for different times of the lunar day. The highest loads can always be seen on the south facings elements[15]. The infrared heat flux is uniform and independent of the general direction of the surface elements but is impacted by the angle to the local zenith vector. The solar heat flux depends on the angle between local normal and sun vector. Elements directing to the west or east have a phase lag compared to elements

---

[15] The shown case considers sample objects on the northern hemisphere of the Moon. For sample objects on the southern hemisphere of the Moon the results must be inverted for north and south.

oriented north or south. Both, the solar as well as infrared heat flux densities, decline with increasing latitude.
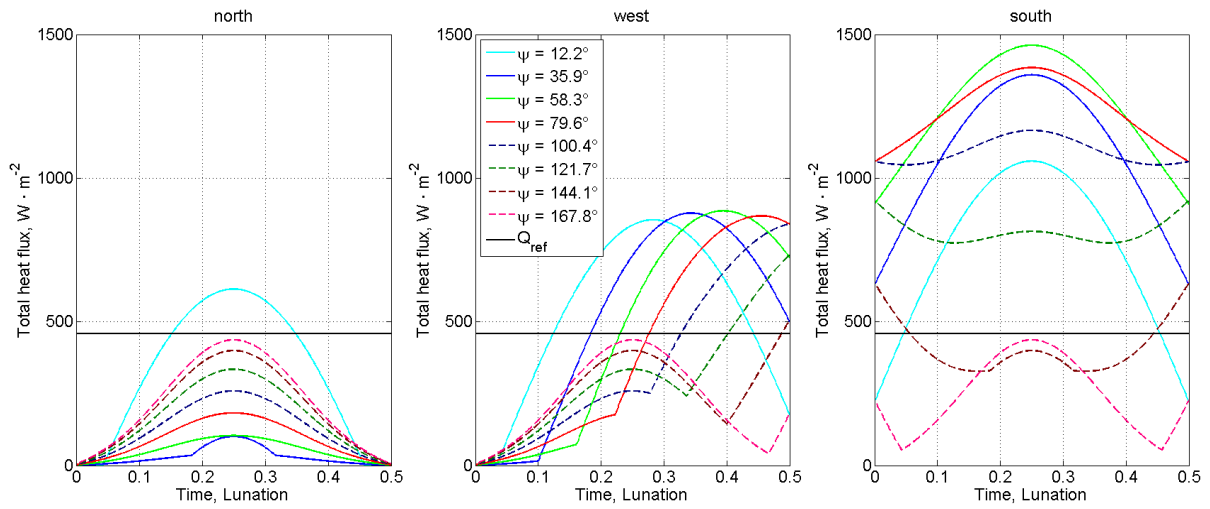
Figure 6-11: Heat flux combined for solar and IR for a static black body at λ_{lat} = 50°. Left) north facing, Middle) west facing, and Right) south facing part of the sample object.
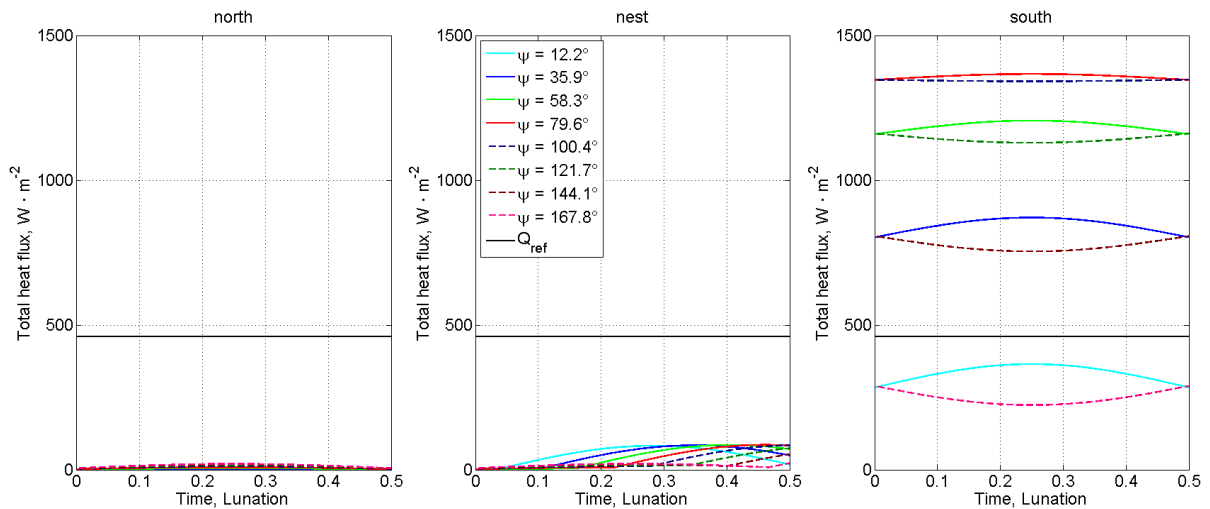
Figure 6-12: Heat flux combined for solar and IR for a static black body at λ_{lat} = 85°. Left) north facing, Middle) west facing, and Right) south facing part of the sample object.

6.4   Transient Long-Term Cases

In this section simulation results are presented which were created in ESATAN-TMS r4®. The *TherMoS* tool was used to create the lunar surface with the surface features: boulder, an inclined slope, and a crater. Furthermore the material properties for the regolith were mapped from the *TherMoS* tool on the ESATAN-TMS® model. The geometry was transferred via *.erg*-files. ESATAN-TMS® allows for fast long-term simulations but is restricted to static objects. It does not allow for relative movement between the surface of a planet and a sample object. The transient movement of the Sun is modeled with 12 positions around one orbit. In the case of the Moon the 'orbit height' is the distance between Earth and Moon. The 'orbit period' is one lunation, i.e. 29.5 Earth days. With this approach the long-term effects of surface features on the temperature inside a sample body can be calculated.

For the long-term-calculations in ESATAN, the sample bodies were simplified as cubes with a thermal node on each surface and one lumped core node. An exact geometric representation of the sample bodies would have created a multitude of internal conductive interfaces and view factors. This increased complexity would have restricted the results to one specific case. By using a cube as sample body, with the material properties of a rover and a human in a spacesuit the results are more generic. The material properties described in section 6.1.3 were used for the rover and the 'spacesuit with human' sample bodies. The six surface elements have a thickness of 0.002 m each. The total surface area of the sample body is scaled to the surface area of a spacesuit, also for the rover. The center of mass of the sample body was placed 1 m above the surface. The linear thermal conductor $G_{L,suit}$ = 0.77 W·K^{-1} and the capacitance C_{suit} = 2.26·10^5 J·K^{-1} for the spacesuit sample body can be derived from the values given above and in Table 6-2. For the rover sample body, the thermal conductor is $G_{L,rov}$ = 68.4 W·K^{-1} and the capacitance is C_{rov} = 1.196·10^5 J·K^{-1}. Further information on the implementation of the models can be found in (Hager and Walter 2012). In section 6.4.1 to 6.4.4 the results for 32 simulation runs are presented. Crater, boulder, inclined slope, and different lunar latitudes were simulated for both spacesuit and rover sample bodies. The calculated core temperatures were compared to undisturbed unobstructed cases for the same sample body at the same lunar latitude on a plane surface. The left sides of Figure 6-13 to Figure 6-16 represent the spacesuit cases. The middle images show the results for the rover sample object. On the right of each figure the regolith temperatures for an unobstructed surface element is shown for comparison.

6.4.1   Crater

The crater cases for the transient long-time calculations comprise eight simulation runs in total. Four runs for the spacesuit and four for the rover sample body (Figure 6-13). The four runs for each sample body are a crater (D_C = 0.035 km) east of the sample body (green full line), a crater to the west of the sample body (green dash-dotted line), in the center of a crater (red full line), and in the center of a crater at λ_{lat} = 85° latitude north (red dash-dotted line). The nighttime temperature is reduced for all eight cases. The behavior during lunar daytime depends on the position of the crater. The highest deviations between unobstructed and crater case are apparent for the sample objects inside the crater. The spacesuit shows maximum deviations of +25 K and -50 K and the rover of +30 K and –65 K.
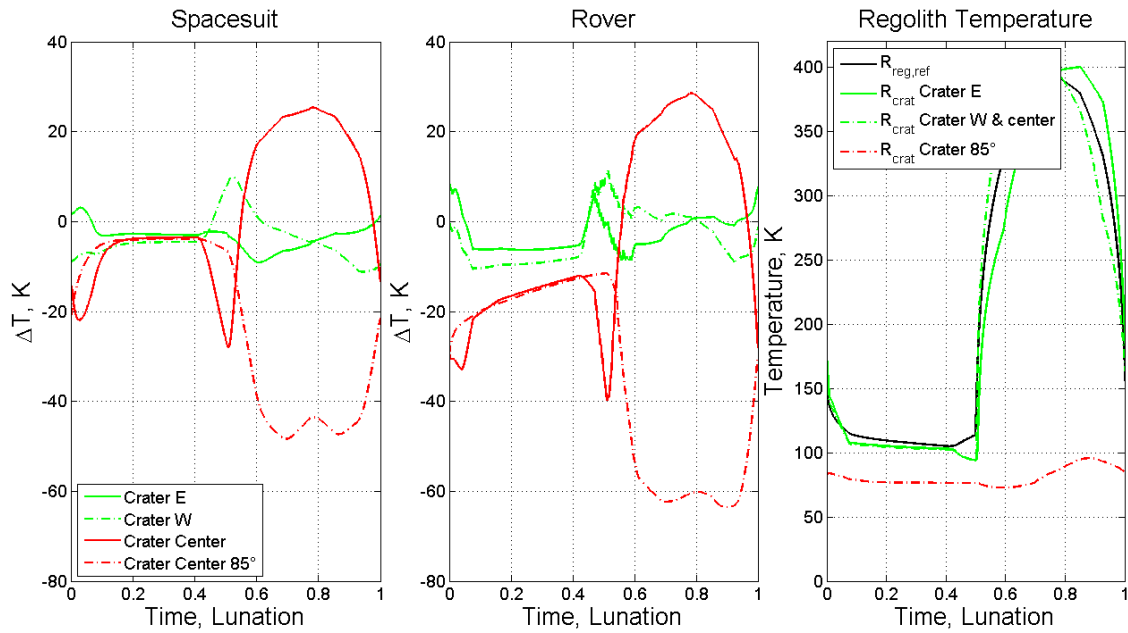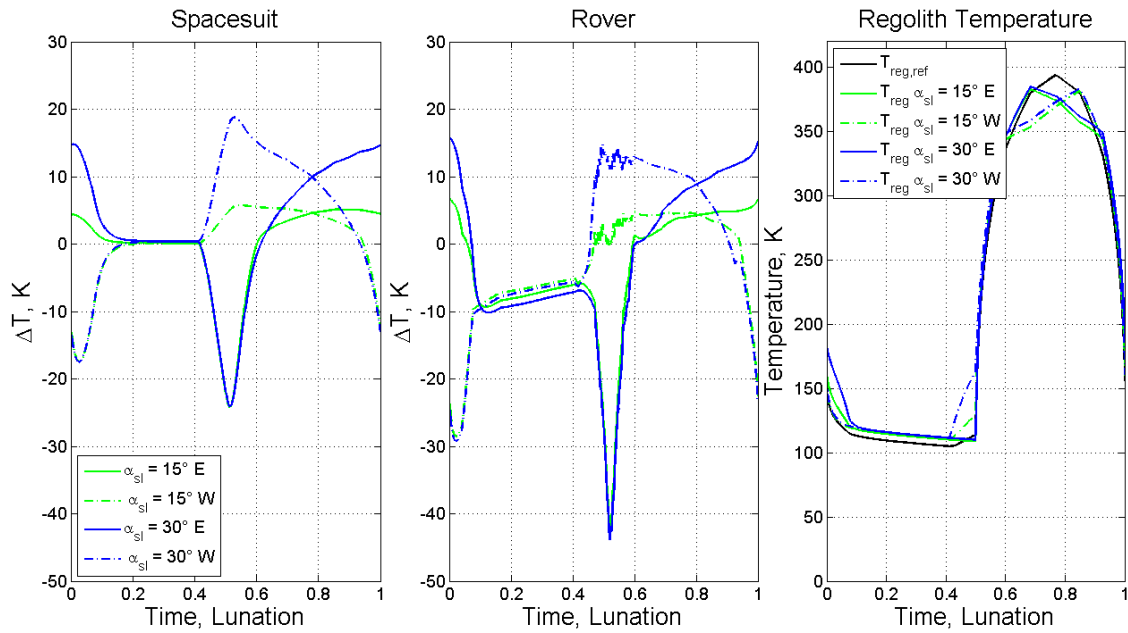
Figure 6-13: Core temperatures of a spacesuit (left) and rover (middle) sample object for four cases on the slopes and inside a crater. The lunar surface temperature (right) is given as reference.

6.4.2 Boulder

The boulder cases for the transient long-time calculations comprise eight simulation runs in total. Four runs for the spacesuit and four for the rover sample body. The four runs for each sample body are a boulder (D_B = 4 m) east of the sample body (green full line), a boulder to the west of the sample body (green dash-dotted line), a boulder on the eastern side at λ_{lat} = 30° latitude north (red full line), and at λ_{lat} = 50° latitude north (blue dashed line) (Figure 6-14).
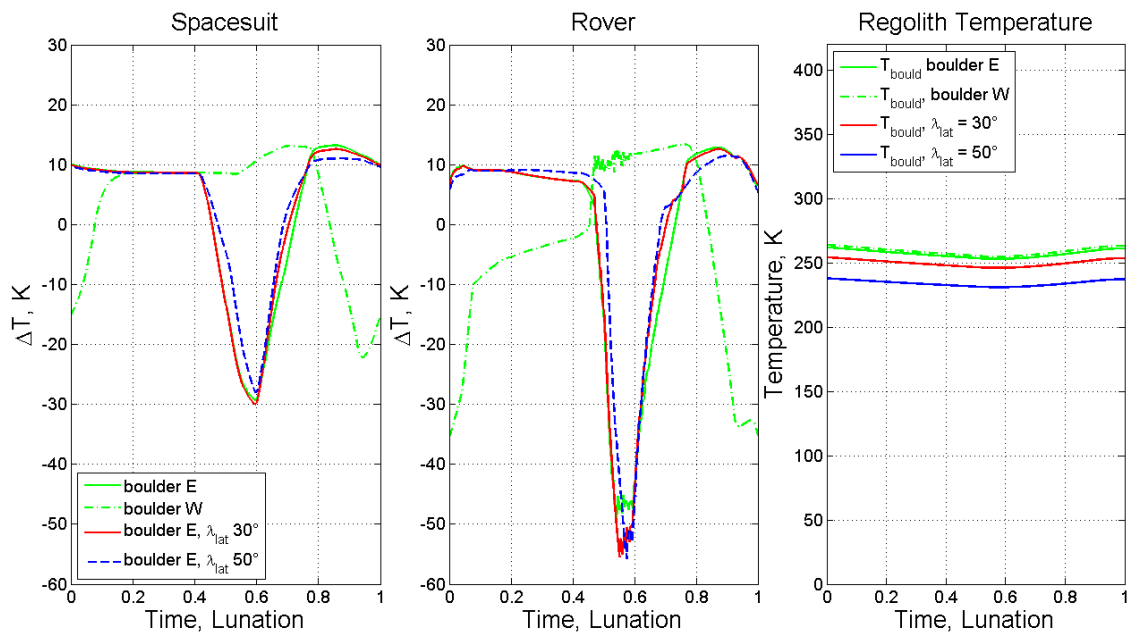
Figure 6-14: Core temperatures of a spacesuit (left) and rover (middle) sample object for four cases in the vicinity of a boulder. The lunar surface temperature (right) is given as reference.

The nighttime temperature is elevated for all cases except for the rover placed to the west of the boulder. The behavior during lunar daytime depends on the position of the sample object in relation to the boulder.

The highest deviations between unobstructed and boulder case are found at lunar noon time. The sample objects temperature than is -30 K (spacesuit) to -55 K (rover) colder than in the unobstructed case. The effect grows slightly with increasing latitude.

6.4.3   Latitude

The latitude cases for the transient long-time calculations comprise eight simulation runs in total. Four runs for the spacesuit and four for the rover sample body. The four runs for each sample body are at lunar latitudes of λ_{lat} = 30° (green dash-dotted line), at λ_{lat} = 50° (blue dotted line), at λ_{lat} = 70° (red dashed line), and at λ_{lat} = 85° (cyan full line), and are depicted in Figure 6-15. The sample body core temperature during nighttime is reduced slightly compared to the reference case at the lunar equator. The temperature difference is higher closer to the lunar Poles and during lunar noon time. The sample objects temperature is -95 K (spacesuit) to -82 K (rover) colder than in the reference case, for a latitude of 85° north.
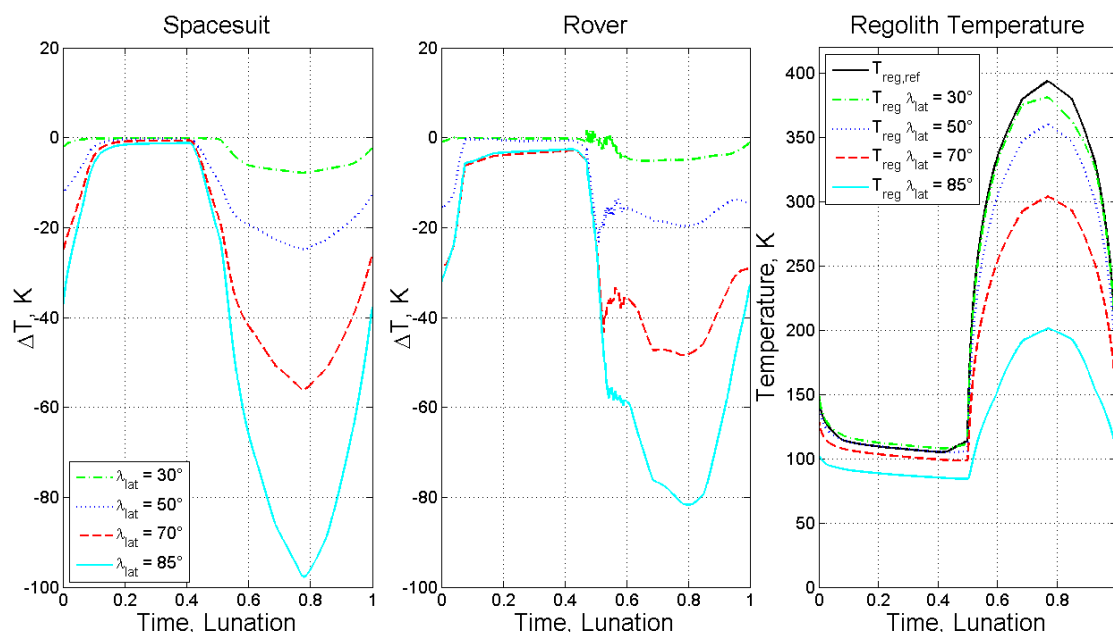
Figure 6-15: Core temperatures of a spacesuit (left) and rover (middle) sample object for four cases at different latitudes. The lunar surface temperature (right) is given as reference.

6.4.4   Inclined slope

The cases for inclined slopes for the transient long-time calculations comprise eight simulation runs in total. Four runs for the spacesuit and four for the rover sample body. The four runs for each sample body are an inclined slope with α_{sl} = 15° (green full line), α_{sl} = 30° (blue full line) to the east, α_{sl} = 15° (green dash-dotted line), and α_{sl} = 30° (blue dash-dotted line) to the west (Figure 6-16). The sample body core temperature during nighttime is reduced slightly compared to the unobstructed case for the rover sample body. The temperature differences compared to unobstructed cases are most pronounced during sunrise and sunset. The highest positive deviation is observed for the spacesuit during lunar morning with + 19 K. The highest negative deviation of -45 K takes place during lunar morning for the rover case. In general, higher slope angles lead to a larger impact on the temperature difference. Rover sample objects are more affected than the spacesuit sample object.

Figure 6-16: Core temperatures of a spacesuit (left) and rover (middle) sample object for four cases in the vicinity of inclined slopes. The lunar surface temperature (right) is given as reference.

6.5 Transient Short Time Cases – Exploration Rovers

In this section the results for 20 simulation runs are presented. In section 6.5.1 three cases at the lunar equator with four different variants of surface features are shown for the equatorial rover (Rov2). In section 6.5.2 one case for the lunar polar region and four different variants of surface features are shown for the polar rover (Rov1). In section 6.5.1 and section 6.5.2 the focus is set on the overall solar and infrared heat flux densities on the entire rover. In section 6.5.3 the polar case is repeated for the more detailed MPE rover. In contrast to sections 6.5.1 and 6.5.2 the focus is set on the differences in heat flux for each individual side of the rover. All results shown hereafter were filtered with a medium low pass filter and outliers beyond $q_{sol,max}$=1,610 W·m^{-2} or $q_{IR,max}$ = 1,524 W·m^{-2} were neglected. The values for $q_{sol,max}$ and $q_{IR,max}$ base on the assumption of a black body with a view factor of 1 to the Sun and the lunar surface, plus an uncertainty of 5 %. The general rover paths were described in section 6.1.2. In Table 6-5 the segments of a rover path are described in more detail. For each segment the task, its duration, and the rover velocity is given. The velocity of rovers navigated from Earth with certain autonomous skills lie in the range of u_{rov} = 0.0054 m·s^{-2} to 0.015 m·s^{-2} (Haarmann et al. 2012; Kubota et al. 1999). A velocity of u_{rov} = 0.01 m·s^{-2} was assumed for the rovers presented in the case studies.

Table 6-5: Description of the different segments of a rover path.

Task	Description	Task duration [s]	Elapsed time [s]	Velocity [m·s^{-2}]
1	Cruise	2,260	2,260	0.006
2	Stop and investigation of sample site	100	2,360	-
3	Maneuvering for sample collection	320	2,680	0.006
4	Sample collection / instrument operations / data transmission	500	3,180	-
5	Departure from sample site	420	3,600	0.006
6	Resume cruise	2,460	5,060	0.006

6.5.1 Lunar Equator

The simulations were made for unobstructed transits (red line), boulder east transit (green line), boulder west transit (blue line), and a transit through 5 boulders (cyan line) of the equatorial rover (Rov2). For reference, the solar and infrared values for a static view factor calculation are shown (black line). The time of lunar day was varied between noon and dusk. In the third case all the different features and transits were set on the 34° inclined slope of a crater with D_C = 1 km.

Figure 6-17 shows the solar (left) and infrared (right) heat flux densities for different parameter settings at the lunar equator at local noon for the equatorial rover (Rover2). The solar heat flux does neither change in the course of time nor in between the different cases or compared to the static reference case. The infrared heat flux is mostly elevated compared to the static sample case. Boulder and 5-boulder transits show a higher overall level of infrared heat flux compared to the unobstructed case.
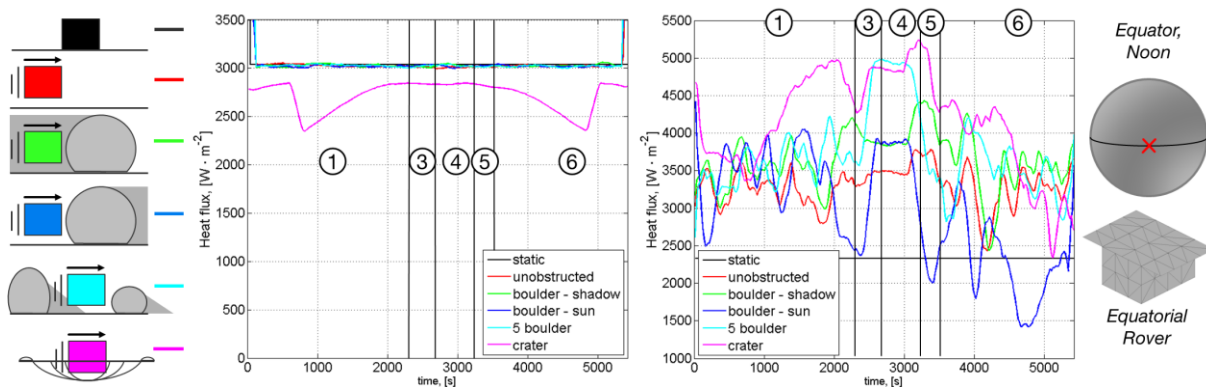
Figure 6-17: *Solar* (left) and *infrared* (right) heat flux densities for different parameter settings at the lunar equator at local noon for Rover2.

Figure 6-18 shows the solar (left) and infrared (right) heat flux densities for the different parameter settings at the lunar equator at local dusk for the equatorial rover (Rover2). The angle of incidence for the solar rays is 10°. The overall level of solar heat flux is lower than in the noon case. The impact of transits through the shadow of a boulder can be seen by the drop in solar heat flux for the 5-boulder and boulder cases. The change in orientation of the rover also alters the amount of incident solar heat flux. An increase in infrared heat flux can be observed in the vicinity of boulders, especially if the transit is on the western side of the boulder. On the western side the boulder reaches higher temperatures and thus emits more infrared radiation. In the unobstructed case and far away from the boulder, the infrared heat flux equals the values calculated with static view factors.
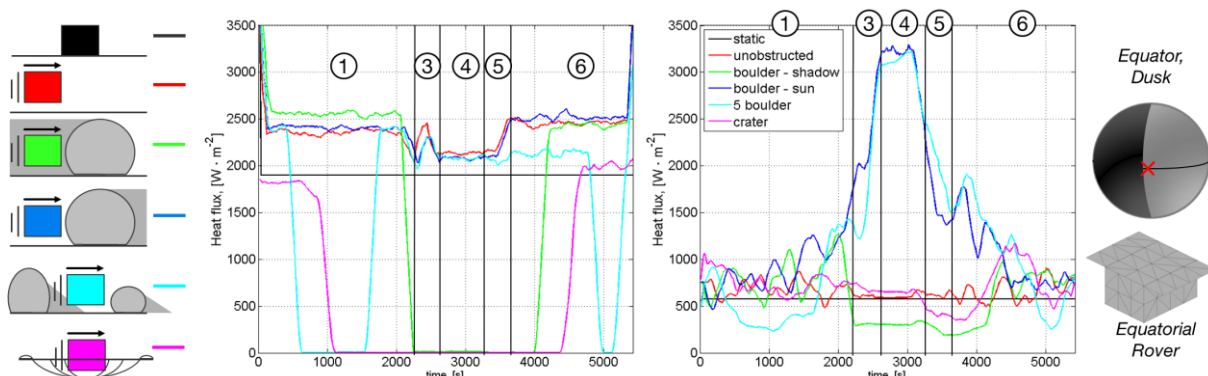
Figure 6-18: *Solar* (left) and *infrared* (right) heat flux densities for different parameter settings at the lunar equator at local dusk for Rover2.

Figure 6-19 shows the solar and infrared heat flux densities for different parameter settings at the lunar equator at local dusk inside a crater with D_C = 1 km. The surface features and rover sample body are placed on a slope with 34° inclination. Together with the 10° solar inclination for local dusk this leads to an angle of incident of 44°. The values for the static view factor calculations resemble the conditions on an unobstructed plane outside the crater. The solar heat flux varies to a large extend in all cases. In general the solar heat flux of all cases is lower than in the static case. In contrast, the infrared heat flux is elevated compared to the static case. Boulder and 5-boulder cases are less elevated than the unobstructed and boulder-west transit cases.
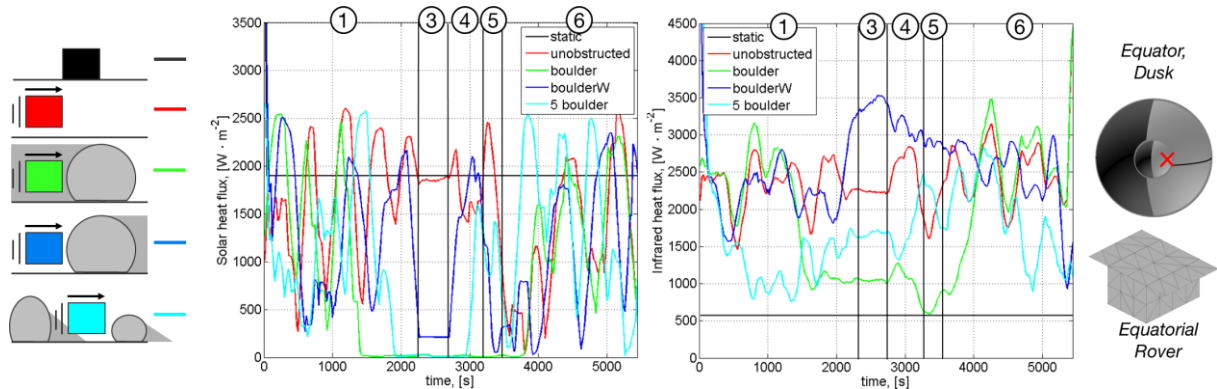
Figure 6-19: *Solar* **(left) and** *infrared* **(right) heat flux densities for different parameter settings at the lunar equator at local dusk, on a 34° slope inside a crater with D_C = 1 km, for Rover2.**

6.5.2 Lunar Poles

The simulations were made for unobstructed transits (red line), boulder east transit (green line), boulder west transit (blue line), and a transit through 5 boulders (cyan line) of the polar rover (Rov1). For reference, the solar and infrared values for a static view factor calculation is shown (black line). The time of lunar day was set to local noon. The angle of incident of solar rays was set to 2°. Figure 6-20 shows the solar (left) and infrared (right) heat flux densities for polar noon and the polar rover (Rover1) sample object.
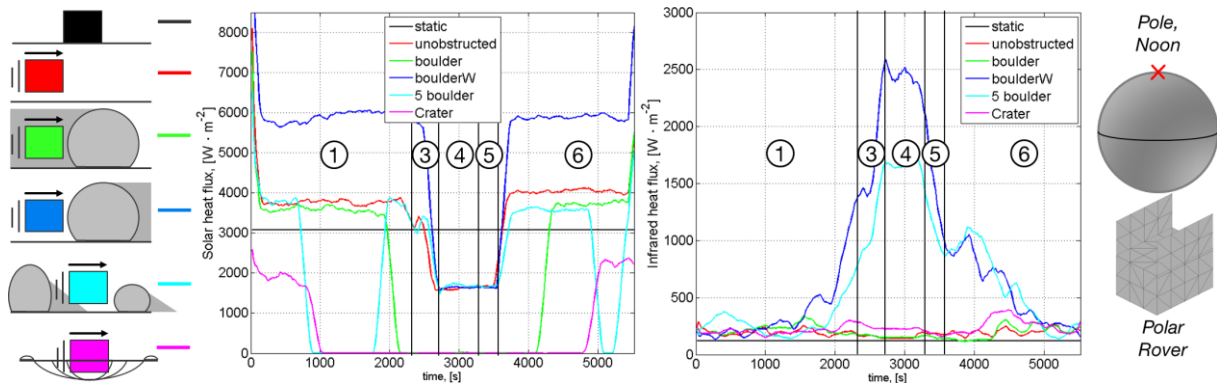
Figure 6-20: *Solar* **(left) and** *infrared* **(right) heat flux densities for different parameter settings at the lunar Poles at local noon for Rover1. The numbers refer to sections of the rover path described in Table 6-5.**

The total solar heat flux as sum over all surface elements is elevated compared to the static view factor calculations for all parameter variants. A reduction of incident solar rays is apparent if the rover changes its orientation and the solar arrays are parallel to the incoming rays. In the boulder case this change in orientation has no effect because the rover is already in the shadow of the boulder. The impact of the shadow is apparent as in the equatorial dusk cases. The infrared heat flux equals the static view factor calculations far away from the boulder. In the vicinity of the boulder, for the west-transit and 5-boulder case the infrared heat flux is elevated. In parallel to the lunar dusk case at the equator, the illuminated boulder side has an elevated temperature leading to higher infrared heat fluxes.

6.5.3 Mobile Payload Element - Polar Cases

In parallel to section 6.5.2 the simulations for the mobile payload element (MPE) rover were made at lunar polar conditions around local noon. The angle of incident of solar rays was set to 2°. The cases were an unobstructed transit (red line), boulder east transit (green line), boulder west transit (blue line), and a transit through 5 boulders (cyan line). For reference, the solar and infrared values for a static view factor calculation is shown (black line). Figure 6-21 to Figure 6-23 shows the infrared heat flux densities on the MPE rover at the lunar Poles at local noon.
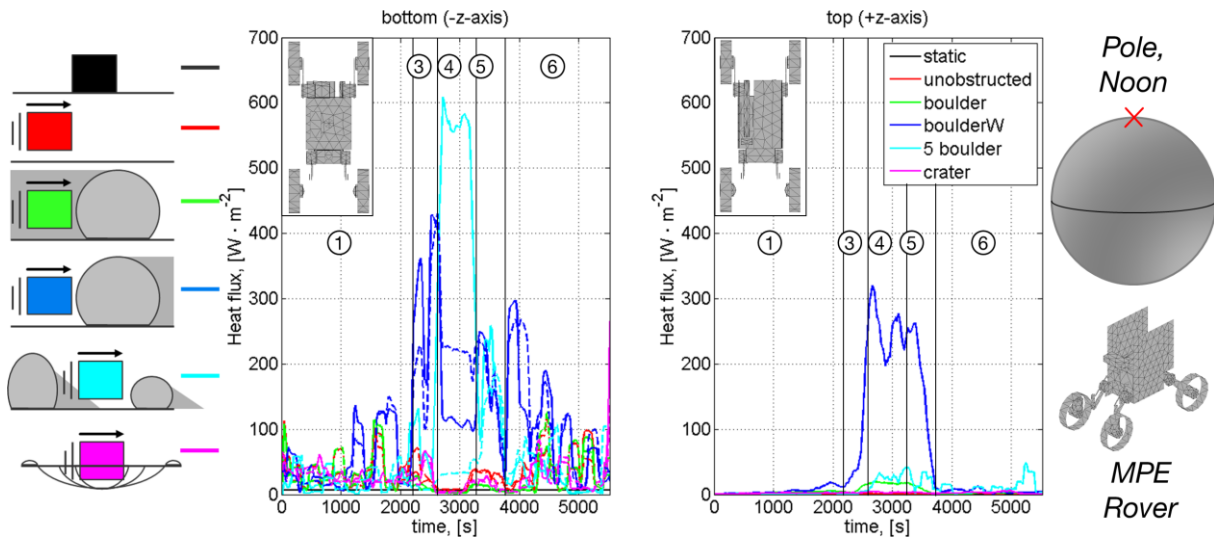
Figure 6-21: *Infrared* **heat flux densities on the bottom (left) and top (right) of the MPE rover at the lunar Poles at local noon. (dash-dotted lines represent the heat switch in the center).**
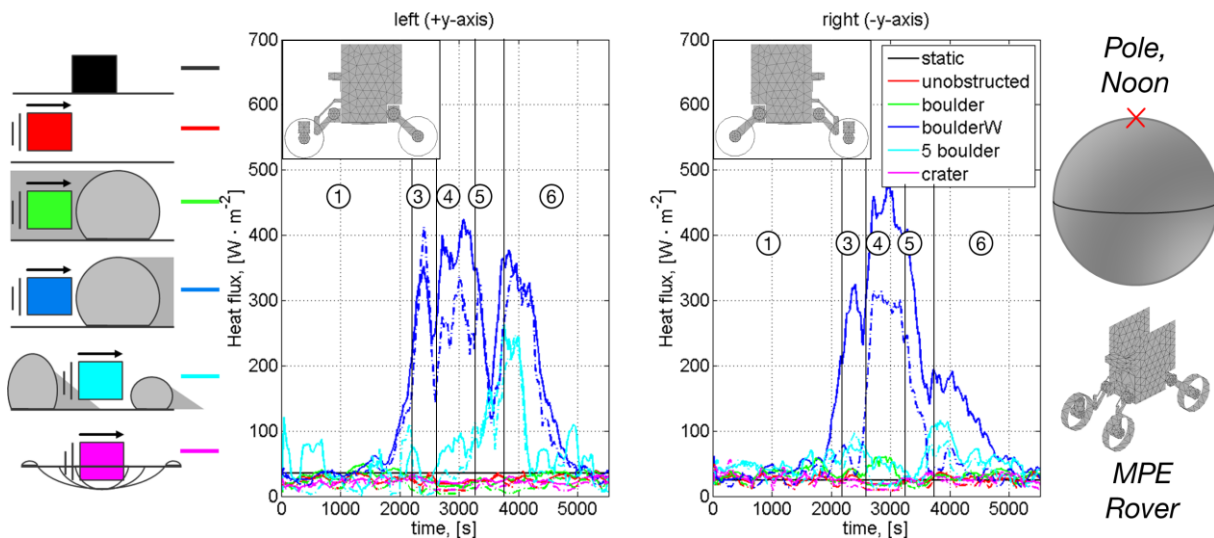
Figure 6-22: *Infrared* **heat flux densities on the left (left) and right (right) sides of the MPE rover at the lunar Poles at local noon (dash-dotted lines represent the upper part and the full lines the lower part of the solar array elements).**
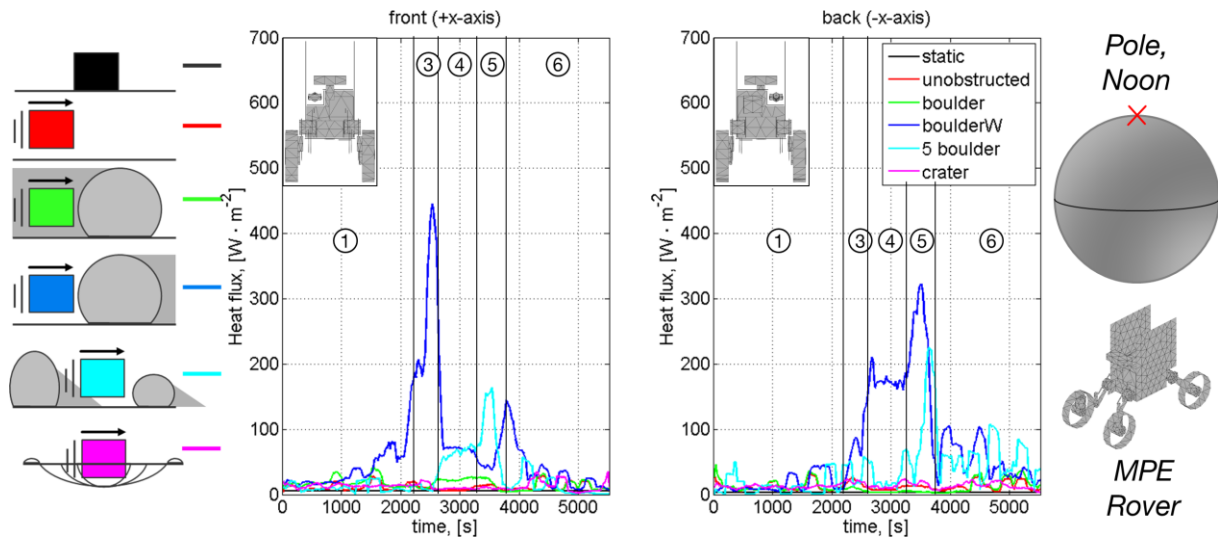
Figure 6-23: *Infrared* **heat flux densities on the front (left) and back (right) sides of the MPE rover at the lunar Poles at local noon.**

From Figure 6-21 to Figure 6-23 it is apparent that especially the transit on the western side of an illuminated boulder has a large impact on the absorbed infrared heat flux on all sides of the rover. The transit through a field of 5-boulders also leads to higher heat loads on all sides of the rover. A transit on the eastern side mainly impacts the infrared heat flux on the top of the rover.

Figure 6-24 to Figure 6-26 shows the solar heat flux densities on the six sides of the MPE rover. The left side of the rover is exposed to the full solar heat flux due to the low angle of incident. The change in rover orientation close to the boulder can be seen in Figure 6-25 and Figure 6-26. The solar heat flux on the left side drops to zero and the back of the rover is illuminated by the Sun. The shadow periods in the boulder-east transit and the 5-boulder cases can also be seen in Figure 6-25.
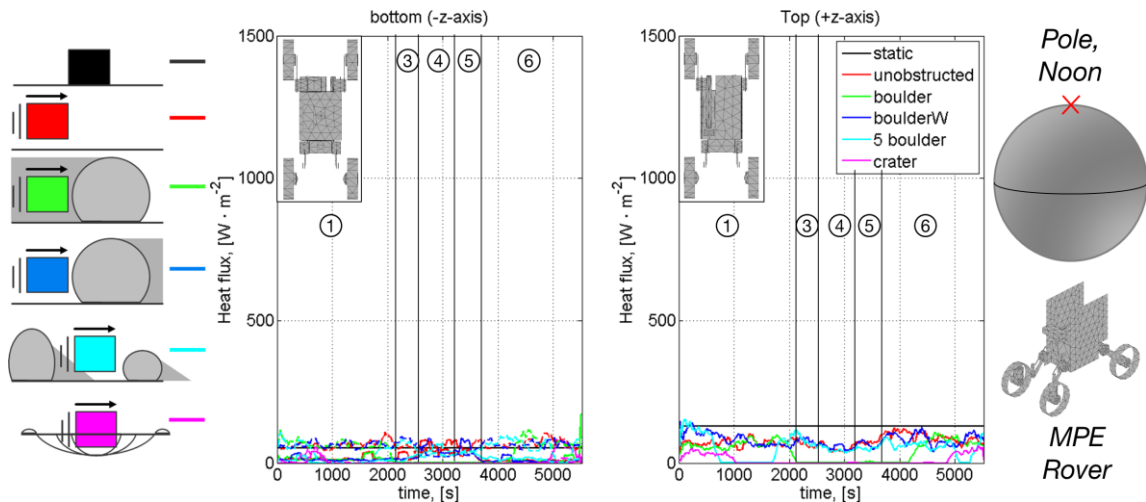
Figure 6-24: *Solar* **heat flux densities on the bottom (left) and top (right) of the MPE rover at the lunar Poles at local noon.**
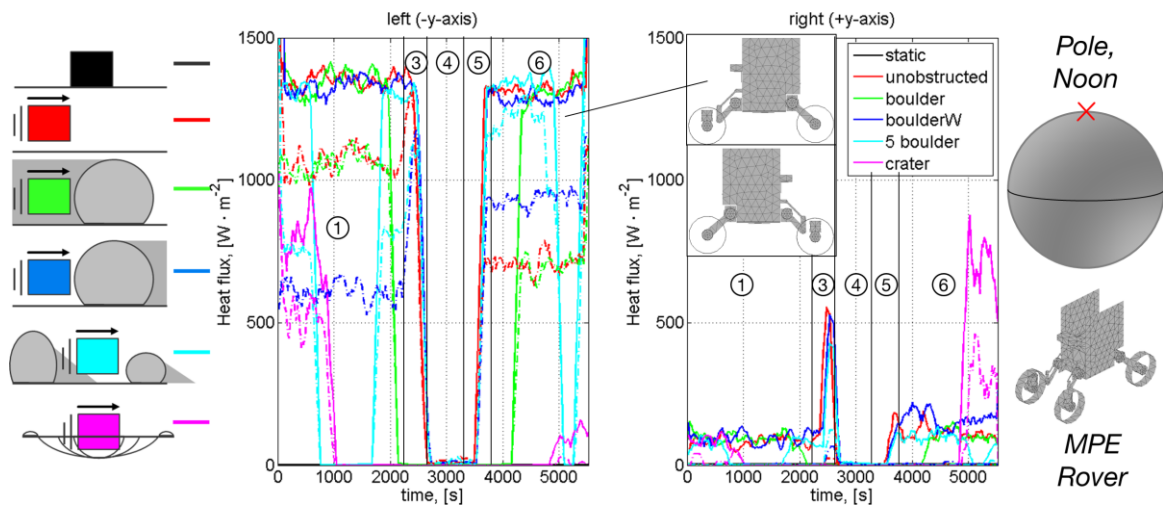
Figure 6-25: *Solar* **heat flux densities on the left (left) and right (right) side of the MPE rover at the lunar Poles at local noon.**
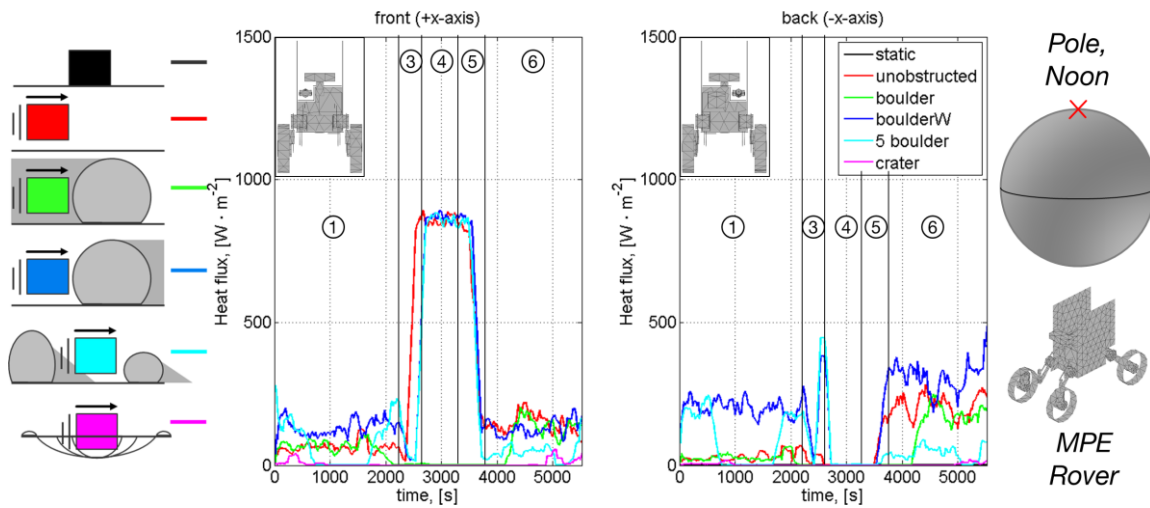
Figure 6-26: *Solar* **heat flux densities on the front (left) and back (right) side of the MPE rover at the lunar Poles at local noon.**

6.6 Transient Short Time Cases – Spacesuits

The spacesuit cases were set in the same environments as the rover sample bodies. The general paths are the same for rovers and spacesuits and can be found in section 6.1.2. Different from the rover cases the spacesuit moves faster and performs more complex tasks. The segments of the spacesuit task are explained in Table 6-6. The tasks range from slow walk, to a bent-over posture for sample collection. The tasks are based on Apollo 15 and 16 mobility reports (Kubis et al. 1972a; Kubis et al. 1972b). Further tables with the velocities for traverses of different length are gathered in Appendix A.5). The dimensions and postures of the suit are depicted in Figure 6-27. The dimensions were derived from the Apollo AS 7 mock-up at the University of Colorado, Boulder. The PLSS dimensions were taken from the "Man-System Integration Standard Vol 1" chapter 14 (NASA 1995). Arms, Legs, and Torso were modeled as cylinders, the PLSS as a cuboid, and the head was modeled as a sphere-segment. The resolution of the spacesuit sample object was selected to have surface elements with at least one edge $\geq$ 0.1 m. The bent posture was derived from the Apollo 16 mobility report. Angles up to 35° were reported for the retrieval of a hammer. The Apollo AS7 suits were not dexterous enough to kneel and the astronauts were unable to see anything closer than 0.6 m in front of their feet, due to the Hasselblatt camera on the front of their suits. To collect geological samples the Apollo astronauts used rakes with a length of 1 m. They had to bend over to survey and collect a sample. The bend posture was assumed to be a representative geological task.
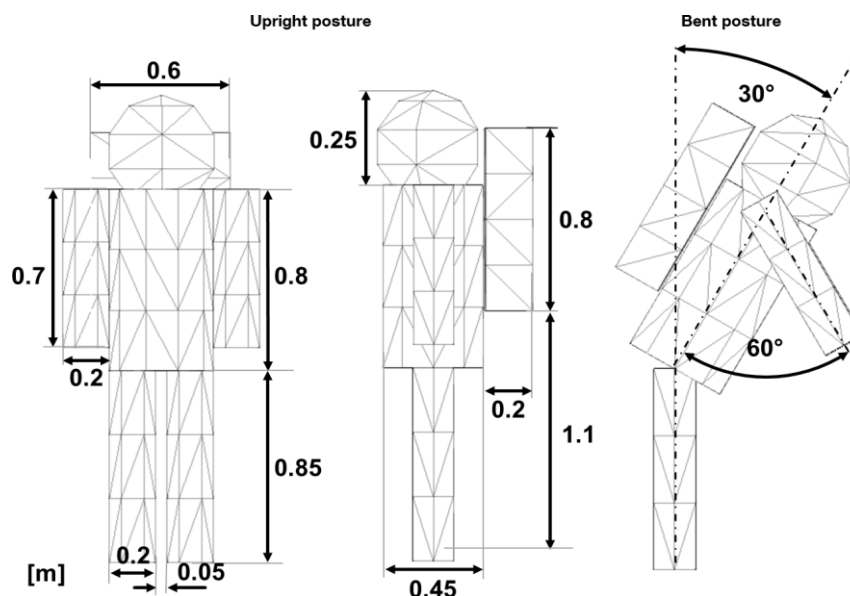
Figure 6-27: Dimensions and body postures of the spacesuit sample body. The dimensions are given in [m].

The spacesuit case focuses on the heat flux rate in heat flux densities for the segments of a path and how they are impacted by nearby surface features at various locations on the lunar surface. The rates of change are important for the design of control algorithms.

In total 15 spacesuit cases were run. The 15 cases were five different spacesuit traverses, each in three different solar incident settings. The solar elevation angle ε_{el} was set to 90°, 10°, and 2°. A solar elevation angle of 90° represents the equatorial noon case, an elevation angle of 10° represents a case close to the terminator or at high latitudes, and an elevation angle of 2° represents a polar noon case. The spacesuit sample object traversed over an unobstructed plane (red), on the shadowed side of a boulder (green), the sunlit side of a boulder (blue), through a field of five boulders (cyan), and through a crater (magenta). The boulder has a diameter of $D_B = 12$ m and the crater a diameter of $D_C = 30$ m. The black lines mark a static reference case. Figure 6-28 to Figure 6-31 show the cases for the a $\varepsilon_{el} = 10°$. The tasks are marked with numbers according to Table 6-6. Figure 6-28 shows the infrared heat fluxes for the elements a) on the

front of the spacesuit torso and b) on the back of the PLSS. Figure 6-29 shows the heat flux rate in the infrared heat flux for each time step. Figure 6-30 shows the infrared heat flux for the elements on a) the top of the spacesuit sample objects arms and b) the front of the legs of the spacesuit sample object. In Figure 6-31 the heat flux rate in infrared heat flux is shown for arms and legs. The highest values for infrared heat flux is encountered on the top of the arms of the spacesuit sample body when it is in a bend posture (Task 5) and the top of the arms are facing the boulder. The heat flux rate is also highest for the arms when the spacesuit sample body moves in front of a sunlit boulder and then turns towards it (Task 3). Furthermore, the torso shows elevated levels of infrared heat flux when turned towards the boulder, for both the sunlit and the shadow transit. The PLSS always faces away from the boulder in the presented cases. Hence, the overall levels are lower than for the torso or arms. At the end of the traverse, when the spacesuit sample object is moving away from the boulder the view factor between PLSS and boulder increases suddenly and declines once the suit moves further away from the boulder. In the crater case (magenta) the torso receives less heat flux than the PLSS. The torso faces the cold side of the crater casted in shadow and the PLSS faces the sunlit wall of the crater. In the case with five boulders (cyan) the PLSS also faces towards the central boulder. The numbers in Figure 6-28 to Figure 6-31 represent the path segments described in Table 6-6.

Table 6-6: Description of the segments for the spacesuit paths. (* durations based on findings in Apollo 15 and Apollo 16 mobility reports (Kubis et al. 1972a; Kubis et al. 1972b).

Task	Description	Task duration [s]	Elapsed time [s]	Velocity [m·s^{-2}]	Remarks*
1	Slow Walk	36	36	0.45	Average velocity reached during Apollo 15 and 16 on level ground, with or without equipment; independent of gait
2	Survey of sample site/ taking pictures	10	46	-	Taking pictures of sites was often mentioned as task; three times were allocated with task; Apollo 15: LRV photo ~5 s; Apollo 16: Photo with flag 1,2 s; LRV photo 10 s
3	Side stepping (jumping in an arch)	4	50	0.375	4 hops to cover 1.5 m and turn 90°
4	Preparation of sampling	30	80	-	
5	Bending over	2	82	-	In reality probably around 1 s.
6	Sample collection	42	124	-	"Rake & Shake" - Sample Collection of larger rocks with a rake (1 meter long) - duration between 0.683 and 0.730 minutes(!) for ground raking and positioning in bag (p. 26/33) - this is done 2 to 4 time per sample site [Apollo 15 mobility report]
7	Return to upright posture	2	126	-	In reality probably around 1 s.
8	Turning toward path	2	128	-	Turn 90° (45°/s) probably to slow but was easier to implement
9	Wait and take pictures	10	138	-	
10	Resume Cruise	39	177	0.7	Highest speed recorded during Apollo 16 on level ground with few boulders
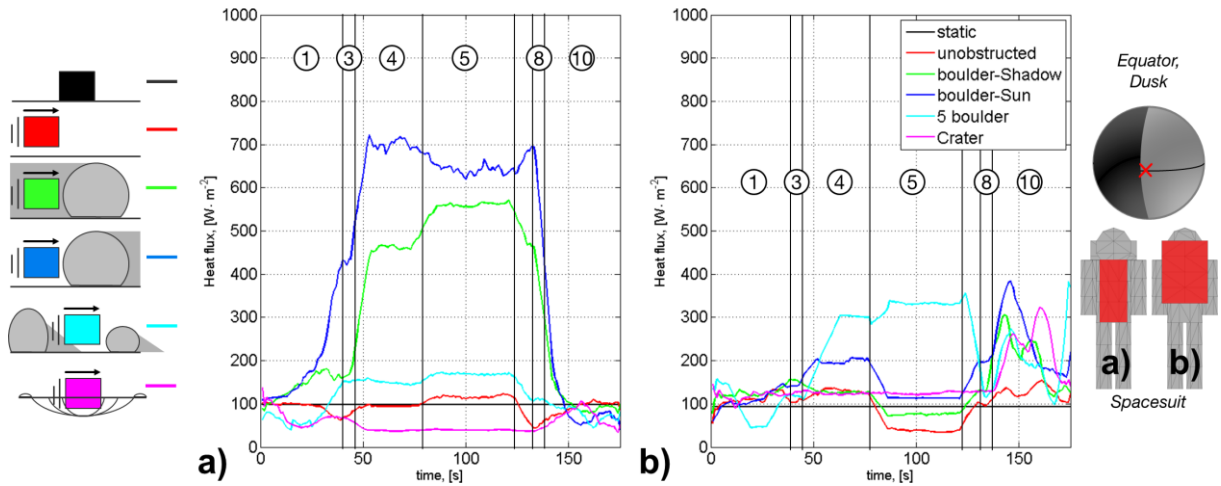
Figure 6-28: Infrared heat flux on a) front of the spacesuit torso and b) back of the personal life support system for five cases and a solar elevation angle of 10°. For numbers see Table 6-6.
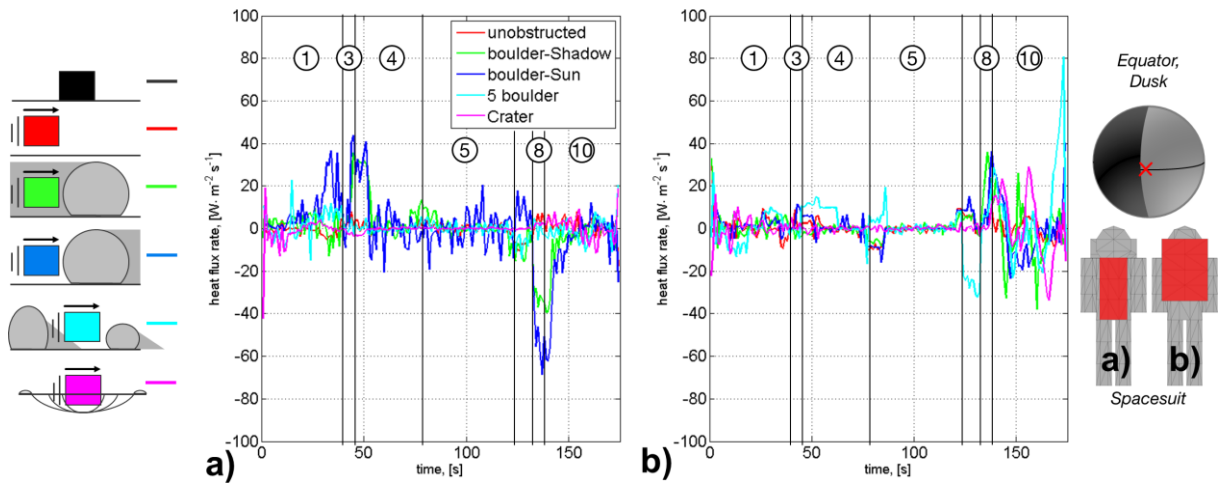
Figure 6-29: Heat flux rate for the infrared heat flux on a) front of the spacesuit torso and b) back of the personal life support system for five cases and a solar elevation angle of 10°. For numbers see Table 6-6.
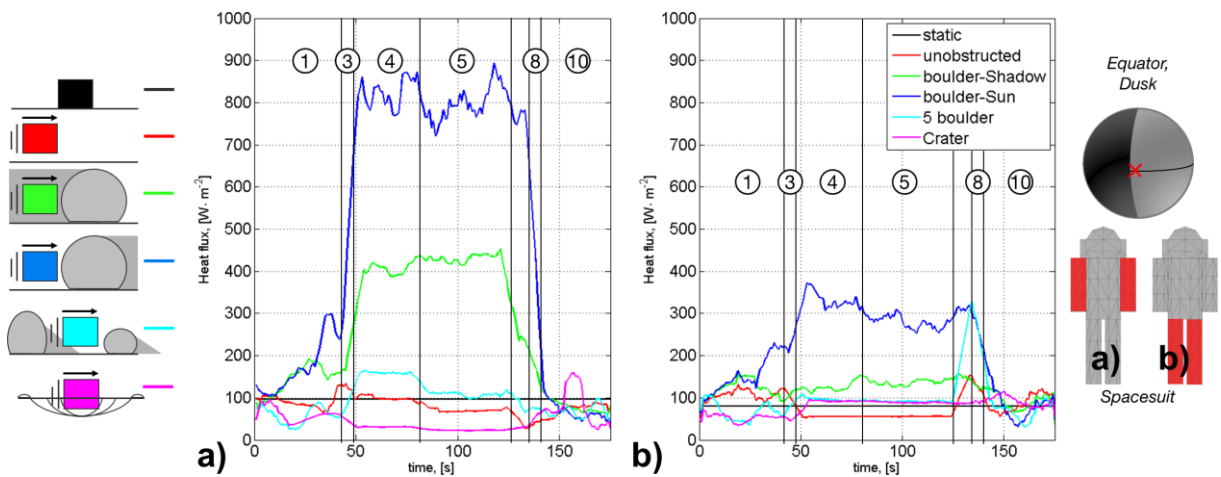
Figure 6-30: Infrared heat flux on a) arms and b) legs of the spacesuit for five cases at the lunar equator and a solar elevation angle of 10°. For numbers see Table 6-6.
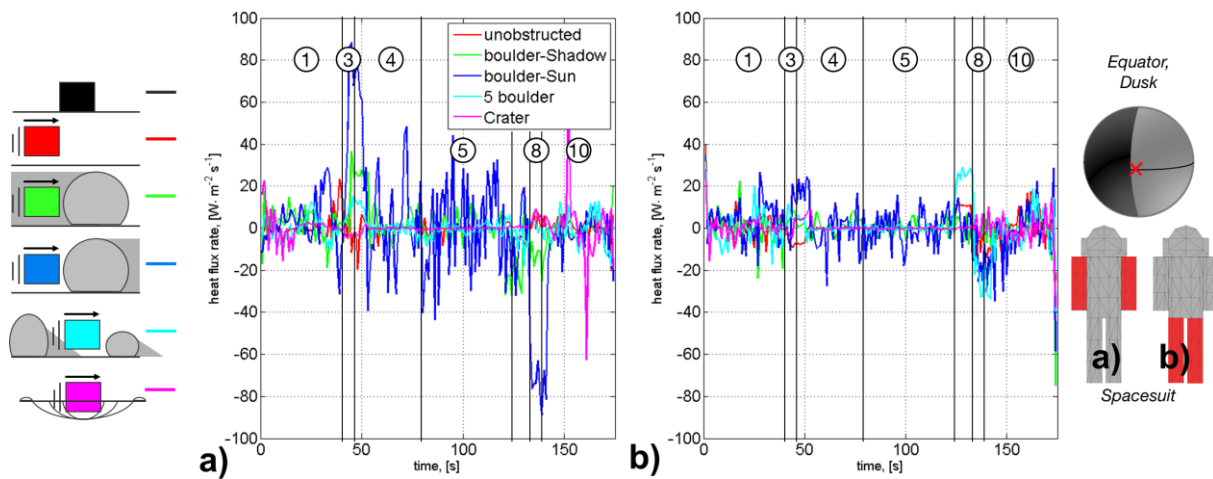
Figure 6-31: Heat flux rate for the infrared heat flux on a) arms and b) legs of the spacesuit for five cases at the lunar equator and a solar elevation angle of 10°. The numbers are according to Table 6-6.

7 Discussion & Conclusions

"It is unwise to be too sure of one's own wisdom. It is healthy to be reminded that the strongest might weaken and the wisest might err."

- Mahatma Gandhi

The thermal lunar surface environment is governed by radiative heat transfer and the material properties of the lunar surface regolith. A man-made vehicle placed on the surface of the Moon is subject to infrared and solar heat flux. The local infrared heat flux and solar heat flux depend on numerous factors. The results in chapter 6 indicate a complex interaction between the factors that cannot be addressed by mere static worst case calculations. In section 7.1 the results for the static, semi-transient, and transient cases from chapter 6 are discussed with respect to past work, to current technological development, and scientific requirements. In section 7.2 the conclusions are drawn and in section 7.3 possible future steps to enhance and pursue this thesis are presented.

7.1 Discussion

The results presented in chapter 6 are numerous and complex, consisting of different sample bodies and lunar environmental settings. The discussion section hence is further subdivided into sections addressing the initial presumptions, the necessity and applicability of transient thermal calculations:

- for rovers in regions with large local temperature gradients,
- to determine the efficiency of optical control surfaces (e.g. electrochromic radiators),
- for spacesuit parameter studies, as boundary condition or "excitation",
- for mission & schedule planning, to determine the accessibility of regions of interest,
- to determine confidence (in terms of thermal behavior) in a given surface-craft or instrument configuration.

In section 7.1.1, the results for the *TherMoS* regolith and *Boulder Models*, hence of the thermal lunar surface environment itself, are discussed. As a consequence of the model and verification process, empirical equations are derived and discussed. The empirical equations can be used a) to simplify the prediction of the local surface environment for the study of future lunar surface-crafts, and b) to calculate initial and boundary conditions for software tools that focus on spacecraft, equipment, scientific instruments, or astronauts on the lunar surface. Accurate initial and boundary conditions enable simulations of static objects in a more complex lunar environment than was possible up to now. In section 7.1.2, the results for the rover cases are discussed with the focus on the total received infrared heat flux. Different cases are compared against each other to predict which surface feature, transit and local surface temperature combinations show the largest impact on a rover. In addition to the infrared and solar heat flux densities, a black body thermal calculation of one rover is shown and discussed. Whereas infrared and solar heat flux densities are indicators for the overall thermal conditions, temperature is more intuitive to understand.

The discussions of the spacesuit cases in section 7.1.3 focus more on the rates of change of infrared heat flux. The rates of change in different lunar surface settings and temperatures are compared for the back of the PLSS, the most likely position for future radiator concepts. Furthermore, the total frequency of rates of change on torso, arms and the PLSS are discussed.

Section 7.1.4 discusses the implications of the results to thermal control technologies and postulates relationships for the impact of transient heat loads on radiator turndown ratio and phase change material layout. The transferability of the developed approach and the results to other celestial bodies such as Mars, the Martian moons, or Near Earth Asteroids, is discussed in section 7.1.5. Section 7.1.6 addresses inherent errors of the simulation tool. In section 7.1.7 the simulation time is discussed. Finally, in section 7.1.8 the confidence of the entire simulation tool is evaluated with a model confidence metric.

7.1.1 Empirical relations

Simulations for moving spacecraft on the Moon focus on short time transients. The simulations are demanding in terms of computation time. In order to reduce the time necessary to perform a transient simulation, the environmental conditions have to be met in a narrow range prior to starting the analysis of moving objects. Thus the initial conditions at a given location have to be defined *a priori* with empirical equations. The importance of empirical initial conditions can also be understood by looking at the work of Christie et al.. Their model on the lunar surface needed 100 lunar cycles (lunations) to reach steady state (Christie et al. 2008). In general sinusoidal approaches are used to model lunar surface temperature in first order approximations. Simplified empirical equations for the lunar surface temperate T_M [K] can be found for example in (Dallas et al. 1971):

$$T_M = 373.9 \cdot \sin^{1/6}\left(90 \cdot \frac{t_E}{7}\right)$$

(108)

or (Racca 1995):

$$T_M(\varphi, \lambda_l) = \left[\frac{(1 - \alpha_{alb})}{\varepsilon_M} \cdot \cos\varphi \cos\lambda_l \cdot \frac{S}{\sigma} + \frac{C_1}{\sigma}\right]^{1/4}$$

(109)

with t_E being the time in Earth days, α_{alb} [-] being the albedo of the Moon, ε_M [-] the emissivity in the infrared, $\sigma = 5.67 \cdot 10^{-8}$ W·m^{-2}·K^{-4} the Stefan-Boltzmann constant and S [W·m^{-2}] the solar constant. The constant C_1 was introduced to model an artificial subsurface cooling flux and has a value of 6 W·m^{-2}. In contrast to the equation given by Dallas et al. (1971), the equation used by Racca (1995) takes into account the local lunar latitude λ_{lat} [°], optical properties of the lunar surface and the solar constant. Racca's equation only is valid for the lunar day and neglects the decline in temperature during lunar night. Both approaches rely on sinusoidal functions to represent the temperature of the lunar surface.
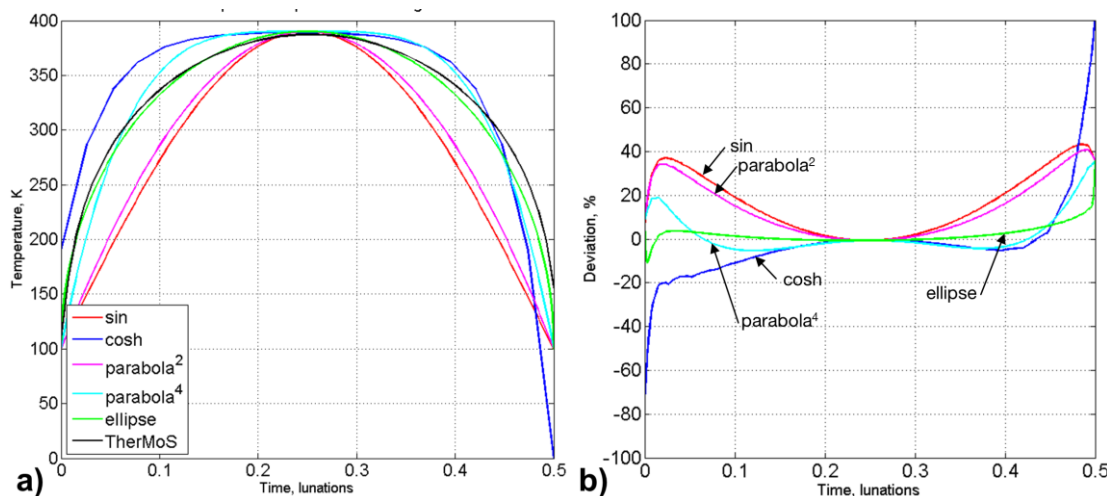
Figure 7-1: a) Comparison of possible mathematical formulas to describe the temperature during the lunar daytime, and b) deviations thereof.

The results of the *TherMoS Regolith Model* (Figure 5-23) and the transient long term cases presented in section 6.4 indicate that sinusoidal functions are not ideal to model the daytime temperature development

on the lunar surface. Figure 7-1 shows a comparison of possible mathematical functions with appropriate general shapes to describe the temperature during the lunar daytime: sinus (red); hyperbolic cosine (blue); parabolic (magenta & cyan); and elliptical (green). It is apparent from Figure 7-1b that a sinus is a poor fit to the shape of the results of the regolith simulation (black line), resulting to deviations of up to 43 %. The best agreement is found for the elliptic shape. Hence, the empiric equation for the initial conditions in the *TherMoS* simulation for short term transient surface-craft simulations has an elliptical shape for the lunar daytime. During lunar nighttime a simple cool down $1/_t$-approach is the best fit to the temperature decline of the lunar surface. The equations derived from the simulations with the *TherMoS Regolith Model* thus result to:

$$T_{reg} = \left(\Delta T_{max,\lambda_{lat}} \cdot \sqrt{1 - \left(1 - 4 \cdot \frac{t}{\tau_{sys}}\right)^2} \right) + T_{min,\lambda_{lat}} \qquad for \quad 0 < t < {}^{\tau_{sys}}/_2 \qquad (110)$$

$$T_{reg} = A + T_{min,\lambda_{lat}} \qquad for \quad {}^{\tau_{sys}}/_2 < t < \tau_{sys} \qquad (111)$$

$$A = \left(\frac{t}{\tau_{syn}} - a_0 + a_1 \cdot \cos(\lambda_{lat}) \right)^{-1}$$

with t [s] being the current time of a synodic month τ_{syn} [s]. The empirical coefficient A has the unit [K]. A consists of the coefficients a_0 and a_1 that describe the temperature decline. The coefficients must be adapted to the results of the regolith model at hand and depend on $T_{max,\lambda_{lat}}$ and $T_{min,\lambda_{lat}}$. The initial temperatures are functions of the local selenographic latitude λ_{lat} [°].

$$T_{max,\lambda_{lat}} = T_{max,90} + \left(T_{max,0} - T_{max,90}\right) \cdot \cos^{1/2} \lambda_{lat} \qquad (112)$$

$$T_{min,\lambda_{lat}} = T_{min,90} + \left(T_{min,0} - T_{min,90}\right) \cdot \cos^{1/3} \lambda_{lat} \qquad (113)$$

$$\Delta T_{max,\lambda_{lat}} = T_{max,\lambda_{lat}} + T_{min,\lambda_{lat}} \qquad (114)$$

The conducted simulation yielded $T_{max,90}$ = 209 K, $T_{max,0}$ = 387 K, $T_{min,90}$ = 91 K, and $T_{min,0}$ = 109 K, which lead to coefficients for equation (111) of a_0 = 0.46 [-] and a_1 = 0.02 [-].
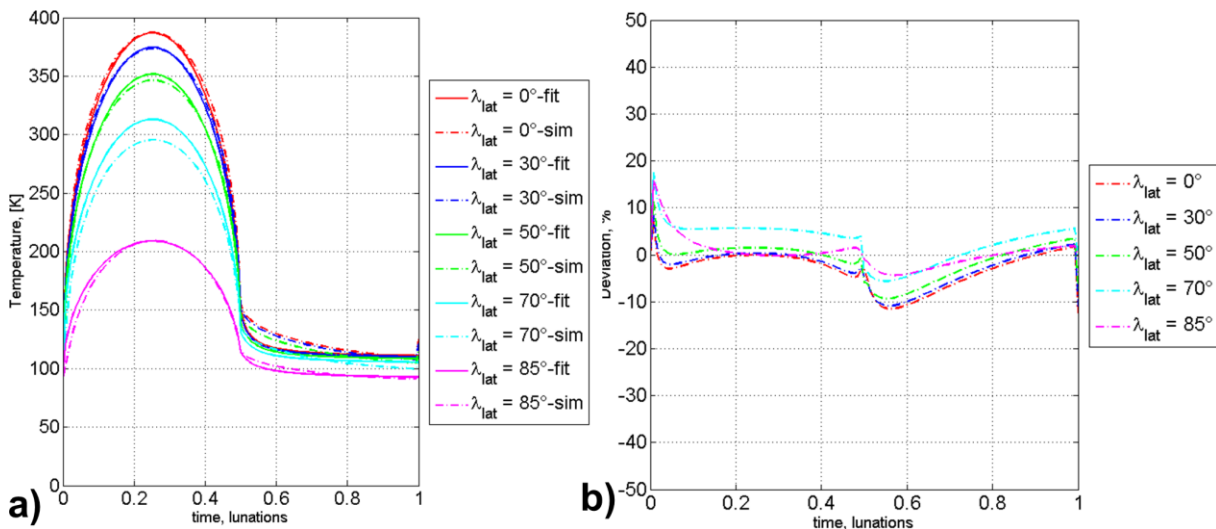
Figure 7-2: a) Comparison between simulated regolith temperatures and the fit calculated with the derived empirical equation; b) deviation between fit and calculated values.

Figure 7-2a shows the comparison between simulated regolith temperatures and the fit calculated with the derived empirical equations (110) and (111). In Figure 7-2b the deviation between fit and calculated

values are presented. The deviation varies between +30 K and – 15 K. The best fit is achieved for the Polar Regions and during local noon. The highest deviations can be seen for local sunset and sunrise.

Boulder Empirical Equation: In parallel to the lunar surface temperature, the core temperature of boulders was derived from a series of simulations and transferred into an empirical equation. The surface elements adapt quickly to the incident solar heat flux by heating up or cooling down. In contrast, the core of the boulder has a higher thermal inertia and its reaction is more benign. Yet, the core temperature of the boulder governs the time-dependent behavior of the entire boulder which in turn alters the infrared heat flux important for nearby surface-craft. Long-term simulations were performed for boulder with a hemisphere. The diameter of the boulder and selenographic latitude were varied. Each simulation was run for 10 to 20 cycles until the change in core temperature between two subsequent cycles was < 1 K for the maximum temperature. In Figure 7-3 the comparison of long-term simulated temperatures for half-sphere shaped boulders are shown. In Figure 7-3a values for boulder diameter of 1 m, 3 m, 10 m, 30 m, and 50 m were calculated for the lunar equator. In Figure 7-3b) the selenographic latitude λ_{lat} [°] was varied from 0°, 15°, 30°, 45°, 60°, 75°, to 85° for a boulder with a diameter of D_B = 3 m. each boulder size was evaluated for each selenographic latitude. This parametric analysis leads to the empirical equation for boulder initial core temperatures $T_{B,ini}$ [K]:

$$T_{B,ini} = [(a_0 - a_1 \cdot D_B) - a_2 \cdot \cos \lambda_{lat}] + \left[\frac{1}{D_B{}^2 \cdot (2 - \cos \lambda_{lat})} \cdot (-b_0 \cdot D_B{}^{c_0} + b_1) \cdot \sin \left(\Omega t + \frac{1}{2}\pi \right) \right] \qquad (115)$$

with the boulder diameter D_B [m] and the coefficients a_0 = 185.93 [K], a_1 = 0.567 [K·m⁻¹], a_2 = 64.36 [K], b_0 = 6312 [K·m], b_1 = 5350 [K·m²], and c_0 = -0.31 [-]. The angular velocity Ω [s⁻¹] is defined by $360°/\tau_{syn}$ with τ_{syn} [s] being the synodic day. Finally, t is the current local time [s] defined as *0* being local sunrise. The empiric equation is valid for a diameter range of 3 m < D_B < 30 m. For boulders with 1 m < D_B < 3 m the values for a 3 meter boulder can be used. For smaller boulders other models will be necessary. The material properties of mare basalt and the optical properties of lunar regolith were used. The derived equation is based on simulation results and generalized from a half-sphere boulder to all shapes, locations on the Moon and to all possible selenologic boulder materials. Thus, the equation must be used with great care. Further simulations with different material properties would be necessary to improve its usability. Finally, a verification against real measurements would improve the credibility of the empirical equation to a large extend.
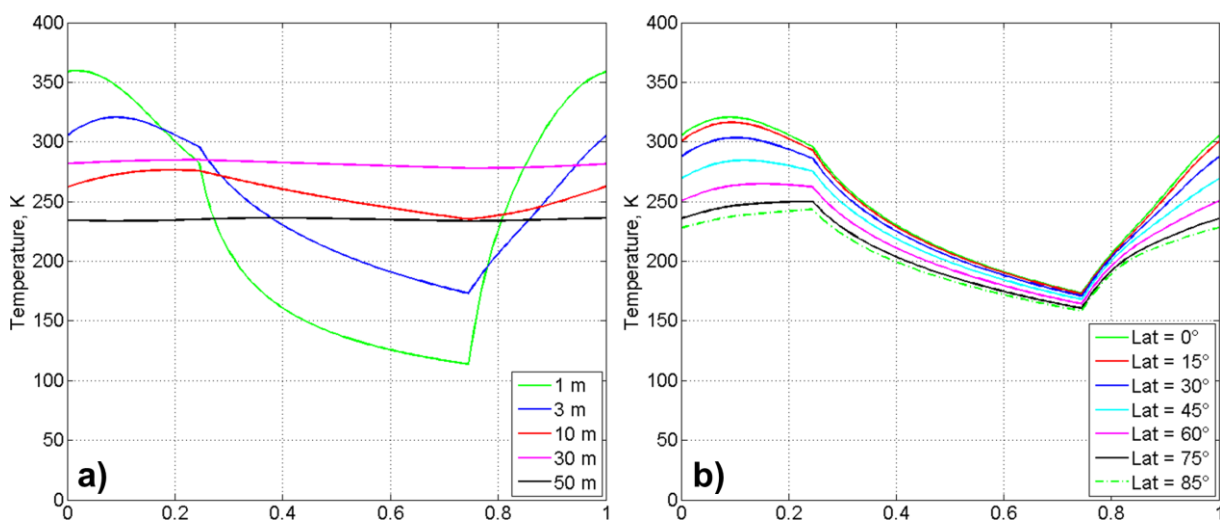
Figure 7-3: Comparison of long time core temperatures for half-sphere shaped boulders a) of different diameter and b) at different selenographic latitudes.

7.1.2 Rovers

A total of 50 cases were simulated for all rover sample objects. A part of the results for the equatorial, the polar rover and the mobile payload element were presented in section 6.5 and further cases are shown in the appendix B. A variation of rover shapes, surface features, different transits and solar elevation angles were simulated. For all cases the incident solar q_{sol} [W·m^{-2}] and infrared heat flux q_{IR} [W·m^{-2}] was recorded. The discussion of the rover cases focuses on the general increase of infrared and solar heat flux on the surface of the rover sample bodies as a result to transit movement on the lunar surface. Exemplarily for all rover sample objects the comparison of all 15 cases simulated for the polar rover (Rover1) sample object is discussed here. The simulated cases were transits over an *unobstructed* plain (red square), the shadow side of a boulder (*boulder-shadow;* green triangle), the sun side of a boulder (*boulder-sun;* blue circle), a field of five boulders (*5 boulders;* cyan diamond), and through a *crater* (magenta triangle). Each case was simulated for a lunar surface temperature of 170 K, 248 K, and 392 K. These values correspond to solar elevation angles of 2°, 10°, and 90° respectively, calculated with the *TherMoS Landscape Module*. It is more intuitive to plot values against the surface temperature than against the solar elevation angle. This way of representation allows applying the findings to any latitude if the lunar surface temperature reaches according values.

In Figure 7-4 the maximum infrared heat flux q_{IR} [W·m^{-2}] for all rover1 cases are shown and compared. The values are averaged for the entire time of each transit. In general, q_{IR} increases for higher local surface temperatures. If the rover transits on the sunlit side of boulders (blue circles and cyan diamonds) the increase in q_{IR} is strongest. Comparing the absolute increase of q_{IR} for the unobstructed case with the obstructed cases (Figure 7-5a) it is obvious that the impact of *boulder* transits can be as high as 289 W·m^{-2} to 446 W·m^{-2}. In relative numbers (Figure 7-5b) the transit on the sunlit side of a boulder increases the overall q_{IR} at factors of up to 330 % at a solar elevation angle of 2°, 56 % for a solar elevation angle of 10°, and even decreases about -14 % at a solar elevation angle of 90°. A likewise decline can be observed for the case with *5 boulders*. In contrast, the impact of a transit through a *crater* on q_{IR} is highest for surface temperatures of 392 K and lowest for a surface temperature of 248 K. In the high solar elevation case additional 661 W·m^{-2} or 26 % respectively are accumulated on the rover body averaged over the entire transit. In contrast, a transit through the *boulder shadow* decreases overall received q_{IR}. Of the calculated cases the largest impact can be seen at a solar elevation angle of 10°. Here the overall received q_{IR} is reduced by 70 W·m^{-2} or 14 %, respectively. In Table 7-1 the absolute and relative deviation values of q_{IR} compared to an *unobstructed* case with the same solar elevation angle, are gathered.
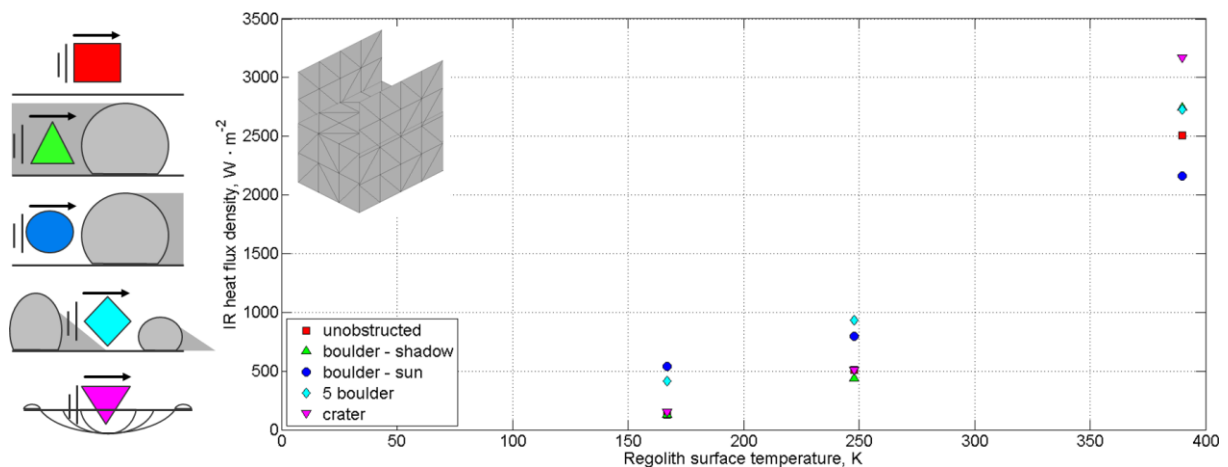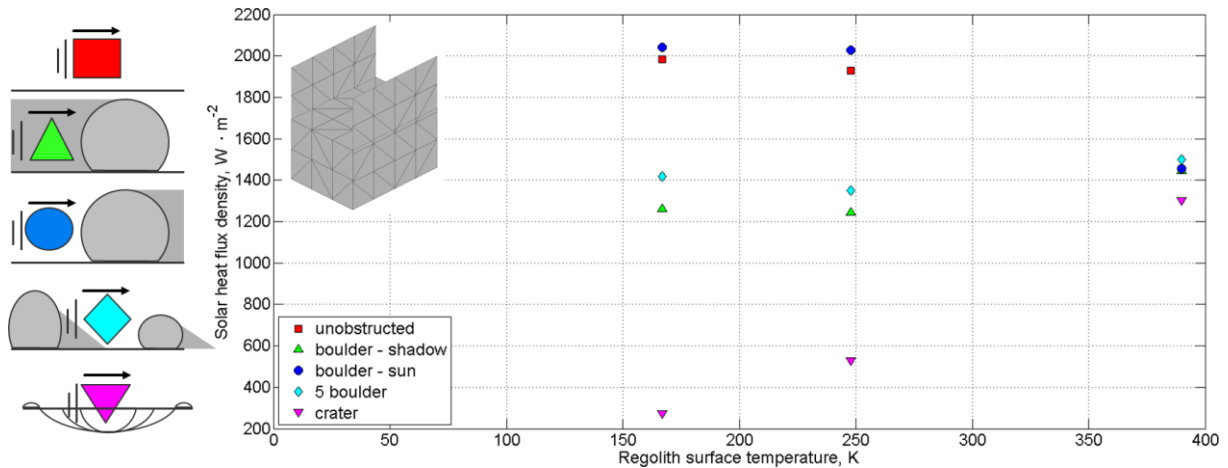

Figure 7-4: Sum of *infrared* heat flux for all surface elements of the Rover1 sample object in all 15 simulated cases.
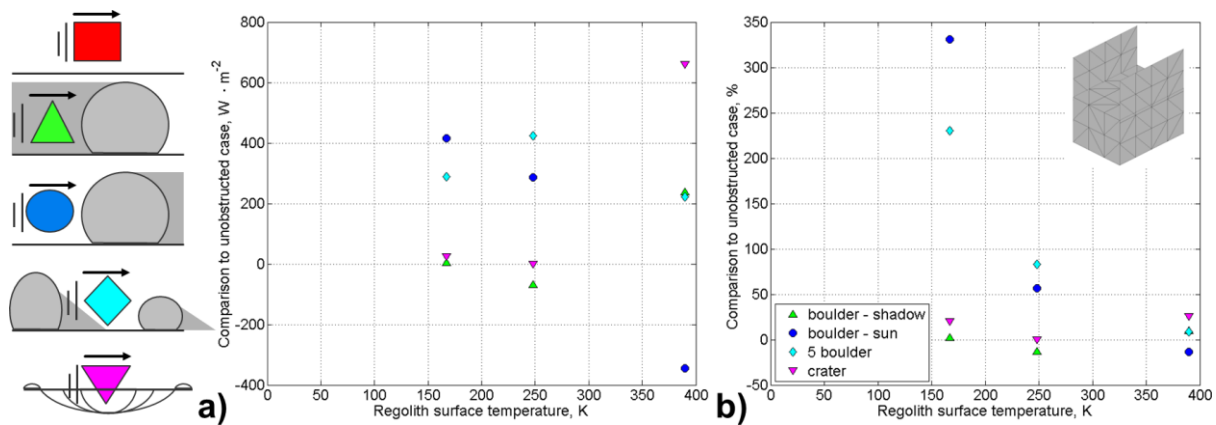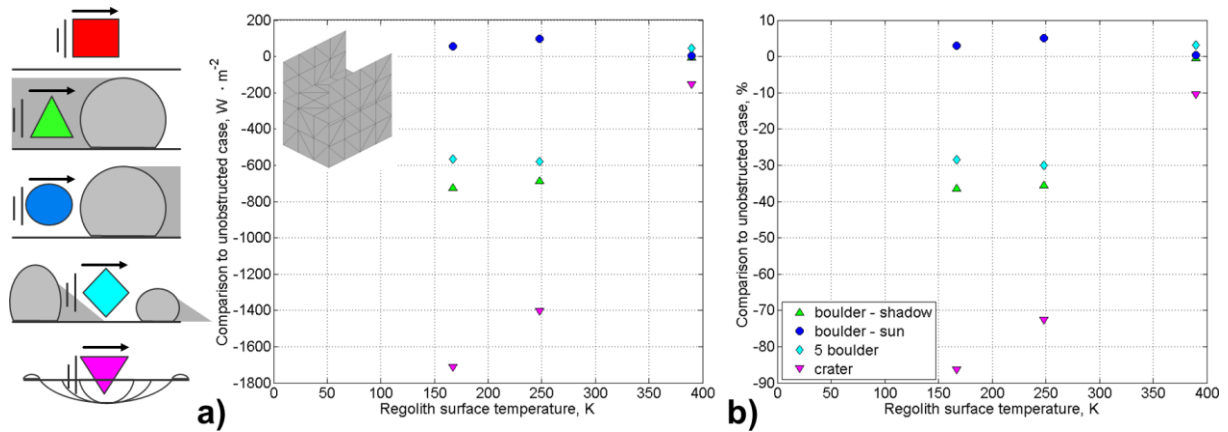
Figure 7-5: Comparison of *infrared* heat flux for all surface elements of the Rover1 sample object in all 15 simulated cases compared to the unobstructed case; a) in absolute value [W·m⁻²] and b) in relative increase [%].

Table 7-1: Absolute and relative deviation of total *infrared* heat flux between obstructed and unobstructed cases for three lunar surface temperatures.

Temp.	Infrared heat flux							
	absolute [W·m⁻²]				relative [%]			
[K]	bo	boW	5bo	cr	bo	boW	5bo	cr
392	236,7	-344,8	221,9	660,5	9,4	-13,8	8,9	26,4
248	-70,3	287,4	423,6	1,1	-13,8	56,4	83,1	0,2
170	2,4	415,0	288,7	25,6	1,9	330,8	230,1	20,4

In Figure 7-6 the maximum solar heat flux q_{Sol} [W·m⁻²] received by all surface elements of rover1 are shown. The values are averaged for the entire time of each transit. The total amount of received q_{Sol} is highest for the cases with a solar elevation angle of 10°, even in the *unobstructed* case. This can be explained by the rectangular shape of the rover. At an angle of incident of 90° only the top of the rover receives q_{Sol}. At a solar elevation angle of 2° only the rover sides receive solar heat flux. The lowest impact of obstacles can be seen for the cases with high lunar surface temperatures. Again the transit on the *sunlit* side of a boulder has the largest impact on the amount of received q_{Sol} due to the portion of the sunlight reflected by the boulder. If the rover transits lead through shadowed areas, as in the *boulder-shadow*, *5 boulder* cases, and *crater* cases, less q_{Sol} is received than in the unobstructed case. This effect is most pronounced for *crater* cases followed by the *boulder-shadow* case to the *5 boulder* case. In the latter the effects are omitted somewhat because the sample object receives q_{Sol} reflected from the central boulder and traverses the shadow of two other boulders relatively quickly. During the *boulder-shadow* and crater cases the rover remains in the shadow for a longer period of time. The absolute and relative increases in q_{Sol} are shown in Figure 7-7a&b. The transit on the *sunlit boulder* side increases the overall received q_{Sol} at about 50 %. The *5 boulder* and *boulder-shadow* case decrease q_{Sol} about 35 and 50 %, respectively. The crater reduces q_{Sol} about 86 % and 73 % at solar elevation angles of 2° and 10°, respectively. Due to the shape of the polar rover the effect is stronger for lower solar elevation angles. In Table 7-2 the absolute and relative deviation values of q_{sol} compared to an *unobstructed* case, with the same solar elevation angle, are gathered. The results are in well agreement with predictions about the impact of boulders presented in (Barraclough et al. 2009).

Figure 7-6: Sum of *solar* heat flux for all surface elements of the Rover1 sample object in all 15 simulated cases.

Figure 7-7: Comparison of *solar* heat flux for all surface elements of the Rover1 sample object in all 15 simulated cases compared to the unobstructed case; a) in absolute value [W·m^{-2}] and b) in relative increase [%].

Table 7-2: Absolute and relative deviation of total *solar* heat flux between obstructed and unobstructed cases for three lunar surface temperatures.

Temp.	Solar heat flux							
	absolute [W·m^{-2}]				relative [%]			
[K]	bo	boW	5bo	cr	bo	boW	5bo	cr
392	-7,3	4,7	46,8	-151,5	-0,5	0,3	3,2	-10,4
248	-685,5	97,7	-579,3	-1401,7	-35,5	5,06	-30,0	-72,6
170	-723,9	57,5	-565,4	-1711,2	-36,5	2,9	-28,5	-86,3

Thermal calculations:

Heat flux densities are important to understand the exposure to external heat loads and to design radiators. Temperatures in turn facilitate the insight in the current status of a system and are more intuitive. In the following, the results for the thermal post-processing of a number of cases are given. The sample objects rover1 and rover2 are used. The thermal calculations presented here are a) a comparison for rover1 and rover2 based on fixed values and black body optical properties, and b) a parameter analysis for a sensitive polar case of rover1. The determination of the temperature requires material properties and the assumption of a certain internal structure of the sample body. The generalized values for rover heat capacity $c_{p,rov}$ = 996.4 J·kg^{-1}·K^{-1}, rover mean density $\rho_{rov,mean}$ = 234.5 kg·m^{-3}, and λ = 171.8 W·m^{-1}·K^{-1},

discussed in section 6.1.3, are used. rover1 and rover2 both have a volume of 0.0693 m³. This yields a mass of 16.4 kg and a core capacitance of C_{rov} = 1.62·10⁴ J·K⁻¹.
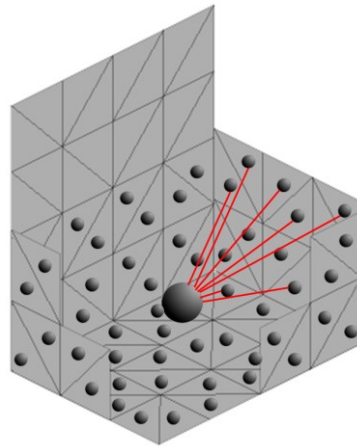
Figure 7-8: Thermal nodes in Rover1.

Each surface element of the sample body is an individual thermal node and connected to the central node (Figure 7-8). The conductor $G_{L,rov}$ is calculated individually between each surface element and the center of gravity of the sample body main structure (without solar array extensions). The surface elements are assumed to be of aluminium with a thickness of 0.002 m, specific heat capacity of $c_{p,alu}$ = 960 J·kg⁻¹·K⁻¹, and a density of ρ_{alu} = 2,770 kg·m⁻³ (Gilmore, ed. 2002-c2003). The capacitance is calculated depending on area and thickness of the surface element. An initial temperature of 300 K for surface nodes and the central core node was assumed. The surface element absorptivity and emissivity were $\alpha_{sol} = \varepsilon_{IR} = 1$. The internal heat load was assumed to be Q_{int} = 10 W. The external heat flux densities presented in Figure 6-20 are used together with the material properties presented earlier in this chapter to calculate the temperature of Rover1. Figure 7-8 depicts the temperature of the central thermal node in Rover1 for five cases. As reference, the *unobstructed* case at the pole (red) is shown. In the *boulder-sun* case (blue) the temperature changes are small. In the *boulder-shadow* (green) and *5-boulder* transit (cyan) cases the central thermal node temperature is reduced. The lowest values are reached at the end of the *boulder shadow* transit and the *crater* transit. In case of the *boulder-shadow* case the core temperature deviation is about -36 K and in the crater case -56 K. It is also important to note that the temperature already decreases by the impact of reduced overall solar exposure. This happens even in the *unobstructed* case when the rover turns, and the exposed area is reduced to the back of the rover.
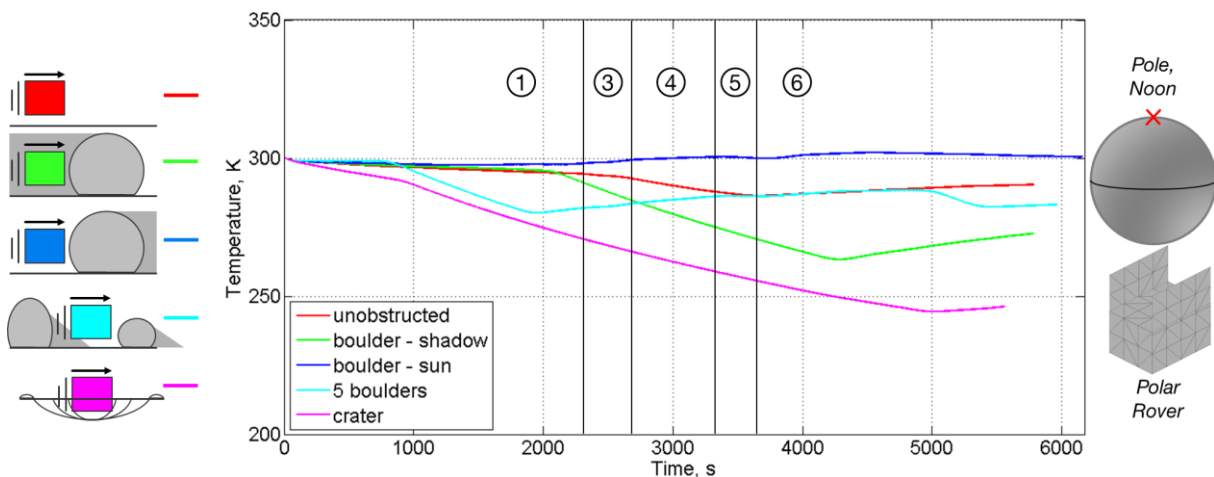
Figure 7-9: Temperatures of the central thermal node for a transit of rover1 in four polar cases compared to an equatorial case.

The temperatures for the core (black) and the two solar array extensions (red and blue) of the rover1 sample body are shown for the crater case (Figure 7-10a) and the *boulder-shadow* case (Figure 7-10b). The shown temperatures for the solar ray extensions are mean values for all surface element thermal nodes. The extensions (vertical solar arrays) are not thermally connected to the central thermal node in this calculation. The extensions are more vulnerable to changes in environmental heat flux.
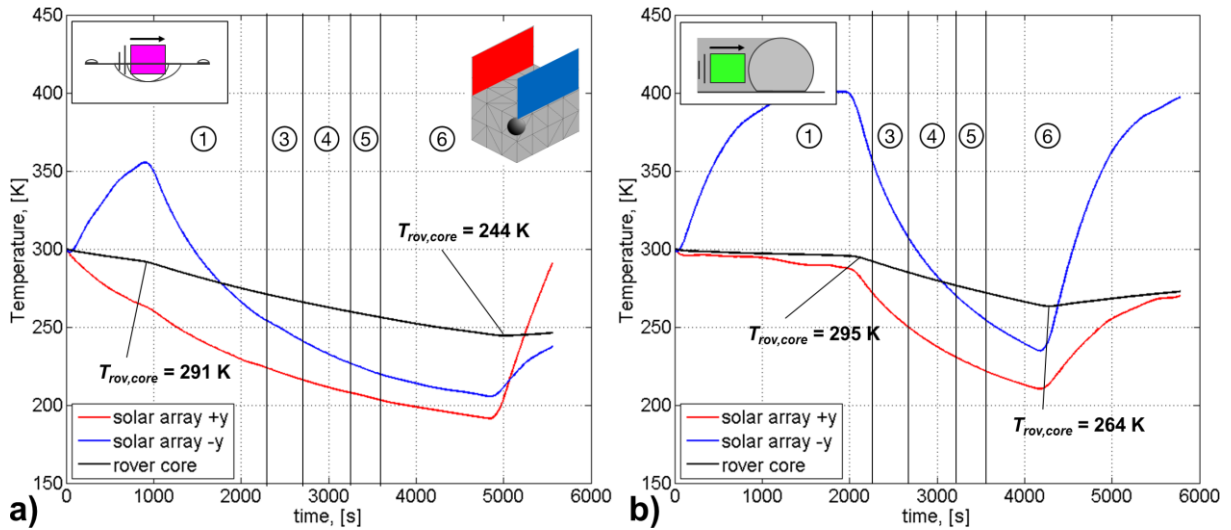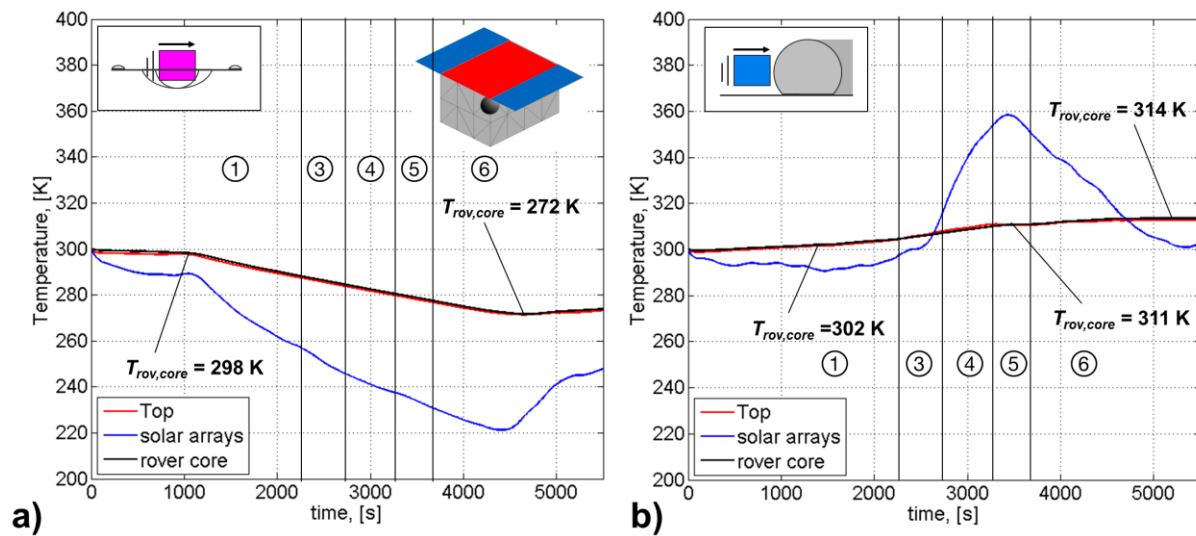

Figure 7-10: Temperatures of the core and the solar array extensions of rover1 for a) the crater case and b) the *boulder-shadow* case, at a solar elevation angle of 2°.

The core temperature is a complex function of the internal structure of the spacecraft, the properties of the used materials, the optical properties of the surface elements and the internally dissipated heat, in addition to the external infrared and solar heat fluxes. Figure 7-11 shows the results of a parametric study for rover1 central node temperature at a *boulder-shadow* case with a solar elevation angle of 2°. The optical properties, the internal conductivity between core and side elements, and the internal dissipated heat load were varied for the same environmental case. Black lines represent the baseline values. The α/ε ratio was varied from 0.1 to 10, the thermal conductivity was reduced from 172 to 0.1 W·m^{-2}·K^{-1} and the internal heat load was varied from 0 to 20 W.
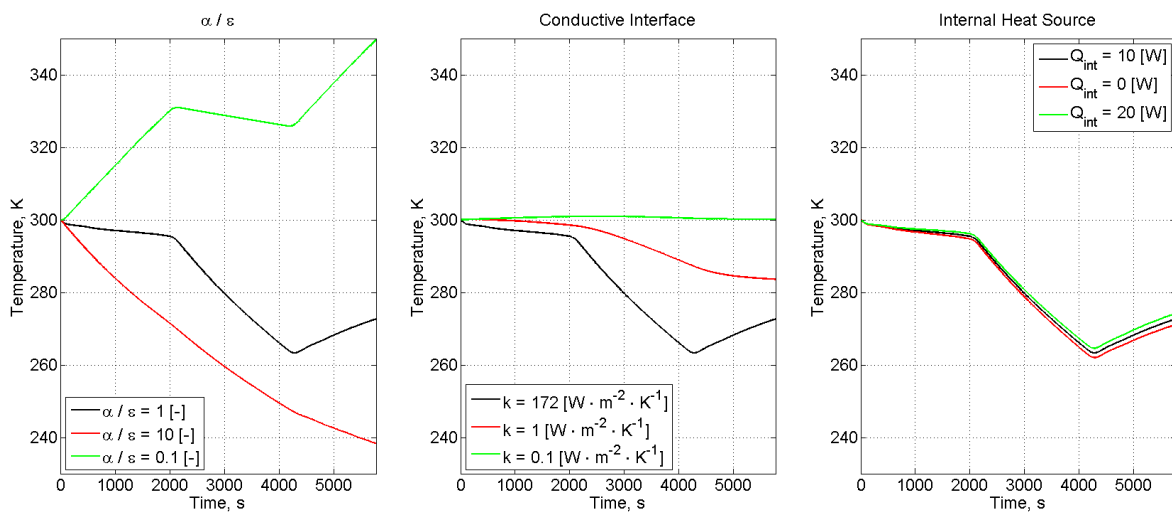
Figure 7-11: Parametric analysis for optical properties, thermal conductivity, and internal heat load for sample body rover1 in the *boulder-shadow* case at a solar elevation angle of 2°: a) varied α/ε; b) varied internal thermal conductivity; and c) varied internally dissipated heat.

The largest impact is caused by extreme α/ε-ratios followed by reduced thermal conductivity values. The internal heat load only has a small impact on the overall temperature behavior for the simulated case, probably due to the high thermal conductivity (172 W·m^{-2}·K^{-1}) and ideal emissivity ($\varepsilon = 1$) in the baseline case.

Rover2 was evaluated for solar elevation angles of 10°, representing a case at the lunar equator during local dusk or dawn. Rover1 and rover2 are equal in terms of the internal structure, model values for material properties, and optical properties. Only the solar array extensions are of different shape according to the operational regions (polar vs. equatorial).

Figure 7-12 shows the results for all rover2 cases in parallel to the rover1 cases shown in Figure 7-9. The increased solar elevation angle leads to overall higher core temperatures. The impact of shadow transits is less severe, which can be traced back to reflected solar heat flux from the environment. Still in the *crater* case the core temperature decreases by -28 K (Figure 7-13a). In contrast to the rover1 cases at solar elevation angles of 2° a transit on a *boulder-sun* side leads to an increase of core temperature by +14 K (Figure 7-13a). The temperature of the decoupled solar array extensions even rises to temperature of almost 360 K because they are exposed to direct and reflected solar heat flux, and infrared heat flux in front of the boulder.

In general, the increase in temperature for long exposure times is less than the decrease in temperature for shadow transits. This effect can be explained by the temperature difference between surface-craft and environment. At rover temperatures around 300 K the radiated heat flux is also high, especially in the examined case with black body optical properties. Although the solar and infrared heat influx is high in front of a boulder, the environment still is colder (248 K at a solar elevation angle of 10°) than the rover. The net heat flux thus points away from the rover for low solar elevation angles. If the solar heat flux is stopped due to a boulder or inside a crater, the net flux away from the rover is even higher. Thus, the impact of environmental heat loads on the temperature of rovers is more severe for shadow transits, compared to transits in front of sunlit boulders.
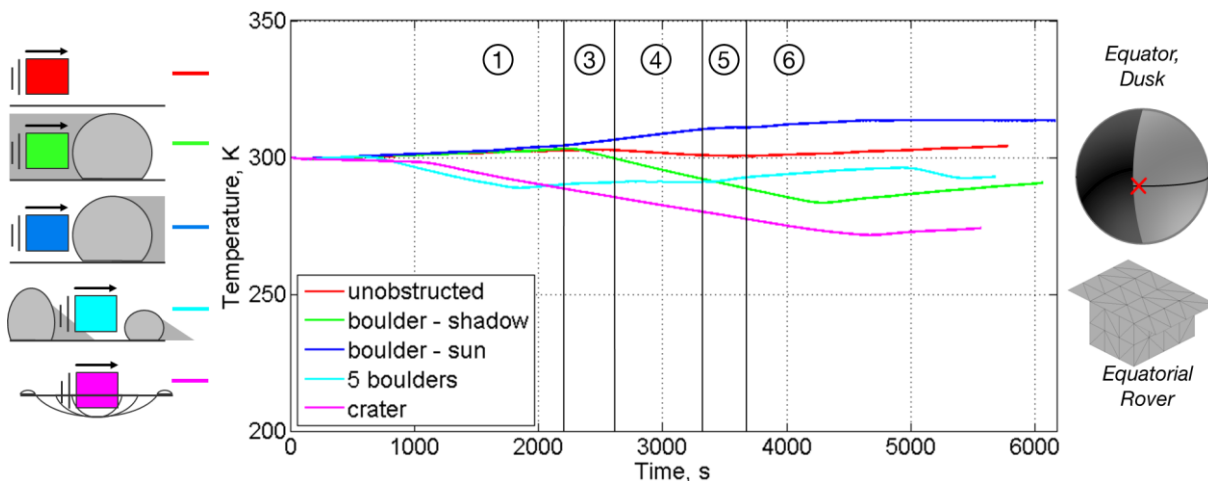
Figure 7-12: Comparison of the temperatures for the central thermal node of rover2 cases with a solar elevation angle of 10°.

This effect is turned to the opposite for instruments and extensions, such as cameras or manipulators, if the initial temperature is lower than 300 K which was assumed for the rover. Instruments with a requirement to maintain a pristine regolith sample are more vulnerable to incident solar and infrared heat fluxes on the sunlit side of a boulder or on crater slopes. Recent findings about volatile elements in lunar samples indicate a vulnerability to solar and infrared heat fluxes (see section 3.2). From the findings on volatile elements, stringent requirements for the protection of samples will be derived. Past sample acquisition

and handling strategies must be questioned in view of the presented results for exploration rovers and their interaction with lunar surface features.

Figure 7-13: Temperatures of the core, top and the solar array extensions of rover2 for a) the crater case and b) the *boulder-sun* case, at a solar elevation angle of 10°.

7.1.3 Spacesuit

The spacesuit sample object is investigated concerning infrared heat fluxes with regard to variable emissivity radiator concepts discussed in section 4.3.2.3. Radiator concepts for spacesuits are commonly designed to be placed on the back of the personal life support system (PLSS). The PLSS provides a relatively large and level area to reject heat. Thus the focus of this section is set on the backside of the PLSS as possible position of radiators. Figure 7-14 to Figure 7-18 compare the infrared heat flux and the maximum heat flux rate of infrared heat flux for all 15 simulated spacesuit cases. The lunar surface temperature was used as reference and is shown on the *x*-axes. A temperature of 170 K refers to a polar noon case with a solar elevation angle of 2°, 250 K to a case with a solar elevation angle of 10°, and 390 K to an equatorial noon case with a solar elevation angle of 90°.

On average, the maximum encountered heat flux q_{IR} [W·m^{-2}] is higher for obstructed compared to the *unobstructed* reference case, as can be seen from Figure 7-14. The elevation of heat flux for the backside of the spacesuit sample object increases with lunar surface temperature. The largest impact and increase of q_{IR} can be seen for the *crater* case (magenta). The *boulder-sun* transit (blue) always causes a larger impact than the *boulder shadow* transit (green). The *5 boulder* case in contrast is relative constant in terms of overall increase in maximum q_{IR}. The elevated q_{IR} inside craters result from a higher view factor with the lunar surface in all cases. This finding is in agreement with earlier view factor calculations made by (Sompayrac et al. 2009). The infrared heat flux is even more increased if the crater walls are sunlit and the temperatures are higher than the surrounding unobstructed lunar surface. A *boulder-sun* transit always leads to an overall increase of received infrared heat flux. One has to keep in mind that the shown elements on the backside of the suit always face away from the sunlit boulder, due to the implemented paths and tasks described in section 6.1.2. The lunar surface in front of the boulder has higher temperatures than the environment. This leads to an increase of infrared heat flux also on the back of the spacesuit sample object.
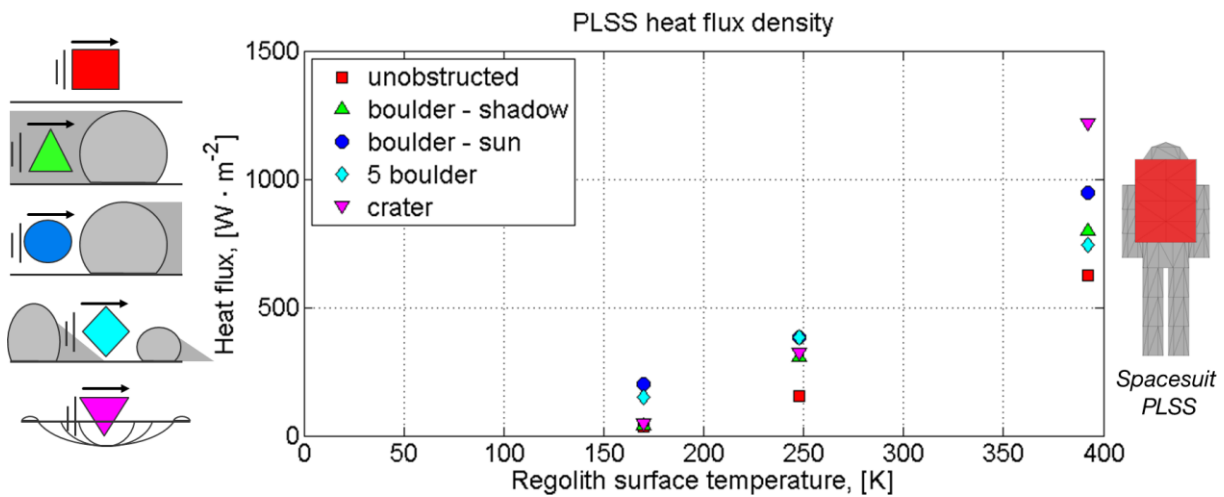
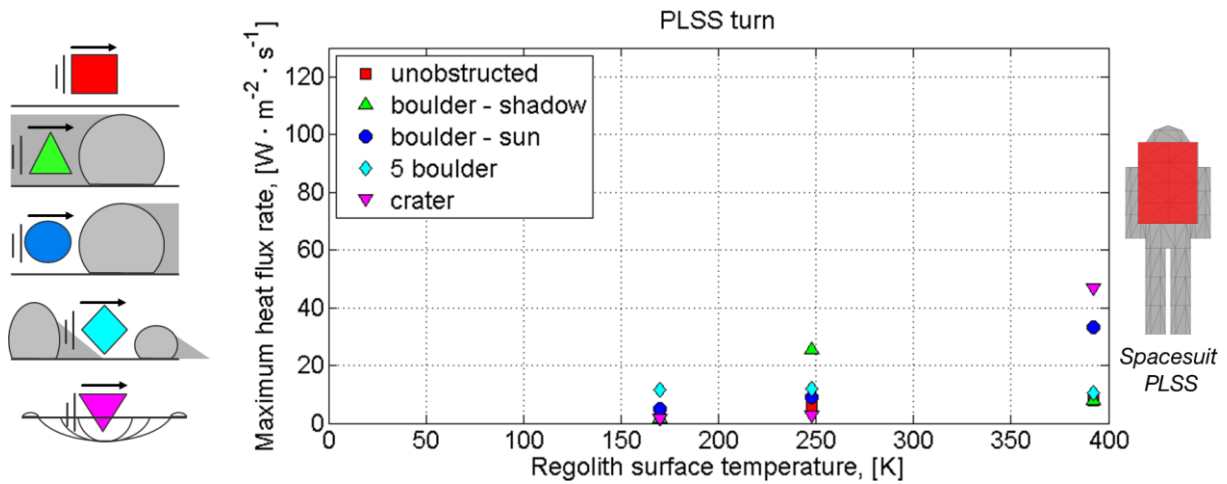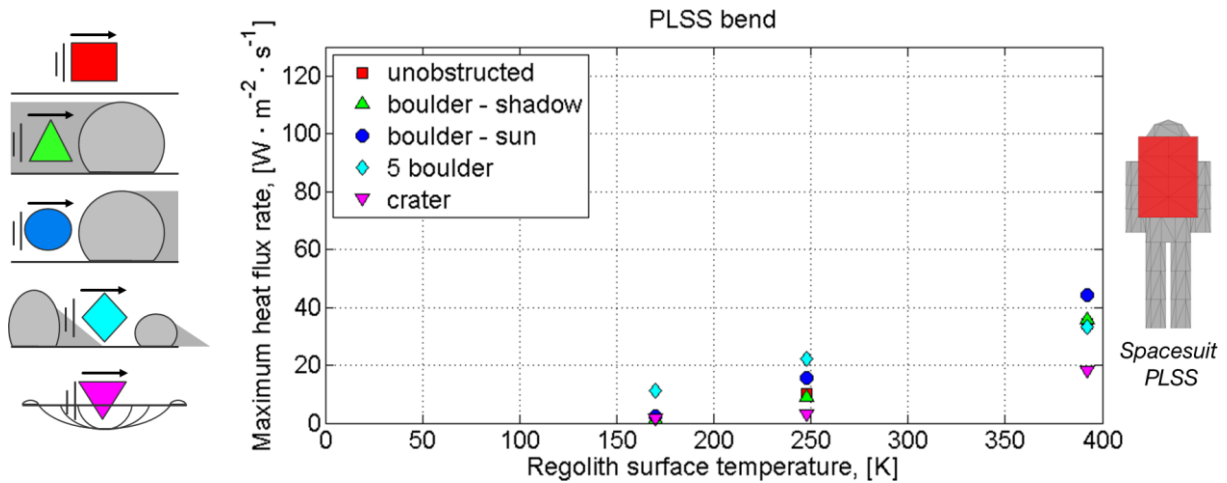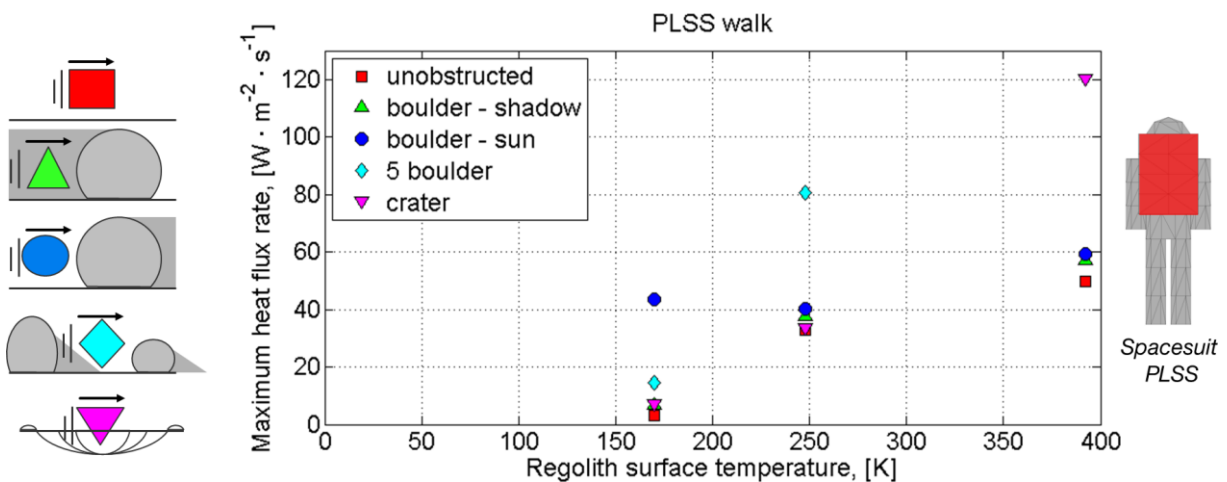**Figure 7-14: Maximum infrared heat flux on the back of the spacesuit sample body for different lunar surface temperatures and transits.**

Table 7-3: Absolute and relative deviation of total *infrared* heat flux on the PLSS, between obstructed and unobstructed cases for three lunar surface temperatures.

Temp.	Infrared heat flux							
	absolute [W·m⁻²]				relative [%]			
[K]	bo	boW	5bo	cr	bo	boW	5bo	cr
392	177,6	324,8	121,7	595,7	28,5	52,1	19,5	95,6
248	150,6	228,5	228,4	167,6	97,3	147,6	147,5	108,3
170	5,1	166,1	116,8	12,9	14,5	475,9	334,6	36,9

Figure 7-15 to Figure 7-17 show the maximum heat flux rate encountered on the back of the spacesuit sample object (PLSS) for three different movements in all of the 15 simulated cases. In Figure 7-15 the maximum heat flux rate in infrared heat flux is shown for a turning spacesuit, in Figure 7-16 for the transition to and the time in the bending posture and in Figure 7-17 for walking at a velocity of $u_{hum} = 0.7$ m·s⁻¹. The values are also gathered in Table 7-4. The highest rates of change are encountered in craters at the lunar equator and can be as high as 130 W·m⁻²·s⁻¹. In general the rates of change on the PLSS is higher for walking than for turning or bending in the simulated cases. This can be traced back to a larger variety of conditions. Whereas the turn and bending only take into account 6 seconds and 44 seconds, respectively, the walking phase has a duration of 71 seconds. The rates of change in infrared heat flux also increase with increasing surface temperature from values of about 5 - 15 W·m⁻²·s⁻¹ to 10 - 50 W·m⁻²·s⁻¹ for the unobstructed cases between surface temperatures of 170 to 390 K. It is difficult to interpret the results because they depend so much on the case and the sample object surface element under investigation. The evaluation for the maximum heat flux rate in heat flux for the torso and arms are shown in Table 7-5 and Table 7-6.

Figure 7-15: Maximum heat flux rate in infrared heat flux on the back of the spacesuit sample body for different lunar surface temperatures and a turn of 90°.

Figure 7-16: Maximum heat flux rate in infrared heat flux on the back of the spacesuit sample body for different lunar surface temperatures and bend body posture.

Figure 7-17: Maximum heat flux rate in infrared heat flux on the back of the spacesuit sample body for different lunar surface temperatures and walking velocities of about 0.7 m·s⁻¹.

Table 7-4: *PLSS* - Heat flux rate of infrared heat flux for 'walk', 'turn' and 'bend' movements in five cases for three lunar surface temperatures each.

Temp. [K]	Heat flux rate – infrared $[W·m^{-2}·s^{-1}]$														
	,walk'					,turn'					,bend'				
	un.	bo	boW	5bo	cr	un.	bo	boW	5bo	cr	un.	bo	boW	5bo	cr
392	49,8	57,1	59,4	262,9	120,4	34,3	35,7	44,4	33,3	18,2	7,7	7,7	33,2	10,5	46,8
248	33,0	37,7	40,2	80,6	33,8	10,0	8,8	15,7	22,2	3,1	6,0	25,4	9,2	12,0	2,8
170	3,0	6,7	43,7	14,6	7,0	1,6	1,3	2,5	11,0	1,8	1,5	1,6	5,1	11,5	1,6

Table 7-5: *Torso* - Heat flux rate of infrared heat flux for 'walk', 'turn' and 'bend' movements in five cases for three lunar surface temperatures each.

Temp. [K]	Heat flux rate – infrared $[W·m^{-2}·s^{-1}]$														
	,walk'					,turn'					,bend'				
	un.	bo	boW	5bo	cr	un.	bo	boW	5bo	cr	un.	bo	boW	5bo	cr
392	20,4	35,0	71,8	83,2	66,6	20,9	26,7	11,4	9,8	10,8	16,7	15,6	44,7	16,4	44,9
248	17,6	39,3	68,4	22,7	42,1	8,7	15,3	20,5	11,3	0,9	7,1	36,8	55,5	5,2	3,6
170	7,0	10,0	43,3	4,3	10,7	0,6	2,0	11,8	3,6	0,4	1,2	1,4	30,6	1,5	0,9

Table 7-6: *Arms* - Heat flux rate of infrared heat flux for 'walk', 'turn' and 'bend' movements in five cases for three lunar surface temperatures each.

Temp. [K]	Heat flux rate – infrared $[W·m^{-2}·s^{-1}]$														
	,walk'					,turn'					,bend'				
	un.	bo	boW	5bo	cr	un.	bo	boW	5bo	cr	un.	bo	boW	5bo	cr
392	44,4	43,3	80,6	111,3	81,4	39,7	60,3	36,6	31,9	22,9	14,2	26,3	52,0	13,4	73,8
248	23,3	25,1	88,7	17,8	62,7	8,3	32,0	44,3	8,6	1,2	19,5	36,5	88,3	15,0	6,2
170	6,9	6,9	54,5	14,2	8,8	3,6	3,5	28,5	4,7	0,5	4,3	5,9	63,5	2,0	0,9
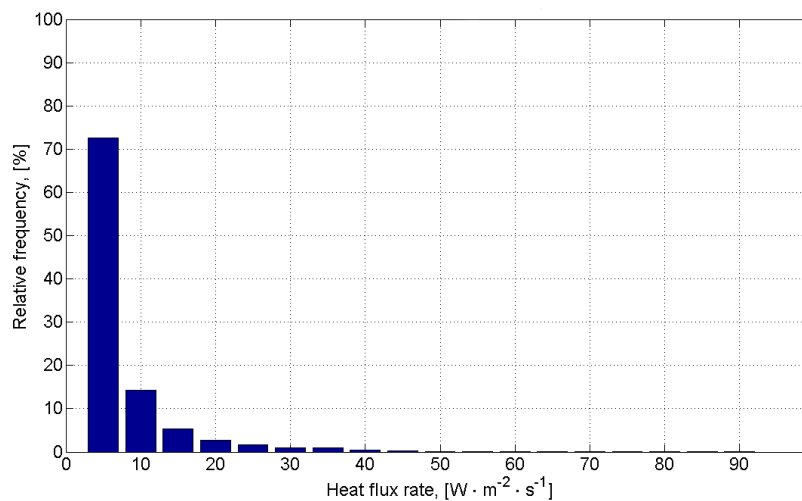
Figure 7-18: Relative frequency for a heat flux rate in infrared heat flux for all cases throughout the entire path and a solar elevation angle of 10° - a surface temperature of 248 K.

In Figure 7-18 the relative frequency of occurrence of a certain heat flux rate throughout all cases, and all parts of the suit is shown, for a solar elevation angle of 10°. In more than 72.6 % of the time the heat flux rate is smaller than 5 $W \cdot m^{-2} \cdot s^{-1}$ and in 15 % of the time the heat flux rate is smaller than 10 $W \cdot m^{-2} \cdot s^{-1}$. This trend shows an asymptotic behavior with rates of change > 40 $W \cdot m^{-2} \cdot s^{-1}$ occurring at less than 1 % of the time. The distribution is slightly changed for different surface temperatures. At higher solar elevation angles, thus higher lunar surface temperatures, the frequency of higher rates of change is higher and in case of lower surface temperature the frequency is shifted towards lower rates of changes. The values from Figure 7-18 are compared to the cases for surface temperatures of 390 K and 170 K in Table 7-22. Further diagrams for 90° and 2° solar elevation angle can be found in the appendix A.6).

Table 7-22: The relative frequency of occurrence [%] for rates of change at three different surface temperatures for the surface elements on torso, arms, legs and PLSS of a spacesuit sample body throughout all cases.

Temp. [K]	Heat flux rate – infrared [$W \cdot m^{-2} \cdot s^{-1}$]																	
	5	10	15	20	25	30	35	40	45	50	55	60	65	70	75	80	85	90
	Relative frequency of occurrence [%]																	
392	55,2	15,7	8,2	6,5	4,2	3,3	2,3	1,7	1,1	0,6	0,4	0,2	0,1	0,1	0,1	0,1	0,1	0,0
248	72,6	14,3	5,3	2,6	1,7	1,0	1,0	0,5	0,2	0,1	0,0	0,1	0,2	0,1	0,1	0,1	0,1	0,1
170	93,0	3,5	1,5	0,8	0,3	0,4	0,1	0,0	0,1	0,0	0,1	0,0	0,0	0,0	0,0	0,0	0,0	0,0

Temperature calculations in long-time simulation:

The long-time calculations performed in ESATAN-TMS® provide the results to compare the impact of local surface features on the core temperature of a simplified spacesuit model. The spacesuit model for the long-term cases is a simple cube with appropriate conductance and capacitance values (see section 6.1.3). Temperature gradients, excess heat as well as total energy deficit were calculated and compared for the spacesuit results presented in section 6.4.1 to 6.4.4. The temperature gradient is denoted as the change in temperature per time step. A sample body core temperature of T_{hum} = 310 K (37°C), a body mass of m_{hum} = 70 kg were assumed and the overall specific heat capacity (Table 6-3) of $c_{p,hum}$ = 3,230 $J \cdot kg^{-1} \cdot K^{-1}$ was used. A time averaged continuous metabolic heat load of 286 W was assumed (Dory 2006).
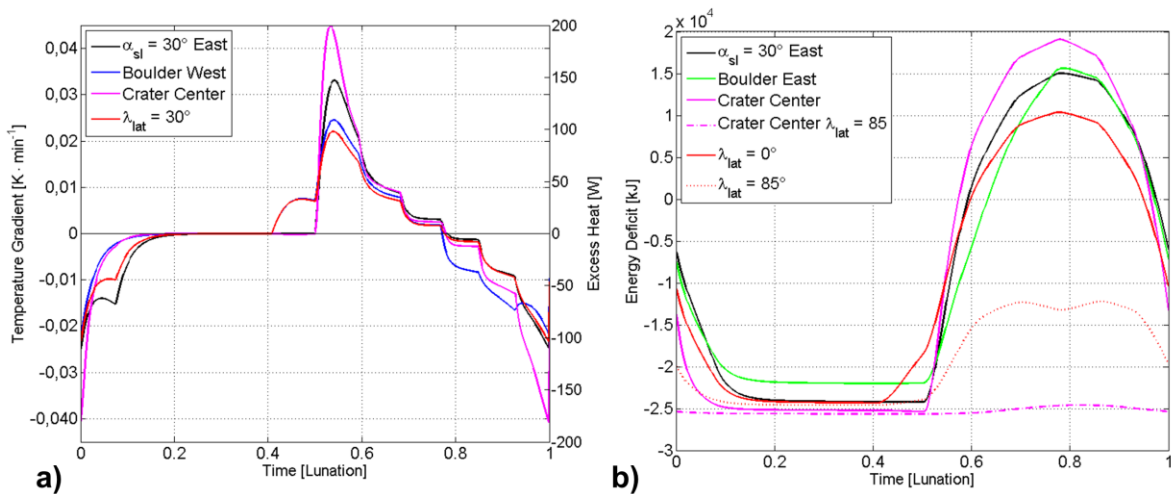
Figure 7-19: Temperature gradient, excess heat and energy deficit for different long time cases with a static spacesuit, cuboid sample body.

Figure 7-19a) depicts the temperature gradients $\Delta T / \Delta t$ [$K \cdot min^{-1}$] that occur in the core of the cuboid spacesuit sample body on the left y-axis. On the right y-axis of Figure 7-19a) the excess heat (positive) or

heat deficit (negative) is depicted that must be removed or added to maintain the human core tempera-ture. Only the cases with the largest impact are depicted here: 30° slope to the east; boulder to the west of the sample body; inside the crater; and lunar latitude of 30°. The temperature gradients vary from -0.041 K·min^{-1} to +0.045 K·min^{-1}. The highest gradient was calculated for the case when the static cuboid spacesuit model was placed on the floor of the crater with D_C = 0.035 km. The values for excess heat and heat deficit give an impression of the maximum and minimum rates that must be handled by radiators or sublimators to maintain a given set point temperature. The values for the deficit and surplus ranged from Q_{env} = -178 W to +196 W for crater cases. The crater case (magenta) yields the highest rates of change and heat load demands, respectively. A static calculation performed by Jones in 2009 lead to maximum environmental heat load from the lunar environment of 77 W for suit core temperature of 293 K, a suit surface temperature of 358 K, an internal heat load of 327 W plus additional 60 W from the PLSS, and an environmental surface temperature of 380 K. The highest heat loss was measured to be -306 W for an environmental temperature of 40 K at permanently shadowed polar craters (Jones 2009). The semi-dynamic longterm calculation in ESATAN-TMS® based on the *TherMoS* landscape model yields higher worst case hot and worst case cold heat loads. Furthermore, it adds the expected heat loads in between. If superimposed with the values obtained from the short time transient calculations, additional short time fluctuations in the heat loads can be observed.

Figure 7-19b) shows the energy deficit for a human sample body. The human body is sensitive to heat deficits and elevated levels of heat storage. Heat deficits below -280 kJ are perceived as uncomfortably cold and stored heat loads beyond +320 kJ are perceived as uncomfortably hot (Dory 2006). The stored energy in a human sample body of T_{hum} = 310 K (37°C) was compared to the simulated (theoretical) core temperatures of the human-spacesuit cuboid sample body. The energy deficit that needed to be either removed or added to return the system to normal temperature conditions ranged from -34,255 kJ to +22,494 kJ, hence the energy deficits are far beyond values endurable by the human body for these long-time simulations with a static and passively controlled spacesuit. From these findings one can conclude the necessity of a further and more refined thermal spacesuit model, taking into account metabolic heat load, PLSS heat loads, as well as environmental heat loads. Such a model would have to include the complex interactions between human, suit, and environment by also addressing the (active) thermal control strategy, and thermal control technologies such as for example the liquid cooling garment (see also the future works section 7.3).

7.1.4 Application to Thermal Control Technologies

The design of control algorithms for electrochromic radiators can make use of the presented results and conclusions from section 7.1.3. The rates of change for spacesuits given in Table 7-4 to Table 7-6 can be used as boundary conditions for control strategies and hardware tests. The equation (51) for the turn-down-ratio of electrochromic radiators $r_{td,EC}$ presented in section 4.3.2.3 could be amended with the factors for increased environmental heat flux from lunar surface features f_i [-] to:

$$r_{td,EC}{}^* = \frac{q_{rad,max}}{\bar{q}_{env} \cdot f_i} \tag{116}$$

The adjusted radiator turndown-ratio $r_{td,EC}{}^*$[-] is the maximum heat flux rejected by the electrochromic radiators $q_{rad,max}$ [W·m^{-2}], and divided by an averaged environmental heat flux $\bar{q}_{env}$ [W·m^{-2}] that is multi-plied with the minimum factor for local surface features (see Table 7-4 to Table 7-6). Additional work will be necessary in the future, to include the capabilities of the electrochromics, to account for local maxi-mum or minimum environmental heat values, as well as the rates of change, in order to identify a time-dependent turndown-ratio.

The results can also be used to qualitatively sketch the necessary regions for the transient control of radiators with variable emissivity. The values from Table 7-22 that determine the relative frequency of

occurrence of a certain heat flux rate can be used as weighting factors or to identify threshold values for the onset of the control algorithm. In Figure 7-20 the relative frequency of occurrence of a certain heat flux rate is depicted qualitatively. The heat flux rates increase with increasing lunar surface temperature. Furthermore, with increasing lunar surface temperatures, the relative frequency of occurrence is shifted towards higher heat flux rates. Low rates of change that occur at a high frequency can be considered as noise. High frequency and medium heat flux rates, as well as extremely high heat flux rates are critical. The worst case would be high heat flux rates occurring at a high frequency. The thresholds for the criticality mainly depend on the material properties of the surface-craft.

$$\frac{\Delta Q}{\Delta t}\bigg|_1, \frac{\Delta Q}{\Delta t}\bigg|_2 = f(c_p, k, \rho, m) \tag{117}$$
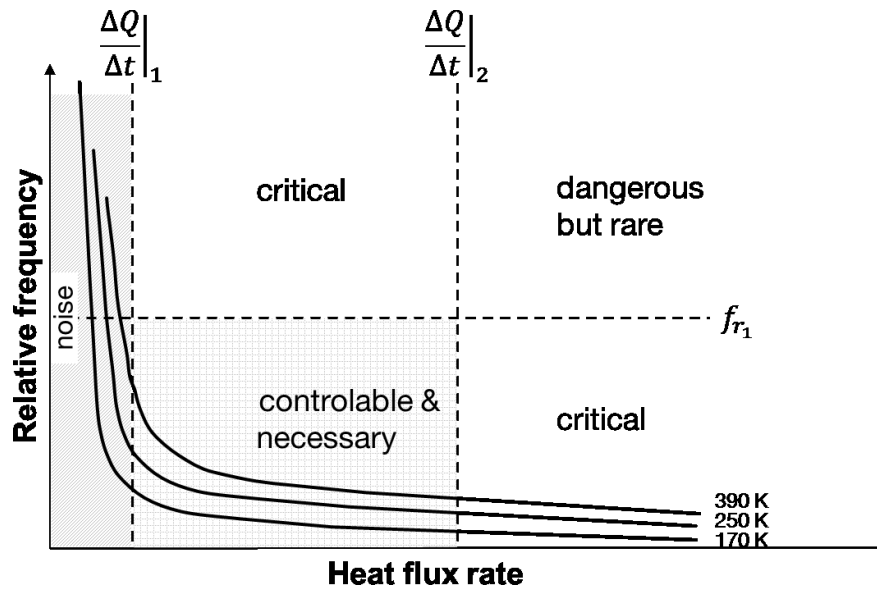
Figure 7-20: Qualitative diagram sketching the regions for the control of variable radiators.

The threshold for the criticality of the relative frequency of occurrence is governed by the abilities of the control algorithm $f_{r_1} = f(control)$.

The equation for radiators with phase change material (PCM) presented in section 4.3.2.1 was developed for cyclic internal heat loads. The impact of fluctuating environmental heat loads is not accounted for, because the standard case for radiators with PCM is for earth orbiting spacecraft with a view to deep space. Equation (50) can be amended with the results from this thesis to postulate an equation that describes the sizing of radiators with PCM for varying environmental heat loads:

$$r_{m,rad,PCM}^{\ *} = \frac{\bar{q}_{env} \cdot r_{rad}}{q_{rad}} + \frac{t_{tot} \cdot \bar{q}_{env}}{e_{PCM}} \cdot \max_i[\beta_i^{\ *} \cdot (f_i - 1)] \tag{118}$$

The area specific radiator mass with PCM $r_{m,rad,PCM}$ [kg·m^{-2}] is defined by the local averaged environmental heat flux $\bar{q}_{env}$ [W·m^{-2}], the maximum heat flux rejected by the radiator q_{rad} [W·m^{-2}] and the mass per radiator area r_{rad} [kg·m^{-2}]. $\bar{q}_{env}$ is the averaged infrared and solar heat flux for the unobstructed case and a given lunar surface temperature, defined for example with equations (110) to (114). The total time of the transit is given with t_{tot} [s] and the specific mass of the heat change material with e_{PCM} [W·s·kg^{-1}]. The index i denotes the number of possible traverses or path cases. $\beta_i^{\ *}$ [-] is the fraction of the total time t_{tot} the surface-craft is subject to a given elevated environmental heat flux, and f_i is the factor of increase for the local average heat flux. The value for f_i can be taken from Table 7-1, Table 7-2, or Table 7-3. The phase change material only must be scaled to the maximum of elevated heat flux multiplied by the exposure time. As was shown in section 7.1.2 the impact of surface features diminishes at the extreme lunar

equatorial noon conditions. The proposed approach to size radiators with PCM for environmental heat loads thus is not applicable to the equator. The threshold for a sensible use of equation (118) must be determined with further simulations. Furthermore, the validity of the proposed sizing method must be proven by experiments in future studies.

7.1.5   Applicability to Other Celestial Bodies

The future exploration of the solar systems is sketched by the International Space Exploration Coordination Group (ISECG). The long time goal is always to bring humans to Mars. Intermittent steps are Near Earth Objects (NEOs). Furthermore, more recently two private companies have proclaimed to investigate the mining of resources from asteroids. The *TherMoS* approach could be easily transferred to any atmosphere-less celestial body in the solar system. The closer the celestial body is to the Sun the higher are the encountered solar and infrared heat fluxes and with that the applicability and necessity for transient simulations. The landscape model must be adapted to the celestial body. The material properties of regolith are comparable to the Moon but in detail, especially thermal and optical properties, differ and depend on the type of asteroid under investigation (Coradini et al. 2011; Harris 1998). The rotation period and distance to the Sun also impacts the transient temperature behavior of the surface. Especially in the case of NEOs highly eccentric orbits are possible with a large variety in incident heat fluxes. In combination with the local surface roughness even in small scale NEOs and asteroids (Barucci et al. 2012), local shadows and bright spots will lead to a demanding thermal environment for exploration spacecraft. Possible stepping stones on the way to explore Mars with humans and robots are the Martian moons Phobos and Deimos. Both are dead worlds similar to our Moon. For both Martian moons the proposed *TherMoS* tool could be adapted with less effort than for asteroids. Comets inside the inner solar system and within the confines of the ice line are active, i.e. volatile elements are heated up by the solar incident heat flux and leave the surface of the comet. Still the comet has no atmosphere and the *TherMoS* approach could be applied, with some modifications, to the thermal environment of a comet.

The Mars is a different matter. The Martian thermal environment is more benign than the lunar environment due to its atmosphere and its larger distance to the Sun. The atmosphere dampens solar influx and reduces the infrared heat flux lost to space. The heat exchange is not dominated by radiation but has a significant part of convection. Yet, since convection is also governed by gravitation, the overall convection on Mars is lower compared to Earth. On the other hand the Mars has seasons and its year is twice as long as the Earths year. Thus, the Martian seasons are longer than season on Earth, and longer than the lunar nights which last 14 Earth days. Hence, the *TherMoS* approach might as well be used for regions on the Mars of high latitude and large seasonal temperature fluctuations. The convective heat transfer would have to be added to the simulation. Also the topography, soil properties, dust coverage, and the more dynamic local surface features would have to be amended since they are different from the Moon, too.

7.1.6   Possible Errors in the Simulation

The errors that apply in computer simulations can be divided into three groups. In the order of abstraction the errors result from a) *hardware errors*, b) *modeling errors,* and c) *numerical errors*. The use of ray tracing algorithms adds a fourth error form, d) *statistical errors*.

Hardware errors are for example uncertainties concerning the properties of the used materials. In the aerospace domain many regulations were implemented, and are strictly controlled, to ensure high material standards. Still material properties can deviate between real material data and literature or, even if the material at hand is investigated thoroughly, there might be difference from material batch to batch. Expensive material tests are performed to define the material properties, if necessary. Especially the conductive interfaces between different parts are critical and often cannot be defined without extensive testing. In those tests, measurement errors are inevitable and will find their way into the simulation. The values of heat capacity, thermal conductivity, density, emissivity, and absorptivity can be determined but

the knowledge about their temperature dependence or timely degradation is less secure. And finally, last minute changes in the design potentially are not accounted for in a thermal model.

In the present work, data from the Apollo and Luna programs, gathered at a limited number of positions, was interpolated for the entire Moon. The material properties depend mainly on the local geology and vary from spot to spot. Furthermore the material properties are altered by the presence of a man-made surface craft. A decent stage will blow away the upper layer of the regolith (Christie et al. 2008), a rover and a spacesuit will create tracks that locally alter absorptivity, emissivity, density, and with that also heat capacity and thermal conductivity. The thermal conductivity and heat flux from the Moons' interior was only measured during the Apollo missions at lunar latitudes of $\lambda_{lat} \leq 30°$. An interpolation to the entire Moon must be subject to further investigation. Although lunar *mare* and *highland* regions are distinguished in the simulation, local differences were not accounted for at this stage. Data on local lunar geology is available but was omitted in the first iteration of the *TherMoS* tool. Local effects might change optical and thermal properties, leading to yet other solar and infrared heat fluxes.

Modeling errors are intrinsic to every modeling approach since the very principle of modeling means a simplification of a real problem, or in this case a part or component. Any simplification is a deviation from reality and leads to less accurate simulation results. This is true for mathematical simplifications as well as for physical simplifications.

Assumptions for randomized boulder and crater shapes do not entirely represent real conditions. The density profile of the *TherMoS Regolith Model* is also just a simplification of the real conditions and has its limitations for inclined slopes. The lunar surface is modeled in discrete triangles. The size of the triangles governs computational time and demand of the numeric thermal calculations inside the regolith model. The lunar surface triangles are large compared to the sample body surface elements. The surface of the Moon hence is discrete instead of continuous, apparent for example in the structure of the crater.

Numerical errors are round-off errors, truncation errors and cancellation errors which are all limitations caused by floating point numbers. Floating point numbers used for computations are discrete representations of real numbers. Due to physical limitations floating point numbers make up only a large, but still finite, space of the entire real numbers. Especially in numeric calculations real numbers are truncated in almost all calculations. Cancellation errors occur if two nearly equal numbers are subtracted. In reality there is always a certain difference, but depending on the number of digits used for the computing, the resulting number will be zero (Bungartz 2009).

During the simulations some surface elements of the sample body received more heat flux than was possible from a physical point-of-view. This effect was traced back to round-off errors in the direction of the rays on the solar parallelogram. Although the rays were mostly parallel, slight errors lead to a misalignment. Hence, the rays of the large parallelogram that carried more power per area hit the small surfaces of the sample object and lead to the unrealistic elevated heat fluxes.

Statistical errors result from the statistical nature of a Monte Carlo ray tracing approach. Since random numbers are used to generate the rays, the accuracy of the results is proportional to the number of rays. The more rays are used the higher the accuracy (Howell 1998).

The fluctuations apparent in the results of sections 6.2 through 6.5 are caused by statistical errors. A finite number of rays, distributed randomly over a hemisphere represent a continuous infrared heat flux from the lunar surface. In addition to the problem of the lunar surface element size mentioned above, the number of emitted rays led to further irregularities in the results. Through the movement of the sample bodies, the encountered infrared heat flux varies with the distance to the origin of the infrared rays which are emitted from the center of the lunar surface triangles.

7.1.7 Simulation Time

The computation time depends primarily on the number of surface elements, both of the lunar landscape and sample body, under investigation. The second driving factor behind the computational time is the number of rays used in the ray tracing algorithm. The infrared rays have a larger impact on the overall computation time than the solar rays. The infrared rays are more time consuming because each surface element emits infrared rays and the number of surface elements depends on the complexity of the land-scape and sample body. Furthermore, the number of infrared rays per surface element can be adjusted by the user as deemed appropriate for the landscape, path, and sample body under investigation. The solar rays in turn are fixed for the size of the lunar landscape and central area in the current implementa-tion. The computation time also depends on the number of reflections for each ray. If a ray hits a surface it is diffusely reflected, this means that further rays are generated carrying less energy. If the new rays also hit a surface they have to be traced further. This process continuous until a certain energy per ray threshold is reached, a predefined number of reflected rays is exceeded, or the ray does not intersect any other surface element. If a ray passes all surface elements, it is truncated by the program automatically.

The computing of a single time step with the implemented OptiX® ray tracing algorithm requires between 7 and 40 seconds for the cases presented in section 6.5 and section 6.6. The cases without obstructing boulders or craters and cases at the lunar equator require the shortest ray tracing calculation times. The longest ray tracing calculation times occur for cases with a large crater (D_C = 1 km) superimposed with 5 boulders in the central region of higher resolution. In the unobstructed cases, the emitted infrared rays are truncated soon after generation, since they are directed away from the landscape. In contrast, in the obstructed cases the rays hit other surface elements. The more lunar surface elements are used, the higher is the probability to hit an element, and in parallel the computation time increases. The same is true for the case with the large crater. Here the emitted infrared rays intersect with other surface elements which cause longer computation times.

The numeric calculations in MATLAB were optimized to achieve the calculations for more than 50.000 thermal nodes in less than 0.1 seconds. This number is connected to the implementation of the *TherMoS Regolith Model*. The used implementation only calculates heat flux normal to the surface elements. If vertical heat transfer between neighboring surface elements was added, the computation time would increase quickly. The efficiency of the implemented solver depends on the topology of the input values. If the input values for capacitor and conductor have similar dimensions the solver is efficient. In this case, the resulting temperature differences can even be scaled by factors of up to 30, thus covering 30 real time seconds with one ray-tracing and thermal calculation step. On the other hand, if capacitor and conductor values are not homogenous, the solver can become unstable. If the density, and with it the heat capacity (capacitor) of the nodes differ significantly, the computation time would also increase. Only if it was possible to rearrange the Capacitor C and Conductor G_L vectors in a way that the heat capacities with similar values are calculated shortly behind each other, the current computations speed might be maintained. If more complex boulder models with more thermal nodes were implemented, an individual solver call for each boulder would enhance the computation time.

7.1.8 Model Confidence

The model confidence level (MCL) is a methodology to categorize the confidence in numeric simulations with a high complexity. The MCL was developed for dynamic life support system models with a heteroge-neous level of depth of its sub-models. The complexity of a model depends mainly on the complexity of each sub-model, as well as on the number and kind of connections between the sub-models. Each model can be divided in further sub-models. The overall model confidence level is defined by the model with the lowest MCL in the total simulation. In general, the confidence level in a model increases with its level of correlation (Czupalla et al. 2009a).

In the MCL approach sub-models are categorized in static, dynamic or correlated. The connections between the sub-models are static, scripted, or environmental sensitive. The MCL has ten levels which are summarized in Table 7-23. One has to bear in mind that the MCL was developed for environmental control systems. The models referred to are models of single life support system technologies, plants, or parts of the human physiology. Still, the development from static to dynamic models and the steps that must be taken are similar to the approach used in this work. Deviation between the initial MCL hierarchy and the presented work are marked in bold in Table 7-23. The static models in MCL 0-3 correspond to the static calculations presented in section 6.2. The dynamic models in MCLS 4 – 6 correspond to the semi transient (MCL 5) and transient long time cases (MCL 6) in sections 6.3 and 6.4, respectively. The transient short time cases presented in sections 6.5 and 6.6 consist of mostly correlated sub-models and thus have an MCL of 7. In sum, the overall *TherMoS* simulation has an MCL of 7 to 8. Some of the models need to be refined and be correlated against test data from thermal-vacuum tests to increase the MCL further.

Table 7-23: Summary of the model confidence level (adapted from Czupalla et al. 2009a)

Model category	MCL	Summary
N/A	0	Definition of in- and outputs of involved subsystems.
STATIC MODELS	1	Spread sheet type models based on averaged data.
	2	Spread sheet type models based on averaged data scaled for certain boundary conditions.
	3	Models consisting of multiple statically linked sub-models.
DYNAMC MODELS	4	Models with time-dependent in- and outputs and scripted responses to **static** environmental conditions.
	5	Models with time-dependent in- and outputs and true responses to **dynamic** environmental conditions.
	6	Interconnected multi-dynamic sub-models, in one relevant **dynamic** environment, sensitive to it and capable of changing it through their presence.
CORRELATED MODELS	7	**Models consisting of some correlated sub-models**. *(Begin of the correlation process for models)*
	8	Models consisting only of correlated sub-models.
	9	Models able to accurately <u>predict</u> a not a priori experimentally demonstrated system response.

7.2 Summary & Conclusions

This chapter will summarize the work, critically assess the accomplished work with respect to the objectives at the outset of this work and provide an outlook for its applicability. In section 7.2.1 the presented work is summarized and the completed thesis objectives (section 3.4) are discussed.

The primary objectives focused on the underlying theory and research for transient thermal analysis of scientific instruments and advanced thermal control technologies. The secondary objectives focused on the feasibility of the underlying transient calculation method, its performance and applicability as developed during this thesis work.

1. The primary objectives were:
   1.1. to calculate time-dependent local solar and infrared heat fluxes,
   1.2. to calculate dynamic infrared heat flux rates, and
   1.3. to provide a higher temporal resolution of core temperatures of sample bodies, compared to static worst case calculations.
2. The secondary objectives, focus on the practical implementation into an analytical software tool and its evaluation, were:
   2.1. to assess the feasibility of a dynamic thermal simulation method,
   2.2. to establish and verify a dynamic thermal simulation tool,
   2.3. to identify cases in which transient thermal simulations are most beneficial,
   2.4. to derive simplified equations for phase 0/A studies, and
   2.5. to provide a framework for further studies.

In section 7.2.2 conclusions are drawn on the applicability of the results to the different phases of space projects.

7.2.1 Summary

This work investigates static, semi-transient to fully transient thermal simulations for moving objects on the lunar surface, and makes a case for dynamic simulations for selected applications. The feasibility and benefits for selected applications of transient thermal calculations for moving objects on the Moon was demonstrated, when compared to the state-of-the-art worst case calculation approach. A new thermal simulation method was implemented and verified that is capable:

- of modeling transient movement of objects in a lunar surface setting,
- of predicting infrared and solar heat fluxes on the outside of a surface-craft,
- to derive heat flux rates for the design of control algorithms of thermal control components,
- to quickly run and re-run temperature calculations for different internal spacecraft configurations, and to perform parameter variations for thermal material properties,
- of reproducing large scale lunar topography based on Kaguya LALT data,
- to create artificial small scale lunar boulders and craters, placed and sized randomly or manually.

The dynamic simulation method was implemented in a self-developed software tool called the *Thermal Moon Simulator (TherMoS)*. Objective 2.2 was met by verifying the implemented models for regolith and *Boulder Models* against literature data from other models and against Lunar Reconnaissance Orbiter (LRO) remote sensing data. The *TherMoS Regolith Model* shows a good agreement with the model of Vasavada et al. for the lunar day, with a deviation of less than 1 %. During lunar night the deviations are higher with a maximum around midnight with a deviation of 10 %. The *TherMoS Boulder Model* was compared to data produced by a model presented by (Roelof 1968). Two empirical equations for initial temperatures of regolith and boulders were derived. Both equations can be used to either predict initial temperatures for more sophisticated time marching numerical methods or be used for static worst case calculations. The equation on regolith enhances pre-existing empirical equations by taking into account

time of day and local selenographic latitude. The empiric equation for the boulder, to the best of my knowledge, is the first of its kind, but should be subject to further discussion and investigations. The derived empiric equations satisfy objective 2.4 and can also be used in other numerical simulations to calculate initial conditions. In global topographic comparisons between the *Regolith Model* and LRO remote sensing data for the lunar craters Calippus, Marius A and Ibn Bajja, the deviation was less than 10 % for surface temperatures between 200 K and 390 K, but up to 33 % at surface temperatures $\leq$ 100 K in a case modeled at the Apollo 15 landing site. Deviations were traced back to two reasons. First, the difference in resolution between the used topographic data from the Japanese Kaguya probe, and the LRO Diviner Radiometer Experiment (DLRE) surface brightness temperature data, and second, to possible locally different regolith material properties, especially on slopes and in depressions. Surface temperature and solar azimuth and elevation were used as basis for two ray tracing algorithms. One ray tracing is started from a parallelogram that represents the Sun. It launches 2,800 x 2,800 rays on the center of the sample scene with boulders, craters and the sample object. The second ray tracing algorithm launches infrared rays from each triangular surface element, according to its temperature in a hemispherical weighted fashion. The solar ray tracing has a repetition deviation of less than 2 % and compared to manual view factor calculations a deviation of less than 8 %. The infrared ray tracing has a repetition deviation and a deviation to values calculated with view factors of less than < 9 %. The number of rays per surface element, random numbers and the size of the surface element need to be improved to increase the accuracy, but as a drawback will also increase computational time. The selected approach on a first glance is more time consuming than the common approach of commercial tools, for example ESATAN-TMS®. The repetition of the ray tracing in each time step is time consuming but allows a subsequent detailed analysis of the surface-craft with varying material properties. For concave surface-craft designs the calculation of view factors still must be implemented to account for the exchange of heat between different parts of the surface-craft.

A multitude of simulation runs were performed on primitive, rover, and spacesuit sample bodies. The sample bodies moved along trajectories in different lunar settings. The lunar settings were a single boulder with D_B = 12 m, a field of five boulders with D_B = 6 to 18.5 m and a crater of D_C = 30 m. Each sample body and each setting was calculated for solar elevation angles of 2°, 10° and 90°. The resulting lunar surface temperatures for an unobstructed plane are 170 K, 248 K and 392 K, respectively. The solar elevation angles and temperatures represent the conditions at the lunar Pole during local noon (170K), at the lunar equator during dawn (248K), and at the sub-solar point at the lunar equator during local noon (392 K). The transient paths were in line with common tasks of rovers. The spacesuit traverse studies are based on Apollo 15 and Apollo 16 mobility studies and represent typical tasks, for example for soil or rock sample acquisition. The paths were a combination of typical tasks at representative velocities. With the results from these transient paths, the first primary objective, to calculate transient solar and infrared heat fluxes, was met. It was found that rover sample bodies receive on average up to 330 % more infrared heat flux throughout a complete transit in front of a sunlit boulder compared to an unobstructed plane at the lunar polar case. At the same location a transit through the small bowl-shaped crater can reduce the received infrared heat flux by 20 % and the solar heat flux even by 86 %. The impact of surface features in relative as well as absolute numbers is more pronounced at lower surface temperatures (solar elevation angles). The impact are highest for the transit in front of sunlit boulders (up to +415 W·m^{-2}) followed by a field of five boulders (up to + 424 W·m^{-2}). In contrast, the transit on the shadow side of the boulder decreases the averaged infrared heat flux by about 14 %. The incident solar heat flux is reduced by almost 100 % in the shadow of the boulder, but the averaging for the entire path leads to a reduction by 37 %. Compared to mere static worst case calculations the transient approach yields a higher resolution of the modeled heat fluxes. The higher resolution in heat flux occurring in complex lunar settings with boulder and shadow transits, for example at times of low solar elevation angles, must be investigated individually and thoroughly. Surface-craft with low thermal inertia such as rovers are vulnerable to increased exposure to solar and infrared heat flux and even more to the lack thereof. This finding shows that the chosen

approach meets the third secondary objective, to identify cases in which transient thermal analysis are most beneficial. Yet, the simulated cases represent only a small fraction of possible combinations from the numerous parameters that impact the absorbed heat fluxes and with it the surface-craft temperatures.

The *TherMoS* approach allows determining the heat fluxes and performing the temperature calculations in a subsequent step. In this way, parameter analyses are easy to implement which addresses objective 2.5. The properties of the rovers were set to: optical properties of a black body, 300 K initial condition, 10 W internal heat, and a rover mass of 16 kg. A study for the transit of the equatorial rover across the sunlit side of a boulder showed an increase of +14 K or +4.6 % of the core temperature in a period of 5,540 s. On the other hand a transit through a small crater (D_C = 30 m) led to a decrease of -56 K or -18.6 % in the same period of time. The transit through the shadow of a boulder led to a decrease of -36 K or -12 %. Furthermore, parametric studies for material properties and internal heat loads were performed followed by reduced thermal conductivity values. The internal heat load only had a small impact on the core temperature for the simulated rover. The third primary objective, to increase the temporal resolution of sample body core temperature compared to static worst case calculations, was accomplished to a large extend by the calculations for the sample body. Yet, in order to increase the temporal resolution and also the spatial resolution, more detailed sample bodies will have to be investigated in the future. This includes more detailed accommodations and accurate materials as well as possible fluid loops for active cooling.

In the spacesuit cases, the suit surface elements were investigated with regard to absorbed infrared heat flux and heat flux rate thereof for certain tasks during a path, thus addressing the second primary objective. The tasks were "walking", "turning" and "bending". These values are interesting for radiator concept as a contrast to the robust, yet water wasting sublimator designs (Hodgson 2007; Klaus et al. 2007; Metts et al. 2011; Jones 2009; Sompayrac et al. 2009; Ochoa et al. 2008). The backside of the spacesuit (PLSS) was analyzed in detail. The evaluation lead to the finding that the absorbed infrared heat flux on the PLSS is highest inside craters at high lunar surface temperatures. In the investigated cases, the parts of the suit facing a surface lunar feature (mainly boulders and crater) yield significantly higher heat flux rates than in transits through unobstructed regions. In general the heat flux rates are higher at higher lunar surface temperatures (high solar elevation angles) and decrease towards lower surface temperatures. For an unobstructed case the encountered rates of change on the PLSS for the task "walk" are 3 W·m^{-2}·s^{-1}, 33 W·m^{-2}·s^{-1}, and 50 W·m^{-2}·s^{-1} for solar elevation angles of 2°, 10°, and 90° respectively. From all cases, it was derived that most of the time (72.6 %) the heat flux rate is smaller than 5 W·m^{-2}·s^{-1} at the lunar equator. With a power law decline with a negative exponent this trend continuous to heat flux rates > 40 W·m^{-2}·s^{-1} occurring at less than 1 % of the time. The smaller heat flux rates have a higher occurrence at lower surface temperatures (93 % for the < 5 W·m^{-2}·s^{-1} bin at surface temperature of 170 K).

The findings for solar and infrared heat fluxes on surface-craft are in line with other studies on radiator sizing for suit radiators (Ochoa et al. 2006; Ochoa et al. 2008; Sompayrac et al. 2009), lunar rover design (Barraclough et al. 2009), or lunar bases (Dallas et al. 1971; Simonsen et al. 1992). The infrared heat flux caused by the lunar surface temperature makes the layout of radiator based thermal control systems demanding. In the past, it was proposed to confine extravehicular activities towards the terminator, i.e. to lunar dusk and dawn or to higher latitudes. This approach would impact surface operations and restrict exploration to certain times (Sompayrac et al. 2009). It was also proposed to avoid local objects with hot surfaces to allow the use of radiators (Ochoa et al. 2006). The present approach confirms the implications found with worst case calculations in the first place. In addition to previous work, the results presented here also indicate that active control of the emitted and received heat fluxes, as well as thermal buffering material that store heat, can be used to dampen short-term effects. In general, the cold cases lead to a faster temperature decrease than exposure to additional infrared cases leads to a temperature increase.

7.2.2 Conclusions

With the presented approach it is now possible to calculate the transient thermal environment for moving objects on the Moon, in addition to the common approach using mere worst case calculations in thermal spacecraft engineering today. The transient simulations provide more detailed information for concepts, design, and mission operation, while the worst case calculations are suited for, but are also restricted to, fast preliminary studies on the general feasibility of a concept, or the extreme boundary condition envelope in early phases of a project. Spacesuits and rovers cannot be designed for compatibility with all possible environments on the Moon. The local thermal conditions on the Moon span too wide a range of temperature ranges compared to Earth, and have a more variable temporal and spatial resolution than in Low-Earth-Orbit. Furthermore, strict mass limitations for the transport of equipment to the surface of the Moon deny surface-craft to support all possible environmental extremes on the Moon. The rovers and spacesuits will therefore be designed for certain acceptable environmental envelopes, for example neglecting shaded craters, the shadows of boulders, or work during high noon at the equator.

a) If only static worst case calculations are used, surface-crafts are restricted to their design envelop, although they might be able to enter thermally demanding regions for a distinct period of time if transients are taken into account.

b) On the other hand, if the surface-crafts would be designed for work in the vicinity of boulders or shaded craters they would be unnecessarily heavy and oversized, since they will only operate in the worst case condition for a fraction of their operation time.

Information about the temporal variation of the heat fluxes can be used to size thermal hardware with buffering capabilities such as phase change material used in radiators or heat exchangers. Heat flux rates are relevant for actively controlled radiator designs such as electrochromic, thermochromic, or digital radiators. The findings of this work reinforce the importance of the correct sizing and maintenance of the optical / thermal properties. Especially the appropriate selection of the infrared emissivity is even more important than for Earth orbiting spacecraft, and more urgent than could be defined or designed by mere worst case steady state calculations. On the sunlit side of a boulder, or on sunlit slopes of a crater, vast amounts of infrared heat can be encountered and absorbed. Thus, a moving surface-object should be decoupled, i.e. insulated from the thermal environment on the Moon, by low values for the infrared emissivity. Yet, such an approach calls for demanding thermal concepts to reject accumulated heat inside the spacecraft, created by electronic equipment or the human metabolism. While the accumulation of heat is a problem for surface-objects hosting humans, as for example spacesuits, small exploration rovers are more sensitive to heat losses through inappropriate radiator design. Thermal designs using radiators therefore have to take into account local surface topography and features. Topography and boulders or operations inside craters lead to an increase of the view factor to the lunar surface. In very disadvantageous settings, the radiator could have high view factors to the hot side of a boulder or to a slope.

Hence the radiator design either has to:

a) steer the pointing direction of the radiator (active steerable radiator, surface-craft design based on local lunar latitude, operation time and remote sensing data),

b) control its absorptivity and emissivity (electrochromics, thermochromics, or digitial radiators),

c) use latent heat sinks to dampen environmental heat fluxes (phase change material, freezable heat exchangers), or

d) protect the radiator from the lunar surface infrared (louvers, parabolic radiator shapes).

The use of technologies developed for a) through c), significantly improve the confidence in a radiator-based thermal concept and will improve operation times and scientific output of future equipment and surface-craft. Radiator performance in cold conditions must be evaluated additionally, even if the radiators are well designed to cope with heat loads from the local topography during periods of high environmental temperatures. Otherwise the radiators might reject too much heat and cool down the entire sys-

tem below acceptable lower temperature limits. Even thermal designs that use sublimators are vulnerable to fluctuating external heat loads caused by lunar surface features. The usability of sublimators is limited by the amount of available water. The additional infrared heat loads absorbed close to boulders or inside craters, the additional solar heat load close to sunlit boulders or slopes, plus possibly elevated metabolic heat due to geological task, will lead to increased water consumption, and, as a consequence, to reduced operational times. The presented approach for transient thermal analysis provides a tool to help sizing the necessary buffers for, and find rates of, incident heat fluxes for the optimized design of thermal control hardware. Hence, taking into account the transient effects, warm-up, cool-down, phase change, or heat flux rates, can save mass or increase factors of safety and increase robustness in a system.

The lunar surface at hand will always deviate from the model used in the design and implementation phases of a space project. The model could be enhanced with *in-situ* produced maps of the topography and knowledge about local material properties. This enhanced model than could "shadow" the mission operations on the Moon, help to plan and optimize paths and to create time schedules. During the operation phase, paths and schedules for surface-crafts with a given design must take into consideration the thermal environment and local surface features. The time of day a certain task can be performed in a given lunar environment, the path a surface-craft can take, and the duration it can stay in a region, either shadowed or exposed to sunlight and high infrared heat loads, cannot be defined by worst case considerations alone. Hence, taking into account the transient effects can improve mission operations and missions capabilities, increase the number of possible tasks, and with that increase scientific output.

In summary, the novel approach to determine transient heat loads for moving objects on the Moon can be used in most of the space project phases.

A) In concept and preliminary design phases (phase 0 to B) the demonstrated approach can be applied to profile mission scenarios, define boundary conditions and derive thermal requirements.

B) In critical design and design implementation (phase C and D) transient thermal analysis can help, to analyze design solutions on system and subsystem level, to optimize a chosen solution, to define test scenarios, to design control strategies for thermal hardware, and to develop new thermal technologies.

C) During mission operation (phase E), the proposed approach can be used as a mission shadowing tool, to define the factors of safety for the real environment, to plan and optimize paths, and to create time schedules.

The threshold at which transient thermal simulations are most beneficial is a complex function of many parameters. These crucial parameters can be separated into lunar environment and surface-craft parameters. The lunar environment parameters are the solar elevation angle, the properties of the local surface material, and the presence, size and number of craters and boulders. The solar elevation angle is a function of latitude and time of lunar day, as well as the local slope angle. The material properties of local surface material depend on the region on the Moon and the slope angle. The presence, size and distribution of craters and boulders is also a function of the region on the Moon. The parameters of the surface-craft are material properties, internal structure, and operation modes. The material properties are optical / thermal properties of the outermost shell, the thermal conductivity of the used materials, the thermal conductivity of the junctions between different components, as well as density and heat capacity of the used materials. The internal structure of the surface-craft determines heat paths through the structure, and the geometrical shape which in turn determines the view factors between components, and between components and the lunar surface. The operation mode finally describes the level and frequency of internal heat loads. These parameters make generalized conclusions for the entire Moon or surface-crafts in general, invalid. Yet, the presented *TherMoS* approach enables to determine the threshold values for important variables in conjunction with a set of fixed parameters. That is, for example optical properties

can be optimized for a given surface-craft design for a certain region on the Moon taking into account local transits.

The results of this work indicate that differences in the thermal environment can occur anywhere on the Moon. The worst cases of permanent shadow at the poles, or full exposure to the Sun overhead at the equator, will not profit or be altered by transient thermal calculations. The impact of local surface features increases with decreasing solar elevation angles. The lower the solar elevation angle, the larger is the influence of local surface features and the demand for transient calculations. This is especially true close to the terminator at the equator, and towards the lunar poles. Local surface features alter the lunar surface temperature, and the view factors to space, to the ground and the Sun. A surface-craft placed in this environment will be subject to fluctuating infrared and solar heat fluxes. One could argue that for an object with a high thermal inertia, the effects of local surface features on the Moon are negligible. This statement is certainly true for narrow lunar surface temperature ranges and a surface-craft designed for this environment, or a surface-craft designed for worst case hot equatorial conditions, and worst case cold polar conditions. Such a surface-craft will have large safety and performance margins and thus will have a high mass. High masses and heat capacity will protect against fluctuating heat fluxes. The transient effects for large base structures therefore are of minor importance. Bases might only be vulnerable to the transient thermal environment with respect to structural loads caused by thermal gradients.

However, most surface-craft will not or cannot be designed for worst case cold and hot conditions due to mass limitations. Most surface-craft will not have a high thermal inertia and for those the *TherMoS* approach provides a tool to acquire vulnerable information. In the light of upcoming governmental and privately funded rovers to the Moon, the thermal environment will play a significant role in achieving the set mission goals. The results of this work indicate that, especially for rovers with lower thermal masses, core temperature is affected mainly by local shadows, but also by increased heat fluxes from boulders, and reduced view factors to space in craters. This is true for surface features with sizes several times larger in diameter than the surface-craft; threshold values for the ratio between surface-craft and surface feature size can be determined with the presented *TherMoS* approach in the future. Exploration rovers used to investigate the lunar surface could increase their performance and extend the operational capabilities by including transient thermal effects.

A human in a spacesuit has a higher thermal inertia than the small exploration rovers considered in this work. Yet, the human is more sensitive to elevated or reduced levels of heat. Tasks and prolonged activities in regions with slightly elevated environmental heat fluxes, in addition to increased metabolic loads, will lead to a higher demand for the surface-craft thermal control system. Depending on the used technologies, increased environmental loads will also lead to a faster depletion of consumables which in turn reduces mission time and thus possibly scientific output. In addition, the unprecedented possibilities of the presented approach environment to produce heat flux rates for movements, body postures, or tasks in a predefined lunar surface setting, enables more detailed design and test of control algorithms for thermal control hardware.

In summary, the presented approach enables a differentiated thermal analysis and design of moving surface-craft, based on transient heat fluxes, in contrast to the worst case design approach prevailing in spacecraft thermal engineering of today. Furthermore, the transient analysis now possible enables the determination of dynamic heat fluxes and heat flux rates for thermal control technologies, and enhances the operational capabilities of moving objects, for the future exploration of the Moon.

7.3 Future Work

The creation, implementation, and verification of a complex modeling environment such as the *TherMoS* tool provides a potent way to address engineering questions for moving objects on the Moon and other atmosphere-less celestial bodies. The presented work was the first step into a research field to investigate threshold values, boundary conditions, optimized paths and design of moving objects for the exploration of the Moon. The possible research questions arising from this work targets optimized designs for rovers and spacesuits. This can be achieved by better understanding the transient effects occurring in the diverse and demanding lunar thermal environments.

The future work section is subdivided into three parts (Figure 7-21). The first part addresses possible improvements of the used models, with a focus on the *Landscape Module* and the *Spacecraft Module*. In the second part, shortcomings of the simulation itself are investigated and possible solutions are proposed. The last part is dedicated to future engineering research topics that arise from the foundation laid by this thesis.
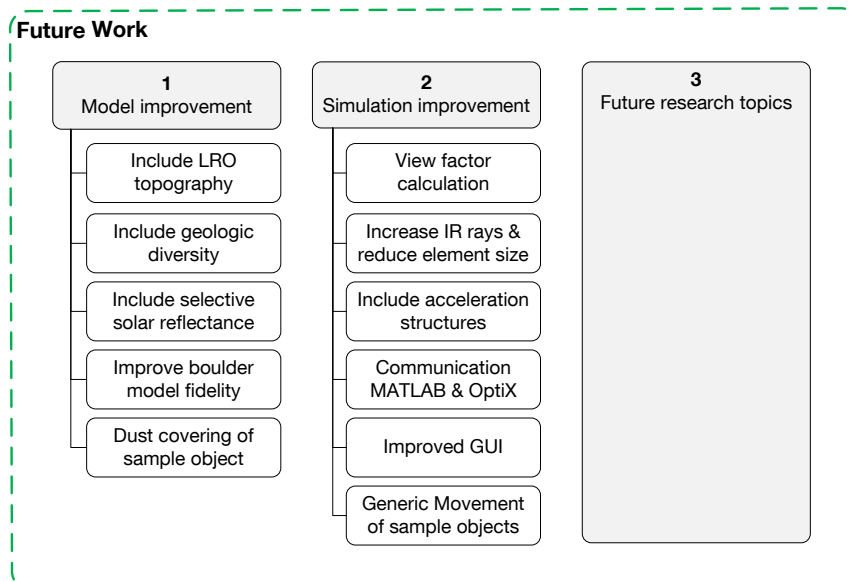
Figure 7-21: Subdivision of the future work chapter.

Improvement of the model:

The improvements of the *TherMoS* models are development tasks that can be conducted on grad-student level. The necessity to improve the models is defined by the research topic that shall be investigated further.

The impact of global topographic features was neglected in the present work. The exact value or ratio between object mass, thermal inertia and heat flux from the global environment could be identified by increasing the resolution of the lunar topography. The lunar topography model is based on the remote sensing data gathered by the Japanese Kaguya probe. The US Lunar Reconnaissance Orbiter (LRO) probe measured, and still measures, the topography with unprecedented accuracy. The constant stream of data reached more than 5.7 billion data points in September 2012 (personal communication, Keith Bennett) as compared to the 16 million data points from the Kaguya probe (Araki et al. 2009). The higher resolution LRO lunar topographic data also contain surface features with smaller dimensions. The integration of the LRO data is a logical next step to improve the accuracy of the entire model and local temperature predictions.

The lunar geology (selenology) is highly diverse. Its impact on local heat fluxes on surface objects could be determined by increasing the geologic diversity, by changing optical properties and thermo physical properties of the regolith. In the current implementation of the *Landscape Module,* thermo physical and optical properties are only distinguished for *mare* and *highland* regions. Further improvements of the *Landscape Module* should incorporate local material properties. In a first step, this could be a change in local regolith α and ε with respect to ejecta blankets around old, in contrast to young, craters. In a second step, the topography could be overlaid with mineralogy maps that exist from Clementine, Chandrayan-1, but also from LRO. A third possible step would be to add the regolith angle of repose. The angle of repose would lead to local exposure of bedrock in craters or on cliffs in mountain ranges. The bare bedrock most likely will have a more dampened temperature behavior compared to regolith due to a higher thermal conductivity and heat capacity.

In addition to mineral and material dependent thermal properties, yet another improvement for the *Regolith Model* would be to include specular light scattering. The lunar regolith shows an increase of reflectivity with lower angles of solar incident (Birkebak and Cremers 1974). The specular reflectivity would further increase the amount of received solar heat flux at low angles of solar incident or in the vicinity of inclined slopes. Furthermore, the regolith reflectivity increases for higher regolith densities (Birkebak and Cremers 1974). Increased reflectivity for higher local density is important for the imminent vicinity of landers or bases, if the local regolith is compressed by rovers or boots of astronauts. For surface-craft models with a high sensitivity of incident heat flux, an even more detailed specular reflectivity of regolith could be added. On the other hand, a specular reflection of the regolith would demand a change in the ray-tracing algorithm. The solar light source must then be subdivided into a number of wavelength sections, and the surface must host functions to treat incident solar rays of different wavelengths accordingly.

The current *Boulder Model* could be improved by a) more surface elements, b) a higher variety in bulk material, c) partial covering with regolith, and d) more accurate shapes. The improvement of the Boulder Model would enable to define a ratio between boulder size and surface-object or their thermal inertias. The number of surface elements increases the fidelity of the *Boulder Model* and the resolution of infrared heat flux in the vicinity of the boulder. The current implementation of the *Boulder Model* only distinguishes between *mare* and *highland* bedrock material, and the optical properties of regolith are used. As mentioned above, the lunar surface has a higher variety of minerals and this also applies to boulders. The choice of core material determines $c_{p,B}$, k_B, ρ_B, $\alpha_{sol,B}$, and ε_B, and with that the transient thermal behavior. Three main processes lead to the covering of boulders with regolith. The regolith is either a) displaced by micrometeorites on the nearby regolith, b) levitated and transported by electrostatic forces, or d) created in-situ on the boulder as a result to the impact of micrometeorites. In addition, man-made sources would be: exhaust from decent engines, or dust kicked up by rovers, astronauts, or construction vehicles. The properties of the porous media on top of a boulder lead to insulation or a change in optical properties. These effects further change the transient behavior of boulders. Finally, the shape of the boulder is created randomly in the current state of the *TherMoS* tool. Real boulders are elongated, partially submerged, broken to pieces, or concave. A more realistic shape would further improve the local heat fluxes encountered by a surface-craft. The size distribution of the implemented *Boulder Model* is currently artificially shifted towards larger boulders to reduce the computation demand. An implementation that also takes into account smaller boulders would increase the computational demand, but improve the accuracy of the local lunar surface temperatures towards more realistic numbers. On the other hand smaller boulders have a lessened impact on surface-crafts.

The *Spacecraft-Module* could be further enhanced by adding the covering with lunar dust and modeling its wavelength dependent selective change in optical properties (Gaier et al. 2008; Gaier et al. 2010). The dust-covering rate could be implemented for different tasks and accounted for throughout the simulation. The conductive interface between surface-craft and the surface of the Moon is presently neglected due to the extremely low thermal conductivity of lunar Regolith. For short contact times and small footprints this

![Fakultät für Maschinenwesen Lehrstuhl für Raumfahrttechnik logo] Dynamic thermal modeling for moving objects on the Moon

Technische Universität München

assumptions is justified. For longer contact times, larger footprints and extremely cold areas the connection must be further investigated. As pointed out by Fullerton (2001) the contact times between gloved astronaut hands and extremely cold rocks are restricted due to occurrence of uncomfortable and potentially dangerous heat leaks through the fingers.

<u>Improve *TherMoS* as a thermal design tool:</u>

In the current state of the *TherMoS* tool, the surface elements of the space-craft do not impact each other. For the scope of this work this approach is acceptable. The heat exchange between different parts of the surface-craft needs to be accounted for in future, more detailed studies. For example, a detailed study on local hot spots on the surface-craft would need specular and diffuse surface properties for different wavelengths for each surface element of the sample object. The same is true for studies on optical instruments. To calculate solar and infrared, specular and infrared heat fluxes, the view factors between the different parts of the surface-craft have to be determined. The two possible ways to determine the heat fluxes between different parts of the surface-craft are to use the ray tracing algorithm to a) calculate the exchanged heat flux in each time step, or b) to determine the view factors. The first option is more accurate, accounts for relative movement of different parts of the sample body, but is also more time consuming. The relative movements could be for example: arms relative to torso, or a manipulator relative to a rover body. Only one calculation is necessary for the second option to use the ray tracing to calculate view factors. The view factors could be stored in a G_R-matrix and be reused in each time step. This approach can be used for sample objects without 'internal' relative movement. It is also the common approach used in commercial tools such as for example ESATAN-TMS®.

An overall improvement of the results of the *TherMoS* tool could be achieved by increasing the number of surface elements. The surface elements of the lunar surface radiate the infrared heat fluxes. The decrease in element size possibly combined with an increase of infrared rays per surface element would homogenize the infrared heat flux on the sample object. A more continuous infrared heat flux distribution would allow for smaller surface elements of the sample objects and simultaneously omit the artificial fluctuations of infrared heat flux apparent in the results (chapter 6). On the other hand the decrease of surface element size and increase in infrared ray numbers also increases the need in computational power and simulation time.

The code for the ray tracing algorithm can be further optimized to reduce the run time for each time step. One of the options is to add more so called *acceleration structures* to the OptiX® code. Currently only the sample object is placed in an OptiX® acceleration structure. To place each boulder and crater in an individual acceleration structure could improve the simulation speed. The same is true for extensions or limbs of rovers and astronauts in spacesuits. To incorporate this form of modularity, the current ray tracing algorithm needs to be generalized further.

The communication between MATLAB® and OptiX® is quite cumbersome in the current implementation. In each time step, MATLAB® starts the ray tracer anew. As a consequence OptiX® rebuilds the entire scene in each time step, reads from and writes to the text files, which also must be opened and closed, and the variables have to be reset. MATLAB® provides means to keep an application such as OptiX® running whilst performing calculations. Another possible way would be to communicate via protocols. The variables could be altered in each time step, and the bulk date of temperatures and heat fluxes could be transmitted without the detour of text files. A step towards a better communication of MATLAB® and OptiX® would further improve the simulation speed.

The temperature calculation for the sample object could be implemented directly in the *TherMoS* tool. The current status requires manual inputs to additional MATLAB® files to calculate the temperature of a sample body. This approach is used deliberately because it facilitates to rerun the temperature case and perform parametric studies on different sample body material configurations. Yet it would be possible to include the temperature into the *TherMoS* tool to improve the handling.

Besides, the handling of the *TherMoS* tool could be further increased by improving the operability of the tool. The operability could be improved by a better graphic user interface (GUI) and the transition to an object oriented modeling approach for the surface-craft.

The current *TherMoS Movement* function needs to be generalized further. The paths and tasks introduced in section 6.1.2 for rover and spacesuit required many manual adaptations and are restricted to the shown movements. Improvements are necessary for more general rotations and translations according to user defined waypoints and tasks. The adaptation of the attitude currently is tailored for the plane surfaces the large and the small crater case. More randomized surfaces are not accounted for. Hence the adaption of the sample body attitude to the local surface roughness has to be improved. The same applies to the sample object velocity. Another interesting feature would be to determine the output of heat loads produced by the drive engines, or metabolism respectively, according to local terrain. An important step would be to include complex tasks and operations. Complex tasks and operations would be for example: turn radius, or the relative movement of extensions and limbs which is of special interest for tasks of astronauts in spacesuit.

Another aspect to improve the *TherMoS* tool would be to shift to an object oriented approach that considers each thermal node as an object with individual properties. An object oriented approach would make the tool more generic in terms of geometries and used materials. Furthermore, it would be the first thermal analysis tool to base on object orientation.

Future research topics:

Throughout the present work, some fields for future studies and research were identified. On one side there are almost infinite possibilities for parametric studies and on the other side there are numerous tasks to enhance the output of the present *TherMoS* approach and providing a basis for future in-depth research.

The parametric studies can be used to create a set of ratios for the impact of environmental parameters on the thermal design of surface-craft. In this way threshold values for the necessity of transient calculations could be derived, and a hierarchy of the danger potential of a lunar surface parameter could be created. Such a hierarchy could lead to maps with hazard zones for operation planning, but also could be used for design guidelines in rover and spacesuit design or technology sizing. Parametric studies on grad-student level could be the impact of boulders of different size, distribution in combination with craters of various sizes, or for parametric studies on altered material properties. Parametric studies could also be performed on the impact of changing optical properties, the change in reflectivity in the vicinity of a base due to rover tracks, astronaut tracks, lander decent stages or construction work. Yet another question would address the vulnerability of surface-craft with different thermal inertia to the size of local boulders and craters.

Further tasks and research questions were gathered in Figure 7-22. Some of the proposed tasks could possibly be driven to a PhD research level.
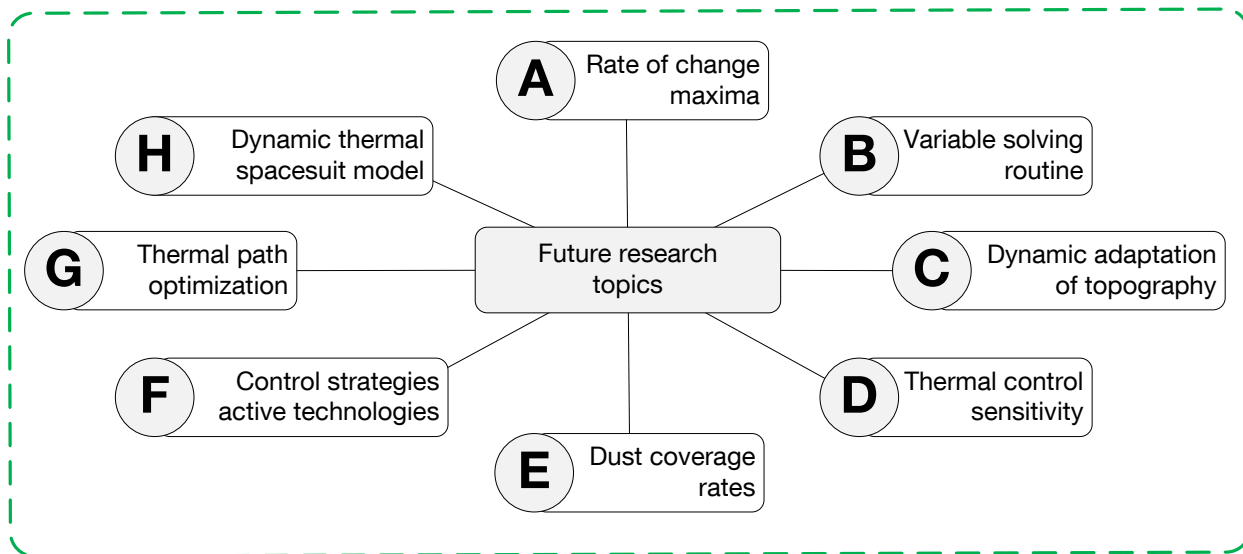
Figure 7-22: Overview of possible future research topics derived from the present work.

A) Define the maximum and minimum of heat flux rate in temperatures of individual parts of the surface-craft as function of local lunar surface temperature, solar elevation angle and exposure to local shadows,

B) Implement a variable solving routine that intelligently switches between view factor and ray tracing depending on the velocity of the surface-craft or its extensions and limbs to achieve an optimum in computational performance and thermal engineering prediction,

C) Implement a dynamic refinement of the local topography in terms of number of local surface features and the surface elements thereof, along the path of the surface-craft,

D) Experimentally identify the threshold values for the sensitivity of thermal control hardware for heat flux rate in heat flux densities and compare them with the simulation results,

E) Experimentally determine rates of coverage with lunar regolith due to frequent tasks and their relevance, plus add the functionality into the simulation,

F) Define control strategies for active thermal control devices such as electrochromatic, thermochromatic, or digital radiators, as well as 2-phase heat exchangers,

G) Determine paths for rovers or astronauts in spacesuits optimized under thermal as well as topographical considerations.

H) Create a dynamic thermal model of a spacesuit taking into account variable metabolic loads, external heat fluxes, heat loads from the PLSS, and a detailed geometry of the spacesuit.

Ad A) The temperature of its individual parts and the core temperature of a surface-craft remains the central objective for the thermal engineering domain. The surface-craft temperature depends on the incident heat fluxes. The impact of local surface feature on surface-craft is not negligible, as was shown in this work. In the simulated cases presented in chapter 6, the relative impact of surface features was most pronounced for low solar elevation angles, but the absolute impact increases with increasing surface temperature. Thus it would be interesting to define the maximum and minimum of absolute heat flux increase at different locations and at different times, i.e. combinations of local surface temperature and incident solar angle. With this knowledge operation modes of surface-craft could be scheduled and no-access areas defined on a top level.

Ad B) In order to use the *TherMoS* approach to predict local hazard zones during operation, its computational time needs to be improved. The main bottleneck currently is the time necessary to perform and repeat the ray-tracing. A surface-craft traversing the lunar surface will not be impacted much by even hotspots that are a long distance away, if the view factor is small. If the surface-craft traverses an unob-

structed plane simple view factor calculations to the surface, determined by a single ray tracing run, are sufficient. As soon as the surface-craft approaches one or several boulders the radiative heat exchange should be calculated with the ray tracing algorithm. This transient not only in the movement of the surface-craft but also of the calculation methods asks for variable time step and an adaptive method that switches between ray tracing and view factor calculation if and when appropriate. In this context, it is interesting and important to investigate the threshold for ray tracing of the complex interaction between approaching velocity, size of sample object, size or/and number of surface features and local temperatures.

Ad C) This task has the same reason as task B – optimizing the computational time. During the traverse of a surface-craft the distances to local surface features change continuously. High fidelity models of boulders and craters with numerous surface elements increase computational demand and time. The infrared rays emitted and received have to be calculated for each time step and surface element. An adaptive method to change the number of surface elements with respect to the size of the surface feature, the size of the sample object and the distance in between (the view factor) could improve the computational demand and accelerate the simulation. The dynamic adaption of surface elements and the subsequent rooting of heat fluxes to the thermal nodes inside the surface features might also be interesting for other applications.

Ad D) The simulation tool so far bases on models and verification against literature and remote sensing data. In order to improve the overall confidence of the simulation experiments would be beneficial. Experiments solely to verify the simulation are not constructive. Instead, experiments on real active control mechanisms are beneficial for the aerospace domain. The confidence in the applicability of given active control mechanisms for the lunar surface could be raised by the experiments. This would also allow identifying scaling laws as design recommendations, as pointed out for electrochromics and phase change materials in section 7.1.4. In addition models of the active control mechanisms under investigation could be included into the *TherMoS* tool and increase its overall fidelity. The experiments must take into account the vacuum environment and fast changing infrared heat fluxes as well as sharp transitions between solar heat flux and shadow.

Ad E) The covering with dust and the change in optical properties is a problem known to lunar surface missions since the Apollo program. Extensive studies have been performed on the levitation of dust by electrostatic forces. Fewer researches have investigated the impact on control surface elements and on mitigation strategies. Almost no work was done on the transients that give the rates of change of dust covering over time and for certain tasks or operations on the lunar surface. Hardware studies will be necessary to acquire the rate of dust-covering for certain tasks. This includes objects moving at slow as well as high velocities, different locomotion, and construction, hauling and digging activities. Moreover the dust-covering rate must be investigated for tasks such as sampling or geological surveillance. The study of dust-coverage rate is not only important for thermal designs but also for operation and maintenance needs (Cain 2010). The limit of dust covering for a given thermal control surface material and its inclination can only be determined experimentally.

Ad F) The *TherMoS* simulation can be used to define heat fluxes for a given sample body configuration. With an improved infrared ray tracing and even more detailed surface-craft models the heat fluxes could be determined to a sub cm² level. But even in the present form, the *TherMoS* results can be used to define boundary conditions and thermal envelopes for the investigation of the control algorithms of active thermal control technologies. The rates of change and the maximum and minimum heat flux densities derived in chapter 6 and discussed in chapter 7 can be used to scale the control laws, integrate exceptions or to define operational restrictions of current as well as upcoming technologies. The work being performed at CU Boulder on electrochromatic devices (Metts et al. 2011) is one example for such an investigation. The same could be applied to more common active devices such as for example loop heat pipes, pumped fluid loops or heaters.

Ad G) On a system engineering and management level the *TherMoS* tool could be extended to optimize paths of rovers and spacesuits. State-of-the-art path optimization concepts focus the reduction of necessary power for driving or walking under the boundary condition of local topography (Gilkey et al. 2011). The necessary power does also depend on the thermal control. Especially active thermal control requires power and dissipates heat. In cold environments heaters can have large impact on the overall power budget and in hot environments the additional heat must be dissipated. Whether a radiator needs to face away from hot surfaces or the water in a sublimator should be saved to allow for longer operations, the thermal environment should be taken into account in the path optimization alongside the topography. This path optimization could be achieved by increasing the simulation speed and perform a multitude of simulation runs to determine locally and time-dependent optimized paths.

Ad H) The work on a spacesuit thermal model could be established in conjunction with the path optimization proposed for tasks F & G. Moreover the work on a dynamic spacesuit thermal model would be in-line with ongoing work at the Institute of Astronautics on a dynamic human model (Czupalla et al. 2009b; Schnaitmann et al. 2012) and a dynamic model on personal life support systems (Olthoff 2012).

Beside the possible research topics defined in A) to H) the derived empirical equations could be improved further. The derived empirical equations only base on results from a series of simulations. Further refinement and verification with real measurements are necessary, taking into account more accurate materials and optical surface properties.

In summary the presented work opens the window to a field of studies in planetary related thermal analysis of spacecraft to a level of detail that was not possible until now.

8 References

Abramov, I., **Pozdnyakov, S.**, **Severin, G.**, and **Stoklitsky, A.** (2001), 'Main problems of the Russian Orlan-M space suit utilization for EVAs on the ISS', *Acta Astronautica*, 48/5-12: 265–273.

Ahrens, T. J. (op. 1995), *Rock physics & phase relations*: *A handbook of physical constants* (Washington: American Geophysical Union).

Allen, D. A. (1971a), 'Infrared Studies of the lunar terrain - part I The background moon', *Earth, Moon, and Planets*, 2/3: 320–337 <DOI: 10.1007/BF00561884>, accessed 10 Nov 2010.

Allen, D. A. (1971b), 'Infrared studies of the Lunar terrain - part II thermal anomalies', *Earth, Moon, and Planets*, 2/4: 435–462 <DOI: 10.1007/BF00562880>, accessed 10 Nov 2010.

Anderson, W. G., **Ellis, M. C.**, **Walker, K. L.**, and **Robertson, G. A.** (2009), 'Variable Conductance Heat Pipe Radiators for Lunar and Martian Environments', in , *AIP Conference Proceedings* (AIP), 57–66.

Araki, H., **Tazawa, S.**, **Noda, H.**, **Ishihara, Y.**, **Goossens, S.**, **Sasaki, S.**, **Nawano, N.**, **Kamiya, I.**, **Otake, H.**, **Oberst, J.**, and **Shum, C.** (2009), 'Lunar Global Shape and Polar Topography Derived from Kagu-ya-LALT Laser Altimetry', *Science*, 323/5916: 897–900 <DOI: 10.1126/science.1164146>, accessed 10 Sep 2010.

Astrobotic (2012), 'Astrobotic Technology, Inc - Red Rover' <http://www.astrobotic.com/>, accessed 3 Apr 2013.

Ball, A. J. (2007), *Planetary landers and entry probes* (Cambridge: Cambridge University Press).

Bandfield, J. L., **Ghent, R. R.**, **Vasavada, A. R.**, **Paige, D. A.**, **Lawrence, S. J.**, and **Robinson, M. S.** (2011), 'Lunar surface rock abundance and regolith fines temperatures derived from LRO Diviner Radiometer data', *Journal of Geophysical Research*, 116 <doi:10.1029/2011JE003866>.

Bannon, E. T., **Bower, C. E.**, **Sheth, R.**, **Stephan, R.**, **Chandrasekhar, P.**, and **Zay, B.** (2010), 'Electrochromatic radiator coupon level testing and full scale math modeling for use on altair lunar lander', *Proceedings of the 40th International Conference on Environmental Systems*, 2010.

Barer, A. S. (1991), 'EVA medical problems', *Acta Astronautica*, 23: 187–193 <doi:10.1016/0094-5765(91)90118-O>.

Barraclough, S., **Huston, K.**, and **Allouis, E.** (2009), 'Thermal Design for Moon-NEXT Polar Rover', *SAE International*, 2009 <2009-01-2461>, accessed 29 Aug 2010.

Bart, G. D., and **Melosh, H. J.** (2005), 'Ejected boulders: implications for secondary craters and the age dating of surfaces', *Lunar and Planetary Science*, XXXVI/Abstract 2022, accessed 5 Feb 2011.

—— (2007), 'Using lunar boulders to distinguish primary from distant secondary impact craters', *Geophyysical Research Letters*, 34, accessed 13 Feb 2011.

Bartlett, P. W., **Wettergreen, D.**, and **Whittaker, W.** (2008), 'Design of the Scarab rover for mobility & drilling in the lunar cold traps', 2008.

Bartoloni, A. (2011), 'White Label Space: Media Corner' <http://www.whitelabelspace.com/2011/02/media-gallery.html>, updated 7 Feb 2013, accessed 3 Apr 2013.

Barucci, M. A., **Cheng, A. F.**, **Michel, P.**, **Benner, L. A. M.**, **Binzel, R. P.**, **Bland, P. A.**, **Böhnhardt, H.**, **Brucato, J. R.**, **Campo Bagatin, A.**, **Cerroni, P.**, **Dotto, E.**, **Fitzsimmons, A.**, **Franchi, I. A.**, **Green, S. F.**, **Lara, L.-M.**, **Licandro, J.**, **Marty, B.**, **Muinonen, K.**, **Nathues, A.**, **Oberst, J.**, **Rivkin, A. S.**, **Robert, F.**, **Saladino, R.**, **Trigo-Rodriguez, J. M.**, **Ulamec, S.**, and **Zolensky, M.** (2012), 'MarcoPolo-R near earth asteroid sample return mission', *Exp Astron*, 33/2-3: 645–684.

Bauch, K., **Hiesinger, H.**, and **Helbert, J.** (2009), 'Estimation of lunar surface temperatures: a numerical model', *EGU General Assembly*, 11 <EGU2009-10395>.

Berg, O. E., **Wolf, H.**, and **Rhee, J.** (1976), 'Lunar soil movement registered by the Apollo 17 cosmic dust experiment', *Interplanetary Dust and Zodiacal Light*, 48: 233–237 <http://link.springer.com/chapter/10.1007%2F3-540-07615-8_486?LI=true#>, accessed 29 Jan 2013.

Berkebile, S., and **Gaier, J. R.** (2012), 'Adhesion in a Vacuum Environment and its Implications for Dust Mitigation Techniques on Airless Bodies', *42nd International Conference on Environmental Systems*, 2012 <AIAA 2012-3465>.

Berkelman, P., **Easudes, J.**, **Martin, M. C.**, **Rollins, E.**, and **Silberman, J.** (1995), *Design of a Day/Night Lunar Rover,* ADA310807 (Pittsburgh, PA).

Bertrand, R., **Brueckner, J.**, and **van Winnendael, M.** (2000), 'The Nanokhod Micro-Rover - A Versatile Platform for Surface Exploration of Celestial Bodies', *Proceedings of the Fourth International Conference on Exploration and Utilisation of the Moon*, 2000: 149–154.

Biele, J., and **Ulamec, S.** (2008), 'Capabilities of Philae, the Rosetta Lander', *Space Sci Rev*, 138/1-4: 275–289.

Birkebak, R. C., and **Cremers, C. J.** (1974), *Thermal Radiation Characteristics and Thermophysical Properties of Lunar Materials,* NASA-CR-139950 (Lexington, Kentucky).

Birkebak, R. C., and **Dawson, J. P.** (1973), 'Thermal radiation properties of Apollo 14 fines', *Earth, Moon, and Planets*, 6/1-2: 93–99 <doi:10.1007/BF02630654>, accessed 27 Jul 2010.

Bledjian, L., **Hale, D. V.**, **Hoover, M. J.**, and **O'Neill, M. J.** (2002-c2003), 'Phase-Change Materials', in D. G. Gilmore (ed.), *Spacecraft Thermal Control Handbook*. *Volume 1: Fundamental Technologies* (1; 2nd edn., El Segundo, California 90245-4691: Aerospace Press), 373–403.

Braukhane, A., **Kreutz, M.**, **Ksenik, E.**, **Lange, C.**, **Richter, L.**, and **Rombert, O.** (2010), 'VELOX – A Demonstration Facility for Lunar Oxygen Extraction in a Laboratory Environment', *GLUC Proceedings 2010*, 2010, accessed 4 Jan 2011.

Bungartz, H.-J. (2009), *Modellbildung und Simulation*: *Eine anwendungsorientierte Einführung* (Berlin: Springer).

Burns, J. O., **Johnson, S.**, **Taylor, J. G.**, and **Duric, N.** (1989), *A lunar far-side very low frequency array,* NASA-CP-3039, NAS 1.55:3039 (Albuquerque, New Mexico) <http://ntrs.nasa.gov/search.jsp?R=19900001489>.

Busby, M. S., and **Mertesdorf, S. J.** (1987), 'The benefit of phase change thermal storage for spacecraft thermal management', *Proceedings of the 22nd Thermophysics Conference*, 1987: 1–7 <DOI: 10.2514/6.1987-1482>.

Cabrol, N. A., **Diaz Chong, G.**, **Dohm, J.**, **Pereira Arredondo, M.**, **Dunfield, G.**, **Gulick, V.**, **Jensen Iglesia, A.**, **Keaten, R.**, **Herrera Lamelli, C.**, **Landheim, R.**, **Lee, P.**, **Pedersen, L.**, **Roush, T.**, **Schwher, K.**, **Stoker, C.**, and **Zent, A.,** 'Atacama I: Science results of the 1997 NOMAD rover field test in the Atacama desert Chile', accessed 10 May 2012.

Cain, J. R. (2010), 'Lunar dust: The Hazard and Astronaut Exposure Risks', *Earth Moon Planets*, 107/1: 107–125.

Calle, C. I., **Chen, A.**, **Immer, C. D.**, **Csonka, M.**, **Hogue, M. D.**, **Snyder, S. J.**, **Rodriquez, M.**, and **Margiotta, D. V.** (2010), 'Dust Removal Technology Demonstration for a Lunar Habitat', *AIAA SPACE 2010 Conference and Exposition*, 2010 <AIAA-2010-8606>, accessed 1 Jul 2011.

Cameron, W. S., and **Coyle, G. J.** (1971), 'An analysis of the distribution of boulders in the vicinity of small lunar craters', *Earth, Moon, and Planets*, 3/2: 159–188 <doi: 10.1007/BF00561907>, accessed 20 Dec 2010.

Campbell, A. B., **French, J. D.**, **Nair, S. S.**, **Miles, J. B.**, and **Lin, C. H.** (1999), *Dynamic Modeling of the Minimum Consumables PLSS* (Warrendale, PA: SAE International).

Campbell, A. B. (2000), 'Thermal Analysis and Design of an Advanced Space Suit', *Journal of Thermophysics and Heat Transfer*, 14/2: 151–160, accessed 2 Jan 2011.

Campbell, A. B., **Nair, S. S.**, **Miles, J. B.**, and **Webbon, B. W.** (1996), *PLSS Transient Thermal Modeling for Control* (Warrendale, PA: SAE International).

Carpenter, J., **Fisackerly, R.**, **Rosa, D. de**, and **Houdou, B.** (2012), 'Scientific Preparations for Lunar Exploration with the European Lunar Lander', *Planetary and Space Science*, 2012.

Cernaianu, M. O., **Cirstea, C.**, and **Gontean, A.** (2012), 'Thermoelectrical Energy Harvesting System: Modelling, Simulation and Implementation', *10th International Symposium on Electronics and Tele-communications*, 2012: 67–70.

Choi, M. K. (2010), 'Thermal Optimization of IXO SXT FMA to Meet 20?C and Stringent Temperature Gradient Requirements and Heater Power Budget', *40th International Conference on Environmental Systems*, 2010 <AIAA 2010-6054>, accessed 1 May 2012.

Christie, R. J., **Plachta, D. W.**, and **Hasan, M. M.** (2008), 'Transient Thermal Model and Analysis of the Lunar Surface and Regolith for Cryogenic Fluid Storage', *NASA STI program*, 2008, accessed 22 May 2010.

Cintala, M. J., **Garvin, J. B.**, and **Wetzel, S. J.** (1982), 'The distribution of blocks around a fresh lunar mare crater', *Lunar and Planetary Science*, 1982: 100–101, accessed 9 Feb 2011.

Claasen, F., **Henn, N.**, **Haarmann, R.**, and **Knigge, T.** (2012), 'Lunar exploration activitites within the german national space program', *Proceedings of the Global Lunar Exploration Conference 2012*, 2012 <GLEX-2012.02.2.2x12258>.

Clawson, J. F., **Tsuyuki, G. T.**, **Anderson, B. J.**, **Justus, C. G.**, **Batts, W.**, **Ferguson, D.**, and **Gilmore, D. G.** (2002-c2003), 'Spacecraft Thermal Environments', in D. G. Gilmore (ed.), *Spacecraft Thermal Control Handbook*. *Volume 1: Fundamental Technologies* (1; 2nd edn., El Segundo, California 90245-4691: Aerospace Press), 21–69.

Cohen, B. A., **Chavers, D. G.**, and **Ballard, B. W.** (2012), 'NASA'S Robotic Lunar Lander Development Project', *Acta Astronautica*, 79: 221–240.

Colaprete, A., **Schultz, P.**, **Heldmann, J.**, **Wooden, D.**, **Shirley, M.**, **Ennico, K.**, **Hermalyn, B.**, **Marshall, W.**, **Ricco, A.**, **Elphic, R. C.**, **Goldstein, D.**, **Summy, D.**, **Bart, G. D.**, **Asphaug, E.**, **Korycansky, D.**, **Landis, D.**, and **Sollitt, L.** (2010), 'Detection of Water in the LCROSS Ejecta Plume', *Science*, 330/6003: 463–468.

Colwell, J. E., **Batiste, S.**, **Horányi, M.**, **Robertson, S.**, and **Sture, S.** (2007), 'Lunar surface: Dust dynamics and regolith mechanics', *Rev. Geophys.*, 45/2.

Coradini, A., **Capaccioni, F.**, **Erard, S.**, **Arnold, G.**, **Sanctis, M. C. de**, **Filacchione, G.**, **Tosi, F.**, **Barucci, M. A.**, **Capria, M. T.**, **Ammannito, E.**, **Grassi, D.**, **Piccioni, G.**, **Giuppi, S.**, **Bellucci, G.**, **Benkhoff, J.**, **Bibring, J. P.**, **Blanco, A.**, **Blecka, M.**, **Bockelee-Morvan, D.**, **Carraro, F.**, **Carlson, R.**, **Carsenty, U.**, **Cerroni, P.**, **Colangeli, L.**, **Combes, M.**, **Combi, M.**, **Crovisier, J.**, **Drossart, P.**, **Encrenaz, E. T.**, **Federico, C.**, **Fink, U.**, **Fonti, S.**, **Giacomini, L.**, **Ip, W. H.**, **Jaumann, R.**, **Kuehrt, E.**, **Langevin, Y.**, **Magni, G.**, **McCord, T.**, **Mennella, V.**, **Mottola, S.**, **Neukum, G.**, **Orofino, V.**, **Palumbo, P.**, **Schade, U.**, **Schmitt, B.**, **Taylor, F.**, **Tiphene, D.**, and **Tozzi, G.** (2011), 'The Surface Composition and Temperature of Asteroid 21 Lutetia As Observed by Rosetta/VIRTIS', *Science*, 334/6055: 492–494.

Cordes, F., **Ahrns, I.**, **Bartsch, S.**, **Birnschein, T.**, **Dettmann, A.**, **Estable, S.**, **Haase, S.**, **Hilljegerdes, J.**, **Koebel, D.**, **Planthaber, S.**, **Roehr, T. M.**, **Scheper, M.**, and **Kirchner, F.** (2010), 'LUNARES: Lunar crater exploration withe heterogeneous multi robot systems', *Intelligent Service Robotics*, 4/1: 61–89 <DOI: 10.1007/s11370-010-0081-4>, accessed 30 Sep 2011.

Crawford, I., **Anand, M.**, **Cockell, C.**, **Falcke, H.**, **Green, D.**, **Jaumann, R.**, and **Wieczorek, M.** (2012), 'Back to the Moon: The scientific rationale for resuming lunar surface exploration', *Planetary and Space Science*, 74/1: 3–14.

Cremers, C. J., and **Birkebak, R. C.** (1971), 'Thermal conductivity of fines from Apollo 12', *Proceedings of the Lunar Science Conference*, 3: 2311–2315, accessed 18 Aug 2010.

Cremers, C. J., **Birkebak, R. C.**, and **White, J. E.** (1971), 'Lunar surface temperatures from apollo 12', *Earth, Moon, and Planets*, 3/3: 346–351 <doi:10.1007/BF00561846>, accessed 24 May 2010.

Cutler, A. H., and **Krag, P.** (1985), 'A Carbothermal Scheme for Lunar Oxygen Production', *Lunar Bases and Space Activities of the 21st Century*, 1985: 559–569 <1985lbsa.conf.559C>.

Czupalla, M., **Hager, P.**, **Hein, A.**, **Dirlich, T.**, **Zhukov, A.**, **Pfeiffer, M.**, and **Klaus, D.** (2009a), *Model Confidence Level - A Systematic Metric for Development of a Virtual Space Habitat* (Warrendale, PA: SAE International).

Czupalla, M., **Hager, P.**, **Pfeiffer, M.**, **Harder, J.**, and **Dirlich, T.** (2009b), 'An environmentally sensitive dynamic human model for LSS robustness studies with the V-HAB simulation', *Advances in Space Research*, 44/12: 1413–1427.

Dallas, T., **Diaguila, A. J.**, and **Saltsman, J. F.** (1971), *Design studies on the effects of orientation, lunation, and location on the performance of lunar radiators,* NASA TM X-1846 (Cleveland , Ohio, USA).

De Rosa, D., **Bussey, B.**, **Cahill, J. T.**, **Lutz, T.**, **Crawford, I.**, **Hackwill, T.**, **van Gasselt, S.**, **Neukum, G.**, **Witte, L.**, **McGovern, A.**, and **Carpenter, J. D.** (2012), 'Landing site characterization activities for the European Space Agency lunar lander mission', *European Planetary Science Congress 2012*, 7 <EPSCS2012-88 2012>.

Della Torre, A., **Ercoli Finzi, A.**, **Genta, G.**, **Curti, F.**, **Schirone, L.**, **Capuano, G.**, **Sacchetti, A.**, **Vukman, I.**, **Mailland, F.**, **Monchieri, E.**, **Guidi, A.**, **Trucco, R.**, **Musso, I.**, and **Lombardi, C.** (2010), 'AMALIA Mission Lunar Rover—The conceptual design of the Team ITALIA Rover, candidate for the Google Lunar X Prize Challenge', *Acta Astronautica*, 67/7-8: 961–978.

Dimarc, N. (2009), 'SYRTE FTP. [Online FTP Server]' <ftp://syrte.obspm.fr/pub/polac/transit/vsop2000/>, accessed 16 Sep 2011.

DOD (1994), *MIL-STD-1540D*: *Product verification requirements for launch, upper stage, and space vehicles,* MIL-STD-1540D.

Dory, J. (2006), *Constellation programm human-system integration requirements; final report,* CxP 70024.

Ehrenfreund, P., **McKay, C.**, **Rummel, J. D.**, **Foing, B. H.**, **Neal, C. R.**, **Masson-Zwaan, T.**, **Ansdell, M.**, **Peter, N.**, **Zarnecki, J.**, **Mackwell, S.**, **Perino, M. A.**, **Billings, L.**, **Mankins, J.**, and **Race, M.** (2012), 'Toward a global space exploration program: A stepping stone approach', *Advances in Space Research*, 49/1: 2–48.

Ernstson, K., and **Claudin, F.** (2012), 'Den Prozess beim Meteoriten-Einschlag verstehen: eine einfache Annäherung' <http://www.impaktstrukturen.de/understanding-the-impact-cratering-process/>, accessed 11 May 2012.

ESA /AOES Medialab (2004), 'Rosetta's Philae lander on comet nucleus' <http://spaceimages.esa.int/Images/2002/02/Rosetta_s_Philae_lander_on_comet_nucleus>, updated 19 Jan 2004, accessed 20 Jan 2013.

ESA - ESTEC (2008), *ECSS-E-ST-31C*: *Space engineering - Thermal control general requirements,* ECSS-E-ST-31C (Noordwijk, The Netherlands).

Fiala, D., **Lomas, K. J.**, and **Stohrer, M.** (1999), 'A computer model of human thermoregulation for a wide range of environmental conditions: the passive system', *Journal of Applied Physiology*, 87/5: 1957–1972 <http://www.jappl.org/content/87/5/1957.short>.

Finckenor, M. M., and **Doolling, D.** (1999), *Multilayer Insulation Material Guidelines,* NASA/TP-1999-209263 (Alabama).

Fisackerly, R., **Carpenter, J. D.**, **De Rosa, D.**, **Houdou, B.**, **Pradier, A.**, **Philippe, C.**, and **Gardini, B.** (2011), 'The european lunar lander: robotic operations in a harsh environment', 2011: 1–6.

Flouris, A. D., and **Cheung, S. S.** (2006), 'Design and Control Optimization of Microclimate Liquid Cooling Systems Underneath Protective Clothing', *Annals of Biomedical Engineering*, 34/3: 359–372 <doi: 10.10007/s10439-005-9061-9>, accessed 23 Dec 2010.

Fullerton, R. K. (2001), 'Advanced EVA Roadmaps and Requirements', *SAE International*, 2001 <2001-01-2200>, accessed 18 Jul 2010.

Gaier, J. R. (2005), *The effects of lunar dust on EVA Systems during the Apollo Missions,* NASA/TM-2005-213610 (Cleveland , Ohio, USA).

Gaier, J. R. (2008), 'The Need for High Fidelity Lunar Regolith Simulants', *NASA STI program*, 2008, accessed 12 Apr 2011.

Gaier, J. R., and **Jaworske, D. A.** (2007), 'Lunar Dust on Heat Rejection System Surfaces: Problems and Prospects', *NASA STI program*, 2007: 1–14, accessed 18 Aug 2010.

Gaier, J. R., and **Sechkar, E. A.** (2007), 'Lunar simulation in the lunar dust adhesion bell jar', *NASA STI program*, 2007, accessed 11 Jul 2010.

Gaier, J. R., **Journey, K.**, **Christophfer, S.**, and **DAvis, S.** (2011), *Evaluation of Brushing as a Lunar Dust Mitigation Strategy for Thermal Control Surfaces,* NASA/TM—2011-217231 (Cleveland , Ohio, USA).

Gaier, J. R., **Siamidis, J.**, **Panko, S. R.**, **Rogers, K. J.**, and **Larkin, E. M.** (2008), *The Effect of Simulated Lunar Dust on the Absorptivity, Emissivity, and Operating Temperature on AZ–93 and Ag/FEP Thermal Control Surfaces,* NASA/TM - 2008-215492 (Cleveland , Ohio, USA).

Gaier, J. R., **Street, K. W.**, and **Gustafsopn, R. J.** (2010), 'Measurements of the solar absorptance and thermal emittance of lunar simulants', *Proceedings of the 40th International Conference on Environmental Systems*, 40 <AIAA 2010-6025>, accessed 29 May 2011.

Ganapathi, G. B., **Sunada, E. T.**, **Birur, G. C.**, **Miller, J. R.**, and **Stephan, R.** (2009), 'Design Description and Initial Characterization Testing of an Active Heat Rejection Radiator with Digital Turn-Down Capability', *SAE International*, 2009 <2009-01-2419>, accessed 14 Nov 2011.

Gernhardt, M. L., **Jones, J. A.**, **Scheuring, R. A.**, **Abercromby, A. F.**, **Tuxhorn, J. A.**, and **Norcross, J. R.** (2009), 'Risk of compromised EVA performance and crew health due to inadequate EVA suit systems', in NASA (ed.), *Human Health and Performance Risks of Space Exploration Missions*, J. C. McPhee and J. B. Charles (Houston, Texas: NASA), 333–58.

Gilkey, A. L., **Galvan, R.**, **Johnson, A. W.**, **Kobrick, R. L.**, **Hoffman, J. A.**, **Melo, P. L.**, and **Newman, D. J.** (2011), 'Evaluation of a Surface Exploration Traverse Analysis and Navigation Tool', *41st International Conference on Environmental Systems*, 2011 <AIAA 2011-5181>, accessed 05.14.2013.

Gilmore, D. G. (2002-c2003) (ed.), *Spacecraft Thermal Control Handbook*: *Volume 1: Fundamental Technologies* (1; 2nd edn., El Segundo, California 90245-4691: Aerospace Press).

Gilmore, D. G., and **Collins, R. L.** (2002-c2003), 'Thermal Design Analysis', in D. G. Gilmore (ed.), *Spacecraft Thermal Control Handbook*. *Volume 1: Fundamental Technologies* (1; 2nd edn., El Segundo, California 90245-4691: Aerospace Press), 523–98.

Gilmore, D. G., **Lyra, J. C.**, and **Stultz, J. W.** (2002-c2003), 'Heaters', in D. G. Gilmore (ed.), *Spacecraft Thermal Control Handbook*. *Volume 1: Fundamental Technologies* (1; 2nd edn., El Segundo, California 90245-4691: Aerospace Press), 223–45.

Glück, B. (1990), *Wärmeübertragung*: *Wärmeabgabe von Raumheizflächen und Rohren* (Bausteine der Heizungstechnik Berechnung, Software; 2nd edn., Berlin: Verl. für Bauwesen).

Goswami, J. N., and **Annadurai, M.** (2011), 'Chandrayaan-2 mission', *42nd Lunar and Planetary Science Conference*, 2011, accessed 29 Oct 2012.

Graham, J. B. (2007), 'Prospecting Rovers for Lunar Exploration', *IEEE Astronautic Conference*, 2007 <1579>.

Greenwood, J. P., **Itoh, S.**, **Sakamoto, N.**, **Warren, P.**, **Taylor, L.**, and **Yurimoto, H.** (2011), 'Hydrogen isotope ratios in lunar rocks indicate delivery of cometary water to the Moon', *Nature Geosci*, 4/2: 79–82, accessed 16 Dec 2011.

Grygorczuk, J., **Seweryn, K.**, **Wawrzaszek, R.**, and **Banaszkiewicz, M.** (2009), 'Technological features in the new mole penetrator "KRET"', *Proceedings of the 13th European Space Mechanisms and Tribology Symposium*, 2009.

Gump, D. P., and **Thornton, J.** (2011), 'Prospects for Robotic Lunar Exploration by Commercial Enterprise', *IEEE Astronautic Conference*, 2011, accessed 29 May 2011.

Gurdeau, J., Leriche, M., and Uherek, E. (2004), 'Albedo' <http://www.atmosphere.mpg.de/enid/3__Sonne_und_Wolken/-_Albedo_3ao.html>, updated 4 Sep 2007, accessed 24 Apr 2013.

Gustafson, R. J., and **White, B. C.** (2009), *Development of a Lunar Dust Simulant* (Warrendale, PA: SAE International).

Gustafson, R. J., **White, B. C.**, and **Fidler, M. J.** (2009), *Oxygen Production via Carbothermal Reduction of Lunar* regolith (Warrendale, PA: SAE International).

Haarmann, R., **Jaumann, R.**, **Claasen, F.**, **Apfelbeck, M.**, **Klinkner, S.**, **Richter, L.**, **Schwendner, J.**, **Wolf, M.**, and **Hofmann, P.** (2012), 'Mobile Payload Element (MPE): Concept study for a sample fetching rover for the ESA Lunar Lander Mission', *Planetary and Space Science*, 74/1: 283–295.

Hager, P., and **Walter, U.** (2012), 'Impact of Lunar Surface Features on the Core Temperatures of Surface-Crafts', in , *42nd International Conference on Environmental Systems* (American Institute of Aeronautics and Astronautics).

Hager, P., **Karanikolov, M.**, **Vogel, F.**, **Lechner, A.**, and **Walter, U.** (2011), 'A lunar surface environment model for the Thermal Moon Simulator (TherMoS)', in , *41st International Conference on Environmental Systems* (American Institute of Aeronautics and Astronautics).

Hale, A., and **Hapke, B.** (2002), 'A Time-Dependent Model of Radiative and Conductive Thermal Energy Transport in Planetary Regoliths with Applications to the Moon and Mercury', *Icarus*, 156/2: 318–334.

Hardt, B. E., **Karam, R. D.**, and **Eby, R. J.** (2002-c2003), 'Louvers', in D. G. Gilmore (ed.), *Spacecraft Thermal Control Handbook*. *Volume 1: Fundamental Technologies* (1; 2nd edn., El Segundo, California 90245-4691: Aerospace Press), 331–52.

Harris, A. W. (1998), 'A Thermal Model for Near-Earth Asteroids', *Icarus*, 131/2: 291–301 <doi:10.1006/icar.1997.5865>, accessed 1 Aug 2010.

Harris, R. S. (1972), *Apollo experience report: Thermal design of Apollo lunar surface experiments package,* NASA-TN-D-6738, MSC-S-310.

Hashimoto, T., **Hoshino, T.**, **Tanaka, S.**, **Otsuki, M.**, **Otake, H.**, and **Morimoto, H.** (2011), 'Japanese moon lander SELENE-2—Present status in 2009', *Acta Astronautica*, 68/7-8: 1386–1391.

Haverley, M., **Maetthews, J.**, **Frost, M.**, and **McQuin, C.** (2010), 'Development of the Tri-ATHLETE Lunar Vehicle Prototype', *Proceedings of the 40th Aerospace Mechanisms Symposium*, 2010: 317–326 <NASA/CP-2010-216272>, accessed 29 Oct 2012.

Hayne, P. O., **Greenhagen, B. T.**, **Foote, M. C.**, **Siegler, M. A.**, **Vasavada, A. R.**, and **Paige, D. A.** (2010), 'Diviner Lunar Radiometer Observations of the LCROSS Impact', *Science*, 330/6003: 477–479.

Head, J. N. (2006), 'Earthshine at the lunar poles and volatile stability', *Lunar and Planetary Science Conference*, 37 <http://adsabs.harvard.edu/abs/2006LPI…37.1886H>.

Heiken, G., **Vaniman, D.**, and **French, B. M.** (1991), *Lunar sourcebook*: *A user's guide to the moon* (Cambridge [England] ;, New York: Cambridge University Press).

Heverly, M., **Matthews, J.**, **Frost, M.**, and **McQuin, C.** (2010), 'Development of the Tri-Athlete lunar vehicle prototype', *Proceedings of the 40th Aerospace Mechanisms Symposium*, 2010: 317–326 <NASA/CP-2010-216272>.

Hiesinger, H., and **Head, J. W.** (2004), 'Lunar South Pole Aitken Impact Basin: Topography and Mineralogy', *35th Lunar an Planetary Science Conference*, 2004 <2004LPI…35.1164H>.

Hodgson, E. (2007), *Gravitational and Space Biology Bulletin*, 16/2.

Hofmann, P., **Haarmann, R.**, **Richter, L.**, **Mühlbauer, Q.**, **Claasen, F.**, and **Henn, N.** (2011), 'MPE, the German lunar mobile payload element', *International Astronautical Congress 2011*, 2011.

Hohn, R., **Ruehe, W.**, and **Jewell, C.** (2004), 'The Cryogenic System of the Herschel Extended Payload Module', *American Institute of Physics Conferencse Proceedings*, 710: 505–512 <http://dx.doi.org/10.1063/1.1774721>, accessed 10 May 2012.

Horai, K.-I., and **Fujii, N.** (1971), 'Thermophysical properties of lunar material returned by Apollo missions', *Earth, Moon, and Planets*, 4/3-4: 447–475 <DOI: 10.1007/BF00562011>, accessed 12 Apr 2011.

Horai, K.-I., **Simmons, G.**, **Kanamori, H.**, and **Wones, D.** (1970), 'Thermal diffusivity, conductivity and thermal inertia of Apollo 11 lunar material', *Proceedings of the Lunar Science Conference*, 3: 2243–2249, accessed 1 Aug 2010.

Hörz, F., and **Cintala, M.** (1997), 'Impact experiments related to the evolution of planetary regoliths', *Meteoritics & Planetary Science*, 32: 179–209, accessed 3 Feb 2011.

Houston, W. N., **Mitchell, J. K.**, and **Carrier, W. D., III** (1974), 'Lunar soil density and porosity', *Proceedings of the Lunar Science Conference*, 3: 2361–2364, accessed 13 Feb 2011.

Hovland, J. H., and **Mitchell, J. K.** (1972), 'Boulder tracks and nature of lunar soil', *Earth, Moon, and Planets*, 6/1-2: 164–175 <DOI: 10.1007/BF02630660>, accessed 13 Feb 2011.

Howell, J. R. (1998), 'The Monte Carlo Method in Radiative Heat Transfer', *Journal of Heat Transfer*, 3/120: 547–560 <http://dx.doi.org/10.1115/1.2824310>, accessed 30 Apr 2012.

Incropera, F. P., and **DeWitt, D. P.** (2002), *Fundamentals of heat and mass transfer* (5th edn., New York: J. Wiley).

Information Office of the State Council (2011), *China's Space Activities in 2011* (Bejing).

ISECG (2011), *The Global Exploration Roadmap*: *International Space Exploration Coordination Group,* NP-2011-09-766-HQ (Washington, DC 20546-0001) <http://www.globalspaceexploration.org>.

ITP Engines (2010), *ESATAN-TMS Thermal Engineering Manual* (Whetstone, Leicester, UK).

Ivankov, A. (2013a), 'Luna 17/Lunokhod 1. NASA - NSSDC - Spacecraft - Details' <http://nssdc.gsfc.nasa.gov/nmc/spacecraftDisplay.do?id=1970-095A>, updated 27 Mar 2013, accessed 3 Apr 2013.

Ivankov, A. (2013b), 'Luna 21/Lunokhod 2. NASA - NSSDC - Spacecraft - Details' <http://nssdc.gsfc.nasa.gov/nmc/spacecraftDisplay.do?id=1973-001A>, updated 27 Mar 2013, accessed 3 Apr 2013.

Jaeger, J. C. (1953), 'The surface temperature of the Moon', *Australian Journal of Physics*, 6: 10–21 <1953AuJPh…6…10J>, accessed 11 Aug 2010.

Jaeger, J. C., and **Harper, A. F. A.** (1950), 'Nature of the Surface of the Moon', *Nature*, 166: 1026 <doi:10.1038/1661026a0>, accessed 11 Aug 2010.

Jaumann, R., **Hiesinger, H.**, **Anand, M.**, **Crawford, I.**, **Wagner, R.**, **Sohl, F.**, **Jolliff, B.**, **Scholten, F.**, **Knapmeyer, M.**, **Hoffmann, H.**, **Hussmann, H.**, **Grott, M.**, **Hempel, S.**, **Köhler, U.**, **Krohn, K.**, **Schmitz, N.**, **Carpenter, J.**, **Wieczorek, M.**, **Spohn, T.**, **Robinson, M.**, and **Oberst, J.** (2012), 'Geology, geochemistry, and geophysics of the Moon: Status of current understanding', *Planetary and Space Science*, 74/1: 15–41.

Jones, E. M., Glover, K., and Roxburgh, G. (1995-2012), 'Apollo 15 Lunar Surface Journal' <http://www.hq.nasa.gov/office/pao/History/alsj/a15/a15.html>, updated 17 Oct 2012, accessed 4 Apr 2013.

Jones, H. (2009), 'Spacesuit Cooling on the Moon and Mars', *SAE International*, 2009 <2009-01-2418>, accessed 10 Sep 2010.

JPL (1969), *Surveyor Project Final Report*: *Part II. Science Results,* TR 32-1265 (Pasadena, California).

JPL, and **NASA** (1996), 'Description of the Rover Sojourner' <http://mars.jpl.nasa.gov/MPF/rover/descrip.html>, updated 6 Oct 2005, accessed 3 Apr 2013.

JPL, and **NASA** (2012), 'Mars Science Laboratory: Rover' <http://mars.jpl.nasa.gov/msl/mission/rover/>, accessed 3 Apr 2013.

Karam, R. D. (1998), *Satellite thermal control for systems engineers* (Reston, Va: American Institute of Aeronautics and Astronautics).

Katuntsev, V. P., **Osipov, Y. Y.**, **Barer, A. S.**, **Gnoevay, N. K.**, and **Tarasenkov, G. G.** (2004), 'The main results of EVA medical support on the Mir Space Station', *Acta Astronautica*, 54/8: 577–583 <doi:10.1016/S0094-5765(03)00231-5>.

Keihm, S. J., **Peters, K.**, **Langseth, M. G.**, and **Chute Jr., J. L.** (1973), 'Apollo 15 measurment of lunar surface brightness temperatures. Thermal conductivity of the upper 1 1/2 meters of lunar regolith', *Earth and Planetary Science Letters*, 19: 337–351, accessed 11 Jul 2010.

Klaus, D. M., **Metts, J.**, **Kobrick, R.**, **Mesloh, M.**, **Monk, T.**, **Gauthier, E.**, **Eberhart, K.**, **Baca, D.**, **Wright, C.**, **Gustafson, A.**, **Oryshchyn, L.**, and **Massey, D.** (2007), 'Space Suit Concepts and Vehicle Interfaces for the Constellation Program', *SAE International*, 2007, accessed 29 May 2011.

Krotikov, V. D., and **Shchuko, O. B.** (1963), 'The Heat Balance of the Lunar Surface Layer During a Lunation', *Soviet Astronomy*, 7/2: 228–232, accessed 23 Jun 2011.

Kubis, J. F., **Elrod, J. T.**, **Rusnak, R.**, and **Barnes, J. E.** (1972a), *Apollo 15 - Time and Motion Study*: *Final Report,* N13.16823 CR.128695 (Houston, Texas).

Kubis, J. F., **Elrod, J. T.**, **Rusnak, R.**, **Barnes, J. E.**, and **Saxon, S. C.** (1972b), *Apollo 16 - Time and Motion Study*: *Final Mission Report*, M72-6, N73_16825, CR1284696 (Houston, Texas).

Kubota, T., **Kuroda, Y.**, **Kunii, Y.**, and **Natakani, I.** (1999), 'Micro Planetary rover "MICRO5"', *Proceedings of the 5th International Symposium on Artifical Intelligence, Robotics and Automation in Space*, 1999: 373–378, accessed 29 Oct 2012.

Lam, T. T., **Birur, G. C.**, and **Bhandari, P.** (2002-c2003), 'Pumped Fluid Loops', in D. G. Gilmore (ed.), *Spacecraft Thermal Control Handbook*. *Volume 1: Fundamental Technologies* (1; 2nd edn., El Segundo, California 90245-4691: Aerospace Press), 405–72.

Lange, C., **Große, J.**, and **Zoest van, T.** (2010), 'Conceptual Study of a Combined hammering/Melting Drill Device for Investigations of Icy Planetary Subsurfaces – The 'Cryo-Mole'', *European Planetary Science Congress 2010*, 5 <EPSC2010-513>.

Langseth, M. G., **Clark, S. P.**, **Chute Jr., J. L.**, and **Keihm, S. J.** (1972), 'The apollo 15 lunar heat-flow measurement', *Earth, Moon, and Planets*, 4/2-3: 390–410 <doi:10.1007/BF00562006>, accessed 18 Jul 2010.

Langseth, M. G., **Keihm, S. J.**, and **Peters, K.** (1976), 'Revised lunar heat-flow values', *Proceedings of the 7th Lunar Science Conference*, 3: 3143–3171 <http://adsabs.harvard.edu/full/1976LPSC…7.3143L>, accessed 11 Feb 2012.

Laurand, X. (2010), 'White Label Space: Rover Thermal Analysis' <http://www.whitelabelspace.com/2010/07/rover-thermal-analysis.html>, updated 7 Feb 2013, accessed 3 Apr 2013.

Laxman, S. (2012), 'Chang'e-3: China To Launch First Moon Rover In 2013 | Asian Scientist Magazine | Science, Technology and Medicine News Updates From Asia' <http://www.asianscientist.com/topnews/chang-e-3-china-first-moon-rover-launch-in-2013/>, updated 1 Apr 2013, accessed 3 Apr 2013.

Lechner, A. (2011), 'Preparation of a distortion-free topological lunar map for thermal calculations', Term Project (München, Technische Universität München).

Lee, S. W., **Thomas, P.**, and **Veverka, J.** (1986), 'Phobos, Deimos, and the Moon: sze and distribution of crater ejecta blocks', *Icarus*, 68/1: 77–86 <doi:10.1016/0019-1035(86)90075-8>, accessed 3 Feb 2011.

Ley, W., **Wittmann, K.**, and **Hallmann, W.** (2009), *Handbook of space technology* (Chichester, U.K: Wiley).

Linsky, J. L. (1966), 'Models of the Lunar Surface Including Temperature-Dependent Thermal Properties', *Icarus*, 5: 606–634, accessed 16 Aug 2010.

Mastropietro, A. J., **Beatty, J.**, **Kelly, F.**, **Birur, G.**, **Bhandari, P.**, **Pauken, M.**, **Illsley, P.**, **Liu, Y.**, **Bame, D.**, and **Miller, J.** (2010), 'Design and preliminary thermal performance of the Mars Science Laboratory rover heat exchangers', *40th International Conference on Environmental Systems*, 2010 <AIAA 2010-6194>.

Mays, C. D., **French, J.**, **Nair, S. S.**, **Miles, J. B.**, and **Lin, C. H.** (1999), 'Design of a transient thermal model of the cryogenic PLSS', *Proceedings of the 29th International Conference on Environmental Systems*, 1999: 1–13 <1999-01-2000>.

Menzel, D. H. (1969), 'Temperature distribution of the Moon', *Discussion on Infrared Astronomy*, 1969: 141–144, accessed 24 May 2010.

Metts, J. G., and **Klaus, D. M.** (2009), 'Conceptual Analysis of Electrochromic Radiators for Space Suits', *SAE International*, 2009 <2009-01-2570>, accessed 26 Jun 2010.

Metts, J. G., **Nabity, J. A.**, and **Klaus, D. M.** (2011), 'Theoretical performance analysis of electrochromic radiators for space suit thermal control', *Advances in Space Research*, 47/7: 1256–1264 <http://dx.doi.org/10.1016/j.asr.2010.11.018>, accessed 29 Jan 2012.

Minco (2012), 'Heater-Product Technologies' <http://www.minco.com/Heaters/Product-Technologies>, accessed 5 Apr 2013.

Mitchell, J. K., **Houston, W. N.**, **Scott, R. F.**, **Costes, N. C.**, **Carrier, W. D. III**, and **Bromwell, L. G.** (1972), 'Mechanical properties of lunar soil- density, porosity, cohesion, and angle of internal friction', *Proceedings of the Lunar Science Conference*, 1972: 3235–3253, accessed 9 Feb 2011.

Modest, M. F. (1993), *Radiative heat transfer* (New York: McGraw-Hill).

Moisson, X., and **Bretagnon, P.** (2001), 'Analytical planetary solution VSOP2000', *Celestial Mechanics and Dynamical Astronomy*, 80/3/4: 205–213.

Molaro, J. L., and **Byrne, S.** (2011), 'Thermal stress weathering on Mercury and other airless bodies', *42nd Lunar and Planetary Science Conference*, 2011 <1494>, accessed 29 Nov 2012.

Moore, H. J. (1970), 'Large blocks around lunar craters. NASA Special Publication', *Analysis of Apollo 10 photography and visual observations*, 1970: 26.

Nabity, J. A., **Mason, G. R.**, **Copeland, R. J.**, and **Trevino, L. A.** (2008), 'A freezable heat exchanger for spacesuit radiator systems', *SAE International*, 38 <2008-01-21111>.

NASA, 'Image AS10-29-4324 (Crater Hypathia)' <http://www.hq.nasa.gov/office/pao/History/alsj/a410/AS10-29-4324.jpg>, accessed 20 Jan 2013.

NASA, 'Image LROC M196308138LR' <http://wms.lroc.asu.edu/lroc_browse/view/M196308138LR>, accessed 6 Feb 2013.

NASA, (1969), 'Image AP010303 (Surveyor 3 & Apollo 12)' <http://apod.nasa.gov/apod/ap010303.html>, updated 3 Mar 2001, accessed 20 Jan 2013.

NASA, (1971a), 'Image AS14-67-9366HR' <http://history.nasa.gov/alsj/a14/AS14-67-9366HR.jpg>, accessed 11 Jan 2013.

NASA, (1971b), 'Image AS15-86-11603HR.jpg', accessed 20 Jan 2013.

NASA, (1971c), 'Image GPN-2000-001147' <http://dayton.hq.nasa.gov/IMAGES/LARGE/GPN-2000-001147.jpg>, accessed 11 Jan 2013.

NASA, (1972a), 'Image AS17-140-2139HR' <http://history.nasa.gov/alsj/a17/AS17-140-21391HR.jpg>, updated 14 May 2012, accessed 5 Apr 2013.

NASA, (1972b), 'Image Pan AS17-140-21488 to AS17-140-21507' <http://www.lpi.usra.edu/resources/apollopanoramas/pans/?pan=JSC2007e045387>.

NASA, *Man-Systems integration standards*: *Volume I* (1995), NASA-STD-3000 VOL I.

NASA, (2005), 'Image S114-E-6647' <http://spaceflight.nasa.gov/gallery/images/shuttle/sts-114/html/s114e6647.html>.

NASA, (2011), 'Image LROC M150062296' <http://www.universetoday.com/84880/look-inside-a-lunar-crater/>, updated 15 Apr 2011, accessed 22 Mar 2013.

NASA, (2012a), 'Image ISS030-E-079955' <http://www.nasa.gov/mission_pages/station/multimedia/gallery/iss030e079955.html>, accessed 5 Apr 2013.

NASA, (2012b), 'Image S115-E-06451' <http://microgravity.grc.nasa.gov/SOPO/ICHO/ISS/Cooling/images/s115e06451SolarArray.jpg>, updated 23 Apr 2012, accessed 10 Jan 2013.

NASA/GSFC/Arizona State University (2011), 'Image Calippus - LROC' <http://lroc.sese.asu.edu/news/?archives/354-Rima-Callippus.html>, updated 1 Mar 2011, accessed 24 Sep 2012.

Neukum, G., **Koenig, B.**, and **Arkani-Hamed, J.** (1975), 'A study of lunar impact crater size-distributions', *The Moon*, 12/2: 201–229.

Nogina, S. (2012), 'Radiation Heat Transfer with Ray Tracing Engine NVIDIA OptiX', Interdisziplinäres Projekt (München, Technische Universität München).

Norcross, J. R., **Lee, L. R.**, **Clowers, K. G.**, **Morency, R. M.**, **Desantis, L.**, **De Witt, J. K.**, **Jones, J. A.**, **Vos, J. R.**, and **Gernhardt, M. L.** (2009), 'Feasibility of performing a suited 10-km ambulation on the Moon - Final Report of the EVA Walkback Test', *NASA STI program*, 2009 <NASA/TP-2009-214796>.

NVIDIA (2008), *OptiX_Programming_Guide_2.1.1* (Santa Clara).

Nyberg, K. L., **Diller, K. R.**, and **Wissler, E. H.** (2001), 'Model of human-liquid cooling garment interaction for space suit automatic thermal control', *Transactions of the ASME*, 123: 114–120 <DOI: 10.1115/1.1336147>, accessed 22 May 2010.

Ochoa, D. A., **Miranda, B. M.**, **Conger, B. C.**, and **Trevino, L. A.** (2006), 'Lunar EVA Thermal Environment Challenges', *SAE International*, 2006, accessed 17 Jan 2011.

Ochoa, D. A., **Vogel, M. R.**, **Trevino, L. A.**, and **Stephan, R. A.** (2008), 'Potential of a New Lunar Surface Radiator Concept for Hot Lunar Thermal Environments', *SAE International*, 2008 <10.4271/2008-01-1960>, accessed 5 Jan 2011.

Okada, T., **Sasaki, S.**, **Sugihara, T.**, **Saiki, K.**, **Akiyama, H.**, **Ohtake, M.**, **Takeda, H.**, **Hasebe, N.**, **Kobayashi, M.**, **Haruyama, J.**, **Shirai, K.**, **Kato, M.**, **Kubota, T.**, **Kunii, Y.**, and **Kuroda, Y.** (2006), 'Lander and rover exploration on the lunar surface: A study for SELENE-B mission', *Advances in Space Research*, 37/1: 88–92.

Olthoff, C. (2012), 'V-SUIT - An Approach Towards a Virtual Space Suit', in , *42nd International Conference on Environmental Systems* (American Institute of Aeronautics and Astronautics).

Özişik, M. N. (1994), *Finite difference methods in heat transfer* (Boca Raton: CRC Press).

Paige, D. A. (2012), 'Diviner News' <http://www.diviner.ucla.edu/blog/>, accessed 19 Dec 2012.

Paige, D. A., **Foote, M. C.**, **Greenhagen, B. T.**, **Schofield, J. T.**, **Calcutt, S.**, **Vasavada, A. R.**, **Preston, D. J.**, **Taylor, F. W.**, **Allen, C. C.**, **Snook, K. J.**, **Jakosky, B. M.**, **Murray, B. C.**, **Soderblom, L. A.**, **Jau, B.**, **Loring, S.**, **Bulharowski, J.**, **Bowles, N. E.**, **Thomas, I. R.**, **Sullivan, M. T.**, **Avis, C.**, **Jong, E. M.**, **Hartford, W.**, and **McCleese, D. J.** (2010a), 'The Lunar Reconnaissance Orbiter Diviner Lunar Radiometer Experiment', *Space Sci Rev*, 150/1-4: 125–160.

Paige, D. A., **Siegler, M. A.**, **Zhang, J. A.**, **Hayne, P. O.**, **Foote, E. J.**, **Bennett, K. A.**, **Vasavada, A. R.**, **Greenhagen, B. T.**, **Schofield, J. T.**, **McCleese, D. J.**, **Foote, M. C.**, **DeJong, E.**, **Bills, B. G.**, **Hartford, W.**, **Murray, B. C.**, **Allen, C. C.**, **Snook, K.**, **Soderblom, L. A.**, **Calcutt, S.**, **Taylor, F. W.**, **Bowles, N. E.**, **Bandfield, J. L.**, **Elphic, R.**, **Ghent, R.**, **Glotch, T. D.**, **Wyatt, M. B.**, and **Lucey, P. G.** (2010b), 'Diviner Lunar Radiometer Observations of Cold Traps in the Moon's South Polar Region', *Science*, 330/6003: 479–482.

Parker, S. G., **Robison, A.**, **Stich, M.**, **Bigler, J.**, **Dietrich, A.**, **Friedrich, H.**, **Hoberock, J.**, **Luebke, D.**, **McAllister, D.**, **McGuire, M.**, and **Morley, K.** (2010), 'OptiX: A general purpose ray tracing engine', *ACM Trans. Graph.*, 29/4: 1.

Parks, S., **Dunstan, M.**, **Martin, I.**, **McCrum, M.**, **Rowell, N.**, and **Dubois-Matra, O.** (2010), 'Simulation of near-earth objects and related lander guidance systems', *International Astronautical Congress 2010*, 2010 <IAC-10.A3.5.9>.

Part-Time-Scientists (2013), 'Part-Time-Scientists | Blog' <http://www.ptscientists.com/>, accessed 3 Apr 2013.

Pecson, J., **Boyd, D. A.**, **Hashemi, A.**, **Aaron, K.**, **Ambrose, J.**, **Maddox, J. F.**, **Mattison, E. M.**, and **Vessot, R. F.** (2002-c2003), 'Precision Temperature Control', in D. G. Gilmore (ed.), *Spacecraft Thermal Control Handbook*. *Volume 1: Fundamental Technologies* (1; 2nd edn., El Segundo, California 90245-4691: Aerospace Press), 739-666.

Peters, C. J., **Hartenstine, J. R.**, **Tarau, C.**, and **Anderson, W. G.** (2011), 'Variable conductance heat pipe for a lunar variable thermal link', *41st International Conference on Environmental Systems*, 2011 <AIAA 2011-5120>.

Pettit, E., and **Nicholson, S. B.** (1930), 'Lunar radiation and temperatures', *Astrophysical Journal*, 71: 102–135 <1930ApJ…71.102P>.

Pfeiffer, M., and **Hager, P.** (2012), 'Experimental setup and results for a simulated solar cavity receiver for thermal processing of lunar regolith', in , *42nd International Conference on Environmental Systems* (American Institute of Aeronautics and Astronautics).

Pieters, C. M., **Goswami, J. N.**, **Clark, R. N.**, **Annadurai, M.**, **Boardman, J.**, **Buratti, B.**, **Combe, J.-P.**, **Dyar, M. D.**, **Green, R.**, **Head, J. W.**, **Hibbitts, C.**, **Hicks, M.**, **Isaacson, P.**, **Klima, R.**, **Kramer, G.**, **Kumar, S.**, **Livo, E.**, **Lundeen, S.**, **Malaret, E.**, **McCord, T.**, **Mustard, J.**, **Nettles, J.**, **Petro, N.**, **Runyon, C.**, **Staid, M.**, **Sunshine, J.**, **Taylor, L. A.**, **Tompkins, S.**, and **Varanasi, P.** (2009), 'Character

and Spatial Distribution of OH/H2O on the Surface of the Moon Seen by M3 on Chandrayaan-1', *Science*, 326/5952: 568–572, accessed 16 Dec 2011.

Plescia, J. (2009), 'Lunar Surface Environmental Conditions: Challenges of Developing an Outpost and Exploiting in Situ Resources', *Proceedings of the 47th Aerospace Science Meeting*, 2009 <AIAA 2009-756>.

Poinas, P. (2004), 'Satellite Thermal Control Engineering. prepared for "SME 2004"'.

Polifke, W., and **Kopitz, J.** (2009), *Wärmeübertragung*: *Grundlagen, analytische und numerische Methoden* (2nd edn., München [u.a.]: Pearson).

Racca, G. D. (1995), 'Moon surface thermal characteristics for moon orbiting spacecraft thermal analysis', *Planetary and Space Science*, 43/6: 835–842 <doi:10.1016/0032-0633(95)00067-F>, accessed 24 May 2010.

Richter, L., **Coste, P.**, **Gromov, V.**, and **Grzesik, A.** (2004), 'The MOLE with sampling mechanism (MSM) - technology development and payload of Beagle2 Mars lander', *Proceedings of the 8th ESA Workshop on Advanced Space Technologies for Robotics and Automation*, 2004: 1–4.

Robie, R. A., **Hemingway, B. S.**, and **Wilson, W. H.** (1970), 'Specific heats of lunar surface materials from 90 to 350 Kelvins', *Science*, 167/3918: 749–750 <10.1126/science.167.3918.749>, accessed 25 May 2011.

Robinson, A. (2009), 'The NVIDIA® OptiX™ ray tracing engine', SIGGRAPH Chapter.

Roelof, E. C. (1968), 'Thermal Behavior of Rocks on the Lunar Surface', *Icarus*, 8: 138–159 <http://dx.doi.org/10.1016/0019-1035(68)90069-9>.

Roos, A., **Chibuye, T.**, and **Karlsson, B.** (1983), 'Properties of oxidized copper surfaces for solar applications I', *Solar Energy Materials*, 7/4: 453–465.

Rowell, N., **Parkes, S.**, **Dunstan, M.**, and **Dubois-Matra, O.** (2009), 'Pangu: virtual spacecraft image generation', 2009.

Salvail, J. R., and **Fanale, F. P.** (1994), 'Near-Surface Ice on Mercury and the Moon A Topographic Thermal Model', *Icarus*, 2/111: 441–455, accessed 4 Feb 2011.

Sanders, G. B., **Moore, L.**, **McKay, D. S.**, **Simon, T. M.**, **Lueck, D. E.**, **Parrish, C. F.**, **Johnson, K. R.**, **Mungas, G.**, **Pelletier, M.**, **Sacksteder, K.**, **Duke, M.**, **Taylor, J.**, **Taylor, L.**, and **Boucher, D.** (2005), 'Regolith & Environment Science, and Oxygen & Lunar Volatile Extraction (RESOLVE) for Robotic Lunar Polar Lander Mission', *International Lunar Conference*, 2005.

Sariano, T. (2010), 'Lunar base thermal analysis with THERMICA', unpublished copy (personal communication) prepared for the, *40th International Conference on Environmental Systems*, 2010.

Schlutz, J. (2012), *Conceptual design of lunar exploration architectures* (1st edn., München: Dr. Hut).

Schlutz, J., and **Messerschmid, E.** (2012), 'Integrating advanced mobility into lunar surface exploration', *Acta Astronautica*, 2012: 15–24 <http://dx.doi.org/10.1016/j.actaastro.2012.01.005>.

Schnaitmann, J., **Zhukov, A.**, **Hager, P.**, **Klaus, D.**, and **Czupalla, M.** (2012), 'The status of the environmentally sensitive dynamic model of the human physiology used in the V-HAB LSS simulation', in , *42nd International Conference on Environmental Systems* (American Institute of Aeronautics and Astronautics).

Seeni, A., **Schäfer, B.**, **Rebele, B.**, and **Krenn, R.** (2009), 'Lunar rover with multiple science payload handling capability', *International Astronautical Congress 2009*, 2009.

Sens-Schönfelder, C., and **Larose, E.** (2010), 'Lunar noise correlation, imaging and monitoring', *Earthq Sci*, 23/5: 519–530.

Shaltens, R. K. (2007), *Future Opportunities for Dynamic Power Systems for NASA Missions* (Cleveland , Ohio, USA), accessed 30 Jul 2010.

Siegel, R., and **Howell, J. R.** (1992), *Thermal radiation heat transfer* (3rd edn., Washington, D.C: Hemisphere Pub. Corp.).

Sievers, A. (2012), 'Modeling the impact of boulders and craters on the heat balance of rovers and spacesuits on the Moon', Term Paper (München, Technische Universität München).

Simonsen, L. C., **DeBarro, M. J.**, and **Farmer, J. T.** (1992), 'Conceptual Design of a lunar base thermal control system', *The Second Conference on Lunar Bases and Space Activities of the 21st Century*, 1992: 579–591 <1992lbsa.conf.579S>, accessed 10 Sep 2010.

Sompayrac, R., **Conger, B.**, and **Trevino, L.** (2009), 'Lunar Portable Life Support System Heat Rejection Study', *SAE International*, 2009 <2009-01-2408>.

Sternovsky, Z. (2002), 'Contact charging of lunar and Martian dust simulants', *J. Geophys. Res.*, 107/E11.

Stubbs, T., **Vondrak, R. R.**, and **Farrell, W. M.** (2007), *Impact of dust on lunar exploration* <http://www.nasa.gov/centers/johnson/pdf/486014main_StubbsImpactOnExploration.4075.pdf>.

Sullivan, M., and **Paige, D.** (2011), *Diviner Lunar Radiometer Experiment*: - reduced data record and derived products software interface specification, V 1.12 (Los Angeles).

Suzuki, N., **Matsumoto, K.**, **Hufenbach, B.**, **Piedboeuf, J.-C.**, **Cirillo, W.**, and **Carey, W.** (2011), 'ISECG space exploration goals, objectives and benefits', *International Astronautical Congress 2011*, 2011 <I-AC-11-A5.4.2>.

Swanson, T. D., and **Birur, G. C.** (2003), 'NASA thermal control technologies for robotic spacecraft', *Applied Thermal Engineering*, 23/9: 1055–1065, accessed 29 Jan 2012.

Tattusch, T. (2011), 'Modeling of the impact of the Earth and Moon Orbits on the solar impact angle on the lunar surface', Bachelor thesis (München, Technische Universität München).

Taylor, D. B., **Bell, S. A.**, **Hilton, J. L.**, and **Sinclair, A. T.** (2010), 'Computation of the quantities describing the lunar librations in the Astronomical Almanac', 2010 <ADA528116>.

Taylor, L. A., and **Carrier, D. W. III.** (1993), 'Oxygen production on the moon: An overview and evaluation', in J. S. Lewis, M. S. Matthews, and M. L. Guerrieri (eds.), *Resources of near-Earth space* (Tucson: University of Arizona Press), 69–108.

Tribble, A. C. (2003), *The space environment*: *Implications for spacecraft design* (Rev. and expanded ed., Princeton, N.J. ;, Woodstock: Princeton University Press).

USGS (1964), 'Image: Rima Hadley' <http://planetarynames.wr.usgs.gov/Feature/5064>, updated 18 Oct 2010, accessed 12 Sep 2012.

USGS (2006), 'Image Marius A' <http://planetarynames.wr.usgs.gov/Feature/11175?__fsk=-435452146>, updated 18 Oct 2010, accessed 10 Aug 2012.

USGS (2009), 'Image: Lunar South Pole & crater Ibn Bajja' <http://planetarynames.wr.usgs.gov/Feature/14534?__fsk=1853995732>, updated 18 Oct 2010, accessed 15 Sep 2012.

Vasavada, A. R., **Bandfield, J. L.**, **Greenhagen, B. T.**, **Hayne, P. O.**, **Siegler, M. A.**, **Williams, J.-P.**, and **Paige, D. A.** (2012), 'Lunar equatorial surface temperatures and regolith properties from the Diviner Lunar Radiometer Experiment', *J. Geophys. Res.*, 117.

Vasavada, A. R., **Paige, D. A.**, and **Wood, S. E.** (1999), 'Near-Surface Temperatures on Mercury and the Moon and the Stability of Polar Ice Deposits', *Icarus*, 141/2: 179–193 <doi:10.1006/icar.1999.6175>, accessed 24 May 2010.

Vining, C. B., and **Bennett, G. L.** (2010), 'Power for science and exploration: upgrading the general-purpose heat source radioisotope thermoelectric generator (GPHS-RTG)', *Proceedings of the 46th Joint Propulsion Conference & Exhibit*, 2010 <AIAA 2010-6598>, accessed 27 Nov 2012.

Vogel, F. Y. (2010), 'Development of a topographic model of the Moon from data gathered by the Kaguya probe, with MATLAB', Term Project (München, Technische Universität München).

Waligora, J. M., and **Horrigan, D. J.** (1975), 'Metabolism and heat dissipation during apollo EVA periods', in NASA (ed.), *Biomedical results of Apollo* (SP-368, Washington: NASA Headquarters).

Walter, U. (2007), *Skriptum zur Vorlesung Raumfahrttechnik II*: *Thermalkontrolle* (München).

Wang, Z., **Deurenberg, P.**, **Wang, W.**, **Pietrobelli, A.**, **Baumgartner, R. N.**, and **Heymsfield, S. B.** (1999), 'Hydration of fat-free body mass: new physiological modeling approach', *American Journal of Physiology Endocrinology and Metabolism*, 276/6.

Washington University (2012a), *DIVRDR_11p41n12p78n_313p41e314p78e_tod14-16_C6_C7_C8_C9*, Diviner Lunar Radiometer Experiment (Moon), updated 12 Sep 2012.

Washington University (2012b), *DIVRDR_25p22n26p97n_2p66e4p53e_C6_C7_C8_C9*, Diviner Lunar Radiometer Experiment (Moon), updated 12 Sep 2012.

Weigert, A., **Wendker, H. J.**, and **Wisotzki, L.** (2009), *Astronomie und Astrophysik*: *Ein Grundkurs* (5th edn., Weinheim, Bergstr: WILEY-VCH).

Welsh, J. W. (2002-c2003), 'Thermal Testing', in D. G. Gilmore (ed.), *Spacecraft Thermal Control Handbook*. *Volume 1: Fundamental Technologies* (1; 2nd edn., El Segundo, California 90245-4691: Aerospace Press), 709–57.

Wertz, J. R., and **Larson, W. J.** (1999), *Space mission analysis and design* (3rd edn., Torrance, Calif, Dordrecht ;, Boston: Microcosm; Kluwer).

Wesselink, A. J. (1948), 'Heat conductivity and nature of the lunar surface material', *Bulletin of the Astronomical Institutes of the Netherlands*, 10/390: 351–363 <1948BAN…10.351W>.

Wettergreen, D., **Jonak, D.**, **Kohanbash, D.**, **Moreland, S.**, **Spiker, S.**, and **Teza, J.** (2010), 'Field Experiments in Mobility and Navigation with a Lunar Rover Prototype', 2010: 489–498.

Wettergreen, D., **Jonak, D.**, **Kohanbash, D.**, **Moreland, S.**, **Spiker, S.**, **Teza, J.**, and **Whittaker, W.** (2009), *Design and Experimentation of a Rover Concept for Lunar Crater Resource Survey* (Pittsburgh, PA).

Williams, J. P., **Paige, D. A.**, and **Vasavada, A. R.** (2011), 'Interpreting LRO Diviner surface temperatures: Modeling lunar regolith thermophysical properties and topography in three-dimensions', *Proceedings of the 42nd Lunar and Planetary Science Conference*, 2011 <2808>.

Winter, D. F. (1967), 'Transient Radiative Heat Exchange at the Surface of the Moon', *Icarus*, 6/Issues 1-3: 229–235 <doi:10.1016/0019-1035(67)90019-X>, accessed 12 Aug 2010.

Winter, D. F., and **Saari, J. M.** (1969), 'A particulate thermophysical model of the lunar soil', *The astrophysical journal*, 156: 1135–1151 <1969ApJ…156.1135W>, accessed 11 Jul 2010.

Zakrajsek, J. J., **McKissok, D. B.**, **Woytach, J. M.**, **Zakrajsek, J. F.**, **Oswald, F. B.**, **McEntire, K. J.**, **Hill, G. M.**, **Abdel, P.**, **Eichenberg, D. J.**, and **Goodnight, T. W.** (2005), 'Exploration rover concepts and development challenges', *NASA STI program*, 2005, accessed 24 Oct 2011.

Appendix A

A.1) List of Figures

A.2) List of Tables

A.3) Verification

In this section supplementary cases are shown from the verification of the *TherMoS* models and modules.

Supplement Boulder Model Verification:

In addition to the long-term boulder simulation runs for cubes and half-spheres of varying sizes in section 5.3, runs for random shaped boulders were performed. The results are in line with the finding for cube and spheres. In Figure A - 1 the temperatures for a random shaped boulder with a diameter of D_B = 10m are shown. The western and eastern sides show sharp increases in temperature as soon as they are exposed to solar illumination. The temperatures increase to a maximum around 395 K. The core temperature fluctuates around 250 K $\pm$ 20 K throughout one lunation. The temperature of none of the thermal nodes drops below 170 K.
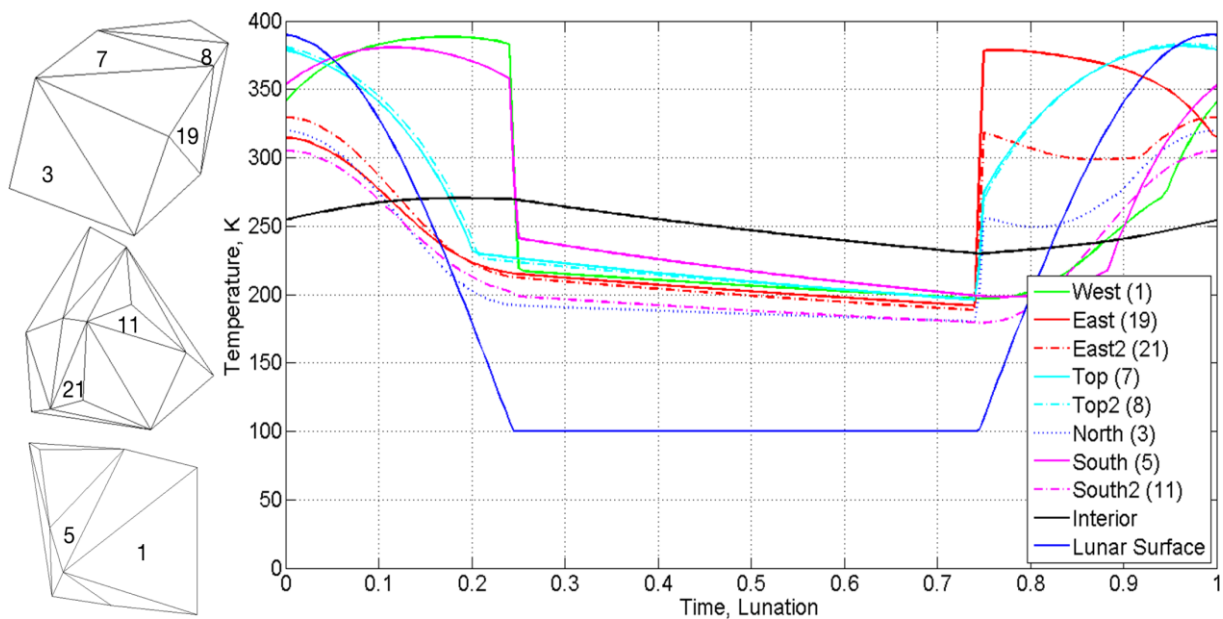
Figure A - 1: Temperatures on the surface elements and in the core of a randomly shaped boulder with a diameter of D_B = 10m.

Supplement Topography Module Verification:

In section 5.3.6 the global lunar landscape module was verified against cases at the crater Calippus and the crater Marius A. Both craters are in the mid-latitudes of the Moon. Crater Calippus covers the entire 40 km surface patch and provides distinct features in a lunar *highland* region. Marius A in contrast is in a *mare* region and surrounded by relatively homogenous undisturbed regolith. In the following two regions with different properties are shown followed by two additional cases for crater Marius A. The crater Ibn Bajja lies at the lunar South Pole at a latitude of approximately -86° S, 72.7° W and has a diameter of D_C = 12 km. The crater is surrounded by mountain ranges. The second case is the Apollo 15 landing site. It was selected because of the prominent Hardley Rille and Apennine Front mountain range. The Apollo 15 landing site lies at approximately 26.1° N and 3.38° E.

In Figure A - 2 and Figure A - 3 show the results for crater Ibn Bajja. Shown is data of numerous flyovers of the LRO orbiter on several dates between 2009 and 2012 for a local lunar time between 12:00 and 12.50 p.m. The solar azimuth was between 47.2° and 91° and the solar elevation angle was in the range of 1.4° to 5.1°. Different from the results shown in section 5.3.6 for crater Calippus and Marius A, the LRO Diviner data points are no straight lines. The curvature is a result of the polar orbit of LRO. Close to the equator and at mid-latitudes the orbiter moves almost parallel to the meridians. Towards the Poles the angle between meridians and spacecraft ground track increase. Another consequence of the polar orbit is the increased number of flyovers, and as a result, a higher density of data points. On the left of Figure A - 2 the LRO surface brightness temperatures are superimposed on a photograph. It is important to note that although the local maximum temperature for an plane should be not more than 170 K, local slopes and crater walls tilted towards the Sun reach temperatures of up to 250 K. On the right side of Figure A - 2 the results of the *TherMoS* calculations are overlaid on the Kaguya topographic map.
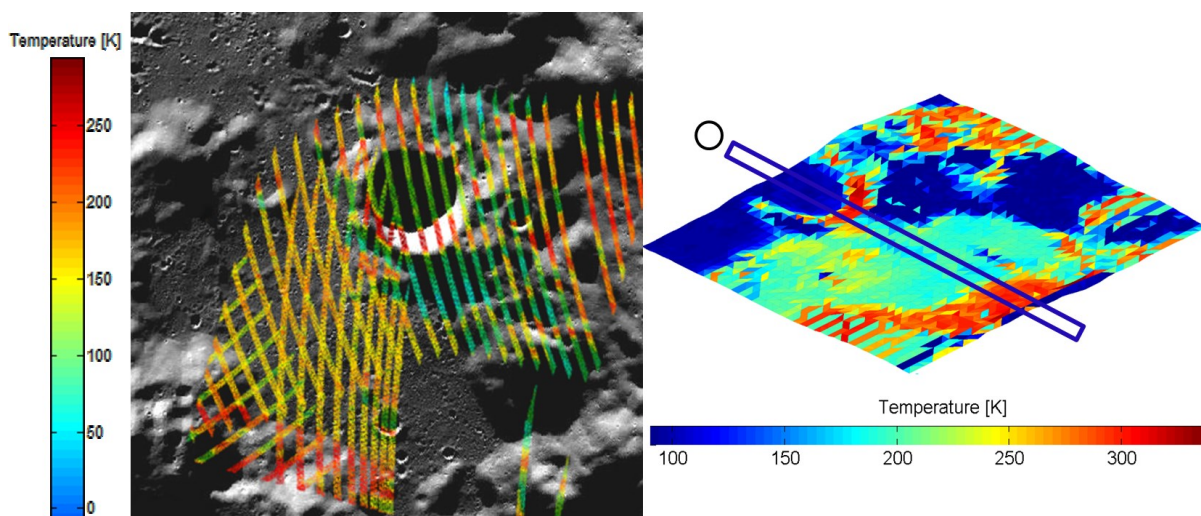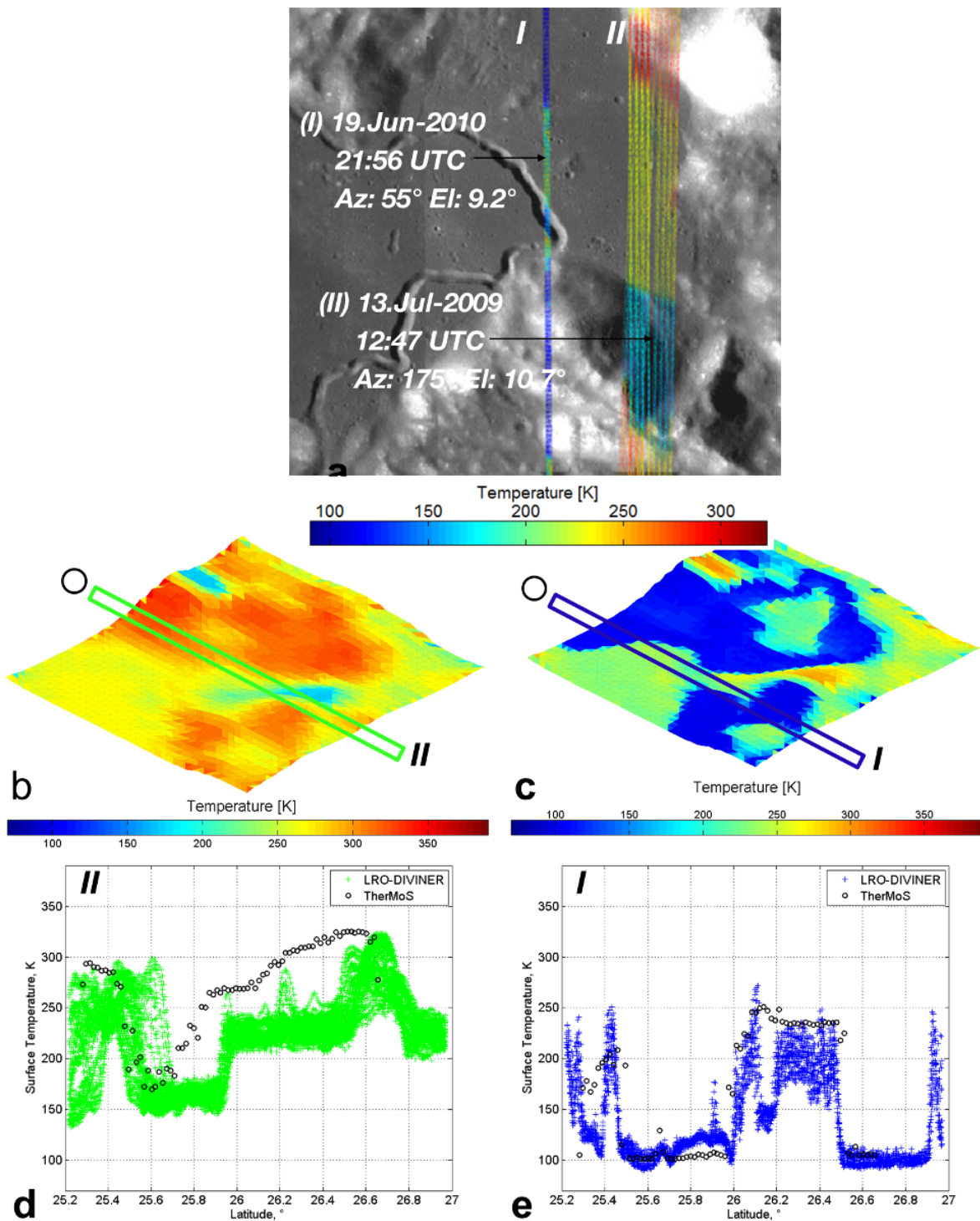

Figure A - 2: Photograph [NASA] superimposed with Diviner data [PDS], Kaguya LALT landscape superimposed with *TherMoS* temperature calculations and comparison of Diviner and *TherMoS* temperature data for crater Ibn Bajja at the lunar South Pole for solar elevations of 2°.

The number of rays per area is higher because the solar parallelogram is smaller, due to low elevation angle. The resolution of the Kaguya data set is higher at the poles. Figure A - 3 shows the comparison between LRO Diviner surface brightness temperature and the results of the *TherMoS* simulations. For the comparison one meridian was selected, depicted in Figure A - 2 with a blue box. The comparison of temperatures in Figure A - 3 shows a good agreement with the LRO Diviner data for the chosen surface patch. One has to keep in mind that the ground track of LRO is neither parallel nor perpendicular to the meridians. Hence, the LRO Diviner data is not available for the entire length of the surface patch.
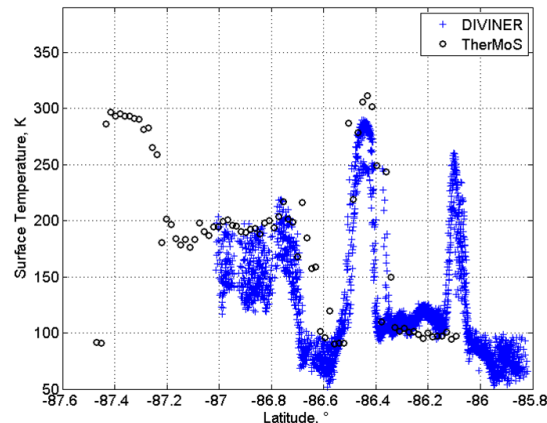
Figure A - 3: Comparison between LRO Diviner surface brightness temperature measurements and the results of the *TherMoS* tool along one meridian.

The results for the Apollo 15 cases are depicted in Figure A - 4. The size of the depicted surface patch is approximately 40 km. The used LRO Diviner surface brightness temperatures originate from two flyovers. The first data set (I) is from the 19th of June 2010 at 21:56 UTC with a solar azimuth of 55° and a solar elevation angle of 9.2°. The second flyover (II) was on the 13th of July 2009 at 12:47 UTC and a solar azimuth of 175° and a solar elevation angle of 10.7°. I) is at lunar morning and II) at lunar afternoon – both cases were selected for low elevation angles and temperature extremes for the entire scene. The *TherMoS* simulation time was 10 hours. The simplified equation described in section 6.2 was used to calculate the initial temperatures.

Figure A - 4a) shows the overlay of a photograph of the Apollo 15 landing site and the LRO Diviner surface brightness temperature for flyover I and II. In Figure A - 4b) and c) the Kaguya topographic map is superimposed with *TherMoS* results for the according times. In Figure A - 4d) and e) finally the LRO Diviner data sets are compared to the *TherMoS* results for the surface patches marked in green and blue boxes, respectively. In the Apollo 15 case the deviation is about 20 % for the high temperatures. The reason could be the inaccuracy of the topographic model, or different material properties on the slopes of the Apennine Front mountain range compared to undisturbed soil. For the second flyover low temperatures are in good agreement but not for elevated temperatures probably due to the same reasons.

In Figure A - 5 two additional cases for crater Marius A are presented in addition to the cases presented in section 5.3.6. Figure A - 1c) and e) show surface temperatures for the 14th of February 2012 at 04:22 UTC with a solar elevation angle of 35.9° and a solar azimuth of 45° (III). Case (IV) is depicted in Figure A - 1b) and d) and represents a data set from the 07th of February 2010 at 04:07 UTC. For case IV the azimuth angle was 45° and the elevation angle is 51°.

The comparison between LRO Diviner surface brightness temperature and *TherMoS* simulation results show a deviation of less than 10 % for undisturbed Regolith. Close to the crater rim, the temperature deviation is higher which most likely is a combination of two effects: local differences in surface properties combined with an inaccuracy in topographic data.

Figure A - 4: Photograph superimposed with Diviner data, Kaguya LALT landscape superimposed with *TherMoS* temperature calculations and comparison of Diviner and *TherMoS* temperature data for the Apollo 15 landing site for solar elevations of 10° different azimuth angles.
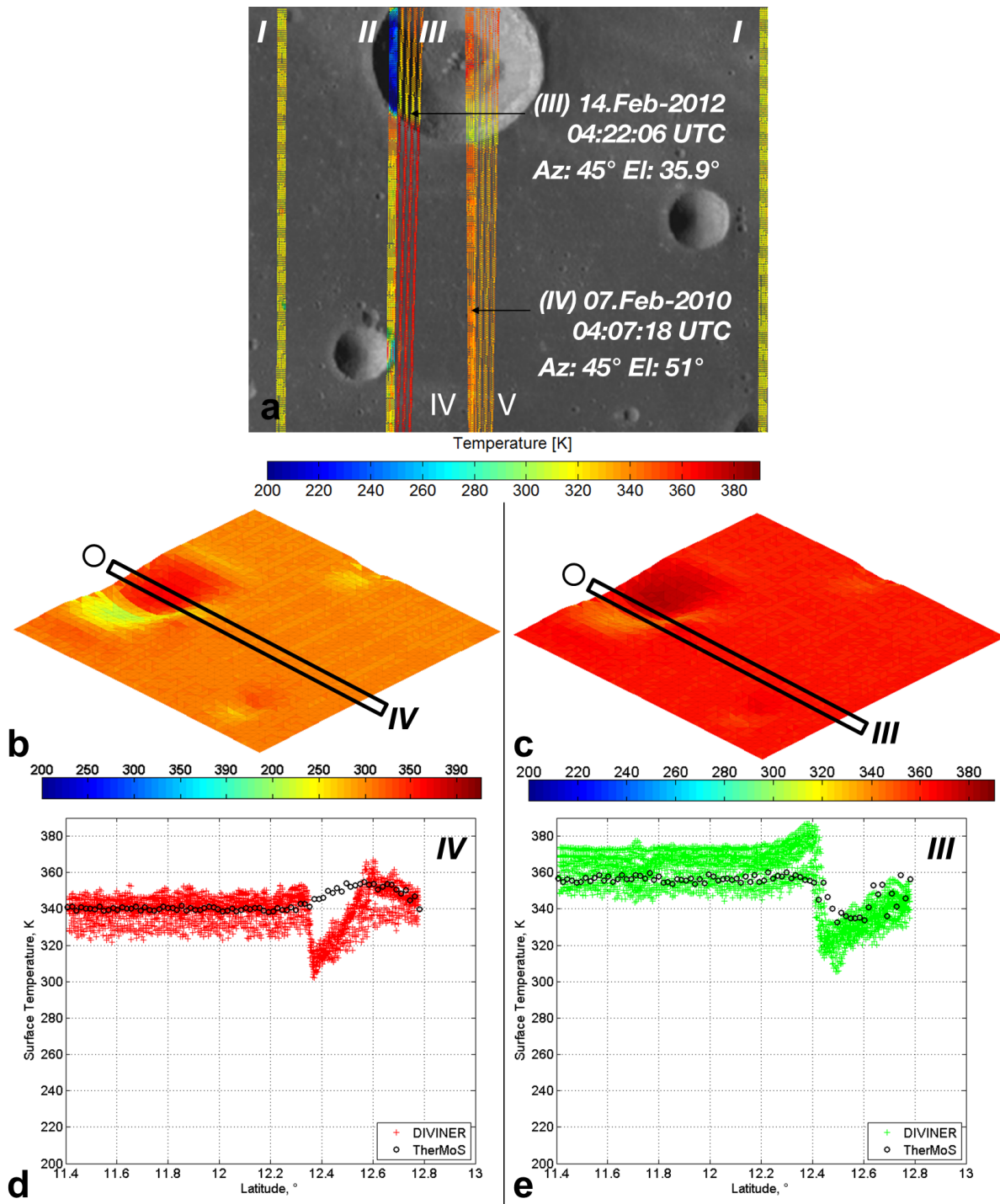
Figure A - 5 Photograph superimposed with Diviner data, Kaguya LALT landscape superimposed with *TherMoS* temperature calculations and comparison of Diviner and *TherMoS* temperature data for the Marius A crater for solar elevations of 35.9° (left) and 51° (right).

A.4) Sample Object Geometries and Element Numbers

In the following the dimensions of the sample bodies are shown. In addition, the numbers of each triangular surface element is given. The number of the triangular elements is important to match the heat fluxes, calculated with the ray tracing algorithm, with the geometry. The numbers are also necessary for the

temperature calculations performed subsequently to the ray tracing. Each figure also contains a coordinate system.

Primitives:
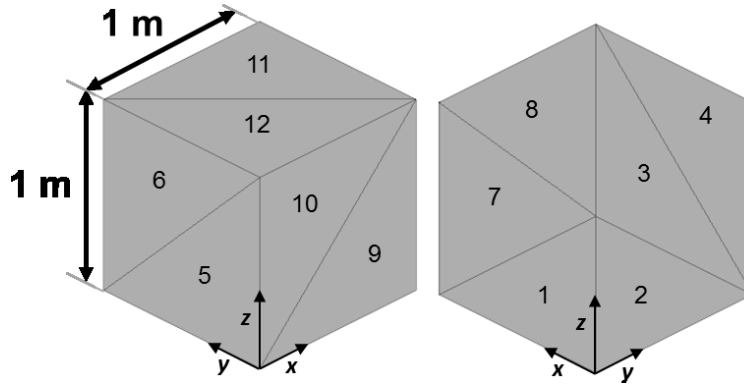
Figure A - 6: Primitive body – cube
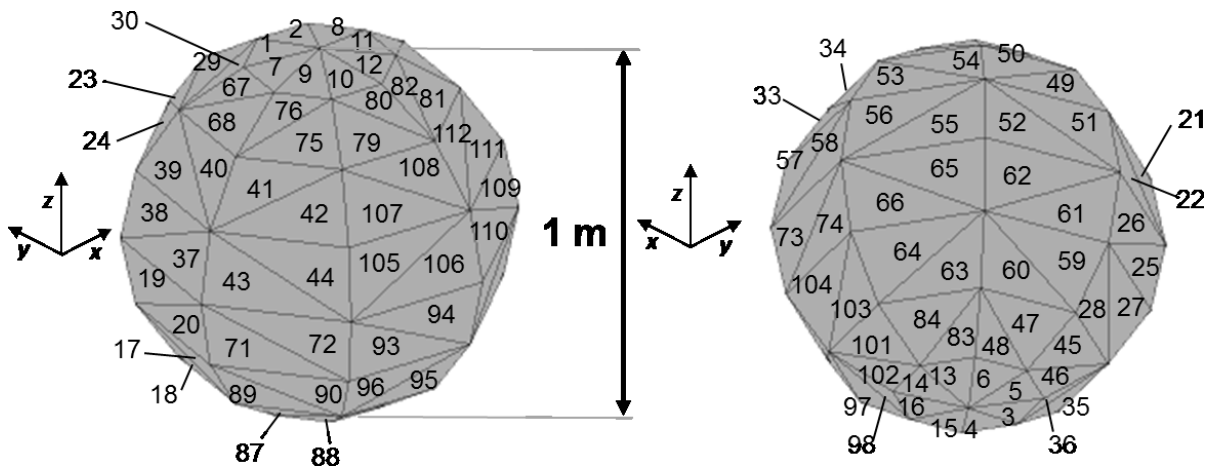
Figure A - 7: Primitive body – sphere

Simplified Rovers:
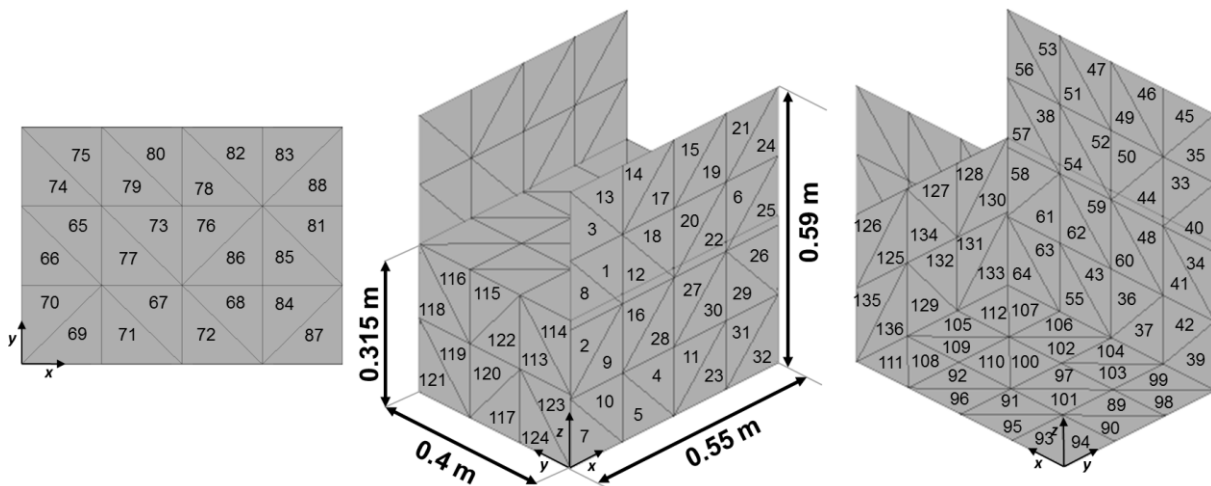
Figure A - 8: Rover1 - polar rover:
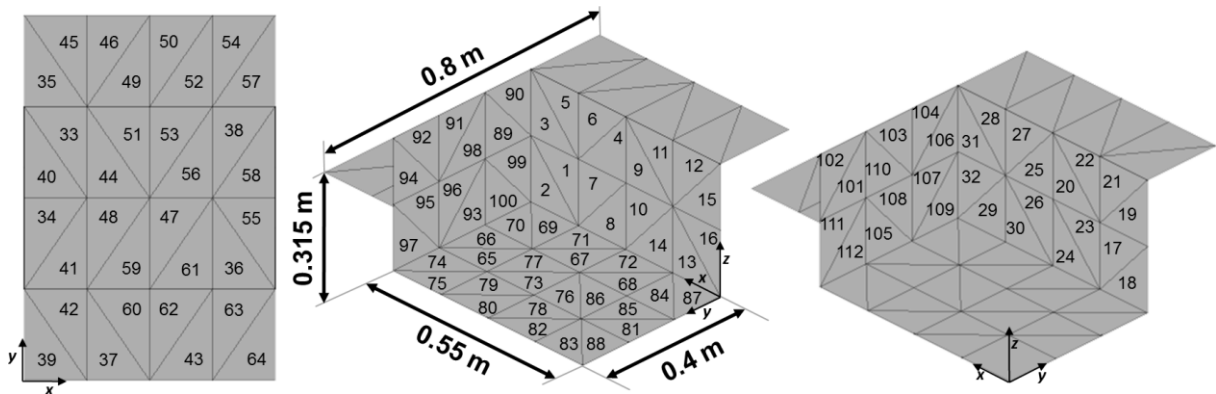
Figure A - 9: Rover2 - equatorial rover.

Detailed Models:

Kayser-Threde Mobile Payload Element (MPE/KT):
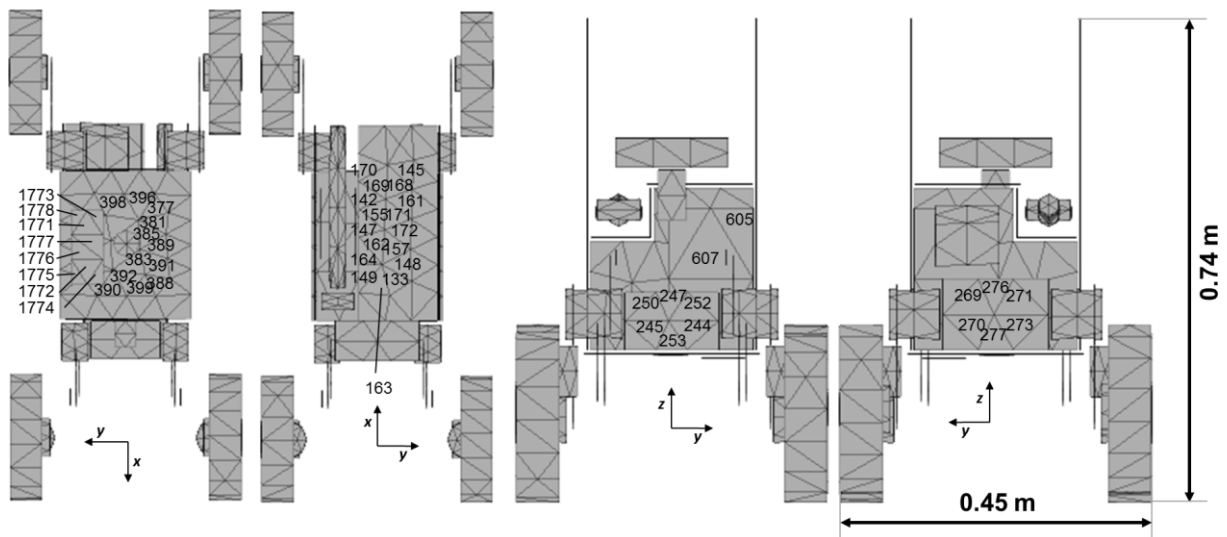
Figure A - 10: MPE - bottom, top, front, and back view.
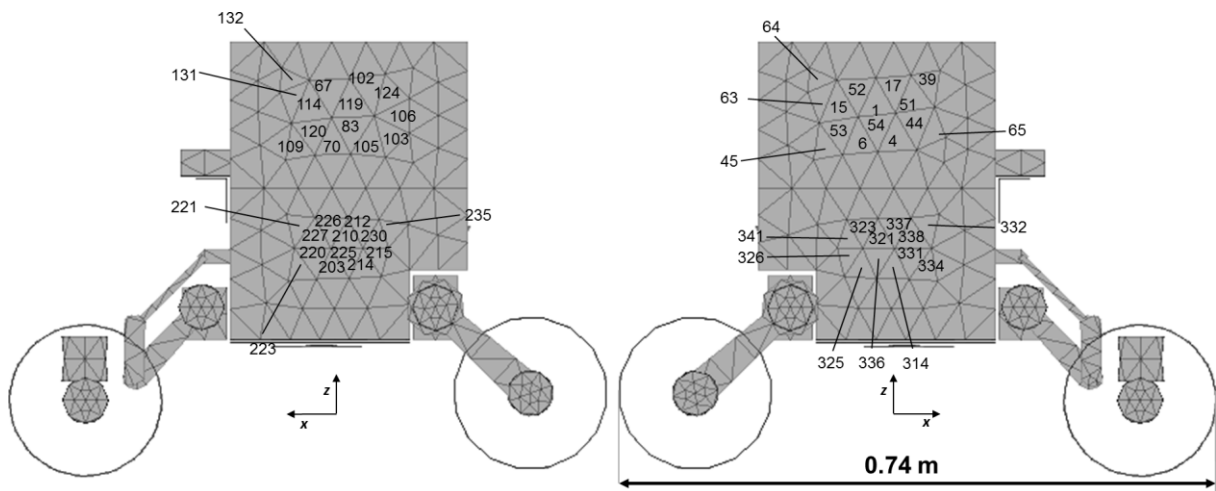
Figure A - 11: MPE - left and right view.

Spacesuit model:
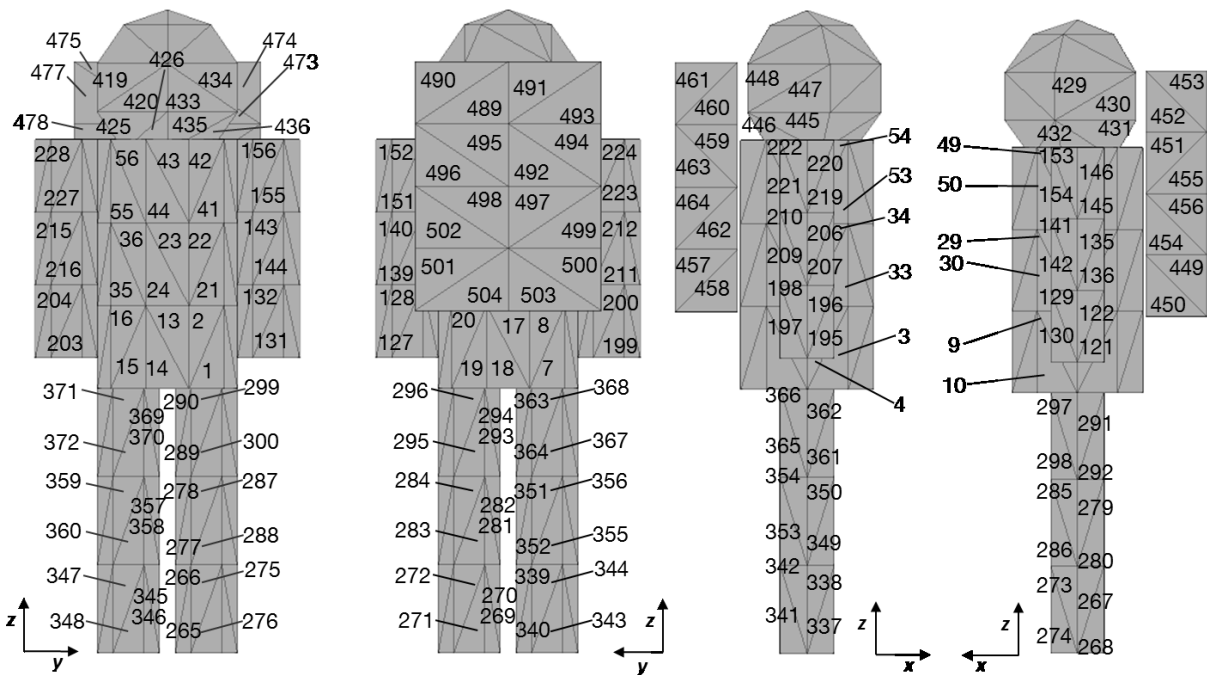
Figure A - 12: Spacesuit model – front, back, left, and right view.
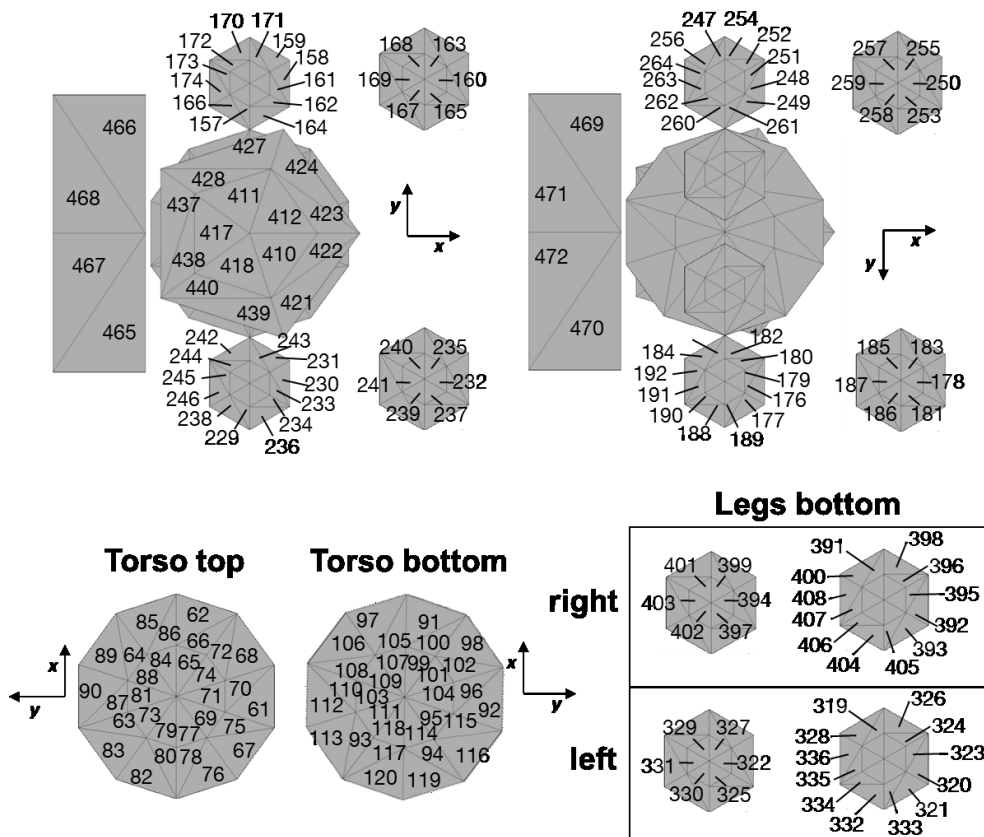
Figure A - 13: Spacesuit - top and bottom view.

A.5) Spacesuit Paths

The following tables were taken from Apollo 15 and Apollo 16 mobility reports. In the reports the TV-video records of Apollo 15 and Apollo 16 EVAs were investigated. One of the main points of investigation was the velocity of the astronauts which are presented in Table A - 1 and Table A - 2. Besides the times necessary to perform certain tasks were evaluated and compared to Earth based tests and the estimates made by the ground crew. Furthermore, the different gaits developed by the astronauts were investigated and their efficiency was compared and evaluated.

Table A - 1: Values from the Apollo 15 mobility report (Kubis et al. 1972a).

Segment	Distance [ft] / [m]	Time [s]	Rate [ft· s⁻¹] // [m·s⁻¹]	Terrain
EVA1				
a	4.80 // 1.46	4.0	1.2 // 0.37	Uphill slope, smooth
b	6.10 // 1.86	6.0	1.0 // 0.31	Uphill slope, smooth
c	6.70 // 2.04	7.5	0.9 // 0.27	Uphill slope, smooth
d	9.00 // 2.74	6.0	1.5 // 0.46	Level, smooth carrying LCRU
e	7.40 // 2.26	5.0	1.5 // 0.45	Level, smooth carrying extension handle
EVA 2				
a1	38.50 // 11.73	20.0	1.9 // 0.59	Downhill slope, smooth
a2	42.00 // 12.80	20.8	2.0 // 0.62	Downhill slope, smooth, carrying camera
b1	5.00 // 1.52	5.5	0.9 // 0.28	Level, smooth
b2	3.00 // 0.91	1.6	1.9 // 0.57	Level, smooth
EVA 3				
a	15.00 // 4.57	12.6	1.2 // 0.36	Level, and relatively rough terrain
b	4.80 // 1.46	2.5	1.9 // 0.59	Level, and relatively rough terrain

Table A - 2: Values from the Apollo 16 mobility report (Kubis et al. 1972b).

Segment	Distance [ft] / [m]	Time [s]	Rate [ft· s⁻¹] // [m·s⁻¹]	Terrain
EVA1				
a	53.00 // 16.15	30.9	1.73 // 0.53	Level, small rocks, carrying scoop.
EVA 2				
b	169.00 // 51.51	76.0	2.22 // 0.68	Downhill, carrying rake and gnomon.
	23.00 // 7.01	11.6	1.98 // 0.60	Level to uphill, small rocks, carrying tongs.
	54.00 // 16.46	21.7	2.49 // 0.76	Level, loose soil, carrying penetrometer.
EVA 3				
	25.00 // 4.57	15.8	1.58 // 0.48	Level, small to large rocks.
	25.00 // 4.57	15.3	1.63 // 0.50	Same as last segment but carrying scoop.
	297.00 // 90.53	99	3.00 // 0.91	Level with depressions, few large rocks.
EVA1				
a	53.00 // 16.15	30.9	1.73 // 0.53	Level, small rocks, carrying scoop.
EVA 2				

b	169.00 // 51.51	76.0	2.22 // 0.68	Downhill, carrying rake and gnomon.

A.6) Overview *TherMoS* Functions

Figure A - 14 shows all functions implemented in the *TherMoS* software package at the time of submission of this thesis. The functions are clustered thematically and stored in different folders. The folders are shown in Figure A - 15.
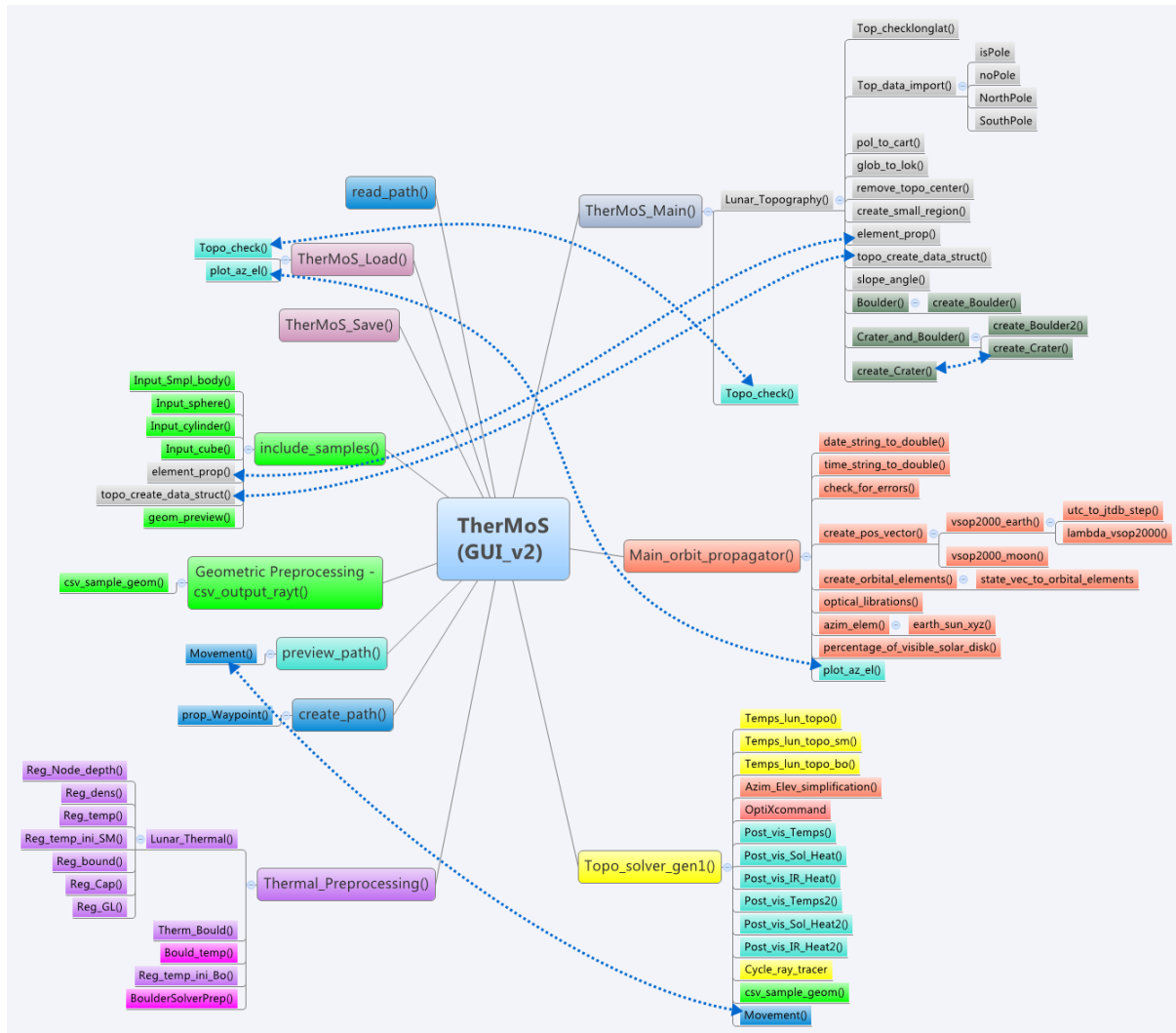

Figure A - 14: MATLAB® Functions in the *TherMoS*-tool. The hierarchy indicates which functions are called from which parent function. The arrows indicate that the same functions are used twice in the tool. The color coding is explained in Figure A - 15.
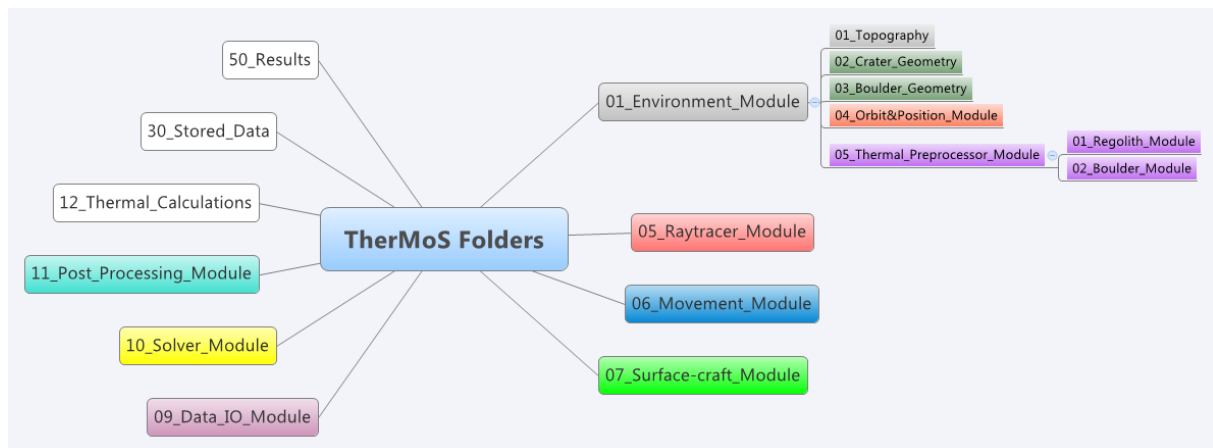
Figure A - 15: Windows® Explorer Folder structure of the *TherMoS*-tool. The colors is also used in Figure A - 14.

Appendix B – Case Study Supplement

This supplement to the results and conclusion chapters (chapters 6 & 7) is also separated in rover and spacesuit cases. Supplement rovers and spacesuit cases cover the ones not discussed in the results section.

Rover:

The depicted rover cases are the *Rover2* (equatorial rover) at the lunar pole during local noon (Figure B - 1), the *Rover1* (polar rover) at the lunar equator during local dusk (Figure B - 2), the *Rover1* at the lunar equator during local noon (Figure B - 3). Six simulation cases were run with static view factors (black line), unobstructed transit (red line), boulder-shadow (green line), boulder (blue-line), field of 5 boulders (cyan line), and crater case (magenta line). Color coding and cases are equal to those presented in section 6.5 and section 6.6. The numbers represent the segments in the rover path according to Table 6-5. On the left side of Figure B - 1 to Figure B - 3 the solar heat fluxes and on the right side the infrared heat fluxes are depicted. The solar and infrared heat fluxes are the sum over all rover surface elements.
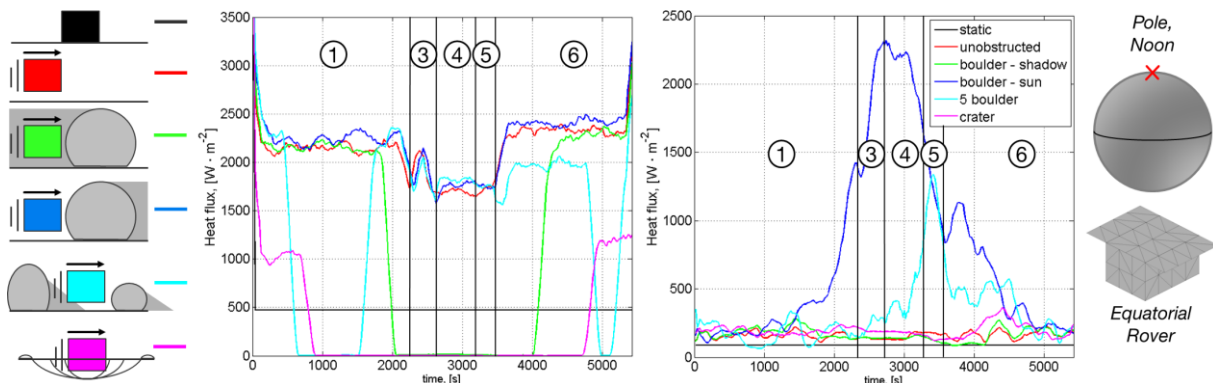
Figure B - 1: *Solar* (left) and *infrared* (right) heat flux densities for different parameter settings at the lunar pole during local noon for Rover2.
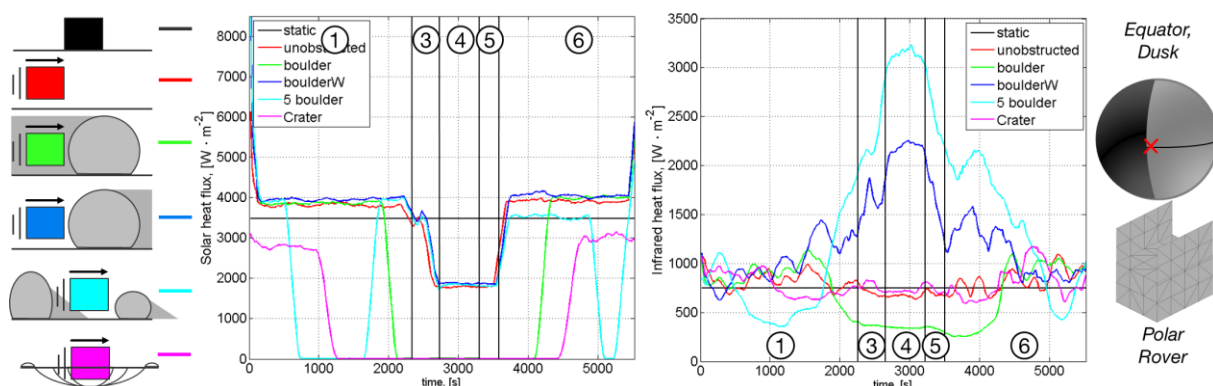
Figure B - 2: *Solar* (left) and *infrared* (right) heat flux densities for different parameter settings at the lunar equator during local dusk for Rover1.
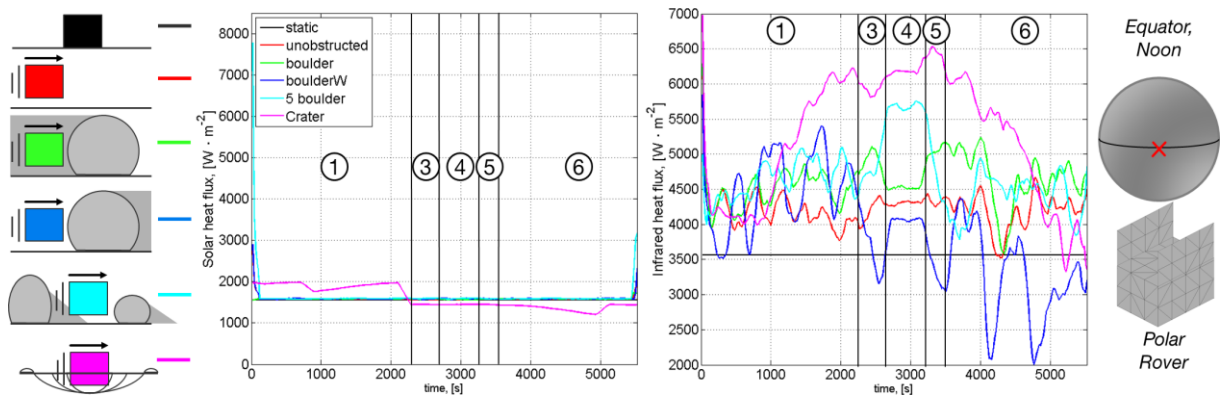
Figure B - 3: *Solar* (left) and *infrared* (right) heat flux densities for different parameter settings at the lunar equator during local noon for Rover1.

Spacesuits:

Figure B - 4 to Figure B - 11 show heat flux and heat flux rates for the spacesuit at the equator and at the pole during local noon. Equator noon and pole noon cases refer to solar elevation angles of 90° and 2°, respectively. The presented cases supplement to the spacesuit equator dusk cases discussed in section 6.6 and section 7.1.3 (a solar elevation angle of 10°). Six simulation cases were run with static view factors (black line), unobstructed transit (red line), boulder-shadow (green line), boulder (blue-line), field of 5 boulders (cyan line), and crater case (magenta line). Color coding and cases are equal to those presented in section 6.5 and section 6.6. The numbers represent the segments in the spacesuit path according to Table 6-6.
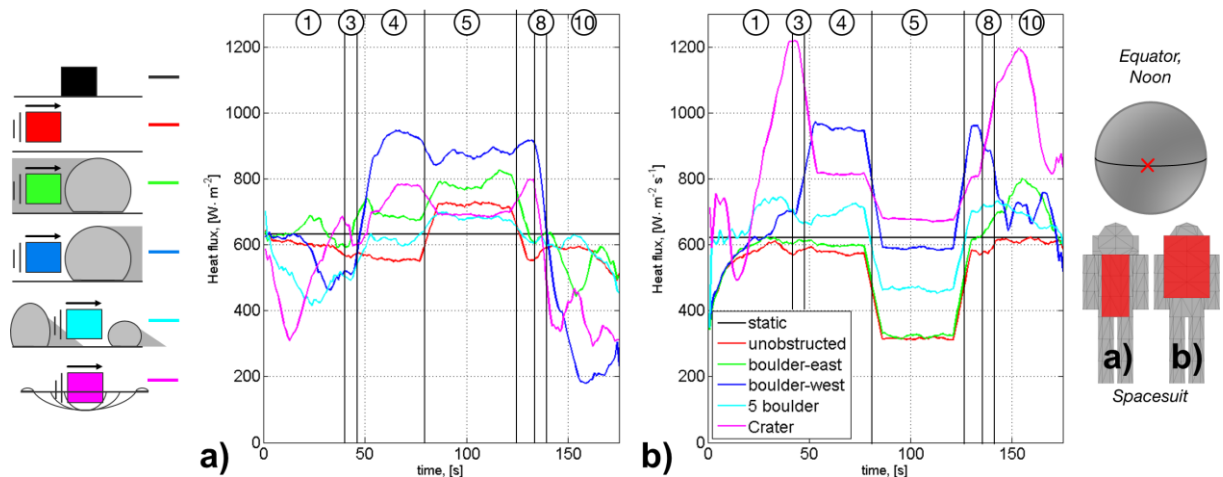
Figure B - 4: Infrared heat flux on a) front of the spacesuit torso and b) back of the personal life support system for five cases and a solar elevation angle of 90°. For numbers see Table 6-6.
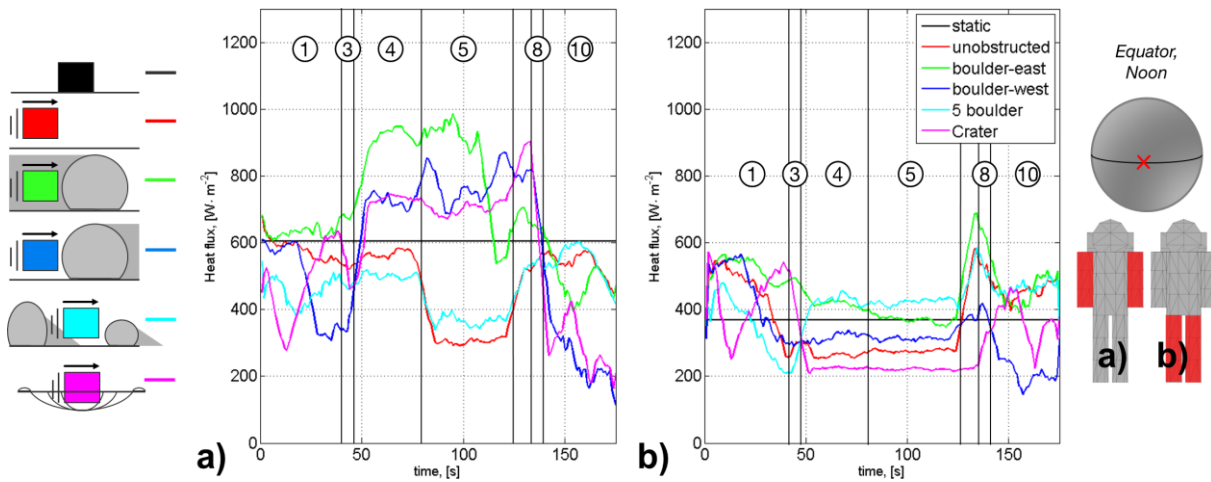
Figure B - 5: Infrared heat flux on a) arms and b) legs of the spacesuit for five cases and a solar elevation angle of 90°. For numbers see Table 6-6.
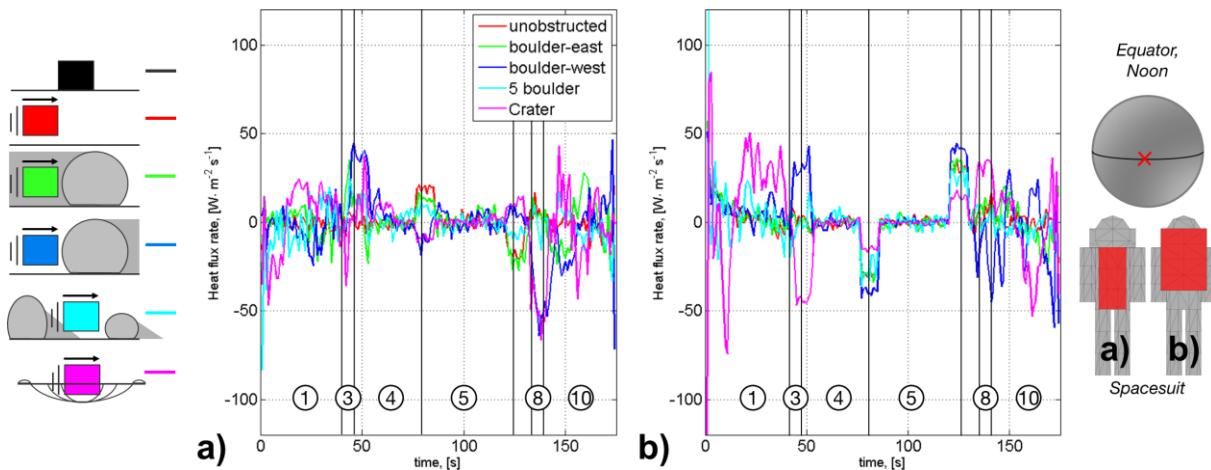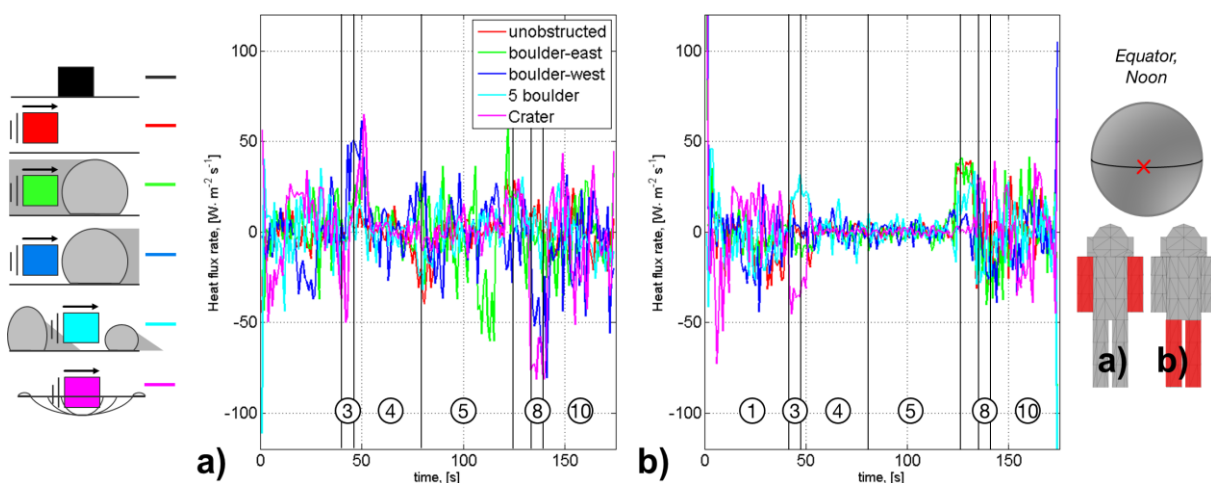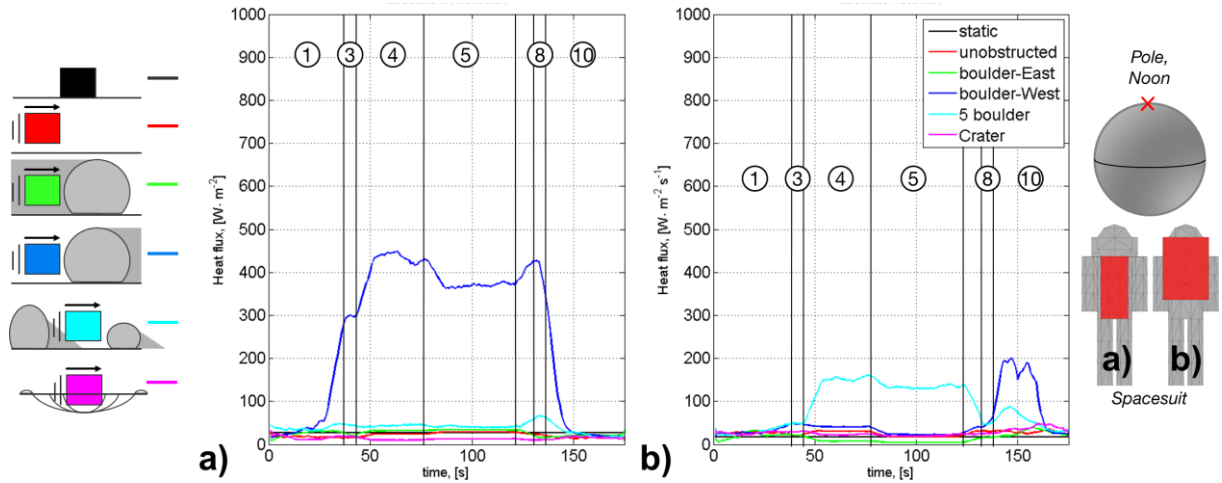

Figure B - 6: Infrared heat flux rate on a) front of the spacesuit torso and b) back of the personal life support system for five cases and a solar elevation angle of 90°. For numbers see Table 6-6.
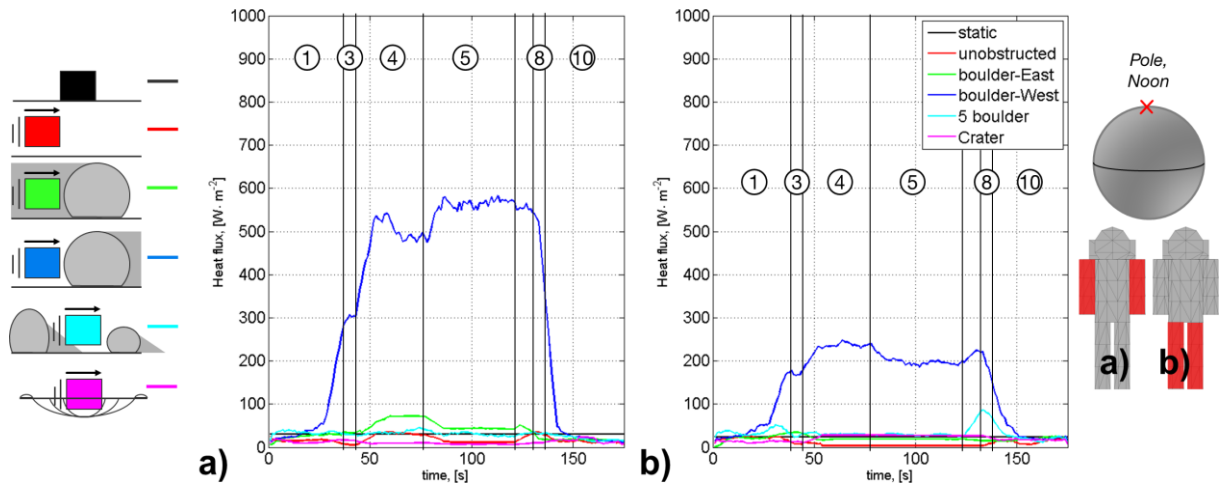

Figure B - 7: Infrared heat flux rate on the top of a) arms and b) legs system for five cases and a solar elevation angle of 90°. For numbers see Table 6-6.

Figure B - 8: Infrared heat flux on a) front of the spacesuit torso and b) back of the personal life support system for five cases and a solar elevation angle of 2°. For numbers see Table 6-6.
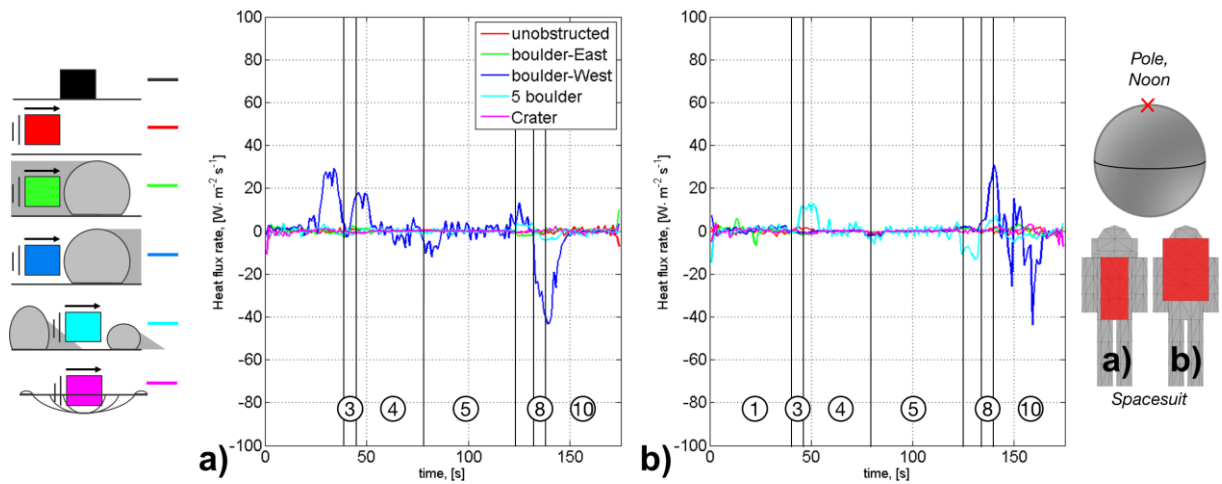

Figure B - 9: Infrared heat flux on a) front of the spacesuit torso and b) back of the personal life support system for five cases and a solar elevation angle of 2°. For numbers see Table 6-6.

Figure B - 10: Infrared heat flux rate on a) front of the spacesuit torso and b) back of the personal life support system for five cases and a solar elevation angle of 2°. For numbers see Table 6-6.
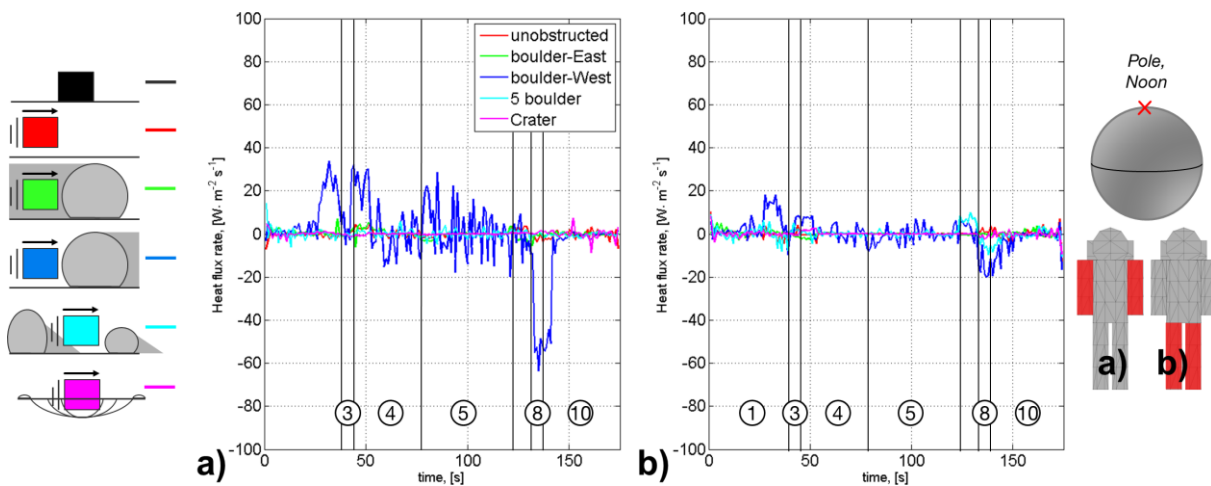
Figure B - 11: Infrared heat flux rate on the top of a) arms and b) legs system for five cases and a solar elevation angle of 2°. For numbers see Table 6-6.

Figure B - 12 and Figure B - 13 show the maximum infrared heat flux on the torso and top of the arms of the spacesuit sample body for different lunar surface temperatures and transits. The values are also gathered in Table A - 3 and Table A - 4. Diagrams and tables are a follow-up to the results presented in section 7.1.3 concerning the maximum heat flux densities on the PLSS. The sun transit has the biggest impact on infrared heat fluxes for each area of the spacesuit. It is followed by the boulder-shadow. Crater and 5-boulder cases show a smaller impact on the received infrared heat flux on torso and the top of the arms.
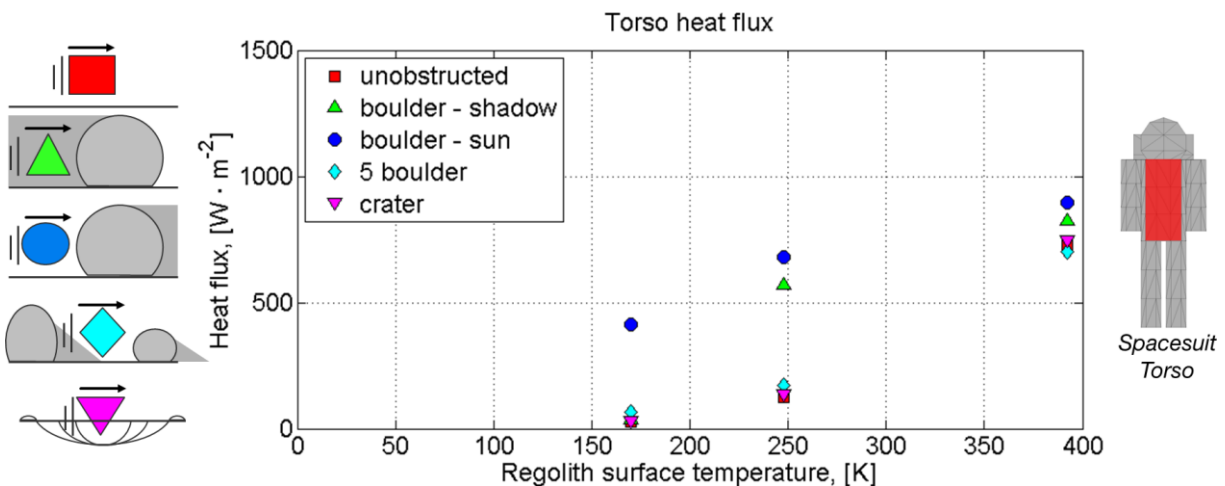

Figure B - 12: Maximum *infrared* heat flux on the front (torso) of the spacesuit sample body for different lunar surface temperatures and transits.

Table A - 3: Absolute and relative deviation of total *infrared* heat flux on the torso, between obstructed and unobstructed cases for three lunar surface temperatures.

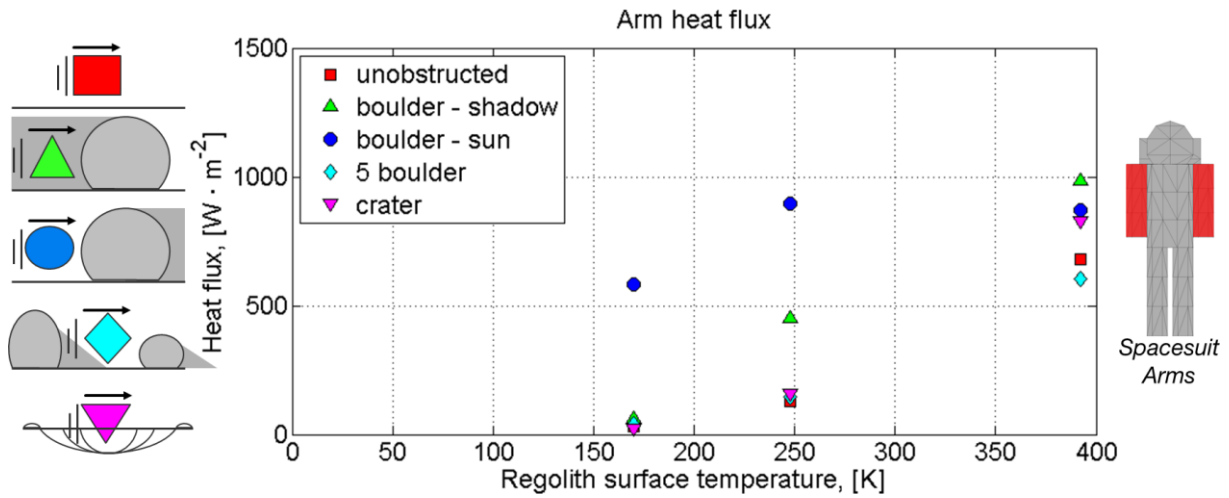| Temp.	Infrared heat flux							
	absolute [W·m⁻²]				relative [%]			
[K]	bo	boW	5bo	cr	bo	boW	5bo	cr
392	97,4	168,4	-27,7	18,8	13,4	23,1	-3,8	2,6
248	447,7	557,4	49,8	14,5	363,8	453,0	40,5	11,7
170	5,3	383,2	37,1	3,6	18,3	1321,2	128,0	12,6

Figure B - 13: Maximum *infrared* heat flux on the top of the arms of the spacesuit sample body for different lunar surface temperatures and transits.

Table A - 4: Absolute and relative deviation of total *infrared* heat flux on the arms, between obstructed and unobstructed cases for three lunar surface temperatures.

Temp.	Infrared heat flux							
[K]	absolute [W·m⁻²]				relative [%]			
	bo	boW	5bo	cr	bo	boW	5bo	cr
392	305,7	191,0	-76,2	147,7	45,0	28,1	-11,2	21,7
248	322,2	763,2	14,0	28,8	245,9	582,3	10,6	22,0
170	28,9	549,8	7,3	-9,1	86,7	1648,2	22,0	-27,3

Figure B - 14 shows the relative frequency for a heat flux rate in infrared heat flux for all cases throughout the entire path and a solar elevation angle of 90°, which corresponds to a surface temperature of 392 K. In contrast to the case with a solar elevation angle of 10°, higher rates of change occur at higher relative frequencies. In Figure B - 15 the relative frequency over heat flux rate in infrared heat flux is shown for the solar elevation angle of 2° which corresponds to surface temperatures of 170 K at the lunar Poles. Contrary to the distribution for solar elevation angles of 90° the polar case with a low angle of solar elevation predominantly exhibits values of rates of change < 5 W·m⁻². The general progression of Figure B - 14 and Figure B - 15 also can be approximated by a power function with negative exponent.
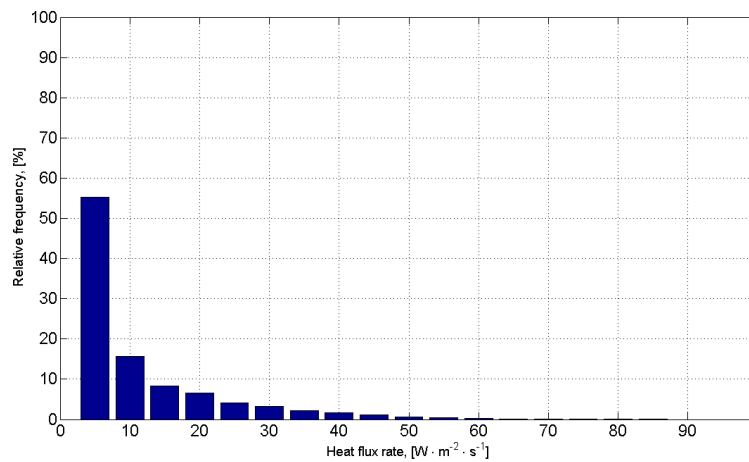
Figure B - 14: Relative frequency for a heat flux rate in infrared heat flux for all cases throughout the entire path and a solar elevation angle of 90° - a surface temperature of 392 K.
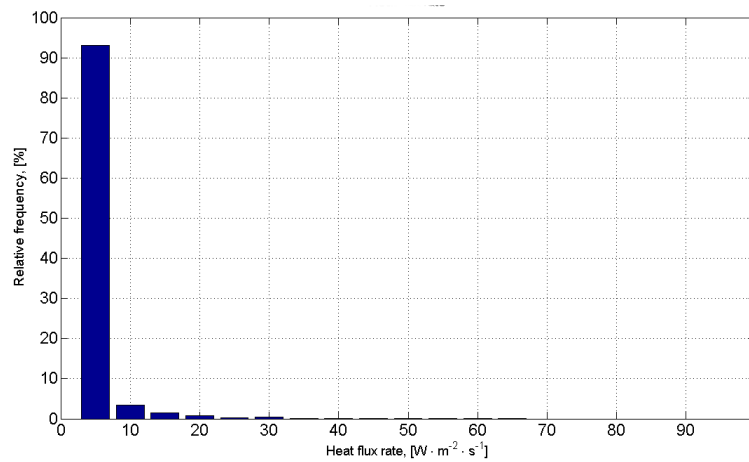

Figure B - 15: Relative frequency for a heat flux rate in infrared heat flux for all cases throughout the entire path and a solar elevation angle of 2° - a surface temperature of 170 K.